INVESTIGATION OF EXCHANGE BIAS PHENOMENON IN MULTIFUNCTIONAL MAGNETIC THIN FILMS AND BILAYER

Ph.D. THESIS

by

ARCHANA MISHRA

CENTRE OF NANOTECHNOLOGY
INDIAN INSTITUTE OF TECHNOLOGY ROORKEE
ROORKEE-247667, INDIA
DECEMBER, 2015

INVESTIGATION OF EXCHANGE BIAS PHENOMENON IN MULTIFUNCTIONAL MAGNETIC THIN FILMS AND BILAYER

A THESIS

Submitted in partial fulfilment of the requirements for the award of the degree **of**

DOCTOR OF PHILOSOPHY

in

PHYSICS

by

ARCHANA MISHRA

CENTRE OF NANOTECHNOLOGY
INDIAN INSTITUTE OF TECHNOLOGY ROORKEE
ROORKEE-247667, INDIA
DECEMBER, 2015

INDIAN INSTITUTE OF TECHNOLOGY ROORKEE
ROORKEE

CANDIDATE'S DECLARATION

I hereby certify that the work which is being presented in the thesis entitled, "**INVESTIGATION OF EXCHANGE BIAS PHENOMENON IN MULTIFUNCTIONAL MAGNETIC THIN FILMS AND BILAYER**" in partial fulfilment of the requirements for the award of the Degree of Doctor of Philosophy and submitted in the Centre of Nanotechnology of the Indian Institute of Technology Roorkee, Roorkee is an authentic record of my own work carried out during a period from Jan 2013 to Dec 2015 under the supervision of Dr. Ramesh Chandra, Professor, Institute Instrumentation Centre, Indian Institute of Technology Roorkee, Roorkee

The matter presented in the thesis has not been submitted by me for the award of any other degree of this or any other Institute.

(**Archana Mishra**)

This is to certify that the above statement made by the candidate is correct to the best of my knowledge.

Dated: (**Ramesh Chandra**)
Supervisor

The Ph.D. Viva-Voce Examination of **Mrs. Archana Mishra**, Research Scholar, has been held

on .....

Chairman, SRC **Signature of External Examiner**

This is to certify that the student has made all the corrections in the thesis.

Signature of Supervisor **Head of the Department**

Date: .....

Dedicated

to

My Family

ABSTRACT

Heusler alloys are one of the important multifunctional alloys that are also magnetically ordered and have properties such as magnetic shape memory effect (MSME), magnetic super elasticity, magnetocaloric effect (MCE) and magnetostriction. These magnetically ordered alloys were first discovered in 1903 by Heusler, Stark and Haupt in Cu_2MnAl showing strong ferromagnetism. The crystal structure of these Heusler alloy has been described as four interpenetrating f.c.c. ($L2_1$ structure) sublattice with stiochiometric composition X_2YZ. Further research indicated that the magnetic properties originating in these alloys system are dependent on the chemical composition, crystal structure, and to the ordering of the atoms on an f.c.c. sublattice. These alloys exhibit most of the properties of metals but have the structure of an ordered compound in which magnetism may originate from several different magnetic exchange mechanisms leading to magnetic properties that are ferromagnetic / antiferromagnetic or intermediate. Consequently Heusler alloys provide an opportunity for investigation of the effects of chemical and structural order on the transport and magnetic exchange interactions in these multifunctional magnetic alloy systems.

In this thesis particular attention has been given to exchange biased thin film systems where the exchange coupling occurs at the interface between ferromagnetic (FM) and antiferromagnetic (AF) layers. This an active field of research due its technological applications in magnetic read heads. The study of magnetic behaviour of a material in thin film form helps in exploring fundamental magnetization phenomenon occurring in the sample. Thin film form also offers the most suitable system for the development of practical systems and devices. With reducing dimension, the properties of a material start deviating from the bulk form. The properties of thin film are different from those of the bulk form of same material and when the thickness of the film reaches nanoscale dimension, the properties are usually completely different from bulk form of same material. Thin films and multilayers / heterostructures offer the advantage of controlling thickness / interface and study the critical phenomenon originating from interfacial effects which is not possible in other low dimension systems like very fine particles. From the early 1980s thin films have played a crucial role in understanding magnetic phenomenon and developing devices like higher-density nonvolatile random access memory and giant magnetoresistance based

systems. Owing to the far reaching consequences of giant magnetoresistance effect in developing devices, thin film has been established as one of the ideal model for understanding some fundamental physical mechanism. The results can then be used for the design of material with improved performance.

Magnetic properties of a FM material are drastically altered in the vicinity of an antiferromagnet giving rise to the phenomenon of exchange bias. Exchange bias has been observed in many systems with antiferromagnet – ferromagnet interfaces such as spin glasses, nanoparticles and bilayers. A class of multifunctional materials with high potential for applications are Heusler alloys. Heusler alloys are one of the important multifunctional alloys that are also magnetically ordered and have properties such as magnetic shape memory effect (MSME), magnetic superelesticity, magnetocaloric effect (MCE) and magnetostriction. Historically Heusler alloys are of two classes: (i) the full Heusler alloys with the general formula X_2YZ and (ii) the half Heusler alloys that have general formula XYZ. The half Heusler alloys are found to be of importance for spintronic materials and are not of interest for this thesis. Among full Heusler alloys (Ni-Mn-X, X= Sn, In, Ga, Sb, Al), Ni-Mn-Al alloys are interesting as their mechanical properties are superior and they are potential high temperature shape memory alloy. Further Ni–Mn–Al system has so far received much less attention. In this thesis exchange bias properties of Ni-Mn-Al off-stoichiometric full Heusler alloy thin films have been studied in detail. Along with this Ni-Mn-Al / Ni bilayer system and Ni-Mn-Al-In thin films have also been explored for their exchange bias effect.

Investigation on exchange bias properties of Heusler alloys and bilayers by several research group including ours reveal that the exchange bias properties exhibited by Heusler alloys are very sensitive to the thinkness, composition and microstructure of the alloy. In order to further elucidate this point, in this thesis, we attempt to study exchange bias in Ni-Mn-Al system, Ni-Mn-Al-In system and Ni-Mn-Al / Ni bilayer system.

Chapter 1 The literature survey, important findings and discussions relavent to the thesis have been discussed. Definition and various models of exchange bias suggested have been mentioned. Details of work carried out for NiMnAl and NiMnIn have also been discussed. The basis of the present thesis work has been discussed and the important results obtained for various systems have been given in tabulated form.

Chapter 2 In this chapter various characterization tools have been discussed which are carried out during this thesis work. This includes XRD, SEM, TEM, Nanoindentation and SQUID. The principal behind every technique and the information obtained have also been discussed.

Chapter 3 Exchange Bias property of Ni rich and Mn rich thin Films have been explored. The films have been cosputter deposited using elemental targets of Ni, Mn & Al. It has been observed that Ni rich compositions exhibit a mixed $L2_1$ + B2 structure at thickness ≤ 1.5 μm. For larger thickness, a pure B2 structure has been observed. The Mn rich compositions exhibit a pure B2 structure independent of thickness. The structure and magnetic properties of Ni rich and Mn rich Heusler alloys have been studied in detail. Martensitic transition has been observed for the films exhibiting B2 as well as mixed (B2+ $L2_1$) structure. For very thin films no martensitic transition has been observed in both the systems. Owing to the presence of ferromagnetic ($L2_1$) and antiferromagnetic (B2) phase in film with mixed structure ($L2_1$+ B2), the exchange bias has been observed in these films. The exchange bias observed in Ni rich samples has been explained in terms of the existence of a spin glass state at low temperature. Exchange bias has also been observed in B2 phase films associated with the field induced ferromagnetic type ordering occurring in the antiferromagnetic matrix. An increase in exchange bias with increasing film thickness has been observed in Ni rich and Mn rich compositions. Large exchange bias has been observed Mn rich compositions.

Chapter 4 In this chapter the effect of ferromagnetic (Ni) layer on Ni rich $Ni_{57}Mn_{24}Al_{19}$ compostion and Mn rich $Ni_{50}Mn_{31}Al_{19}$ compositionhas been studied in detail. Thickness of both NiMnAl layer and Ni layer has been varied. The effect of cooling field and varying ferro – antiferro layer has been studied in detail.

For the Ni layer deposited on Ni rich compositions, exchange bias increases with increasing cooling field. For a particular thickness of Ni rich NiMnAl layer, effect of Ni variation is non monotonic. The thickness of Ni layer at which maximum exchange bias occurs depends on the thickness of NiMnAl layer. Maximum EB has been obtained for Ni layer thickness of 60nm.

For the Ni layer deposited on Mn rich compositions, exchange bias shows non-monotonic variation with increasing cooling field. For a particular thickness of Mn rich NiMnAl layer, effect of Ni variation is non monotonic. The thickness of Ni layer at which maximum exchange bias occurs depends on the thickness of NiMnAl layer. For 1 μm thick film maximum H_{EB} has been

obtained for 30 nm thick film. For 2.5 μm thick film maximum H_{EB} has been obtained for 60 nm thick film. The exchange bias increases with Ni layer for NiMnAl thickness of 1 μm, for other films H_{EB} decreases with Ni layer. Variation of EB with temperature has also been discussed in terms of existing models.

Chapter 5 In this chapter exchange bias properties of NiMnAlIn thin films have been studied. Thin films have been deposited by co-sputtering from target of NiMnAl and In. Thin films of thickness have been deposited. Owing to the ferromagnetic nature of NiMnIn films and antiferromagnetic NiMnAl films, coexisting ferro – antiferro interactions occur in the deposited films which give rise to exchange bias interactions. The effect of cooling field and temperature on exchange bias properties has been discussed. Training effect has also been done to study the exact nature of exchange bias phenomenon in this alloy system. Large exchange bias of 475 Oe at 10 K has been obtained for the film with thickness 1.2 μm.

Chapter 7 Summarizes the results and findings of the present work discussed in this thesis. The future directions in which these studies can be extended have been suggested at the end.

ACKNOWLEDGEMENTS

The research presented in this doctoral thesis has been carried out at Centre of Nanotechnology and Institute Instrumentation Centre IIT Roorkee, Roorkee, India. The completion of my thesis has been due to enormous support and encouragement of numerous people. At this moment of accomplishment, first of all I pay my sincere appreciation to my supervisor, Prof. Ramesh Chandra, who assisted and guided me throughout the entire study. His smiling face persona, frank and friendly temperament provided a stimulating and fun filled environment in the laboratory for pursuing the research work. His invaluable guidance, support, encouragement and suggestions from the initial to the final level of my work helped me to improve the quality of work and enabled me to develop an understanding of the subject. His gracious approach and motivation were the major strength in successfully overcoming tough times during my research work. He not only boosted my moral in tough conditions but also injected a fair degree of self confidence in me. I express my sincere thanks to Prof. S.K. Nath, Head of Centre of Nanotechnology, and all other faculty members of Centre of Nanotechnology for their keen interest in this work. I take this opportunity to thank all the members of my SRC committee, Prof. G.D. Verma (Chairman CRC), Department of Physics, Prof. R. P. Singh (Chairman SRC), Department of Biotechnology, Dr. Sanjeev Manhas (Internal member), E & C Department and Dr. A. K. Sharma (External Member), Department of Biotechnology, IIT Roorkee for their invaluable suggestions and encouragement to carry out this work. I am highly obliged and express my sincere thanks to the official & technical staff of Centre of Nanotechnology (Mr. R. Pal and Mr. Naresh) and Institute Instrumentation Centre, IIT Roorkee. I wish to acknowledge Mr. Kamal Singh Gotyan, Mr. R.K. Sharma, Mr. Rajneesh, Mr. Ashok kumar, Mr. Birendar Dutt, Mr. S.D.Sharma, Mr. D.R.S. Pundir, Mr. Mahavir Singh, Mr. Yashpal, Mr Anil, and Mr. Shiv Kumar in our lab for their cooperation and affection. I wish to give my heartiest thanks to Mr. Subhash Pai for designing and manufacturing the experimental equipments.

I greatly enjoyed working with all my lab mates Dr. Amit Kumar Chawla, Dr. Vipin Chawla, Dr. Preetam, Dr. Ashwani, Dr. Y.K. Gautam, Dr. Mukesh Kumar, Dr. Rajan Walia, Dr

Paritosh Dubey, Ravish Jain, Samta Chauhan, Monu Verma, Amit Rajput, Ashwani Kumar, Amit Sanger, Jyoti, Arvind, Gaurav Malik, Satyendra, Sneha, Mukesh Tripathi, Dr. Padmanabhan, Kiran, Nitin, Harish, Rahul, Nabhjot and Ankita singh, and I thank them all for their full cooperation and ever needed help throughout to carry out this work and also for being around all the time. During my research work in lab I greatly enjoyed my interaction with M.Tech students Vivek Surana, Anuj Kumar, Gurjinder Kaur, Sandhya, Amit Singh, and Sonam Jain. I have been blessed with a friendly and cheerful group of buddies like Aneeta, Geetanjali, Yogita, Nidhi, Sarita and Ritu. I enjoyed every single moment spent with them. Their friendly behavior helped me to feel home away from home. The financial support provided by Ministry of Human Resource Development (MHRD), Govt. of India as a fellowship for this work is gratefully acknowledged.

I am grateful to Paritosh Dubey for his support in the experimental work carried out in the lab. I am grateful to Paritosh Dubey, Amit Rajput, Samta Chauhan, Jyoti, Jyoti Aggarwal, Preeti, Gurjinder, Mukesh Tripathi, Vivek Surana, Anuj Kumar and Amit Singh for providing me homely atmosphere at IIT Roorkee. Friendship and social support provided by friends like Mr. Amit chauhan, Dr. Neeta, Dr. Paritosh Singh, Mrs. Nisha, Dr. Vindesh is also acknowledged.

I would like to express my sincere thanks to all my parents for their moral support. I also thank my husband Dr. Saurabh Srivastava for his guidance, suggestions and full time support. It would be impossible what I am today without my loving husband. A special thanks to my Mother in law and my daughter for their support. Words cannot express how grateful I am to my family for all of the sacrifices that they've made on my behalf. Their prayer for me was what sustained me thus far. At the outset, let me thank the almighty God who is the most graceful and generous for his blessing that has given me courage, strength to face any adverse situation, wisdom to make wise decisions and pleasant, memorable moments of my life.

Our work greatly improved thanks to the comments of the anonymous reviewers and editors of the articles published with contributions of this thesis. I would like to thanks everybody who was important to the successful realization of thesis, as well as expressing my apology that I could not mention personally one by one.

(Archana Mishra)

CONTENTS

LIST OF FIGURES

LIST OF TABLES

NOMENCLATURE

T_m	Martensitic Transition Temperature
T_C	Curie Temperature
T_N	Neel Temperature
E_g	Fermi Level (Energy in eV)
14M	7-layered Orthorhombic
10M	5-layered Tetragonal
χ	Magnetic Susceptibility
M_S	Matensite Start Temperature
M_F	Matensite Finish Temperature
A_S	Austenite Start Temperature
A_F	Austenite Finish Temperature
k_B	Boltzmann Constant
N_A	Avogadro Number
H_{EB}	Exchange bias field

LIST OF PUBLICATIONS

1. Archana Mishra, S. K. Srivastava, Arvind Kumar, Paritosh Dubey, Samta Chauhan, D. Kaur, R.Chandra *"Thickness dependent exchange bias in co-sputter deposited Ni-Mn-Al Heusler alloy hard nanostructured thin films*", *Thin Solid Films* 572, 142-146 (2014).

2. Anand Kamlapure, Mintu Mondal, Madhavi chand, *Archana Mishra*, John Jesudasan, Vivas Bagwe, L. Benfatto, Vikram Tripathi and Pratap Raychaudhuri "Penetration depth and tunnelling studies in very thin epitaxial NbN films" *Appl. Phys. Lett.* 96, 072509 (2010).

3. Madhavi Chand, *Archana Mishra*, Y. M. Xiong, Anand Kamlapure, S. P. Chockalingam, John Jesudasan, Vivas Bagwe, Mintu Mondal, P. W. Adams, Vikram Tripathi, and Pratap Raychaudhuri "Temperature dependence of resistivity and Hall coefficient in strongly disordered NbN thin films" *Phys. Rev. B* 80, 134514 (2009).

4. S. P. Chockalingam, Madhavi Chand, AnandKamlapure, John Jesudasan, *Archana Mishra*, Vikram Tripathi and Pratap Raychaudhuri "Tunneling studies in a homogeneously disordered s-wave superconductor: NbN" *Phys. Rev. B* 79, 094509 (2009)

CHAPTER 1

INTRODUCTION AND LITERATURE REVIEWS

1.1 Introduction

The study of magnetic behaviour of a material in thin film form helps in exploring fundamental magnetization phenomena occurring in the sample. Thin film form offers the most suitable system for the development of practical systems and devices. With reducing dimension, the properties of a material start deviating from the bulk form. The properties of thin film are different from those of the bulk form of same material and when the thickness of the film reaches nanoscale dimension, the properties are usually completely different from bulk. Thin films and multilayers / heterostructures offer the advantage of controlling thickness / interface and study the critical phenomenon originating from interfacial effects which is not possible in other low dimension systems like very fine particles. From the early 1980s thin films have played a crucial role in understanding magnetic phenomenon and developing devices like higher-density nonvolatile random access memory [1,2] and giant magnetoresistance based systems. Owing to the far reaching consequences of giant magnetoresistance effect in developing devices, thin film has been established as one of the ideal model for understanding some fundamental physical mechanism. The results can then be used for the design of material with improved performance.

In this thesis particular attention has been given to exchange biased thin film systems where the exchange coupling occurs at the interface between ferromagnetic (FM) and antiferromagnetic (AF) layers. This an active field of research due its technological applications in magnetic read heads. Magnetic properties of a FM material are drastically altered in the vicinity of an antiferromagnet giving rise to the phenomenon of exchange bias. Exchange bias has been observed in many systems with antiferromagnet –ferromagnet interfaces such as spin glasses, nanoparticles and bilayers [3-5]. Given the trend of minimization in electronics, there is currently a focus on the exchange bias effect in small scale systems such as thin films.

Multifunctional alloys are those “smart” or “intelligent” materials for which more than one physical parameters vary with an externally applied stimulus; giving rise to utility of these materials for more than one purposes. In recent years, research in the field of novel multifunctional alloys has attracted growing interest among researchers. A class of multifunctional materials with high potential for applications are Heusler alloys [6]. Heusler alloys are one of the important multifunctional alloys that are also magnetically ordered and have properties such as magnetic shape memory effect (MSME) [7], magnetic superelesticity [8], magnetocaloric effect (MCE) [9] and magnetostriction [10]. Historically Heusler alloys are of two classes: (i) the full Heusler alloys with the general formula X_2YZ and (ii) the half Heusler alloys that have general formula XYZ. The half Heusler alloys are found to be of importance for spintronic materials and are not of interest for this thesis. Among full Heusler alloys (Ni-Mn-X, X= Sn, In, Ga, Sb, Al), Ni-Mn-Al alloys are interesting as their mechanical properties are superior and they are potential high temperature shape memory alloy [11]. Further Ni–Mn–Al system has so far received much less attention. In this thesis exchange bias properties of Ni-Mn-Al off-stoichiometric full Heusler alloy thin films have been studied in detail. Along with this Ni-Mn-Al / Ni bilayer system and Ni-Mn-Al-In thin films have also been explored for their exchange bias properties.

1.2 Exchange bias

In 1956, Meiklejohn and Bean [12-14] while studying Co particles surrounded by antiferromagnetic CoO oxide observed the phenomenon of magnetic exchange anisotropy and a shift of hysteresis loop along the field axis called exchange bias (**Fig. 1.1**).

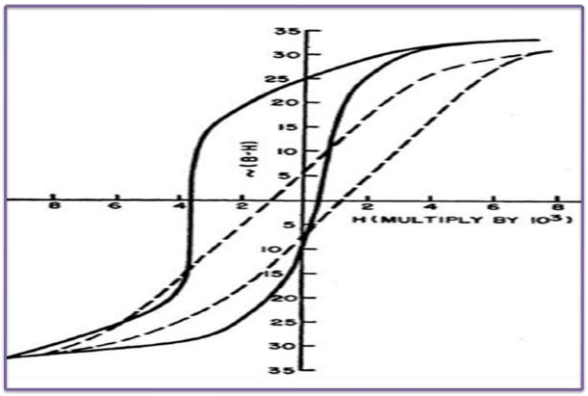

Figure 1.1 The shifted hysteresis loop of the Co particles after cooling in field of 10kOe (solid line) cooling in zero field (dashed lines) [12,13]

The signature of occurrence of exchange bias phenomenon is the shift of hysteresis loop schematically shown in **Fig. 1.1**. This unidirectional anisotropy produces an easy direction of the magnetization that arises due to the direct exchange coupling which occurs at the interface between an AFM and a FM when the specimen is cooled through Neel temperature T_N under a magnetic field. The interfacial interaction between the FM-AFM spins at the interface tries to keep them in their original position. Thus, the field needed to reverse completely a FM layer will be larger if it is in contact with an AFM.

The coercivity $H_C$and exchange bias H_E are defined as –

$$H_E = (H_{C1} + H_{C2}) / 2$$

$$H_E = (H_{C1} - H_{C2}) / 2$$

where H_{C1} and H_{C2} are the left hand side coercivity and right hand side coercivity respectively. In most of the cases, H_C is positive and H_E is negative.

Since its discovery by Bean and Meiklejohn, exchange bias is an important part of advanced magnetic devices with potential application for basic research along with device applications like read head of recording devices, magnetoresistive random access memory, spin valve based giant magnetoresistive devices and high density magnetic recording media. Variety of systems has been studied for EB effect. This includes systems containing antiferromagnetic (AFM) / ferromagnetic(FM) interfaces, such as small particles (core/shell clusters, embedded clusters) [13,14,15], inhomogeneous materials [14,16], FM thin films on AFM single crystals [17,18] and multilayers of thin films, and patterned thin films [5,16,19]. Apart from AFM / FM interfaces, other types of interfaces have also shown the phenomenon of exchange bias, e.g. involving ferrimagnets (ferri): ferri / AFM, FM / ferri or diluted magnetic semiconductors (DMS): DMS / AFM [20-24].The structure of the particular interface is a crucial element in the mechanism of exchange bias. Most widely studied interface structures between AFM and FM are fully uncompensated interface and fully compensated interface. In fully uncompensated interface first layer of antiferromagnetic spins align ferromagnetically to the ferromagnetic spins while in fully compensated interface there is no net spin moment due to equal numbers of two antiferromagnetic sublattice spins at the interface. Fully uncompensated interface and fully compensated interfaceare shown in **Fig. 1.2 (a)** and **Fig. 1.2 (b)** respectively.

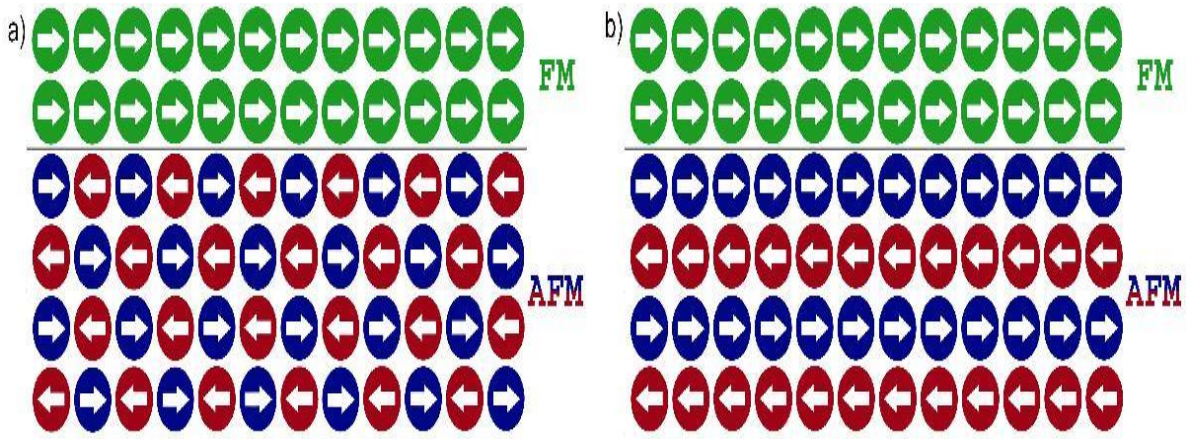

Figure 1.2 a) Exchange bias system with AFM having compensated spins on the interface, **b)** Exchange bias system with AFM having uncompensated spins on the interface.

1.3 Phenomenological model of EB and Training effect

In order to explain the shift of hysteresis loop, a simple phenomenological model used has been used which takes into consideration the microstructure magnetic phenomenon at the FM / AFM interface. The phenomenological observation of exchange bias at an FM / AFM interface is shown in **Fig. 1.3**. The essential condition for the existence of exchange bias should be satisfied i.e. the Curie temperature of ferromagnetic layer T_C should be more than the Néel temperature of antiferromagnetic phase T_N; $T_C > T_N$. At temperature T ($T_N < T < T_C$) the spins of the ferromagnetic layer are aligned along the direction of the applied field, whereas the spins of the antiferromagnetic layer remain oriented randomly in the paramagnetic state. In this state, the hysteresis loop of the sample is not affected by antiferromagnetic layer and is centered at zero. As the system is further cooled below T_N a magnetic phase transition from the paramagnetic phase to the AFM phase occurs in the system. Owing to the exchange interaction occurring between the ferromagnetic layer and the Antiferromagnetic layer at the interface, the first monolayer will align antiparallel (or parallel) to the ferromagnetic spins. The next monolayer of the antiferromagnetic layer will align antiparallel to the previous antiferromagnetic layer as to complete the AFM order, and so on (**Fig. 1.3-2)**). Due to this there are uncompensated spins in the first monolayer of antiferromagnetic (at the interface) which results in a finite net magnetization of this antiferromagnetic monolayer. On the reversal

of magnetic field, the ferromagnetic spins in the ferromagnetic layer will try to orient themselves towards the opposite direction. Owing to the exchange coupling with the antiferromagnetic spins, a largerforce and therefore a stronger external field is required to rotate the ferromagnetic spins. As a result, a larger coercive field of the hysteresis loop is obtained as compare to its value at $T > T_N$, where the FM/AFM interaction is not active. As we move back from negative saturation to positive field values (**Fig. 1.3-4)**), the ferromagnetic spins in this case need a magnetic field smaller in magnitude to rotate back to the initial direction (**Fig. 1.3-5**). On the ferromagnetic spins, torque is acting at all angles except the one which is stable direction along the field cooling direction (unidirectional anisotropy). Due to this, there is a shift of magnetization curve along the negative values of the applied magnetic field. This displacement / shifting that occurs for the centre of the hysteresis loop is known as exchange bias field H_{EB}, and isfound to be negative in comparison to the orientation of the ferromagnetic spins after field cooling (negative exchange bias). In addition to this, the hysteresis loop of the FM / AFM bilayer shows an increase in coercivity in comparison to that of an isolated ferromagnet. This is however not explained by this simple phenomenological model.

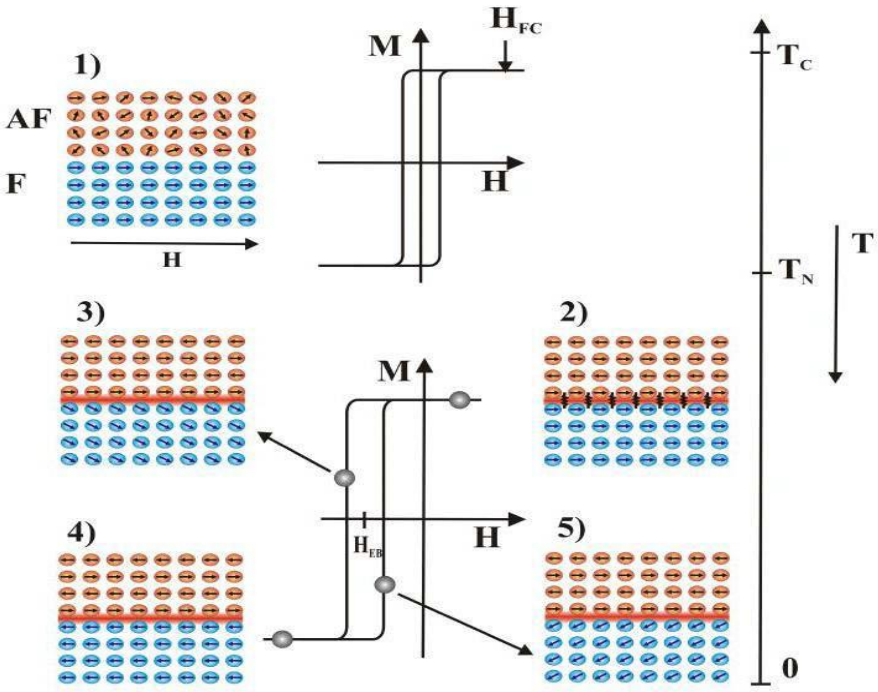

Figure 1.3. Phenomenological model of spin configuration for AFM / FM bilayer. **1)** At temp. $T_N < T < T_C$. **2)** after field cooling the system through T_N of the antiferromagnet **3)** represents the saturated state at the negative fields. **4)** and **5)** show the configuration of the spins during the positive magnetization. [12,13]

In most systems exhibiting exchange bias phenomenons, training effect has been observed. The training effect is the decrease of the shift, coercivity and the change of the shape of a hysteresis loop after several consecutive hysteresis loops for a fixed temperature. The training effect was discovered by Paccard et al.[25] in 1966 in three systems exhibiting FM-AFM coupling with uniaxial anisotropy. The first loop appears to be shifted more than the others. Also, this decrease in the shift is more significant on the left-hand branch of the loop than on the right hand, causing a decrease of the hysteresis loop's coercivity. It is common for the training effect to be separated into two categories: the effect between the first and the second loop, and the other between consecutive hysteresis loops. Especially during the first cycle the system behaves in irreversible way, because of the non-equilibrium state of the AFM that is gained during the cooling process. The second type of training effect show that the shifting decreases with the increase of the number of consecutive hysteresis loops and follows a inverse power law, as proved by Paccard et al. [25]. The cause of this is suggested to be the reconfiguration of the spins or of the domain state of the AFM during the consecutive cycles, causing fluctuations in the FM-AFM coupling. Lastly, the importance of the training effect rests on the stability of exchange bias bilayer which is inside many devices.

1.4 Models of Exchange Bias

Since its discovery exchange bias has been explored both theoretically and experimentally to reveal the details of this effect. Various models have been suggested to understand the origin of exchange bias in fully uncompensated and fully compensated systems. Most relevant models are discussed below –

1.4.1 The ideal model

A very simple qualitative model can be derived using the macroscopic observation of the hysteresis loop shift due to unidirectional anisotropy [26]. A schematic of the model is shown in **Fig. 1.4**, where T_C is the Curie temperature of the FM layer, T_N is the Néel temperature of the AFM layer, below which AFM is on the long-range AFM state. EB system materials must satisfy the condition $T_N < T_C$ for a successful cooling process.

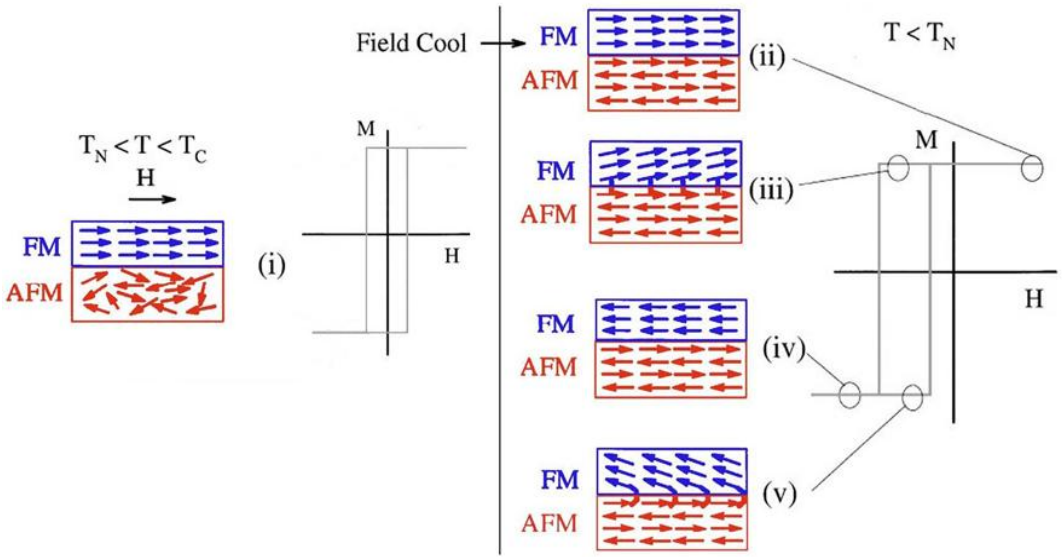

Figure 1.4: Phenomenological model of EB.

At the beginning, the system is at temperature lower than the T_C and higher than T_N ($T_N < T < T_C$). The AFM is a paramagnetic state where there occurs a random orientation of the spins, however for the FM region the orientation of the spins occur according to the external magnetic field. The hysteresis loop is centered around zero magnetic field without being affected by the AFM. The cooling process involves the application of a strong external magnetic field while decreasing the temperature to a desired value, which is smaller than the Néel temperature of the AFM. At the end of the cooling process, the AFM, due to the exchange interaction at the interface and the external magnetic field, will be in a long-range AFM state. This state will consist of uncompensated layers, anti-parallel to each other, and with the interface layer to be aligned ferromagnetically or antiferromagnetically to the FM interface layer. The interface, being uncompensated, will lead to a finite net magnetization in this layer. Both the FM and the AFM are considered to be in the single domain state remaining like that during the whole hysteresis loop. As the magnetic field reverses, the spins of the FM begin to rotate. Due to the exchange coupling between the AFM and FM, the AFM, which is considered to be rigid, will exert a small torque on the spins of the FM, opposing to the change of the direction from their original position. Consequently, an extra magnetic field is needed to reverse the magnetization, meaning that only one direction is energetically favorable (unidirectional anisotropy). In terms of the hysteresis loop, the negative coercive field will be smaller than the one at temperatures higher than the Néel temperature. During the reverse process, the small torque is exerted on the spins of the FM helping them to change back to the

original direction. So the positive coercive field will be smaller than the one at temperatures higher than the Néel temperature. Finally, the resulting hysteresis loop appears shifted to negative values of the magnetic field, with the shift called EB field and being negative. Based on the phenomenology of the previous description, Meiklejohn and Bean [13] developed a model with the following assumptions:

1. The FM rotates coherently, and has uniaxial anisotropy with the easy axis in-plane.
2. The AFM also has uniaxial anisotropy with the easy axis in-plane.
3. The AFM's spins are rigid. They remain unchanged during the magnetization reversal of the FM.
4. FM layers are in uncompensated state, so the interface layer has a net magnetic moment
5. At the interface, the AFM and the FM are coupled with an exchange interaction.

The initial model was based on the Stoner-Wohlfarth model [27], for coherent rotation of the FM magnetization. So the energy per unit area, before the cooling process can be written as:

$$H = -\mu_o H M_{FM} t_{FM} \cos(\beta) + K_{FM} t_{FM} \sin^2(\beta) \qquad \textbf{(1.1)}$$

where H is the applied magnetic field, M_{FM} is the magnetization of the FM spins during the reversal, t_{FM} is the FM's thickness, K_{FM} is the magnetocrystalline FM anisotropy constant and β is the angle between the FM magnetization and the anisotropy. The applied magnetic field is parallel to the easy axis of the FM. So, the first term describes the Zeeman energy of the system and the second term the uniaxial anisotropy. The above expression 1.1, using the stability condition give the familiar result for the coercivity:

$$H_c = \frac{2K_{FM}}{\mu_o M_{FM}} \qquad \textbf{(1.2)}$$

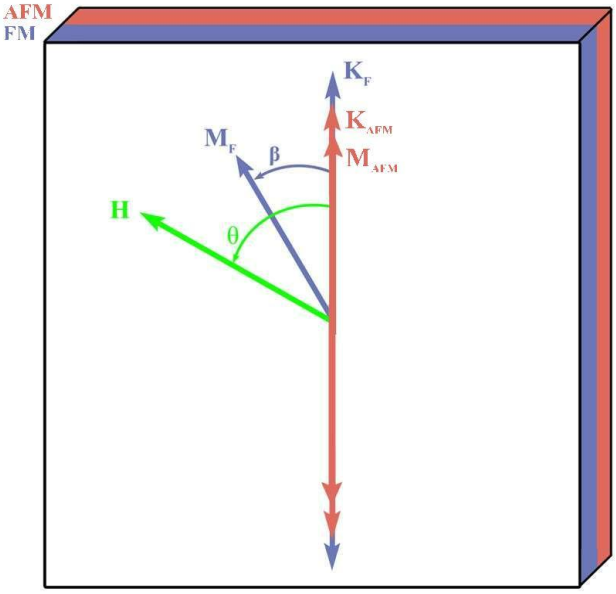

Figure 1.5: Phenomenological model with the schematic view of the vectors and angles. K_{AFM} and K_{FM} is the easy axes of the uniaxial anisotropy of the AFM and the FM, respectively. β is the angle between FM magnetization M_{FM} and the anisotropy easy axis K_{FM}. This angle is changing during the magnetization reversal. M_{AFM} is the sub-lattice magnetization of the AFM, which remains constant. The other sub-lattice magnetization is pointing to the opposite direction as showed. H is the applied magnetic field which for this model has direction parallel to the easy axis of the AFM and the cooling field ($\theta = 0$).

1.4.2 The Meiklejohn Model

A model was developed from Meiklejohn [28] based on the previous intuitive model. A new degree of freedom for the AFM magnetization was introduced in order to account for the measured non-vanishing rotational hysteresis at high fields. The AFM can rotate during the magnetization reversal, as shown in **Fig. 1.6**, without losing the generalization of rigid state of the AFM. This is because the AFM can rotate only as a whole.

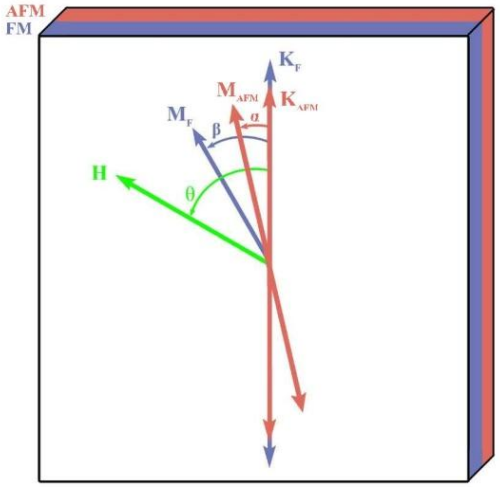

Figure 1.6: Meiklejohn model of EB with the schematic view of the vectors and angles [28].

So the energy per unit area, after the cooling process, for the previous model using the new assumption, can be written as:

$$H = -\mu_o H M_{FM} t_{FM} \cos(\theta - \beta) + K_{FM} t_{FM} \sin^2(\beta) + K_{FM} t_{FM} \sin^2(\alpha) - J_{INT} \cos(\beta - \alpha) \qquad \textbf{(1.3)}$$

where α is the angle between the AFM magnetization and the K_{AFM} uniaxial easy axis direction and t_{AFM} is the thickness of the AFM. The new term, in comparison to the previous model is the AFM anisotropy energy. It considers again that the reversal field is parallel to the AFM easy axis (θ = 0). Also, the anisotropy of the FM was neglected (K_{FM} = 0) in the above model, so the resulting coercivity is due to the exchange interaction between the FM and the AFM.

1.4.3 Planar AFM Domain wall model-Néel's approach

Since, the previous models predicted EB several orders of magnitude higher than the experimental values, and therefore new assumptions were made for this loss of coupling energy. A novel theoretical approach was made firstly by Néel [29] in which he introduced the concept of the planar domain wall in the AFM or FM layer, developed during the magnetization reversal. Particularly, he considered coupling of the FM with a low anisotropy AFM, leading to the creation of an AFM or a FM domain wall parallel to the interface. Thus,

the planar domain wall will absorb a fraction of the interface exchange coupling energy, lowering the EB phenomenon. This is the so called Néel domain wall, having the form of a partial domain wall because of the weak coupling. The model is based in calculation of the orientation of magnetization of each layer through a differential equation, predicting a minimum AFM thickness for producing of hysteresis loop shift.

1.4.4 Mauri model-Partial domain wall

Based in the idea of a partial domain wall parallel to the interface in the AFM, Mauri et al. [30] introduced a macroscopic model for the description of this domain wall which is uniform in its volume, as shown in **Fig. 1.7**. As Néel's model, the motivation of this hypothesis was to explore a possible reduction of the EB field from Meiklejohn model. The basic difference in the assumptions of this model with the Meiklejonh model is that the AFM layer develops a domain wall parallel to the interface.

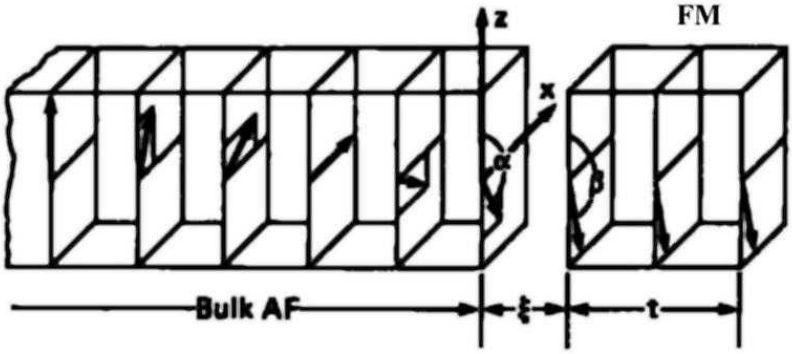

Figure 1.7: The partial domain wall developed at the interface of the AFM [30], for a system with a thin FM film on a thick AFM substrate. The magnetization of only one sublattice of the AFM is shown.

The AFM interface layer magnetization is oriented in different direction from the FM orientation making an angle α with the AFM anisotropy easy axis. The next AFM layers gradually form a magnetization perpendicular to the first one. Schematically in **Fig. 1.7**, only the one sublattice is depicted, with the magnetization of the other sublattice being oppositely oriented to complete the AFM order.

Geshev [31] used the Mauri et al. [30] model considering analytical and numerical derivation for the EB field and the coercivity. The results show discrepancies with the results of Mauri model but excellent agreement with the experimental results. These quantitative discrepancies are claimed to result from the energy minimization methodology used in each publication. The analytical derivation gave five different sets of expressions for the hysteresis loop shift and coercivity.

Xi et al. [32,33] developed a model similar to Mauri's model where they consider that a helical structure (planar domain wall) is developed as the AFM moments at the interface try to follow the magnetization of the FM during reversal. Specifically, when the AFM moments at the interface reach the AFM hard axis, the helical structure becomes unstable and the AFM moments rotate into the opposite direction. So the moments settled down to a new stable state which still contains some twisted moments. This irreversible motion was predicted by Mauri's and Néel's model.

Morosov et al. [34-36] presented a model based on Mauri's but with uncompensated AFM interface. Also, they considered rough and smooth interface using an analytical expression for its description. It is the only EB model found in the literature that used strictly analytical methods. For flat AFM interfaces they found similar domain wall behavior as Mauri's model and for rough AFM interfaces they found that EB field is caused by static spin vortices at the interface.

1.4.5 Frozen canted interface spins-Kiwi model

Kiwi et al.[37-39] introduced a new model for EB systems. This model is based on the assumption that the AFM interface is fully compensated and freezes into a canted spin state after the cooling process, keeping the AFM order, as shown in **Fig. 1.8**. Also, the magnetization of the FM is orthogonal to the AFM easy axis. They found that the energy is stored in an incomplete domain wall within the FM but no domain wall is developed in the AFM. Specifically, an exchange-spring magnet results, with EB effect and enhancement of the coercivity consistent with experimental results, as is claimed.

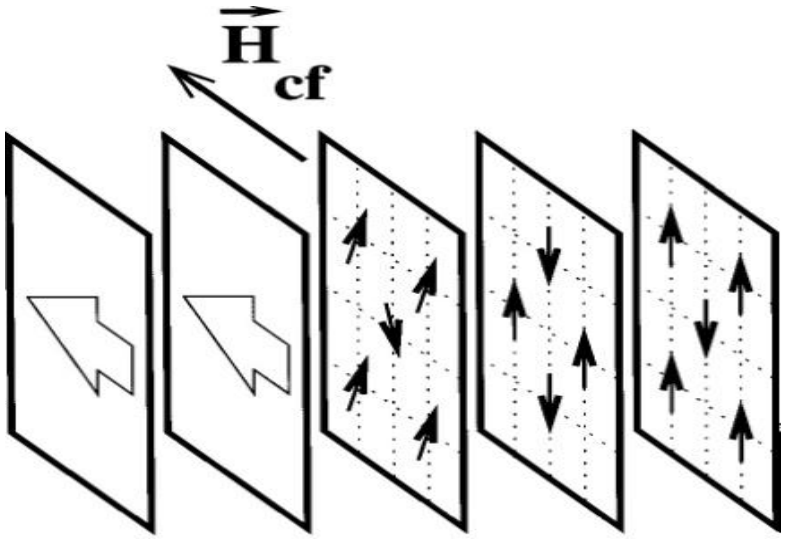

Figure 1.8: Spin configuration of the FM and the AFM layers. The AFM spins are canted relatively to the cooling field H_{cf}. [38]

1.4.6 Partial domain wall-Kim-Stamps approach

Kim and Stamps [40-46] using the previous assumptions of Néel, Mauri *et al.* and Kiwi et *al.*, they introduced the concept of the partial domain wall. More specifically, they used a bilinear and a biquadratic term for the description of exchange coupling, a spin-flop configuration in the AFM interface. They investigated compensated, partially compensated and uncompensated interfaces. A structure similar to that of Kiwi et al. with canted spins is found.

The calculated magnetization curve for the FM / AFM system is shown in **Fig. 1.9**, with the corresponding spin structure at three different values of the magnetic field. A partial domain wall in the AFM twists as the FM rotates, an effect more favorable energetically than the breaking of the interlayer coupling. Despite that, the hysteresis loop is reversible, meaning that the coercivity is zero. To overcome this problem Kiwi and Stamps [38] introduced magnetic defects in the system, which lead to the pinning of the domain wall. They argued that the wall pinning and depinning transitions, give rise to assymetric hysteresis loops with irreversible rotation.

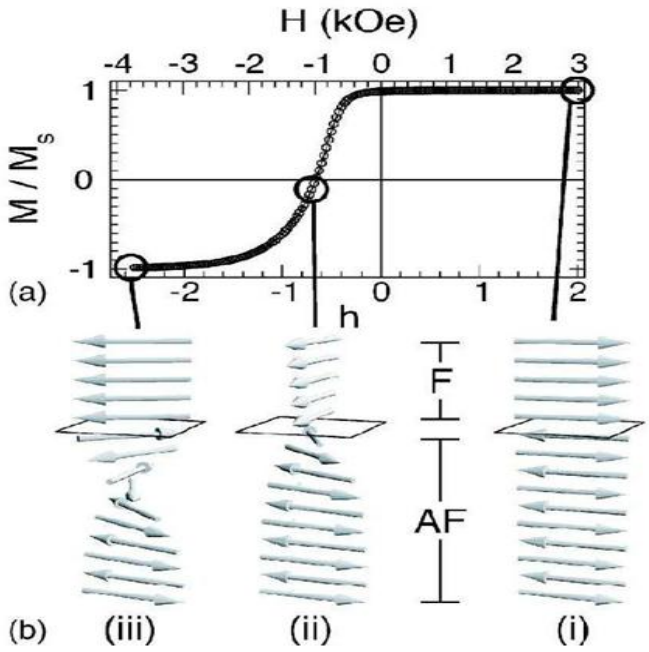

Figure 1.9: Magnetization curve **(a)** and spin configuration **(b)** at three different points of the magnetic field. A partial domain wall is created on the AFM in point **(iii)** Only the spins close to the FM / AFM interface are shown. [44]

1.4.7 Hoffmann model-Training effect

A model used specifically for the training effect of EB was created by Hoffmann [47], similar to that of Kiwi *et al.* The model, contrary to the planar domain wall model, considers two independent magnetic sublattices for the AFM using the Stoner-Wolfarth model. The model was modified for uniaxial and biaxial AFM anisotropy. In this model, the FM couples to both AFM sublattice which corresponds to both compensated or uncompensated interface of the AFM. In this model no FM anisotropy is considered.

An analysis using the parameters of the model plus an extra parameter describing the cooling field was made. The author connected specific orientations of the AFM sublattices with EB effect on consecutive hysteresis loops. They show that irreversible training effects (first loop EB) can occur as a result of inherent frustration of the AFM interface magnetic moments and symmetry of the AFM anisotropy.

1.4.8 Radu approach-The spin glass model

Radu [41] introduced the phenomenon of the frustration inside the Meiklejohn model, considering that the interface between FM and AFM layer is magnetically disordered behaving similar to a spin glass system. More specifically, it is considered that the AFM can contain, in a first approximation, two types of AFM state. One part has large anisotropy which freezes the AFM spins and another part with low anisotropy which allows the spins to rotate with the applied field. The latter kind of spins are frustrated (spin-glass state) and give rise to an increased coercivity.

A spin glass system is comprised of a collection of magnetic moments whose low-temperature state is a frozen disordered one, rather than e.g. a ferromagnetically ordered state. Two main requirements need to be fulfilled: 1) competition among different interactions between the moments, meaning that no single configuration of the spins is favored by the interactions (frustration) and 2) these interactions must be "random". In the specific case, the spin glass region can be formed due to the non-ideal interfaces e.g. interface roughness, non magnetic defects etc. So a new term is introduced to the energy expression. The energy per unit area, after the cooling process, for the Meiklejohn model using the new assumption, can be written as:

$$H = -\mu_o H M_{FM} t_{FM} \cos(\theta - \beta) + K_{FM} t_{FM} \sin^2(\beta) + K_{FM} t_{FM} \sin^2(\alpha) + K_{SG}{}^{ef} \sin(\beta - \gamma)^2 - JINT\cos(\beta - \alpha) \quad \textbf{(1.4)}$$

where $K_{SG}{}^{eff}$ is the effective spin glass anisotropy at the AFM interface, γ is the average orientation of the effective spin glass anisotropy and $J_{INT}{}^{eff}$ is the effective interface coupling between FM and AFM. With this model, the dependence of EB field and coercivity on angle between easy axes and applied magnetic field and thickness of the AFM was investigated with excellent agreement with CoFe/IrMn bilayers.

1.4.9 Spin flop - Koon's model

A well-known contribution in the category of microscopic models is the one of Koon [48]. Koon considered a system with compensated spins at the interface and investigated the

energy per area for multiple angles between the two outer monolayers (one of the AFM and one of the FM). It is found that the angle between the two outer layers (with the minimum energy) was 90^o and the internal layers had frustrated spins. So he concluded that the spins at the interface between AFM and FM must be perpendicular in order to minimize the energy. This 90^o coupling of the AFM and FM spins was called spin-flop state. This state is described by the biquadratic term: $J_{INT}\ (S_{AFM}S_F\ cos(a-b))^2$, where is S_{AFM}, S_F is the spins of AFM and FM at the interface, and *a*, *b* the angles of the AFM and FM spins, respectively. In addition, for reproducing an EB system he used the above conditions plus a restriction of the AFM spins to move in the plane of the interface during field reversal. At the end, it was concluded that domain walls parallel to the interface do appear, following an argument similar to that of Mauri et al. [30]. The produced magnetization curve was reversible i.e. no hysteresis loop, and was shifted by a quantity quite close to experimental EB field.

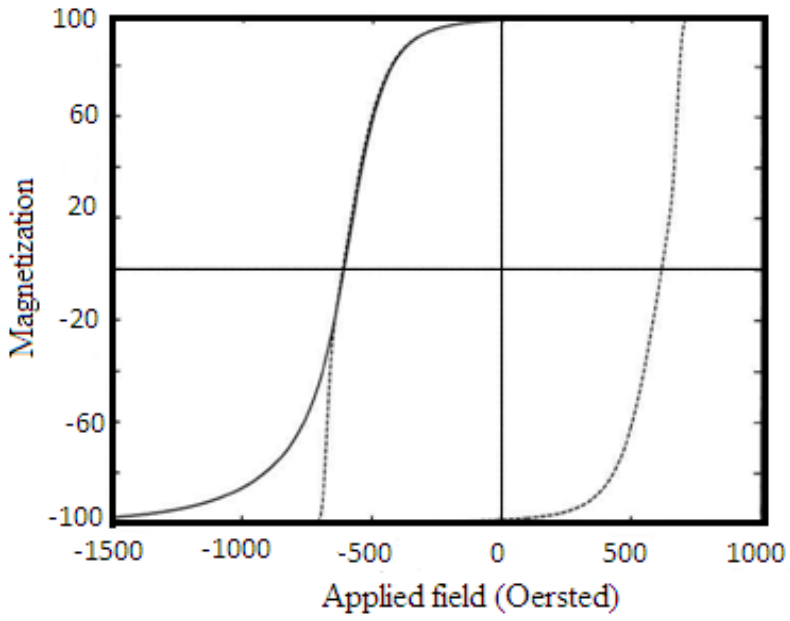

Figure 1.10: EB with reversible cycling is exhibited when the spin motion is restricted on the interfacial plane (solid line) but when the spins are free (dashed line) to move in any direction, the EB disappears showing a hysteresis cycling. [49]

At 1998, Schulthess and Butler [49], proved that Koon's model does not present EB. They used a microscopic Heisenberg model using the Landau-Lifshitz-Gilbert equation of motion, applying Koon's arguments about the spin-flop coupling. They did not consider restrictions to the movement of the interface spins as Koon did (movement only at the interface plane). The

result was that EB disappears under this assumption and no domain wall is created parallel to the AFM-FM interface. Particularly, when they used Koon's spin restriction, they found the same results as Koon, i.e. a shifted reversible magnetization loop, as shown in **Fig. 1.10**. When they used the unrestricted spins, they found a non shifted hysteresis loop showing that the energy of this configuration is smaller that the one for the creation of domain wall in the AFM parallel to the interface i.e. Koon argument. On the other hand, Schulthess and Butler showed that this model is very promising for the explanation of the enhancement of coercivity of EB systems as well as that the model transformed to have interface roughness gives EB field with the correct order of magnitude.

1.4.10 Domain state model

Miltenyi et al. [50] first showed experimentally that EB phenomenon is magnified by dilution of the AFM. Using a simple model and through Monte Carlo calculations, they proved the existence of domain states boosted from dilution of the AFM, which exhibits a phase diagram like the one which is shown in **Fig. 1.11(a)**. A phase transition in zero magnetic fields from the paramagnetic state to the long-range AFM state is shown at the dilution dependent Néel temperature. For higher magnetic fields, at low temperatures the AFM develops a domain state. The formation of the AFM domains originates from the statistical imbalance of the non-magnetic defects of the two sublattices. Hence, the formation of a domain wall can be minimized when it passes through the non-magnetic defects.

In 2001 Nowak et al. [51] used an Ising model for the diluted AFM and a Heisenberg model for the simulation of a system similar to Co / CoO. The dependence of the EB field on the thickness and the dilution of the AFM were shown. Also, it was shown that formation of domains with a surplus magnetization, which causes the exchange bias, is boosted from the dilution of AFM. The creation of small domains for small thickness leads to large surplus magnetization, causing larger EB field and vice versa, as Imry and Ma. [52] showed. The same writer [53] in a later publication showed that the creation of domains in the AFM is a result of the Imry-Ma argument, as mentioned before and shown in **Fig. 1.11(b)**. An extensive investigation of EB carried out using a Heisenberg model for both materials, with showing the dependence of EB on the dilution, the thickness of AFM, the temperature, where hysteresis loop is acquired, the cooling field as well as the number of consecutive hysteresis loop i.e. training effect. Also, they found that EB has a non-trivial dependence on the anisotropy of the AFM [54].

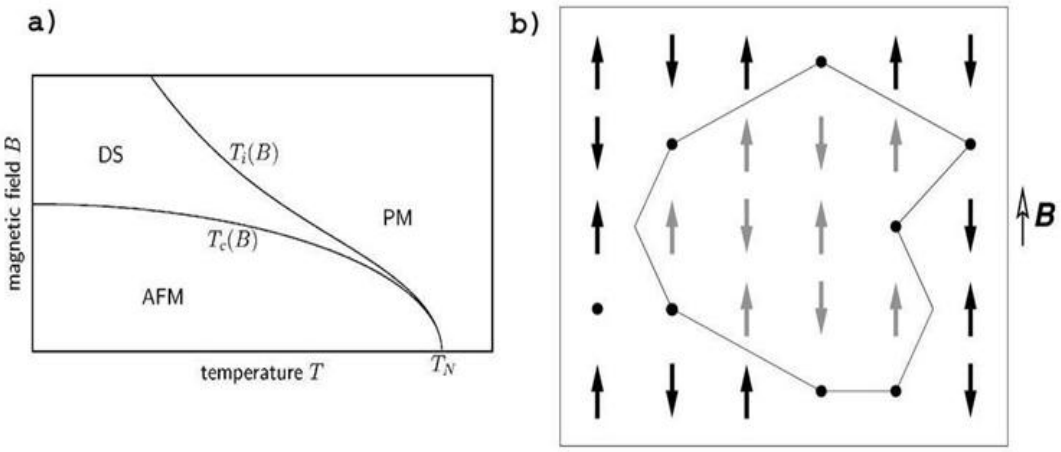

Figure 1.11: a) Schematic phase diagram of a three dimensional diluted AFM. DS is the domain state, PM is the paramagnetic state and AFM is AFM long-range state of an AFM. **b)** Schematic illustration of Imry-Ma argument. [53]

Misra at al.[55] using the domain state model, investigated the structure of interface domains as a function of the thickness and anisotropy of the AFM. They found that the size distribution of the domains of the interface follows a power law. Also, they showed that the interface magnetization after the cooling as well as its stability is crucial for the EB effect. The quantification of stability is introduced by the stability factor which is calculated from the average value of the stability of individual spin at the interface. The stability of spin is defined as the time average of z component of spin during the hysteresis loop divided by the initial value of the spin. Thus, using the above quantity they showed that the interface magnetization is due to an irreversible domain causing the upward shift of the hysteresis loop of the interface. Also, using a similar model [56] with a secondary dilution caused after the cooling process and taking the hysteresis loop, showed that this characteristic enhances further the EB field. This procedure simulates the experimental method of enhancement of dilution of FeNi/FeMn system using irradiation of the sample with He ions in presence of magnetic field [57,58].

Beckmann et al.[59] used a Monte Carlo simulation for the explanation of asymmetric reversal modes, within the context of the domain state model for EB. The asymmetric reversal mode is the phenomenon in which different reversal modes on the descending and the ascending branches are observed, during the hysteresis loop. They investigated the effect of different angles between the easy axes of the AFM and the magnetic field. As they showed, for

a range of angles the reversal was asymmetric, with a coherent rotation of the spin for the descending branch and a non-uniform reversal for the ascending branch. On the other hand, for the rest of the angles, spins rotated coherently both for the descending and ascending branch of the hysteresis loop.

Scholten et al. [60] using the same model, performed mean-field-type calculations. They focused their interest on the behavior of coercivity around Néel temperature of the AFM, where coercivity appeared significantly enhanced. This was attributed in the coupling of FM to the AFM interface magnetization. In addition, qualitative agreement was found with the previous investigations on the domain state model using Monte-Carlo simulations.

Spray et al. [61] investigated the influence of a rough interface on EB field and ceorcivity within the framework of the domain state model. More specifically, they quantified the interface roughness as the proportion of AFM interface layer spins which are replaced by FM spins. They found that the EB as well as coercivity are strongly dependent on the interface roughness. This dependence is affected by the dilution of the AFM. It is showed that the interface roughness leads to EB even without any dilution in the AFM, result which is in agreement with Malozemff's model. Finally, the thickness dependence of the EB field is influenced significantly by the roughness of the interface.

1.4.11 Multiscale models

A special category of models is those that mix microscopic and mesoscopic ideas at the final simulation. More specifically, grain models is considered to have non-coherent magnetiza-tion e.g. spins. Papusoi et al. [62] used domain state model considering a granular AFM structure in which the grains are cuboid and non-interacting. Furthermore, the grains have the same easy axis direction. They investigated the role of the nonmagnetic defect concentration and of the temperature on the dependence of coercivity and EB field, showing that the latter presents a maximum as a function of this concentration. They also found that for increasing concentration the temperature dependence of the coercivity changes from a monotonic decrease to a nonmonotonic dependence, exhibiting a maximum near the blocking temperature.

Usov and Gudoshnikov [63,64] developed a model using a classical Heisenberg Hamilto-nian for atomic magnetic moments with a dipolar interaction term and dividing the AFM layer to grains with random easy axis. Also, a perpendicular exchange coupling is considered in the

FM/AFM interface. They used this model to compare the case of a uniform AFM with the case of a granular one, which was the only one that exhibited non-symmetrical hysteresis loop, with finite EB field.

Apart from this various other materials like nanowires, nonocomposites, nanostructure [65-67] etc. have been explored for their multifunctional: electrical, magnetic and transport properties [68,69]. Magnetic and transport properties of thin films, heterointerface and composites have also been reported [70-73].

1.5 Brief overview of Heusler alloys and thin films

Heusler alloys are one of the important multifunctional alloys that are also magnetically ordered and have properties such as magnetic shape memory effect (MSME) [7], magnetic superelesticity [8], magnetocaloric effect (MCE) [9] and magnetostriction [10]. These magnetically ordered alloys were first discovered in 1903 by Heusler, Starck and Haupt [64] in Cu_2MnAl showing strong ferromagnetism. It was interesting to note that this unique class of alloys were strongly ferromagnetic although none of its constituent atoms were ferromagnetic. Some class of X_2MnZ Heusler alloy system are found to exhibit a thermoelastic martensitic transformation andcrystallographically reversible which results in the shape memory effect. The crystal structure of these Heusler alloy has been described as four interpenetrating f.c.c. ($L2_1$ structure) sublattice with stiochiometric composition X_2YZ. Further research indicated that the magnetic properties originating in these alloys system are dependent on the chemical composition, crystal structure, and to the ordering of the atoms on an f.c.c. sublattice. These alloys exhibit most of the properties of metals but have the structure of an ordered compound in which magnetism may originate from several different magnetic exchange mechanisms leading to magnetic properties that are ferromagnetic / antiferromagnetic or intermediate. Consequently Heusler alloys provide an opportunity for investigation of the effects of chemical and structural order on the transport and magnetic exchange interactions in these multifunctional magnetic alloy systems.

Till 1996 various Heusler alloys were developed with the general formula X_2YZ, where X and Y are transition metals and Z is a group III-V element, include Cu_2MnSb, Ag_2MnAl, Au_2MnAl, Au_2MnIn, Ni_2MnIn, Mi_2MnGa, Co_2MnGa and Pd_2MnSb [74]. Efforts were made to study the thermal and magnetic properties of Heusler alloys both theoretically and experimentally. Various theoretical models like Heisenberg theory, Zener theory and Ruderman-Kittel-Kasuya-Yosida (RKKY) interactions were used to explain the magnetic

properties of Heusler alloys [75-77]. Experimental methods like Mossbaur effect and spin echo techniques were used to study the hyperfine field at different sites in the Heusler alloys. The understanding of the origin of magnetic properties in Heusler alloys still remained partially inconclusive due to complex unit cell of this type of materials.

The main properties of Heusler alloy are Magnetic shape memory effect (MSME) and Magnetocaloric effect (MCE). By definition, shape memory effect is a unique property of certain alloys which when deformed in the low temperature phase, recover their original shape when they are heated to critical temperature called the reverse transformation temperature. This effect was first found in Au-47.5at % Cd alloy by Chang and Read [78]. The possibility of magnetic control over shape memory effect was observed in certain alloys exhibiting complex crystal structure and unique magnetic properties categorized as Heusler alloys.

A good control of the parameters that govern phase stability is necessary to optimize materials design and to improve their functional properties. Giant MFIS, at room temperature, has only been shown in single crystals of Ni-Mn-Ga. Single crystal growth is time consuming with high production costs. Consequently there are many hindrances in studying and producing single crystals with reproducible properties. Polycrystalline materials show chemical homogeneity and have much lower production costs. However, polycrystalline Ni-Mn-Ga gives very small MFIS (< 0.01%) due to the small grains [79-81] as grain suppress the motion of twin boundaries, or equivalently, neighboring grains have incompatible MFIS. It is of both technological and fundamental interest to overcosme the hindrance of grain boundaries (and other constraints) which suppresses magnetic-field-induced actuation of MSMAs. In 2009, U. Gaitzsch *et al.* [82] demonstrated that large MFIS can be generated in magnetically trained, highly textured, course-grained samples called oligocrystals [83,84]. They are intermediate between mono and polycrystals and defined as materials with low numbers of grains relative to their volume. While a vast majority of reported results have dealt with bulk Heusler alloys (Ni-Mn-X), for many electronic applications, it would be extremely desirable to synthesize such materials (with corresponding properties) in thin film forms. The use of thin films would make it possibleto realize microscopic components in a small volume by utilizing lithographic techniques [85]. In addition, in thin-film form MSM materialsprovide an opportunityfor the integration of mechanicalelements with semiconductors which can serve as novel microelectromechanical or micromechanical devices [86]. Ni-Mn-Gafilms have been prepared by molecular beam epitaxy (MBE) [85, 87-89], magnetron sputtering [90,91], and pulsed laser deposition (PLD) [92-94].

At present, it is known that the properties exhibited by thin films are very sensitive to the method of preparations, compositions and microstructure. Various approaches have been undertaken to fabricate thin films of Heusler alloys.

1.5.1 Structural properties of Heusler alloys and thin films

In order to magnetically control the structural transition from lower symmetric martensite phase to higher symmetric austenite phase, the Martensite to Austenite transition should occur within the magnetically ordered phase. In order to understand how the typical structure of Heusler alloys effect the magnetic exchange interaction, we need to study the chemical structure of Heusler alloy and their magnetic properties and how the interplay between them affects the novel magnetic properties exhibited by Heusler alloy (magnetic shape memory effect, magnetocaloric effect and metamagnetic shape memory effect).

The original alloy studied by F. Heusler was cubic $L2_1$ type structure (X_2YZ). Their structure has been described in detail by Webster *et al*. [93]. In practice it is observed that, in general, this is dictated by considerations of energy which dictate generally the sort of disordering in atomic positions which is represented by α, which is a disorder parameter, which is given as the fraction of either Y or Z atoms whose position in the sublattice are not correct. Among the sites which are mostly occupied the most important are those which exhibit C1b, $L2_1$ (complete order) $D0_3$ and B2 as summarized in **Table 1.1**.

Structure type	Space group	composition	Asite occupancy	Bsite occupancy	Csite occupancy	Dsite occupancy	Disorder parameter (α)
$L2_1$	Fm3m	X_2YZ	X	Y	X	Z	0
B2	Pm3m	X(Y or Z)	X	Y	X	Z	0.5
C1b	F43m	XYZ	X	Y	Vacant	Z	1
$D0_3$	Fm3m	X_3(Y or Z)	X	X	X	Z	0.75

Table 1.1 - $L2_1$, B2, $C1_b$ and $D0_3$ structure [93]

The details of the structures are mentioned below. In the present thesis the focus is mainly on $L2_1$ and B2 structure so details of these structures have been discussed.

$L2_1$ structure

Heusler alloys are intermetallic compounds which crystallize in an L21 structure, consisting of 4 interpenetrating f.c.c. sublattices A, B, C and D. The coordinates of sublattices are given in **Table 1.2**.

A	B	C	D
000	$\frac{1}{4}\frac{1}{4}\frac{1}{4}$	$\frac{1}{2}\frac{1}{2}\frac{1}{2}$	$\frac{3}{4}\frac{3}{4}\frac{3}{4}$
$0\frac{1}{2}\frac{1}{2}$	$\frac{1}{4}\frac{3}{4}\frac{3}{4}$	$\frac{1}{2}00$	$\frac{3}{4}\frac{1}{4}\frac{1}{4}$
$\frac{1}{2}0\frac{1}{2}$	$\frac{3}{4}\frac{1}{4}\frac{3}{4}$	$0\frac{1}{2}0$	$\frac{1}{4}\frac{3}{4}\frac{1}{4}$
$\frac{1}{2}\frac{1}{2}0$	$\frac{3}{4}\frac{3}{4}\frac{1}{4}$	$00\frac{1}{2}$	$\frac{1}{4}\frac{1}{4}\frac{3}{4}$

Table 1.2 – Coordinates of f.c.c sublattice [93]

In the composition which is stoichiometric X_2YZ, the X atoms are mainly situated at A and C sites, Y atoms are mainly situated at B sites and and Z atoms are mainly situated at D sites. In the original alloy described by F. Heusler (Cu_2MnSn) [64] the lattices are occupied as $X_1 = X_2 = Cu$, Y = Mn and Z = Sn. This structure may be regarded as that atomic arrangement which is correct and exhibit no disorder parameter.

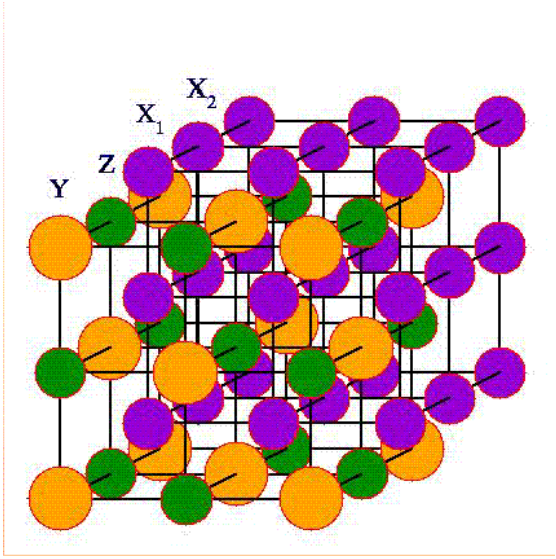

Figure 1.12 $L2_1$ structure with *Fm3m* space group [95].

In the $L2_1$ type structure, generally the position of X atoms are in the centre to position occupied by late transition metal elements, the position of Y atoms are centre to the position of starting transition metal elements and position of the Z atoms are metalloids. These different sites have been occupied typically by following elements

Typical X atoms - Mn, Fe, Co, Ni, Cu, Ru, Rh and Pd

Typical Y atoms – Ti, V, Cr, Mn, Fe, Co, Zr, Nb, Hf and Ta

Typical Z atoms – Al, Si, Ga, Ge, In, Sn, Sb and Pb

The conventional cell exhibits lattice parameter ~ 6 A^0 (**Fig. 1.12**). Kubler *et al* [96] studied few compounds with X_2MnZ composition where X = Cu, Pd, Ni, Co and Z = Al, In, Sb for the $L2_1$ type structure. It has been shown by Kubler *et al.* that in the alloys based on Ni- and Co-, the X sublattice mediates the ferromagnetic interaction between Mn–Mn atoms. Rigid-band model has been used to explain these Mn based alloys, i.e. shift of Fermi level by the impact of substituting Y (element different from Mn). The symmetry is lowered through distortions which are tetragonal induces some removal of degeneracy of the electronic energy levels, and there is a splitting of some of the peaks near the Fermi level (in the density of states). Ni_2MnGa and Ni_2MnAl alloys are likely candidates for martensitic transformations as with small deformations, Fermi level have been crossed by splitting.

The Heusler alloys which contain Mn have been found to exhibit indirect exchange interaction among magnetic ions which further results in magnetism. They are of current interest owing to the shape memory effect [97] that results from the certain type of instability in structural in the Heusler alloys which contain Mn. This instability results from structural transition which occurs from austenite phase which is a high-temperature phase to martensitic phase which is a low-temperature state which results in crystal cell of lower symmetry (modulated orthorhombic, tetragonal, monoclinic or tetragonal).

B2 structure

In the case where there is ordering among X atoms and disordering occurs between Y and Z sites. The complete binary order is indicated $\alpha = 0.5$ where Maximum disorder occurs. This crystal structure is called *B*2 type. If there is resemblance between the corner atoms and centre atoms then this is identical to the bcc structure. There is a difference between B2 abd bcc in terms of their Bravais lattices. For B2 the specified space group is *Pm*3*m* and in case of bcc, the space group is *Im*3*m*. Given below are the positions occupied by atoms in the B2 phase,

Y/Z: 0, 0, 0

X: ½ , ½ , ½

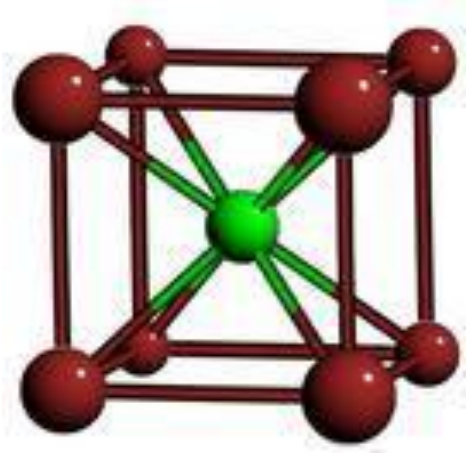

Figure 1.13 B2 structure with *Pm3m* space group [98].

Formation of Heusler structure takes place when two binary compounds in the B2 structure namely XY and XZ combine in an ordered state for exampleCoAl and CoMn combine to form Co_2MnAl. This indicates the compounds existing in B2 structure exhibit the possibility that new Heusler compounds can be formed by their combination. In Ni-Mn based

Heusler alloys (X_2YZ), the band structure at Fermi level is altered due to the strong hybridization between the X and Z species that result in martensitic transformation. In the B2 structure as there occurs complete disorder sites which hare referred to as Y and Z, it is not possible to identify the Mn atom which hybridizes the Ni atom or Mn atom situated at Y-site or with atom situated at Z-site. Although, the presence of few Ni-d and Mn-d hybridization is indicated by the bond lengths difference exhibited by Ni-Z and Ni-Mn bonds. In B2 structures martensitic transformation is initiated by these d−d hybridization. In comparison to the structure which is $L2_1$, the characteristics of B2 structure is that interatomic distance which is smaller along with an energetically favorable antiferromagnetic magnetic ordering. For the sample in a single phase B2 structure the super-lattice reflections with $h + k + l$ odd are absent. There is a possibility that alloys having high temperature B2 structure, below T_M may also transforms to a structure that is layered (like $L2_1$) having stalks which can be both monoclinic and orthorhombic. For example, Ni_2MnIn and Ni_2MnAl alloys in an off-stoichiometric form may transform to 10M phases, 14M phase or a 2M phase at low temperatures [104].

In this thesis, the studies are reported on off-stoichiometric Ni-Mn-Al thin films and NiMnAlIn thin films. The high temperature structure (austenite phase) of Ni-Mn-Al alloy is mostly B2. $L2_1$/B2 ratio is controlled by heat treatments.

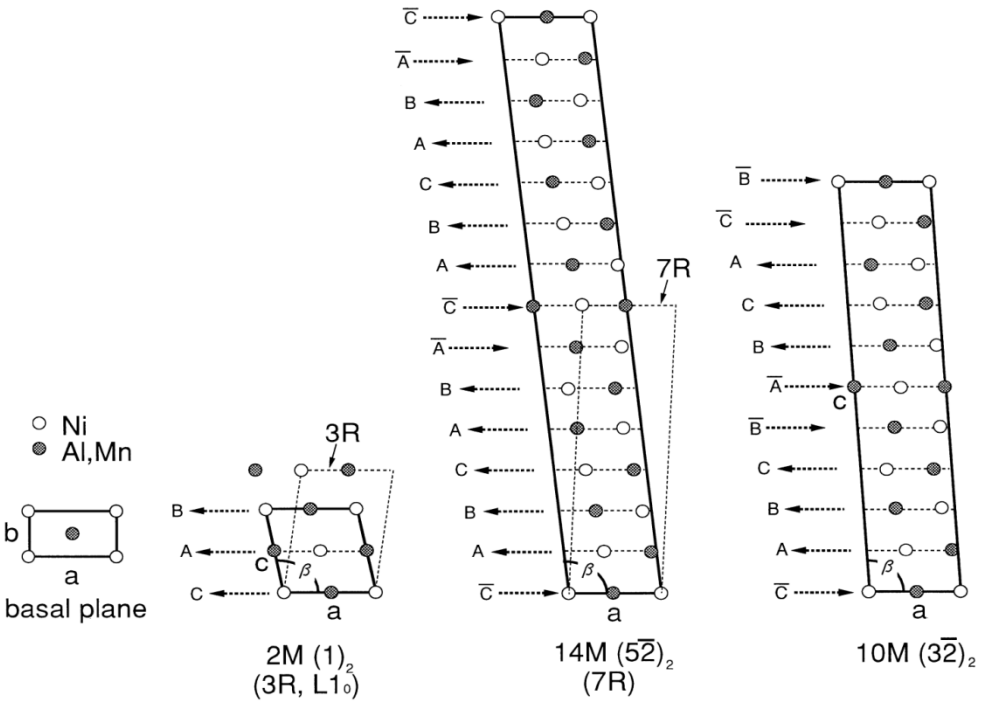

Figure 1.14 Crystal structures of the 2M, 14 M and 10 M phases in Ni-Mn-Al system [99].

1.5.2 Martensitic transformation in Heusler and related alloys

Shape memory alloys (SMA) are materials of extraordinary scientific and technological appeal due to their ability to undergo a reversible structural transformation at a characteristic temperature and recover the original shape or size. SMA's have two stable structural phases - the high-temperature, high-symmetric phase, called *austenite* (named after William Chandler Austen) and the low-temperature, low-symmetric phase, called *martensite* (named after Adolf Martens). When a SMA is cooled below its transition temperature, it undergoes a transformation from austenite to martensite. This structural transformation, referred to as martensitic transformation, is associated with a non-diffusive inelastic deformation of the crystal lattice that results from a cooperative and collective motion of atoms [77]. The motion of the atoms is caused by a sudden shearing of the lattice, with the atoms moving only a fraction of the normal interatomic distance. The martensitic phase grows at speeds which can approach that of sound in the material. In the martensitic phase, with comparatively little force, the deformed of the material is possibleinto other shapes, and the new shape (detwinned martensite) is retained when the material is kept below the martensitic transformation temperature T_M. On heating the material above martensitic transformation temperature T_M, the austenite phase is regained where the parent structure of the material is regained and it returns to original shape. In martensitic transformations, martensite can form through a number of equivalent shear directions which the within a region of parent-phase. Due to this martensitic variants are formed within the microstructure of the transformed alloy and the boundary between these variants is called twin boundary. The two components of the twin have the same crystal structure, but different orientations, and are known as variants [100, 101]. The elastic stain energy ar the boundaries is lowered by the formation of the martensitic domains. Due to the first-order nature of the transition, there coexists the higher symmetry austenite (high temperature) and lower symmetry martensite (low temperature) phases. This coexistence is observed in the particular temperature range due to the elastic strains that exist when the martensitic phase starts nucleating. If there is a difference in the magnetic substructure of the martensite phase and the austenite phase, the magnetic energy of each macro-domain will depend on its orientation with respect to an external magnetic field.The normally oriented martensitic phase will have a higher magnetic energy as compare to the martensitic plate which is oriented along the direction of the magnetic field. The twinning shear along the twin boundaries is one of the elementary processes in the migration of the twin boundary, and the shear magnitude s is given by

$$s = \frac{2(c/a)^2 - 1}{\sqrt{2}\,(c/a)} \qquad (1.4)$$

This equation indicates that an incease in c/a ratio would decrease the mobility of twin boundaries. Grain boundaries also suppress twining due to internal geometric constraints at the grain boundary. At the grain boundary twinning incompatibilities will wither lead to the formation of voids or suppression of twin boundary motion. Grain boundaries can constrain MFIS (or inhibit twin boundary motion) in a polycrystalline material in multiple directions depending on the grain structure and the direction of strain (**Fig. 1.15**). For comparison single crystals have no grain boundaries and can show up to 6 and 10% maximum strain for 10M and 14M respectively. Ni-Mn-Ga fibers with bamboo grains where grains span the thickness of the fiber have one dimensional constraint. Fibers with bamboo grains have been reported to show up to 1% MFIS [102]. Thin films, in which the grains span the thickness of the film, have two dimensional constraints and show up to 0.04% MFIS [103]. Bulk large grained polycrystals of Ni-Mn-Ga have three dimensional constraints and show minimal MFIS. MFIS of up to 0.3% is only found in highly textured, mechanical trained, bulk polycrystals [81,104].

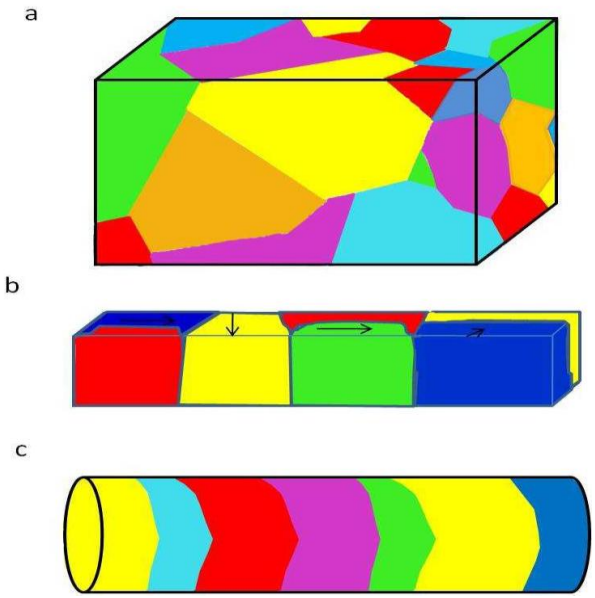

Figure 1.15 Grain Structures in Different Polycrystalline Magnetic Shape Memory Alloys. a) Bulk Course Grained Polycrystal b) Thin Films and C) Fibers [113].

1.5.3 Magnetic properties of Heusler alloy and thin films

In the X_2MnY - Mn based Heusler alloys, the formation of magnetic moments and their coupling has been experimentally studied and theoretically investigated. Initially it has been obsercved that the magnetic properties of this material play a crutial role in estimating the chemical structure and it has been indicated that Mn carries the magnetic moment.

In these MSM alloy system, a martensitic phase which is ferromagnetic may be obtained from austenite phase which is not magnetic or vice versa [106]. In few alloys, there is a large shifting of martensitic transition temperature T_m by the application of a magnetic field which may induce structural transformation which is reversible and instantaneous, reversible at a constant stress and temperature [107]. The main requirement ofr this type of magneto-structural phase transition is that $T_M \leq T_C$.

As per the data available in literature, the valence electron concentration e/a is mainly correlated with T_m and thus these alloys may be catagorized as Hume Rothery alloys [95]. The interaction among the Brillouin zone boundary and Fermi surface results in martensitic transition [108]. Such type of model indicate that alteration of the no. of velence electrons abd change in the Brillouin zone boundary are the main reasons due to which structural instabilities appear in these alloys. If the consequences of hybridization and other factors are ignored, which may include electronegativity difference [109], what may be expected is that the change in T_m with composition is linear associated with the modification in the chemical pressure and no. of valence electrons, this has actually been indicated by few systems which include $Ni_{2-x}Mn_{1+x}Ga$ [100], $Ni_{2-x}MnGa_{1+x}$ [110], and $Ni_2Mn_{1-x}Ga_{1+x}$ [111] alloys. As we move towards Curie point, this condition is not satisfied as volume magnetostriction substantially alter the lattice parameters. The coincidence of the temperatures of the martensitic and magnetic transitions Tm and T_C is also observed in other ferromagnetic shape-memory alloys, e.g., Co-Ni-X (X. Al, Ga) [112, 113], Ni-Fe-Ga [114, 115], and Ni-Mn-X (X = In, Sn, Sb) [6]. Heusler alloys in bulk exhibit cubic anisotropy, however, in thin films, the anisotropy is known to be film structure dependent [116]. This has a large effect on the magnetic domain structure in the thin films which controls magnetisation reversal.

1.5.4 Exchange Interactions

(i) Direct Exchange

Direct exchange is a phenomenon by which the quantum-mechanical wave functions of neighbouring atoms overlap when their spins interact. In this the electrons become indistinguishable from one another in the overlapping region and thus the associated atoms can 'exchange' electrons [117]. The exchange energy is given by equation 2.1

$$H = -\frac{1}{2}\Sigma J_{ex} S_i . S_j \qquad (1.5)$$

where S_i and S_j are the spin angular momentum vectors of two atoms i and j. The strength and direction of spin alignment is given by the exchange integral J_{ex}. The sign of J_{ex} determines the alignment, negative value indicates that the alignment is antiparallel (antiferromagnetic) whereas positive value indicates that thealignment is parallel (ferromagnetic) [118].

In case of metallic systems where a band structure is formed by the electrons, the magnetic moment of the system is estimated by the energy required to align the spins antiparallel or parallel in specific bands near the Fermi energy (E_F). Stoner criterion determines the condition for ferromagnetism [119]. Ferromagnetism is favoured when the exchange integral $J_{ex}(E_F)$ and density of states n(E_F) at the Fermi energy is large. J_{ex} itself is dependent upon the separation of the d orbitals of the localised electrons or, on the separation of atoms in the material. The variation in Jex with atomic separation (ra) is often shown using the Bethe-Slater curve.

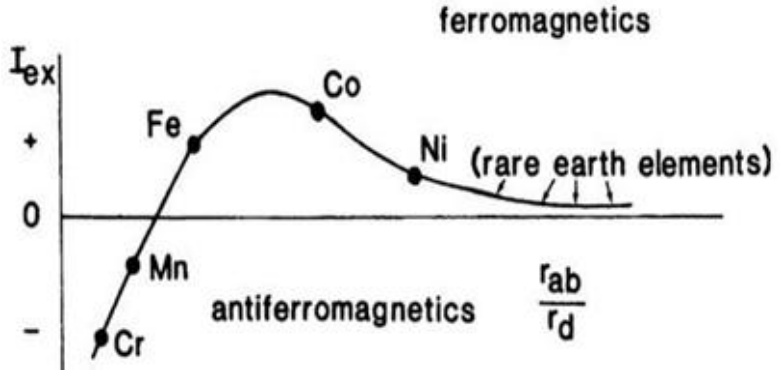

Figure 1.16 Ferromagnetic alignment of spins is favoured when the atomic separations is large,J_{ex} is positive.

The limit of this alignment is the spacing at which the electrostatic interaction and as a result the exchange interaction vanishes. With decrease in atomic separation from this limit, the exchange integral increases and reaches a maximum value where most of the ferromagnetic elements Fe, Co, and Ni reside. As the spacing becomes further smaller, the exchange integral J_{ex} becomes negative and an antiferromagnetic order starts dominating. At the spacing becomes further extremely small Pauli exclusion principle starts dominating, spins are forced for antiparallel alignment and electrons can be regarded as having the same spatial co-ordinates. At larger spacing the electrons inhabit separate spatial co-ordinates but exhibit the same wave function resulting in favourable parallel alignment [119,120]. This model correctly predicts the magnetic properties for elements.

(ii) Indirect Exchange

Indirect exchange coupling occurs when separated but localised magnetic moments are coupled by conduction electrons in a metallic systems. It was suggested and developed by Ruderman and Kittel [121], Kasuya [122], and Yosida [123] to explain the coupling of nuclear spins to s-electrons. Exchange interaction of this type is often known as the RKKY interaction.

This model has subsequently been used to describe the magnetic moments of rare earth metals [124] as well as intergranular exchange coupling and the coupling between magnetic layers separated by non-magnetic spacers [125]. When a localised magnetic impurity is placed in a typical electron gas, that is a system of electrons free from their ions which are treated as a non-interacting gas [126], the wave functions change to accommodate the impurity. This effectively adds more possible states for the conduction electrons when their spins are aligned with that of the magnetic impurity. This also forms a series of charge oscillations. These oscillations are all in phase at the impurity but as the electrons have different energies and therefore wavelengths, these charge oscillations interfere at some distance from the impurity [119]. These electrons all contain information about the initial spin state of the magnetic impurity so these oscillations in charge are also oscillations in the spin density. Therefore if a second localised magnetic moment is placed within the range of these oscillations it will become coupled either ferromagnetically or antiferromagnetically to the initial atom depending upon the spin density at its position in the system [127]. The dependence on the position of the coupled atoms makes this exchange extremely susceptible to any change in the distance between local moments. This was shown experimentally by Parkin et al. in a series of

experiments using different transition metal spacer layers of varying thickness to separate two ferromagnetic layers [125,128]. There exists oscillatory nature of the coupling of two ferromagnetic layers on their separation. The strength and nature of the exchange coupling is represented by the magnitude of the applied field at which the sample saturates. Antiferromagnetic coupling requires a large field to saturate while ferromagnetic coupling requires a lower saturating field. Coupling can occur across grain boundaries making the RKKY interaction particularly important in granular thin films. Individual grains can become exchange coupled and reverse their magnetisation as if they were a single entity. This process is well documented in thin film granular media [129]. This makes intergranular exchange an important consideration when studying the polycrystalline Heusler alloy films.

1.5.5 Magnetic properties arising from $L2_1$ structure

Heusler alloys have a generic formula X_2YZ and display an $L2_1$ structure at high temperature. In the Ni-Mn-based Heusler alloys (Ni_2MnZ), the magnetic moment are located mostly at the Mn atoms sites with $\mu > 3\ \mu_B$. Ni has only a small magnetic moment and the moment of Z atom is negligible. But Ni atoms are responsible for the ferromagnetic coupling in the $L2_1$ structure. The magnetic moments localized at Mn atoms are magnetically coupled through an oscillatory interaction via conduction electrons. It has been shown from neutron-scattering experiments that the 3d electrons are found to be well localized on the Mn atoms and resulting in a longe range interaction in Heusler alloys, which extends to more than eight neighbors. The exchange interaction occurring in these alloys has been explanation by Zener [130]. In this model, an energy band is formed by 4s electrons while 3d electrons are localized. There exists an antiferromagnetic direct exchange between the adjacent atoms 3d shells however spin of conduction electrons are strongly coupled to the 3d spins to the and this is considered to be ferromagnetic. Heisenberg Hamiltonian has been used to describeordering of the moments and discusses the exchange constants in terms of indirect RKKY-type exchange which has been mediated by free electron in the systems [75-77].

1.5.6 Magnetic properties arising from B2 structure

Although, ferromagnetic order has been observed in most of the Heusler alloys, some of the Heusler alloys exhibit anantiferromagnet order, mainly the systems which contain 3*d*

element and where Mn atoms at Y site mainly carry the magnetic moment. Although, both B2 and $L2_1$ phase have been found to exhibit antiferromagnetic coupling, however, it has been observed that those Heusler alloys which have B2-type phase mostly exhibit antiferromagnetic ordering associated with the anti-ferromagnetic coupling between neighbouring Mn atoms which are situated at the cube corner sites and body center sites. There has been reports on the ntiferromagnetic ordering in few disordered B2-type X_2MnZ (X=Ni, Pd; Z=Al, In) Heusler alloys [131]. It has been observed for compositions which exhibit Mn atoms in excess that there occurs a decrement of lattice parameter on structural transition on cooling associated with closer-neighbors Mn-Mn positions which become antiferromagnetically coupled.

The magnetc moment of compounds having Mn shows large number of magnetic ground state phases. There is a compotition between the antiferromagnetic interactions that exist among the nearest neighbour atoms with ferromagnetic interaction between more distant atoms. A major alteration in the arrangement of spin may be caused by outside parameters which control the geometry. In this regard it is worth mentioning that Mn in bulk form itself crystallizes in complex structures such as the α and β phases with noncollinear spin arrangements [132-134]. Complex magnetic configurations depending on the Mn-Mn distance has been exhibited by intermetallic compounds of the type RMn_2X_2 (R = Ca, La, Ba, Y, etc., and X = Si, Ge) or R_2MnX Heusler alloy (R = Ni, Cu, etc., X = Ga, Al, Sn, In, etc.). The spins on the Mn sublattice can arrange in spiral spin-density waves (SSDW), antiferromagnetic (AFM), ferromagnetic (FM), or/ and canted magnetic structures [135-138].

Exchange bias has been extensively studied in oxides [139-141] and metallic systems [142-152]. In the perspective of this thesis main result obtained for Heusler alloy has been discussed.

1.6 Exchange bias in Heusler alloy, thin film and Heterostructure

1.6.1 Exchange Bias in Heusler alloys

Multifunctional Heusler alloys are found to exhibit exchange bias effect in the martensite state. The exchange bias has been found due to coexisting high temperature austenite and low temperature martensite phases below martensitic transformation temperature. Depending on

the system and deposition conditions, the martensite may exhibit different behaviour such as ferromagnetic, antiferromagnetic, paramagnetic, and spin glass depending on the exact composition. Heusler type Ni-Mn-X and Ni-Mn-X-Y(X = Ga, Sn, In and Sb, Y = Co and Fe) systems have been the focus of research due to their multifunctional properties like magnetic shape memory, magnetocaloric effect, magnetoresistance, metamagnetic shape memory, and direct conversion of heat to electricity and recently these alloys are also shown to exhibit EB effect in the martensitic state [100, 101, 143-152].

Important results on the development of alloys exhibiting exchange bias effect are tabulated below

Alloy	Exchange bias (Oe)	Observation
NiCoMnSb [147]	480 Oe at T = 3K	"EB is attributed to the coexistence of ferromagnetic (FM) and antiferromagnetic (AFM) phases in the martensitic phase. The phase coexistence is possibly due to the supercooling of the high temperature FM phase and the predominant AFM component in the martensitic phase. The presence of EB is well supported by the observation of the training effect. Increase in the AFM coupling after Co substitution is found to be responsible for the increase in the EB".
$Ni_{50}Mn_{36}Sn_{14}$ [148]	175 Oe at 2 K	"The hysteresis loops shift along the axis of an applied field and its magnitude significantly increased with decreasing temperature below 70 K. This effect could be understood as a result of exchange anisotropy created at the interface between an antiferromagnet and a ferromagnet in the phase separated of martensitic state. Above 70 K, however, the exchange bias field disappeared and the coercivity significantly reduced owing to the fact that the pinning between an antiferromagnet and a ferromagnet becomes weaker with increasing temperature".
$Mn_{50}Ni_{40}Sn_{10}$ [149]	910 Oe at 2 K	"These are the Heusler alloys with high content of Mn. In these alloys, the excess Mn atoms would occupy not only the Sn sites but also the Ni sites, and the moments of Mn on Sn or Ni sites are

		coupled antiferromagnetically to those on the regular Mn sites, respectively".
$Ni_{50}Mn_{50-x}Sn_x$ [150]	225 Oe at 5 K	"Martensitic transformations have been observed in the alloys for some critical Sn concentrations. The alloys, while in their respective martensitic phases, are found to exhibit exchange bias effect. The observed exchange bias behavior in $Ni_{50}Mn_{50-x}Sn_x$ is attributed to the coexistence of antiferromagnetic and ferromagnetic exchange interactions in the system".
Ni–Co–Mn–Sb [152]	3.2 kOe at 5 K	"The existence of a wide range of grain sizes in the ball milled samples results in dramatic changes in the structural and magnetic properties. For x=0, a large EB field of 3.2 kOe is observed in the ball milled sample, compared to a value of 245 Oe of the bulk sample. This increase is attributed to the enhanced exchange coupling between the soft and hard magnetic particles".

1.6.2 Exchange Bias in thin films of Heusler alloy and Heterostructure

Thin films of Heusler alloy are promising candidate for device applications. These materials are a possible candidate for new micro-devices which include magnetically driven microelectromechanical system (MEMS) requiring a high quality thin FSMA film grown on semiconductor substrate. Owing to the multifunctional properties of Heusler alloys and their potential application in thin film form, exchange bias has been explored Heusler alloy thin films and related heterostrcuture. There also are only few reports available on thin films of Heusler alloy and related heterostructure exhibiting exchange bias [153-155]. The important results on exchange bias in thin film and heterostructure are tabulated below.

Thin film / Heterostructure	Exchange bias	Observation
Ni-Co-Mn-Sn [156]	350 Oe at 5 K	"Effect of substrate temperature (T_S) and Ar gas pressure (P_D) on the martensitic transformations, magnetic and exchange bias properties in Heusler type Ni-Co-Mn-Sn epitaxial thin films. Martensitic transformation temperatures and EB fields were found to increase with increasing T_S. The observed exchange bias is

		attributed to the coexistence of ferromagnetic (FM) and antiferromagnetic (AF) phases in the martensitic state".
$Ni_{45.0}Co_{4.4}Mn_{41.5}Sn_{9.1}$ [139]	139 Oe at 5K	"Exchange bias effect has been observed at low temperature below 60K. Both EB field and coercivity decreased with increase in temperature. The observed EB is attributed to the coexistence of antiferromagnetic and ferromagnetic exchange interactions in the system".
$Ni_{50}Mn_{32}Sn_{18}$ [157]	140 Oe at 10 K	"Thickness dependent exchange bias in the low temperature martensitic state of epitaxial Ni-Mn-Sn thin films has been investigated. The effect can be retained down to very small thicknesses. The film which does not undergo a martensitic transformation, no exchange bias is observed. A significant interplay between ferromagnetic and antiferromagnetic regions, which is the origin for exchange bias, is only present in the martensite".
$Ni_{49.8}Mn_{36.1}Sn_{13.9}$ [140]	41 Oe at 5 K	"The observed exchange bias behaviour is attributed to the presenceof AFM–FM interactions that result from the coexistence of antiferromagnetic and ferromagnetic phasesin the martensite phase of the film at low temperature".
$Ni_{50}Mn_{43}Sn_7$ [158]	180 Oe at 5 K	"The result suggest that the role of AFM / FM anterface is not substantial in formation of exchange bias in Ni-Mn-Sn Heusler alloy films and exchange bias is rather related to FM / AFM interfaces in nanoscale".
Ni_2MnSn / IrMn Co_2MnSn / IrMn Co_2FeSi / IrMn [141]	56 Oe at RT 89 Oe at RT 230 Oe at RT	"Exchange bias has been studied in thin film systems, in which three types of Heusler alloys (Ni2MnSn,Co2MnSn, and Co2FeSi) are in contact with an antiferromagnet. Magnetic exchange interactionsbetween the constituting atoms (i.e., Ni-Mn, Mn-Mn, Co-Mn, and Co-Fe, or Co-Co) differsubstantially in these Heusler alloys. We explain the influence of the exchange stiffness A withinthe Heusler alloys and of the exchange coupling between Heusler alloy and an antiferromagnet in afinite interface volume. Insertion of an ultrathin Co layer at interfaces brings about an enhancementof the exchange bias in Heusler alloy/antiferromagnet layer system".
$Ni_{50}Mn_{36.8}Sb_{13.2}$ / CrN	148 Oe at	"Exchange bias has been studied in $Ni_{50}Mn_{36.8}Sb_{13.2}$ / CrN system

[159]	10 K	with different CrN thickness. The exchange bias has been related to uncompensated and pinned AFM spins at FM-AFM interface and different AFM domain structures for different thickness of CrN layer".

Apart from this multilayer systems have also been studied for the existence of exchange bias. The observed exchange bias in multilayers depend critically on the thickness of ferro and antiferro layers. H_{EB} is expected to show an inversely linear dependence on the FM layer thickness t_{FM} , that is, $H_{EB} \alpha 1/ t_{FM}$. This inversely linear is experimentally supported if the FM layer thickness of t_{FM} is larger than a critical value [160,161] being suggestive of the interfacial snature of exchange bias. The critical FM thickness depends on FM material and the growth conditions.

Compared to the FM layer, the AFM layer exhibits quite complex influences on H_{EB}. It has been revealed that the H_{EB} is dependent on many factors related to the AFM layer. In the abovementioned expression of H_{EB}, the exchange coupling is considered to involve just the interfacial spins in the FM and AFM layers. The AFM layer thickness does not appear, suggesting that H_{EB} should be independent on the AFM layer thickness. However, the experimental investigations indicate that H_{EB} has strong dependence on the AFM layer thickness [162]. When the AFM layer is sufficiently thin, H_{EB} exhibits an abrupt drop with the decrease in the AFM thickness in a narrow range. When the AFM thickness is less than a critical value, H_{EB} is rendered to zero. This critical AFM thickness depends on the specific AFM material and the measurement temperature. This AFM thickness dependence of H_{EB} is a common phenomenon. When the AFM layer is relatively thick, the dependence of H_{EB} on the AFM thickness becomes quite complex. Relying on the specific layered system, its layered configuration and microstructure, and the measurement temperature, the variation of H_{EB} with the increase in the AFM thickness can be generally separated into two main categories: 1) H_{EB} increases to a constant value when the AFM layer is thick enough [5,32, 163-168]; 2) H_{EB} first increases to a maximum and then decreases with increasing the AFM thickness [169, 170].

1.7 Review of NiMnAl alloys and thin films

Ni-Mn-Al alloys exhibit interest as they are expected to be high temperature SMA along with the low temperature martensite phase exhibiting complex crystal structures. Off-stoichiometric Ni_2MnAl compounds have been explored by Kainuma *et al.* [98]. The results indicate that that during cooling of the alloy, Ni_2MnAl β structure changes martesitically to the 14 M, 10 M, and $L1_0$ (2M) phases. The $L1_0$ structre is seen when the concentration of both Al and Mn is low, where as when the concentration of both Al and Mn is high, the phase which appear are 10M and the 14M. It has been observed that the martesititc start temperature may be varied from 0^0C and 600^0C depending on the concentration of Mn and Al. Ni_2MnAl compound has also been explored by Webster and Ziebeck [171] who concluded that the studied compound exhibits B2 structure and have an antiferromagnetic cone spiral structure. Actually, Ni_2MnZ compound exhibit $L2_1$ phase where nearest neighbour Mn are situated at a distance $a/\sqrt{2}$ apart and next neighbours are situated at a distance a apart, the corresponding distances in the case of Ni_2MnAl are $a/2$ and $a/\sqrt{2}$ respectively. In these circumstances, many couplings might exist which may include super-exchange and direct exchange through the Ni atoms which in this case are magnetically inert. Further exploration of magnetic phase indicates that predominant coupling should be of long range nature and oscillatory in real space. It has been observed that RKKY and double resonance scattering mechanisms both exhibit such type of behaviour and have potential to exhibit helical order. In this respect, Ni_2MnAl has been widely explored to identify the exact magnetic state but the whether a single $L2_1$ parent phase that is not mixed with the B2 phase can be stabilized is still controversial.

There are reports on melt spun ribbons and thin films of Ni-Mn-Al [172]. off-stoichiometric Ni-Mn-Al compounds have been studied by Fujita *et al.* [173] for their complex magnetic properties and MFIS. They concluded that the Al based alloys can only exhibit magnetic shape memory the alloy is in $L2_1$ phase. Further, the precessing parameters play the key role in order to obtain the desired phase.

1.8 Review of NiMnIn alloys and thin films

Ni-Mn-Al is another class of Heusler alloy with interesting structural and magnetic properties. Interest in these alloys accelerated after the observation of 0.12 % reversible MFIS at an applied magnetic field of 4T by Kerenke et al. [174]. They have also reported that the

crystal structure if Ni-Mn-In is similar to NiMnGa where the parent phase has L21 structure with a=0.6011 nm and martensite has 10 M modulated martensite structure having a monoclinic unit cell with γ=86.97° and lattice constants a=0.4398 nm, b=0.5635 nm, and c=2.1720 nm [174]

The relationship of alloying composition-martensitic transformation temperature-crystal structure of the Ni-Mn-In alloy had been systematically studied by T. Krenke *et al.* [101].According to the research results of Thorsten Krenke *et al.*, when the concentration of the indium component is higher than 16%, no structural transformation was observed in Ni-Mn-In alloy system. It is known that forNi-X-In systems, the shape memory effect is obtained by magnetic field induced reversibleaustenite-martensite phase transformations. If there are no such transformations, no shapememory can be realized. Thus the stoichiometric Ni_2MnIn cannot be used asmagnetic shape memory alloys. Composition modification could be an alternative to obtainmartensitic transformation and thus the shape memory effect.The calculated total magnetic moments and the magnetic moments carried by theindividual atoms in Ni_2MnIn, as a function of the c/a ratio shows that the principal contribution to the total magnetic moment is given by Mn atom. The influence of In atom can be neglected for its limited contribution.

The magnetic and structural transformations in the Heusler-based $Ni_{0.50}Mn_{0.50-x}In_x$alloy has been studied by Krenke et al. in thecomposition range $0.05 \leq x \leq 0.25$ [197]. It has been shown that the phase present depends on the composition of the alloy.

x (nominal)	Ni	Mn	In	*e/a*
0.25	50.6	24.6	24.8	7.526
0.235	50.0	26.5	23.5	7.560
0.225	50.4	27.0	22.6	7.608
0.215	50.1	28.5	21.4	7.647
0.20	50.1	30.3	19.6	7.719
0.175	50.2	32.4	17.4	7.810
0.17	49.7	33.2	17.1	7.807
0.165	49.8	33.7	16.5	7.834
0.16	50.3	33.7	16.0	7.869
0.155	51.3	33.2	15.5	7.919
0.15	49.8	35.4	14.8	7.902
0.10	49.9	40.2	9.9	8.101
0.05	49.6	45.5	4.9	8.292

Table 1.3: Variation in compositions of $Ni_{0.50}Mn_{0.50-x}In_x$ samples determined by EDX analysis with valence electron concentrations peratom e/a.

For x = 0.25, superstructure reflections of the $L2_1$ phase ($Fm3m$) have been obtained. The effect of substituting In with Mn is that the there is a contaction of the austenitic phase lattice and thus the lattice constants are smaller, this results in a shift in the position of the peak towerds higher angles. The superstructure reflections are absent in case of x = 0.16. The samples having $x \leq 15.5$ are in the low temperature martensite phase at room temperature. The alloy having x = 0.155 and x = 0.15 exhibit the 10 M modulated martensite structure. Monoclinic unit cells are observed with β = 88.45° and 88.93° with x = 0.155 and x = 0.15, respectively. The reflections of the sample having x = 0.10 is that of a 14 M martensitic phase. For x = 0.05, an unmodulated tetragonal $L1_0$ structure has been observed in the martensite phase.

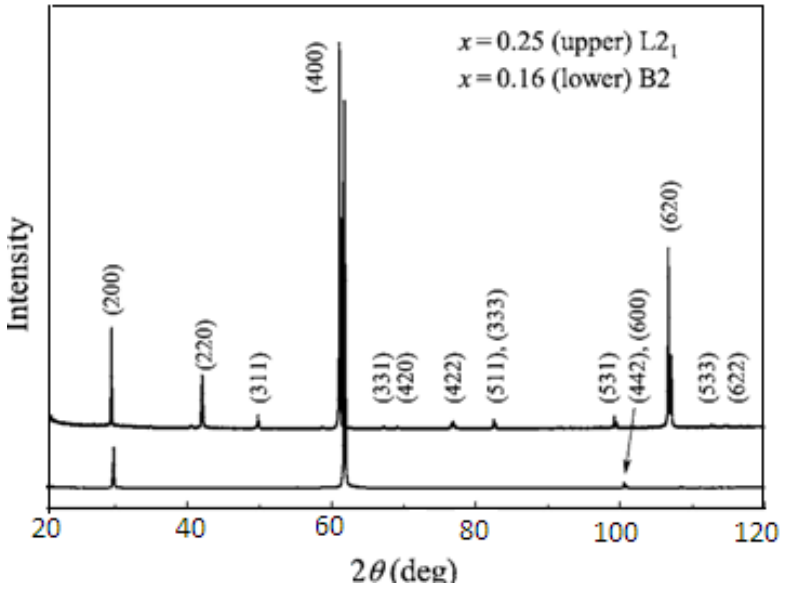

Figure 1.17: X-ray diffraction pattern at room temperature for x = 0.25 (upper) with $L2_1$ structure and x = 0.16 (lower) with B2 structure. [101]

The structure, magnetic, and martensitic properties of Fe doped Ni-Mn-In magnetic shape memory alloys have been studied. While $Ni_2MnIn_{1-x}Fe_x$ ($0 \leq x \leq 0.6$) alloys are ferromagnetic and non martensitic, the martensitic transformation temperature in $Ni_2Mn_{1.5}In_{1-y}Fe_y$ and $Ni_2Mn_{1.6}In_{1-y}Fe_y$ increases for lower Fe concentrations (y = 0.05) before decreasing sharply for higher Fe concentrations. In alloys, presence of ferromagnetic interactions and structural disorder induced by Fe affect Mn-Ni-Mn antiferromagnetic interactions resulting in suppression of martensitic transformation in these Fe doped alloys [175].

Thin films of NiMnIn have been studied for the presence of martensitic transformation and exchange bias phenomenon in thin films of NiMnAl. It has been observed [176] that the phase depends on the substrate on which film has been deposited. A martensitic transformation has been observed for the film deposited on MgO substrate.

1.9 Motivation and Main objectives of the thesis

Investigation on exchange bias properties of Heusler alloys and bilayers by several research groups including ours reveal that the exchange bias properties exhibited by Heusler alloys are very sensitive to the thinkness, composition and microstructure of the alloy. In order to further elucidate this point, in this thesis, we attempt to study exchange bias in Ni-Mn-Al system, Ni-Mn-Al-In system and Ni-Mn-Al bilayer system.

1. Study of exchange bias properties of Ni rich and Mn rich Ni-Mn-Al thin films –

Ni-Mn-Al alloys are interesting as potential high temperature shape memory alloy and as alloys which exhibit different crystal structures of the martensite. The magnetic properties of off-stoichiometric Ni-Mn-Al alloys are structural dependent. The literature on Ni-Mn-Al alloy suggests that the antiferromagnetism of Ni–Mn–Al is associated with the quenched B2 structure, whereas $L2_1$ structure promotes ferromagnetic ordering of the magnetic moments [173]. The studied alloys are always found in a state that incorporates both ferromagnetic and antiferromagnetic ordering associated with $L2_1$ and B2 structures respectively. The Neel temperature of antiferromagnetic phase T_N ~ 300 K and the curie temperature of the ferromagnetic phase T_C ~ 375 K. The presence of both ferro and antiferro moments in the same alloy with $T_C > T_N$ which is the prime requisite of exchange bias makes these alloy interesting for study of exchange bias phenomenon. Thus NiMnAl offer a potential candidate for the study of exchange bias. For practical applicabiblity, thin film is the most desirable form.

To explore the exchange bias properties, Ni rich and Mn rich Ni-Mn-Al thin films have been synthesizes with varying thickness. Ni rich compositions exhibit a mixed $L2_1$ + B2 structure at thickness ≤ 1.5 μm. For larger thickness, a pure B2 structure has been observed. The Mn rich compositions exhibit a pure B2 structure independent of thickness. The result demonstrate that exchange bias observed in Ni rich samples may been explained in terms of the existence of a spin glass state at low temperature. However, the exchange bias observed in

the films with B2 phase finds its origin in field induced ferromagnetic type ordering occurring in the antiferromagnetic matrix. An increase in exchange bias with increasing film thickness has been observed in Ni rich and Mn rich compositions. Large exchange bias has been observed Mn rich compositions.

2. Study of exchange bias properties of NiMnAl/ Ni bilayer films

Further increase in exchange bias may be obtained by fabricating thin films in ferro-antiferro bi-layer form. In this regards, Heusler alloy has also been explored for exchange bias properties in bilayer [155,159] form. The underlying mechanism for the observation of exchange bias in bulk and thin films of Heusler alloy is the interplay between ferromagnetic and antiferromagnetic regions present in the low temperature phase. Among FM / AFM bilayer films Ni layer has been extensively used as the FM layer. The Ni layer has been chosen due to limited space for source material. As per the literature, exchange bias has been found to be inversely proportional to the magnetization of the ferromagnetic. In view of this it has been observed that Ni has low magnetization of 485 emu/cc as compared to 1707 emu/cc for Fe, 1400 emu/cc for Co and 880 emu/cc for $Ni_{80}Fe_{20}$. Thus Ni is the suitable candidate for bi-layer.

Ni layer with varying thickness have been deposited on Ni rich and Mn rich Ni-Mn-Al thin films. The results demonstrate that that for a particular thickness of Mn rich NiMnAl layer, effect of Ni variation is non monotonic. The thickness of Ni layer at which maximum exchange bias occurs depends on the thickness of NiMnAl layer. Maximum EB has been obtained for Ni layer thickness of 60 nm for Ni rich samples. For the Ni layer deposited on Mn rich compositions, exchange bias shows non-monotonic variation with increasing cooling field. For 1 μm thick film maximum H_{EB} has been obtained for 30 nm thick film. For 2.5 μm thick film maximum H_{EB} has been obtained for 60 nm thick film. The exchange bias increases with Ni layer for NiMnAl thickness of 1 μm, for other films H_{EB} decreases with Ni layer. The effect on H_{EB} for Ni layer on Mn rich samples is much more pronounced as compare to the Ni rich samples.

3. Study of exchange bias properties of Ni-Mn-Al-In thin films

Off-stoichiometric Ni-Mn-In ferromagnetic shape memory alloys have become the focus of intensive research due to the observation of magnetic field-induced reverse martensitic

transformation. NiMnIn exhibits vide scale applications owing to their T_C around room temperature. Dependng on the Mn/In T_C of the alloy can be varied from 290 K to 310 K [101]. It has been observed that in thin films, T_C has been observed to be ~ 334 K. As T_C of the alloy in thin film form is above room temperature and T_N of NiMnAl is around room temperature, exchange bias may be studied in NiMnAlIn thni films.

Thin films have been deposited by co-sputtering from target of NiMnAl and In. Large exchange bias of 2300 Oe has been observed at 2 K for the film with thickness 1.2 μm. The effect of cooling field and temperature on exchange bias properties has been discussed. Training effect has also been done to study the exact nature of exchange bias phenomenon in this alloy system. The results demonstrate that that the system can be modelled as FM/SG interface.

The technical objectives of the present work can be enumerated as:

Chapter 3 - Investigation on Ni rich and Mn rich Ni-Mn-Al thin films

Exchange Bias property of Ni rich and Mn rich thin Films have been explored. The films have been cosputter deposited using elemental targets of Ni, Mn & Al. It has been observed that Ni rich compositions exhibit a mixed $L2_1$ + B2 structure at thickness ≤ 1.5 μm. For larger thickness, a pure B2 structure has been observed. The Mn rich compositions exhibit a pure B2 structure independent of thickness. The structure and magnetic properties of Ni rich and Mn rich Heusler alloys have been studied in detail. Martensitic transition has been observed for the films exhibiting B2 as well as mixed (B2+ $L2_1$) structure. For very thin films no martensitic transition has been observed in both the systems. Owing to the presence of ferromagnetic ($L2_1$) and antiferromagnetic (B2) phase in film with mixed structure (L21+ B2), the exchange bias has been observed in these films. The exchange bias observed in Ni rich samples has been explained in terms of the existence of a spin glass state at low temperature. Exchange bias has also been observed in B2 phase films associated with the field induced ferromagnetic type ordering occurring in the antiferromagnetic matrix. An increase in exchange bias with increasing film thickness has been observed in Ni rich and Mn rich compositions. Large exchange bias has been observed Mn rich compositions.

Chapter 4 Investigation of exchange bias properties of NiMnAl/ Ni bilayer films

In this chapter the effect of ferromagnetic (Ni) layer on Ni rich $Ni_{57}Mn_{24}Al_{19}$ compostion and Mn rich $Ni_{50}Mn_{31}Al_{19}$ compositionhas been studied in detail. Thickness of both NiMnAl layer and Ni layer has been varied. The effect of cooling field and varying ferro – antiferro layer has been studied in detail.

For the Ni layer deposited on Ni rich compositions, exchange bias increases with increasing cooling field. For a particular thickness of Ni rich NiMnAl layer, effect of Ni variation is non monotonic. The thickness of Ni layer at which maximum exchange bias occurs depends on the thickness of NiMnAl layer. Maximum EB has been obtained for Ni layer thickness of 60nm. For the Ni layer deposited on Mn rich compositions, exchange bias shows non-monotonic variation with increasing cooling field. For a particular thickness of Mn rich NiMnAl layer, effect of Ni variation is non monotonic. The thickness of Ni layer at which maximum exchange bias occurs depends on the thickness of NiMnAl layer. For 1 μm thick film maximum H_{EB} has been obtained for 30 nm thick film. For 2.5 μm thick film maximum H_{EB} has been obtained for 60 nm thick film. The exchange bias increases with Ni layer for NiMnAl thickness of 1 μm, for other films H_{EB} decreases with Ni layer. Variation of EB with temperature has also been discussed in terms of existing models.

Chapter 5 Investigation of exchange bias properties of Ni-Mn-Al-In thin films

In this chapter exchange bias properties of NiMnAlIn thin films have been studied. Thin films have been deposited by co-sputtering from target of NiMnAl and In. Thin films of thickness have been deposited. Owing to the ferromagnetic nature of NiMnIn films and antiferromagnetic NiMnAl films, coexisting ferro – antiferro interactions occur in the deposited films which give rise to exchange bias interactions. The effect of cooling field and temperature on exchange bias properties has been discussed. Training effect has also been done to study the exact nature of exchange bias phenomenon in this alloy system. Large exchange bias of 475 Oe at 10 K has been obtained for the film with thickness 1.2 μm.

CHAPTER 2

EXPERIMENTAL DETAILS AND CHARACTERIZATION TECHNIQUES

2.1 Thin films

Thin films are thin material layers ranging from fractions of a nanometer to several micrometers in thickness. The synthesis if thin film on the substrate occurs by the deposition of individual atoms. There is a difference between thin films and thick films. A thick film is defined as a low-dimensional material created by thinning a three-dimensional material or assembling large clusters/aggregates/ grains of atomic/molecular/ionic species.

2.2 Thin film synthesis techniques

Nanocrystalline thin films have been synthesized by various chemical vapor deposition (CVD) and physical vapor deposition (PVD) techniques such as pulse laser deposition (PLD), spray pyrolysis, magnetron sputtering, sol-gel, metal- organic chemical vapor deposition (MOCVD) and molecular beam epitaxy (MBE). Every technique has its own advantages and disadvantages. The properties expected form the film is usually the deciding factor for the selection of a specific technique. If the primary need is to obtain highly uniform composite thin films in which the distribution of size is moderate, then PVD) techniques which include laser ablation, evaporation and magnetron sputtering are very efficient whereas when the deposition area is large, CVD techniques such as spin coating and spray pyrolysis technique are found to be more efficient. In the present work, sputtering technique has been used to synthesize magnetic thin films. The detailed description of sputtering technique and process has been given below

2.2.1 Sputtering Technique

Sputter deposition is widely used technique for the erosion of surfaces and the deposition of films. In the sputtering process which is PVD process there occurs physical vaporization of atoms from a surface by momentum transfer from bombarding energetic atomic sized particles.

Among the different physical vapor deposition (PVD) techniques, magnetron sputtering is used extensively in the scientific community. The schematic diagram of a simple DC sputtering system is shown in fig. 2.1 which consists of a vacuum chamber, target, power supply and a substrate holder. The target in the sputtering process is a 2 inch diameter disc of material to be deposited which is given negative potential by a DC power supply. Target and substrate face each other and serve as electrodes in this case.

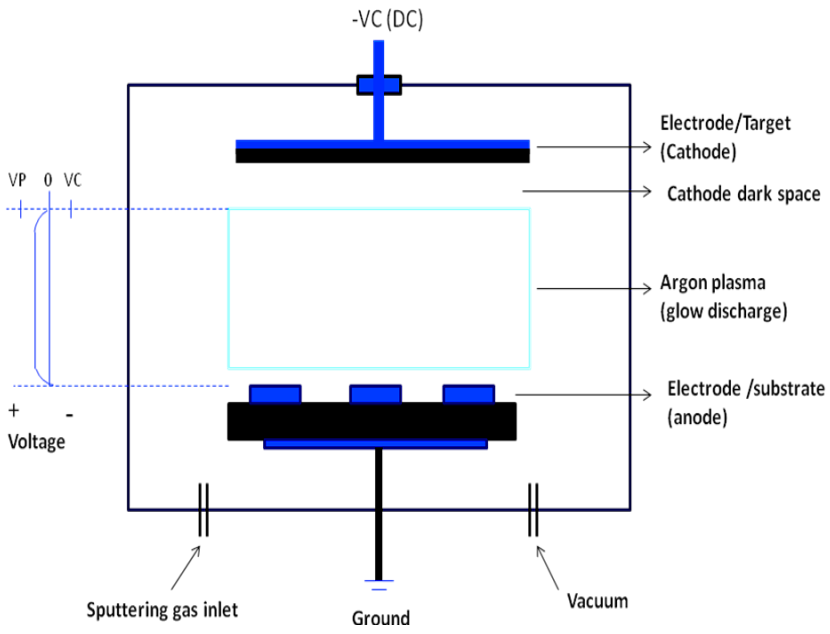

Figure 2.1 A schematic diagram of a simple DC sputtering system and voltage distribution.

2.2.2 Process of Sputtering

The first step in the sputtering process is the pumping of the vacuum chamber to a typical base pressure of 10^{-6} torr or more by vaccum pumps like rotary and turbo molecular pumps etc. An inert gas, usually argon or helium with a pressure ranging from a few to 100mtorr depending upon the requirement, is introduced into the system as the medium to initiate the discharge and maintain the plasma once initiated. When an electric field of several kilovolts per centimeter is applied between cathode and anode, a glow discharge is initiated and maintained between these two electrodes. A very little current flows at first due to the small

number of charge carriers in the system after the initial application of the voltage. Once sufficient number of charge carriers builds up, the free electrons strike the neutral Ar atoms to create Ar^+ ions and more free electrons. The newly created free electrons can now ionize additional Ar neutrals thus multiplying the number of Ar^+ ions. In this visible glow maintained between the electrodes, the Ar^+ ions in the plasma gets accelerated towards direction of the cathode and strike the target. So, the positive ions (Ar^+) in the discharge strike the cathode (the source target) and this bombardment creates a cascade of collisions in the target material's surface. These multiple collisions results in the ejection of neutral target (or sputter) atoms through momentum transfer.

Since sputtering is the result of momentum and energy transfer, the incoming argon ions should have high enough energy to break the bonds holding the target atom in place. The typical surface binding energy is ~5-10 eV. With high enough energy of argon ions, the collision cascade can be 5-10 nm below the target's surface. However, the particles ejected are usually within 1nm of the surface. Only a small fraction of collisions produce sputtering. The process of sputtering has been shown schematically in fig. 2.2. To measure the efficiency of sputtering, the sputter yield, S, is defined as the number of sputtered atoms per incident particle. In a practical sputtering process, the yield is from 0.1 to 10 %. During the collision with the target surface, secondary electrons are emitted. They are accelerated away from the cathode. These electrons then travel back into the argon plasma and collide with the argon atoms, ionizing some of them and sustaining the plasma.

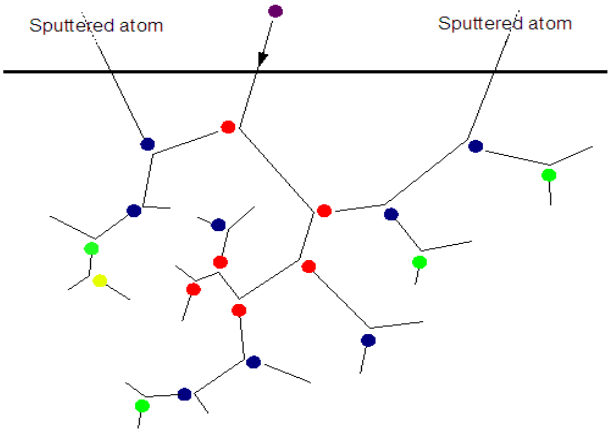

Figure 2.2 Schematic of physical sputtering process.

Magnetic fields (magnetron) can also be applied to the plasma region in order to improve the sputtering performance. A magnetron uses a static magnetic field configured at the cathode location. If the magnetic field is set up correctly, this **E×B** drift can be arranged to close on itself, forming a current loop of drifting secondary electrons.

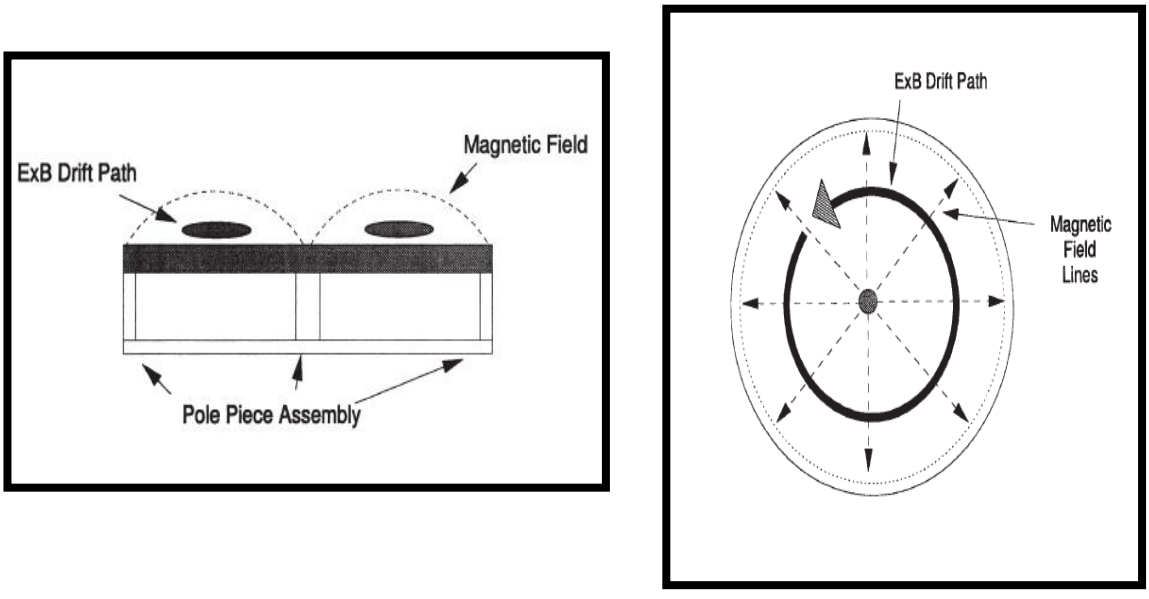

Figure2.3 (a) Side and **(b)** top view of magnetic field configuration

In this arrangement, secondary electrons are mainly bound in a place near the cathode. There occurs collision which results in a loss of kinetic energy. RF (Radio Frequency) power supply can also be used in magnetron sputtering for electrically insulating targets. It is also important to note that since RF power supplies are designed to look into circuits with a purely resistive 50Ω load, a tunable matching network is required to damp out the complex reactance (both capacitance and inductance) of the discharge. RF sputtering can be performed at low gas pressures (<1mtorr) and can be used to sputter electrically insulating and semiconductor materials. The primary disadvantage in the use of RF power supplies for magnetron sputtering in addition to being expensive is the inherently low deposition rate.

In our lab, we use DC/RF magnetron sputtering system. **Figure 2.4** shows the turbo based magnetron sputtering system assembled in our laboratory (Nanoscience Laboratory, Institute Instrumentation Centre, IIT Roorkee). The pumps and gauges fitted in to the chamber are from Pfeiffer Vacuum. For DC sputtering, 'Aplab' high voltage DC power supply H10110 (**50-1000 V,** 0-1 A) was used. The substrate is put on the heater cum substrate holder which can be rotated by a DC motor to bring the substrate beneath the required target. The same chamber could be used for the co-deposition of three different targets at the same time by mounting the sputtering guns in the ports which are at 60^{o} with the vertical.

Figure 2.4: Magnetron Sputtering System.

2.3 Thin films growth mechanisms

The initial period of growth in thin film may be divided in two forms. First is Frank-Vander Merwe growth mode in which substrate is evenly coveraged and then layer by layer growth occurs. Second is Volmer-Weber growth mode in which islands formation takes place by nucleation and agglomeration. Depending on the interaction energies of substrate and film atoms, any of following three growth modes can occur:

- **Layer by layer**:

Frank-Vander Merwe growth mode in which substrate is evenly coveraged and then layer by layer growth occurs. In this case the boundation of atoms with the substrate is stronger than each other. This growth mode is observed in the case of adsorbed gases. This is also referred as epitaxial growth.

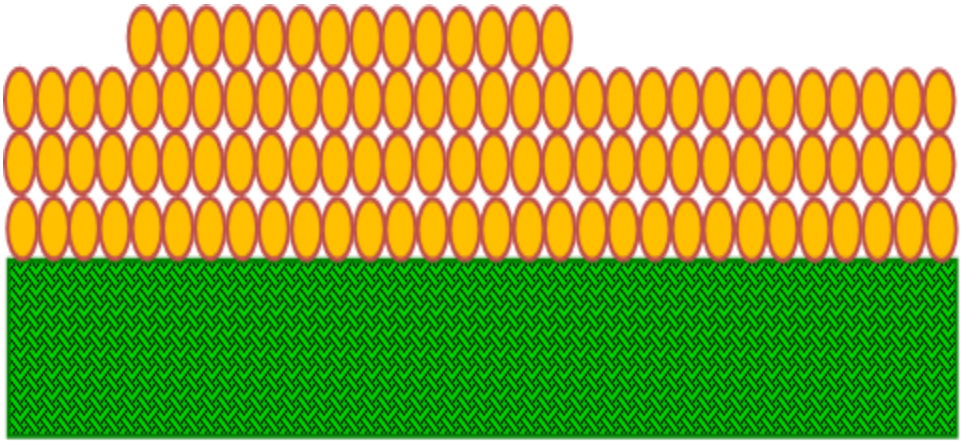

Figure 2.5 Frank-Vander Merwe: Layer growth (ideal epitaxy)

- **Islands:**

The occurs a island sort of growth in the initial atomic layers which generally around nucleation sites. In this case boundation of atoms to excha other is stronger than to the substrate.

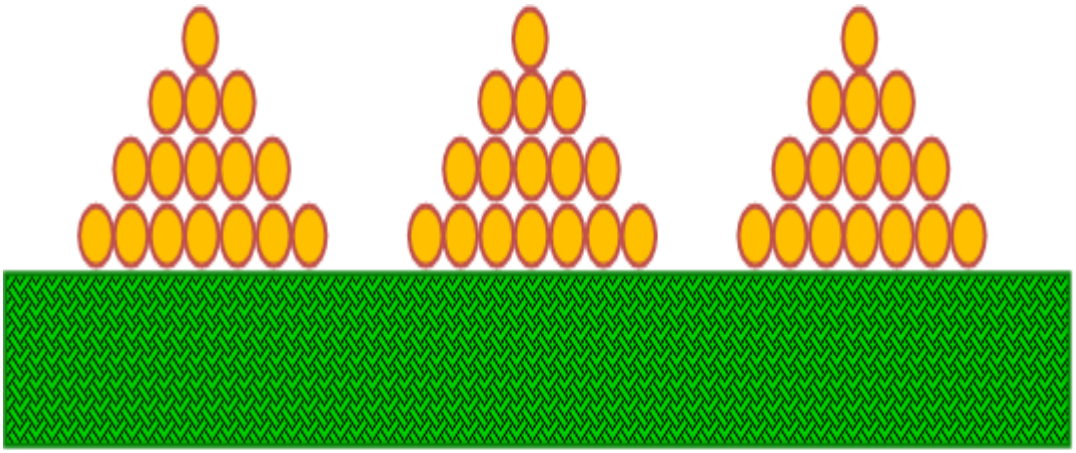

Figure 2.6 Volmer-Weber: Island growth

- **Layer plus islands**:

The mixed layer-island or Stranski-Krastanov growth mode is an interesting intermediate case. Growth modes can be systematically classified in terms of surface energies **(Fig. 2.7)**

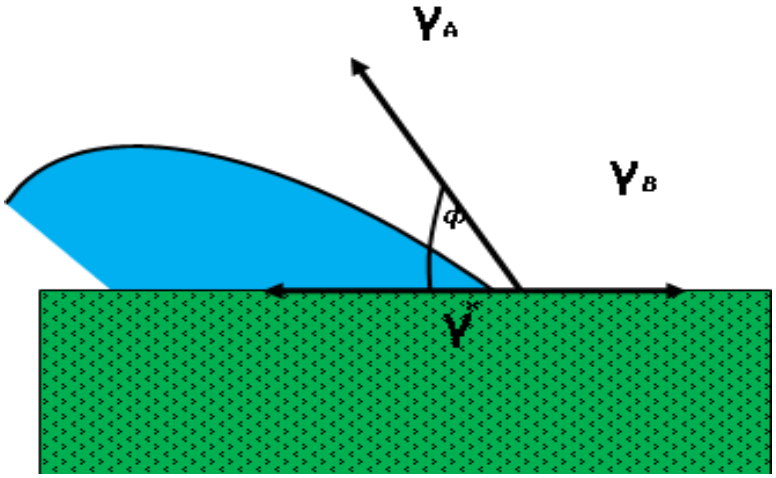

Figure 2.7 Schematic diagram of surface energy of substrate, thin film material and interface energy of film-substrate.

2.4 X-Ray Diffraction

The crystallographic structure of the samples was identified by x-ray diffraction(XRD) using a Panalytical x-ray diffractometer with filtered Cu Kα radiation of wavelength λ = 0.154056 nm. Schematic diagram of is shown in Fig. 2.3. The X-ray waves interact with the periodic medium due the crystalline nature and results in diffraction according to Bragg's law. In essence when the lattice spacing is an integer multiple of the wave length, diffraction will occur at a characteristic angle.

$$n\lambda = 2d \sin\theta \qquad \text{.....(2.2)}$$

where n is the order of the reflection (normally in XRD only first order is observed), θ isthe Bragg angle for diffraction and λ is the wavelength of source. In the present case,diffractometer is equipped with a 2 KW x-ray tube.

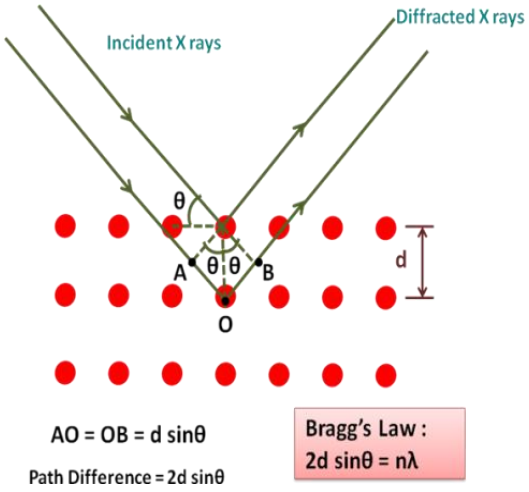

Figure 2.8: Schematic diagram of X-ray scattering to show Bragg's law

For XRD, ribbon samples were stuck onto a glass microscope slide with double sided tape. The slide was then assembled with the diffractometers sample holder so as toensure each sample was in the same position relative to the beam. XRD of thin film samples were carried our using thin film assembly. For powder samples the conventional Bragg Brentano geometry is used. The schematic diagram of Bragg Brentano Geometry is shown in **Fig. 2.9**.

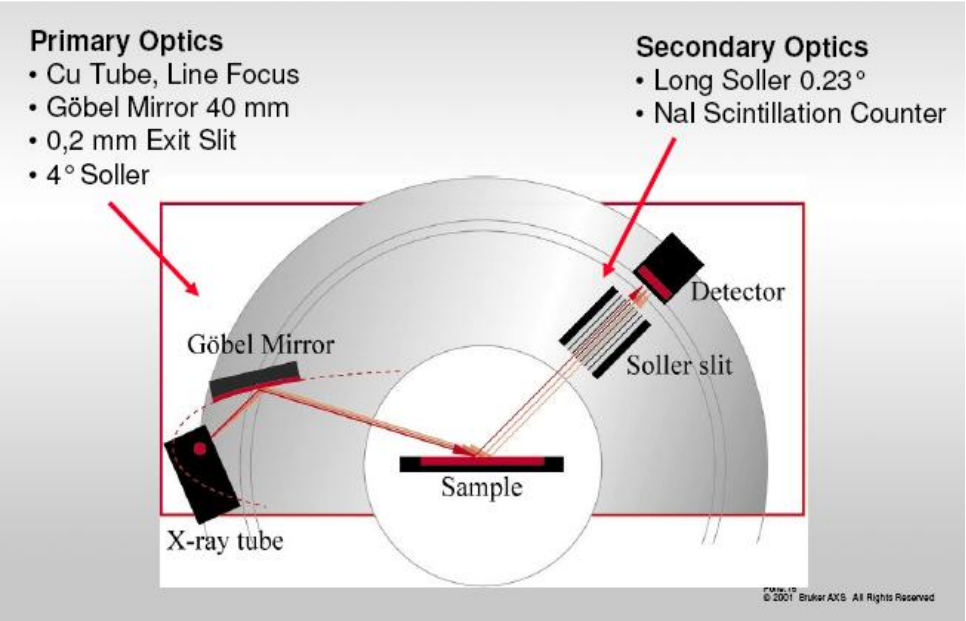

Figure 2.9: Schematic diagram of Bragg Brentano Geometry

The angle that occurs among plane of specimen and X-ray source is θ, the Bragg angle.The angle between the projection of X-ray source and detector is 2θ. In the Bragg Brentano geometry, the X-ray source and the detector move in the vertical plane in opposite directions above the center of specimen. The diffractometer circle is different from the focusing circle, it is centered at the specimen, and both x-ray source and detector lie on the circumference of the circle. The radius of diffractometer circle is fixed.

It is also referred to as goniometer circle or measurement circle. On the source side, the X-rays pass through sollar slits, which define and collimate the incident beam. After passing sollar slits, X-rays pass through the divergence slits which defines the width of the incident beam. After the beam has been diffracted by the specimen, it passes through another set of slits. The antiscatter slit reduces the background radiation, improving peak to background ratio, by making sure that detector receives X-rays from specimen only. The beam then passes through the receiving slit and sollar slits before finally entering the detector.

2.5 Transmission electron microscopy (TEM)

Transmission electron microscope (TEM) operates on the same basic principle as the optical (light) microscope but uses electrons instead of visible light. The shorter wavelength of electrons (200 keV electrons have a wavelength of 0.025 Å) makes it possible to get a high-resolution (0.2 nm) and high-magnification thousand times better than the light microscope. Also, in an optical microscope, the lenses are made up of glass and have fixed focal lengths, whereas in TEM, the electromagnetic lenses are constructed with ferromagnets and copper coils. The focal length of electromagnetic lenses could be changed by varying the current through the coil. TEM is used to characterize the microstructure of materials such as grain size, morphology, crystal structure and defects, crystal phases and composition, and in biological sciences, especially in the study of cells at the molecular level. The model of TEM used in the present study is 200 kV FEI TECHNAI G2. The ray-diagram is shown in **Fig. 2.10**.

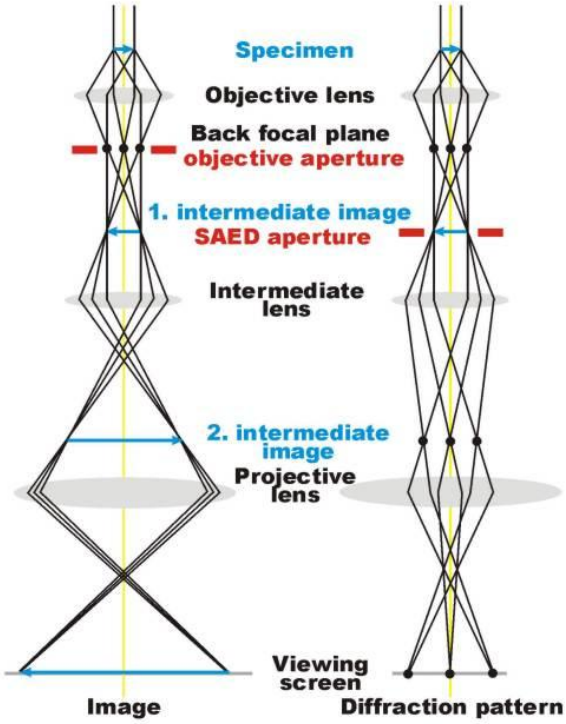

Figure 2.10 Ray diagram for the production of specimen image and diffraction pattern.

The system consists of an electron source made of a LaB_6 (Lanthanum hexaboride), focussing column and fluorescent screen. The accelerating voltage is variable between 20-200 kV. Adding a condenser lens provides a means of varying the illumination of the

specimen by changing the excitation of the lens. Modern TEMs have two condenser lenses. The first condenser lens (C1) is a strong lens, which can give different spot sizes by giving different current to it. Second condenser (weak lens) lens is now used to bring the first condenser lens cross-over down to the specimen. The maximum size of the second condenser lens (C2) aperture is determined by the spherical aberration of C2. Sometimes, smaller apertures are selected to obtain better coherent illumination. In practice, spot sizes down to approximately 100 nm can be obtained by using this double condenser system. The condenser lenses are fitted with apertures, which are usually small platinum disks with holes of various sizes. Condenser lens apertures protect specimen from too many stray electrons, which can contribute to excessive heat and limit X-ray production further down the column. The objective lens forms the so- called first intermediate image of the object, which will be enlarged by a lens lower in the column. Because defects of the objective lens are magnified by the total magnification factor, this lens is the most critical lens in the microscope. In general, smaller the focal length (1 to 5 mm) and the lens aberration constants better will be the resolving power of the microscope.

The objective aperture is positioned in the back focal plane of the objective lens for two main reasons:

- Limiting the angular aperture to reduce spherical and chromatic errors, which otherwise would blur the image and reduce the resolving power.
- Intercepting unwanted strongly scattered electrons from the specimen to prevent them from contributing to the image which would otherwise reduce the contrast of the final image.

Final image magnification in TEM is the result of the magnification of each magnifying lens: the objective lens, the diffraction lens, the intermediate lens and the projector lens. The objective lens, the first magnifying lens in the TEM, is a high power lens. The diffraction lens, below the objective lens, is a very low power lens. The intermediate lens is a weak lens but with variable power. The current of this lens is adjusted to control the final magnification of the image. The last lens is the projector lens, which is a high power lens that projects the final magnified image on to the viewing screen.

TEM has following modes of operation:

1. Image Mode: Imaging mode allows the imaging of the crystallographic structure of a specimen at an atomic scale. Because of its high resolution, it is an invaluable tool to study nanoscale properties of crystalline material. In image mode, image contrast comes from the scattering of the incident electron beam by the specimen. By using electrons accelerated to high voltages, atomic planes of the crystal can be resolved. In this mode, intermediate aperture is removed and only objective aperture is used. Intermediate lens is used to focus on the image plane of the objective lens. In image mode, two imaging systems are used:

(a) Bright field image mode: When an incident electron beam strikes a sample, some of the electrons pass directly through, while others may undergo slight inelastic scattering from the transmitted beam. Contrast in an image appears by differences in scattering. By inserting an aperture in the back focal plane, an image can be produced with these transmitted electrons. The resulting image is known as a bright field image. Bright field images are commonly used to examine micro-structural related features.

(b) Dark field image mode: If a sample is crystalline, many of the electrons will undergo elastic scattering from the various planes. This scattering produces many diffracted beams. If any one of these diffracted beams is allowed to pass through the objective aperture, an image can be obtained. This image is known as a dark field image. Dark field images are particularly useful in examining microstructural detail in a single crystalline phase.

2. Diffraction mode: The diffraction pattern that is always present in the back focal plane of the objective is brought into focus by the objective lens. Individual spots are seen when the specimen is a single crystal, while for polycrystalline material concentric rings are observed. In diffraction mode, objective aperture is removed and only intermediate aperture is used which passes the diffraction pattern of a selected region. For a single crystal, the diffraction spots from planes which are equivalent by symmetry are placed symmetrically around the central spot. Interplanar distance, *d* can be calculated from the expression:

$$R.d = L.\lambda \qquad \ldots\ldots\ldots\ldots\ldots\ldots\ldots\ldots\ldots\ldots(2.3)$$

where, λ is the wavelength of the electron beam (0.025 Å for 200 kV), *R* is the distance of a particular spot form the central bright spot and *L* is the distance between the specimen and the diffraction plane, known as the lens constant or camera length.

Figure 2.11: Photograph of 200 KeV FEI Tecnai G^2 TEM at Institute Instrumentation Centre, Indian Institute of Technology, Roorkee.

2.6 Field emission scanning electron microscopy (FE-SEM):

The scanning electron microscope (SEM) is one of the most versatile instruments available for the examination and analysis of the microstructure morphology and chemical composition characterizations. To understand the working principle of FESEM, first we need to know the kind of interaction an energetic electron beam has with samples and the phenomena which take place after this interaction.

Interaction of Electron with Samples

When an incident electron beam strikes the specimen composed of a crystalline and/or amorphous structure, it undergoes a series of complex interactions with the nuclei and electrons of the atoms of the sample. These interactions can be elastic interactions and inelastic interactions. **Fig. 2.12** schematically shows the interaction of electron beam with the specimen and shows the regions from which different signals are detected. **Fig. 2.13** shows the tear drop model for electron beam interaction with solids and explains the interaction volume in the specimen and shows different kind of signals coming from the sample from various depths.

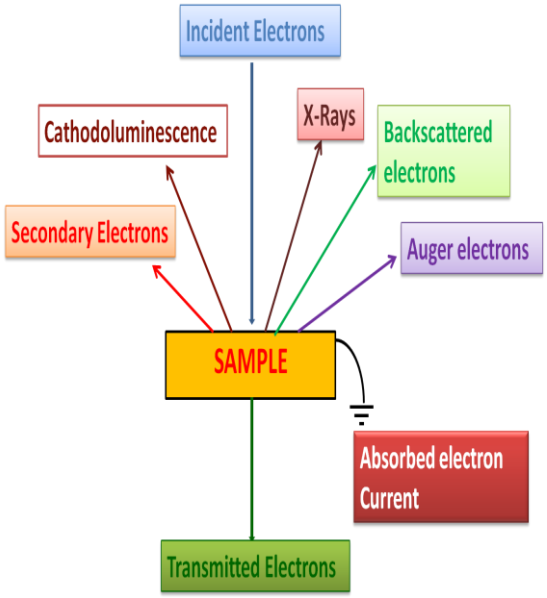

Figure 2.12 Schematic view of electron beam interaction with specimen.

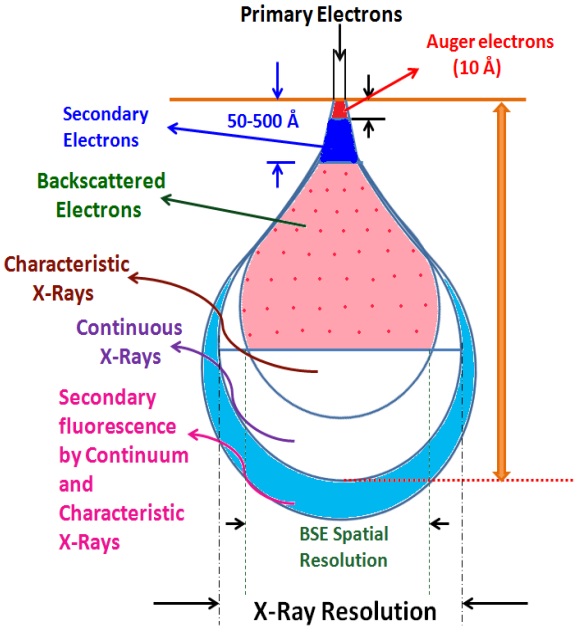

Figure 2.13 Tear drop model for electron beam interaction with solids.

Secondary electrons: When the primary beam strikes the sample surface causing the ionization of specimen atoms, loosely bound electrons may be emitted and these are referred to as secondary electrons.

Backscattered electrons: A backscattered electron (BSE) is defined as one which has undergoes a single or multiple scattering events and which escapes from the surface with energy greater than 50 eV.

Characteristic X-rays: The analysis of these characteristic X-rays is very helpful in providing chemical composition the material used as specimen.

Auger Electrons: Auger electrons are produced following the ionization of an atom by the incident electron beam and the falling back of an outer shell electron to fill an inner shell vacancy.

Having understood the electron beam interaction with solids, it is easy to understand the working of FESEM. A schematic diagram of the optical column of the FESEM is shown in **Fig. 2.16 (a)**. The electron beam is energized by the accelerating potential of few hundred eV to 50 keV and the divergent beam is focused by two condenser lenses into a beam with a very

fine focal spot size. The first condenser lens that works in conjunction with the condenser aperture. At each point the secondary and back-scattered electrons reaching the detector are counted to be used for determining the relative intensity of the pixel representing that point in the final image. The higher the atomic number of the specimen material, the greater is the number of secondary electrons that reach the detector, giving rise to a higher intensity in the image. Limitation associated with the SEM is that the specimen that has to be analyzed should be conducting. In case of non-metals, it is required to make them conducting by covering the sample with a thin layer of conductive material like gold or platinum in order to enhance the signals.

In the present study, field emission scanning electron microscope (FEI Quanta 200F model) with resolution of 2 nm and 80000X magnification were used (**Fig. 2.14 b**). Elemental composition analysis can also be performed by using the energy dispersive X-ray analysis (EDAX) attached with the FE-SEM system. An EDAX spectrum normally displays peaks corresponding to the energy levels for which the most X-rays had been received. Each of these peaks is unique to an atom, and therefore corresponds to a single element. The higher a peak in a spectrum, the more concentrated the element is in the specimen.

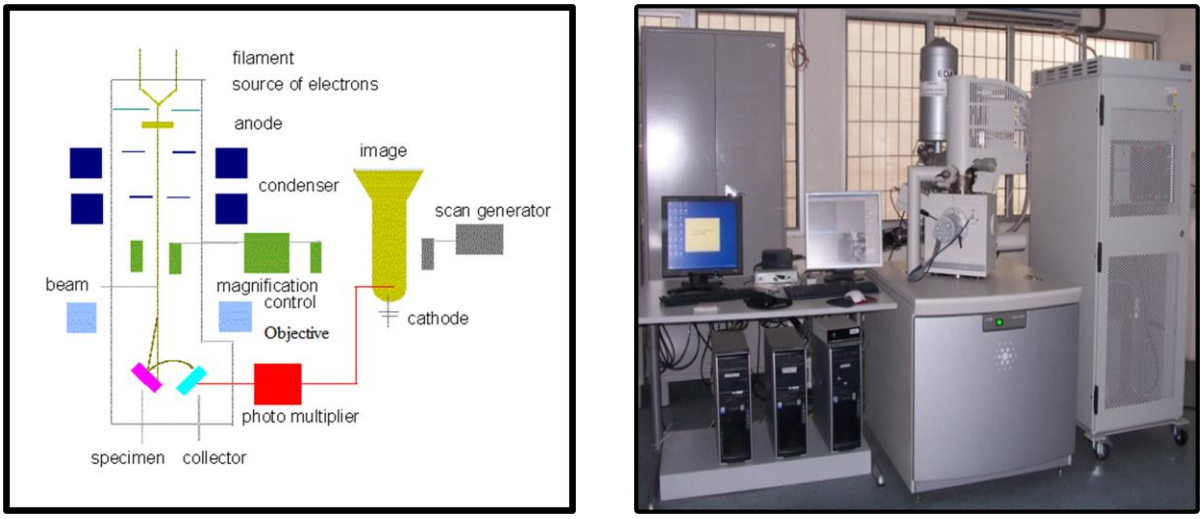

Figure 2.14 (a) A Schematic diagram of the Scanning electron microscope **(b)** Photograph of FESEM available in IIT Roorkee

2.7 Energy Dispersive X-ray Spectrometry (EDS)

EDS makes use of the X-ray spectrum emitted by a solid sample bombarded with a focused beam of electrons to obtain a localized chemical analysis. An ED detector has several components like Collimator assembly, 'Be' window, a semiconductor crystal, Field-effect transistor, Cryostat etc.

Semiconductor Crystal: When an electron is raised into the conduction band, it leaves behind a 'hole', which behaves like a free positive charge within the crystal (**Fig. 2.15).**

Field-effect transistor: The charge is converted to a voltage signal by the FET preamplifier (**Fig. 2.15 b**).

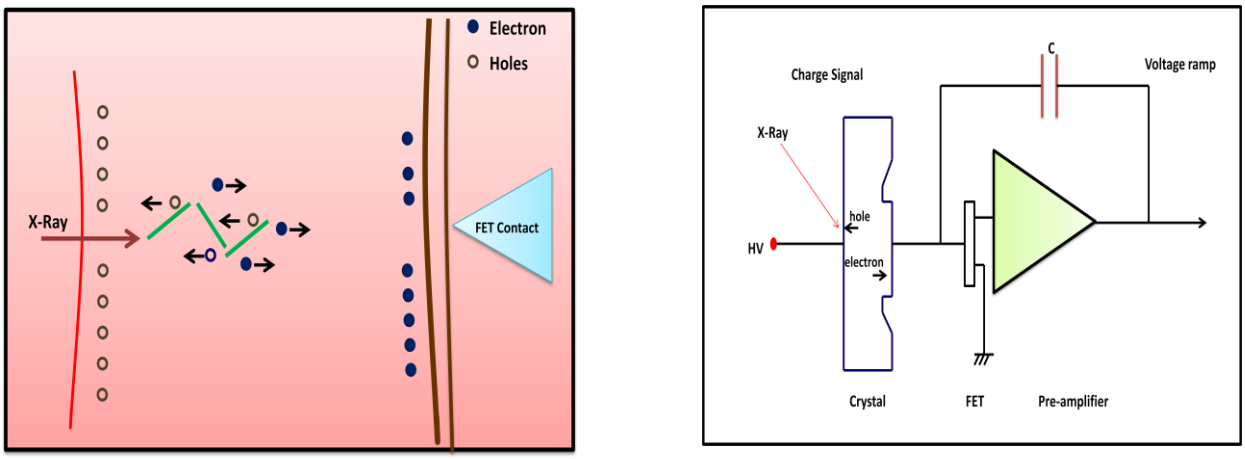

Figure 2.15 Conversion of X-ray signals into a voltage 'ramp' by the EDS detector **(a)** Generation and measurement of electron-hole pairs in the crystal. **(b)** Circuit diagram of the EDS detector.

In the present study EDX attached to FE-SEM (Model: FEI Quanta 200F) procured from FEI Company Netherland was used to study the chemical composition of thin films.

2.8 Atomic Force Microscopy:

Atomic force microscopy is an amazing technique that allows us to see and measure surface structure with unprecedented resolution and accuracy. AFM has a great advantage in that almost any sample can be imaged, be it very hard, such as the surface of a ceramic

material, or a dispersion of metallic nanoparticles, or very soft, such as highly flexible polymers, human cells, or individual molecules of DNA. In the present study, atomic force microscope from NT-MDT from NTEGRA, Russia was used and the photograph is shown in **Fig. 2.16**. AFM monitors the force between a sharp tip and the sample and utilizes this force to produce images. There is a piezoelectric actuator to precisely control the sensor above the surface and to raster the tip across the sample, there is a control system to

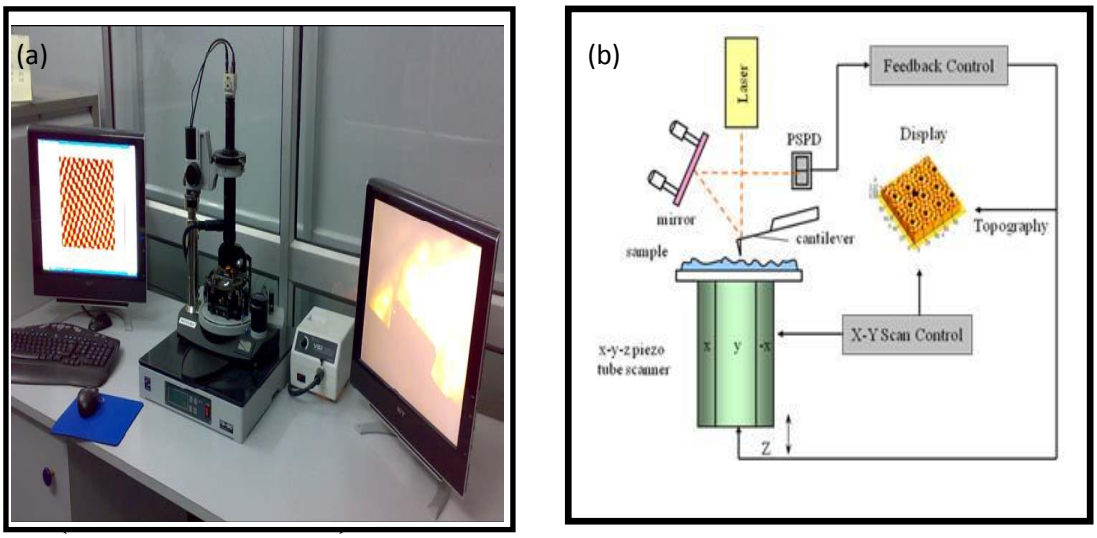

Figure 2.16: Atomic force microscope (AFM)

2.9 Superconducting Quantum Interference Device (SQUID):

The SQUID is the world's most sensitive magnetic flux detector. It can detect incredibly small magnetic moments of the order of 10^{-9}emu. SQUID is used in a wide range of applications, including biomagnetism, susceptometors , nondestructive evaluation, geophysics, scanning SQUID microscope, and nuclear magnetic resonance etc. SQUID exploits the physical phenomena of flux quantization and Josephson tunneling. There are two main types of SQUID magnetometers: direct current (DC) and radio frequency (RF). RF SQUIDs can work with only one Josephson junction, which might make them cheaper to produce, but are less sensitive whereas, DC SQUIDs work with two Josephson junctions and are very sensitive to measure the extremely weak magnetic signals. To understand the working principle of SQUID

it is imperative to first understand the behavior of Josephson junction and the concept of flux quantization. The flux quantization requires that a magnetic flux enclosed by a superconducting loop be quantized in units of the flux quantum $_0 = h/2e \approx 2.07\times10^{-15}$ Tm^2, where h is Planck constant and *e* is the electron charge.

DC SQUID (The Two-Junction SQUID): This device consists of two Josephson junctions connected in parallel. In practice, the circuit consists of two bulk superconductors which, together with the Josephson junctions 'J_1' and 'J_2', form a ring as in **Fig.2.17 a**. The flux through the loop of the SQUID is generated by a magnetic coil placed in the interior of the ring. The critical current, I_C, of the junctions is much less than the critical current of the main ring. This produces a very low current density making the momentum of the electron-pairs small. To understand the working of SQUID, let's consider the scenario when we bias it with a current well below its critical current value. Then, if we apply a tiny magnetic field to the SQUID, the applied magnetic field tends to change the superconducting wave function (r). But the superconducting wavefunction doesn't want to change. According to the flux quantization, it must maintain an integral number of wavefunction cycles around the loop. So the superconducting loop opposes the applied magnetic field by generating a screening current I_s , that flows around the loop as shown in **Fig.2.17 a**. The screening current creates a magnetic field equal but opposite to the applied field, effectively canceling out the net flux in the ring. In this way, the applied magnetic field has lowered the effective critical current of the SQUID. In other words, it has reduced the amount of bias current we can pass through the SQUID without generating a resistive voltage, since the screening current has superimposed itself on top of the bias current. The situation is depicted in **Fig.2.17 a**, where I_s flows parallel to $I_{bias}/2$ in one of the arms, increasing the total current, making it more likely to achieve the superconducting to normal transition. Now, as we increase the applied magnetic flux, the screening current increases. But when the applied magnetic flux reaches half a flux quantum, something interesting happens: the superconducting junctions momentarily become resistive. If we try to observe this transition in terms of screening current, we can conclude that in order to have lower energy at $\boldsymbol{\phi} \approx \boldsymbol{\phi}_0/2$, it is little easier for the SQUID to keep 0.49 flux quanta in rather than keeping 0.51 flux quanta out. Of course, the screening current will have to change direction at this point. The variation of I_S with $\boldsymbol{\phi}$ is shown in **Fig.2.17 (b)**.

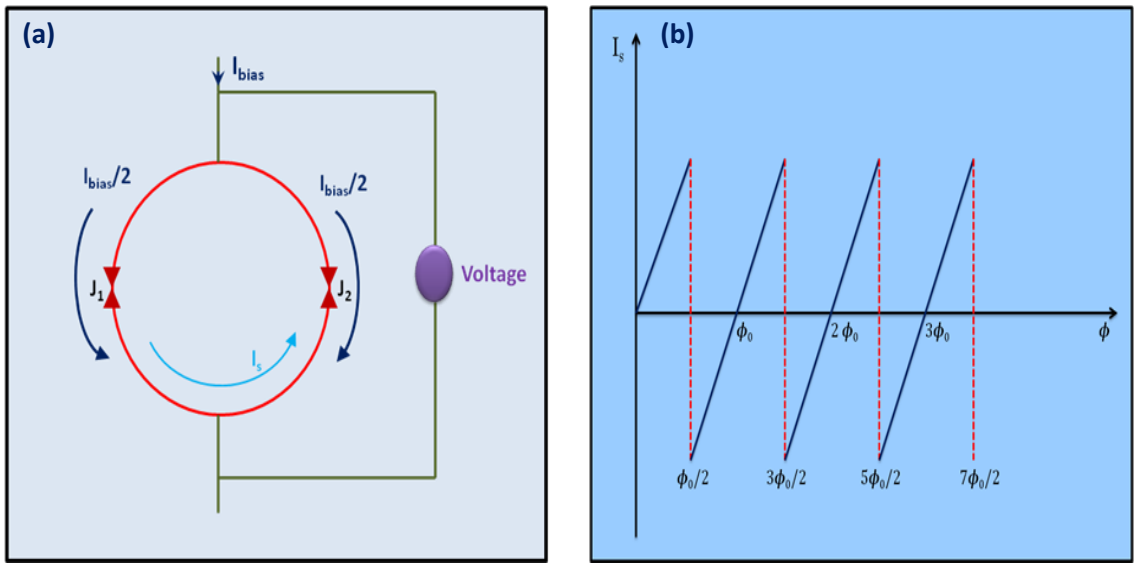

Figure 2.17 (a) Schematic of DC SQUID **(b)** Relationship between screening current and applied magnetic flux.

Hence the following conclusions can be drawn:

a) the screening current of a SQUID is periodic in the applied flux, and
b) the critical current of a SQUID depends on the screening current.

Thus the SQUID critical current is also periodic in the applied magnetic flux. To make a magnetometer, the SQUID is operated at a biasing current slightly greater than I_C, so the SQUID always operates in the resistive mode. Under these conditions, there is a periodic relationship between the voltage across the SQUID and the applied magnetic flux with a period of one flux quantum $\boldsymbol{\phi}_0$. This is shown in **Fig. 2.18.**

The periodically varying critical current as a function of applied magnetic flux can be expressed mathematically as:

$$I_c(\phi) \propto I_c(0) \left|\cos\frac{\pi\phi}{\phi_0}\right| \qquad (2.4)$$

Thus by monitoring the current through the SQUID one can measure the magnetic flux.

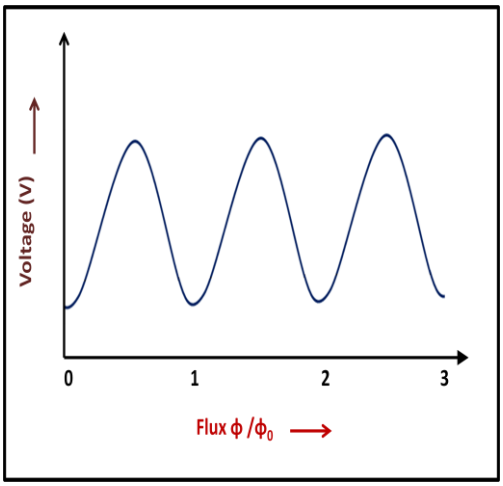

Figure 2.18: Depicting the periodic relationship between the voltage across the SQUID and the applied magnetic flux with a period of one flux quantum $\boldsymbol{\phi}_{0.}$

The sinusoidally varying critical current is, in fact, a direct demonstration of quantum interference. The variation in the current can be compared to the variation in the intensity of light detected on the screen of a Young's double-slit experiment. In Young's double-slit experiment, a phase difference is achieved by varying the optical path length. In the case of the SQUID, the phase difference is maintained by the currents owing through the two arms of the SQUID. Thus the phenomena of interference and flux quantization are exploited to create the world's most sensitive magnetic field detectors. When using the SQUID as a highly sensitive superconducting detector for magnetic flux, we bias it with a current slightly higher than the critical current I_C so that a voltage drop occurs across the Joesephson junctions with the SQUID operative in the resistive mode.

All the SQUID measurements in the present thesis were taken by Quantum Design, MPMS evercool XL (photographs shown in **Fig. 2.19**) which is a DC squid magnetometer. The schematic of the SQUID instrument is shown in **Fig. 2.20.** The magnet induces a magnetic moment allowing a measurement of response of the sample. At the centre of the magnet an array of superconducting detection coils are mounted. This array is configured as a gradient coil to reject external noise sources. As the sample passes through a coil, it induces the flux change that coil by an amount proportional to the magnetic moment (M) of the sample. The SQUID sensor is located in such a place where the effects of fringe fields generated by the superconducting magnets are less than 10 mT. Generally, SQUID sensor is shielded inside an

Nb can. The detection coils are constructed using NbTi. This allows measurements to be taken in applied fields of 7 T while maintaining sensitivities of 10^{-8} emu **[40].** With a variable temperature insert, measurements can be taken over a wide range from 1.9 K – 400 K. The sample temperature is controlled by the flow of helium gas passing the sample. A heater is used to regulate the temperature of He gas which is located below the sample measuring region and also by a thermometer located above the sample region. This arrangement is made to ensure that the entire region is in thermal equilibrium before the data acquisition. The system used for the present thesis is Quantum Design MPMS Evercool (**Fig. 2.19**) The key features of the system used in this study are the following;

1. Maximum Sample Size : 9 mm
2. Temperature range : 1.9K-400 K
3. Temperature sweep rate range: 0.001 –10K/min
4. Temperature stability: ±0.5% (1.9 to 4.2 K)
5. Field range: ± 7.0 Tesla (70,000 Gauss)
6. Field uniformity: 0.01% (over 4 cm length)
7. Helium Capacity-56 Liters
8. Reciprocating Sample Option (RSO) – DC Magnetization absolute sensitivity: 1 x 10^{-8} emu @ 2,500 Oe
9. Sensitivity-10^{-08} emu

This is the most sensitive instrument to measure the magnetic property of asample. We have used the Quantum Design MPMS SQUID magnetometer. It measures the change in the magnetic flux density produced by the sample as it moves through superconducting pick up coils, placed at the center of a superconducting magnet. The schematic of the set-up is shown in Fig. 2.6. The sample is mounted in a plastic straw (with negligible magnetic moment) which is held at the end of the sample rod. The rod is inserted in the sample space in aliquid He Dewar, at the end of which there is a stepper motor used to position the sampleat the center of the pick up coils. The pickup coils are made of Nb wire, wound in four coils configured as a second-order gradiometer.

If the sample is not centered, the coils read only part ofthe magnetic moment. Two type of transports were used to load the sample; (i) Standardtransport and (ii) Reciprocating sample option (RSO). The RSO transport is used for high sensitivity measurements (10-9 emu).

Figure 2.19: Schematic diagram of SQUID magnetometer.

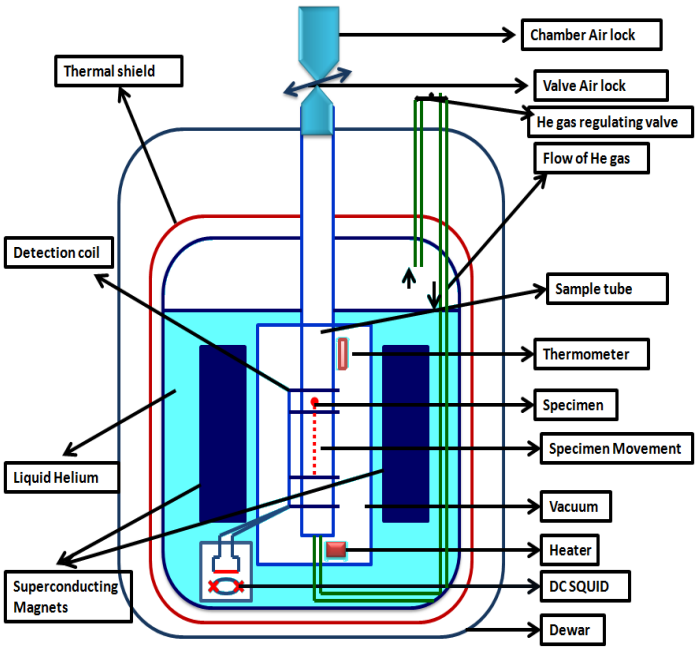

Figure 2.20 Schematic Diagram of DC squid magnetometer

2.10 AC Susceptibility Measurements

In an AC susceptometer, an oscillating AC magnetic field is applied to the sample. The change in flux seen by the detection circuitry is caused only by the changing magnetic moment of the sample as it responds to the applied AC field. The differential or AC susceptibility of χac = *dM/dH* obtained from these measurements is described ashaving both real and imaginary components χ' and χ'', where the imaginary component is proportional to the energy losses in the sample. The complex susceptibility can provide various types of information on properties such as the structural details of materials, resonance phenomena, elecrtical conductivity by induced currents, relaxation processes such as flux profiles and flux creep in superconductors, and energy exchange between magnetic spins.

In *ac* magnetic measurements, a small *ac* drive magnetic field is superimposed onthe *dc* field, causing a time-dependent moment in the sample. Similar to that of the *dc*magnetic measurement units, the pick-up coil arrangement is used in the *ac*measurements also. However, the main difference in both the measurement techniques isthat in the *dc* measurements the induced emf in the pick-up coils is induced by change inthe induction due to sample movement whereas in *ac* measurements the emf is generated due to time dependent moment of the sample. In the *ac* measurement the detection circuitry is configured to detect only in a narrow frequency band, normally at the fundamental (that of the *ac* drive field).

During the measurements, the induced *ac* moment is

$$M_{ac} = \left(\frac{dM}{dH}\right).H_{ac}Sin(wt) \qquad \text{.....(2.5)}$$

where *Hac* is the amplitude of the *ac* field, *w* is the driving frequency and

$$\chi = \left(\frac{dM}{dH}\right) \qquad (2.6)$$

is the slope of *M-H* curve, called the susceptibility. The susceptibility is the quantity ofinterest in *ac* magnetometry. It may be noted from the above equation that the *ac*measurement is sensitive to the slope of M-H curve and not to the absolute value ofmagnetization. This feature enables the *ac* magnetometry to be very sensitive becausesmall magnetic shifts can be detected even when the absolute moment is large. Themeasurements were made in the range 1.9 K – 400 K. Separate assembly is used for hightemperature measurements from 400 K to 700 K.

2.11 Nanoindentation

Indentation testing is a simple method that consists essentially of touching the material of interest whose mechnical proprties such as elastic modulus and hardness are unknown with another material whose properties are known. Nanoindentation is simply an indentation test in which the length scale of the penetration is measured in nanometeres rather than in microns or millimeters. Nanoindentation is a technique used to investigate hardness, elastic modulus and other mechanical properties of materials in which an indenter tip of known geometry is driven into a specific site of the sample by applying an increased normal load and then the load is decreased linearly; while it continuously measures the force-displacement response. The materials with features less than 100 nm across and thin films less than 5 nm thick can be tested to understand its mechanical behavior. It is used to study the relationship between microstructure and strength and toughness of materials. In film-substrate system, a "rule of thumb" for hardness measurements is 1/10-rule that the indentation depth is smaller than 10-15% of the film thickness, so that there will be no substrate effect on the measured mechanical properties of the film and this statement is a first approximation. However, in cases like soft films on hard substrates or hard films on soft substrates, it tends to be either too strict or too lax. The applications of nanoindentation technique include: to study the mechanical behavior of thin films (such as hardness, elastic modulus, adhesion evaluations and wear durability), bone, and biomaterials. Hardness measurements for submicron-size features, elastic behavior of metals, ceramics, polymers, etc.

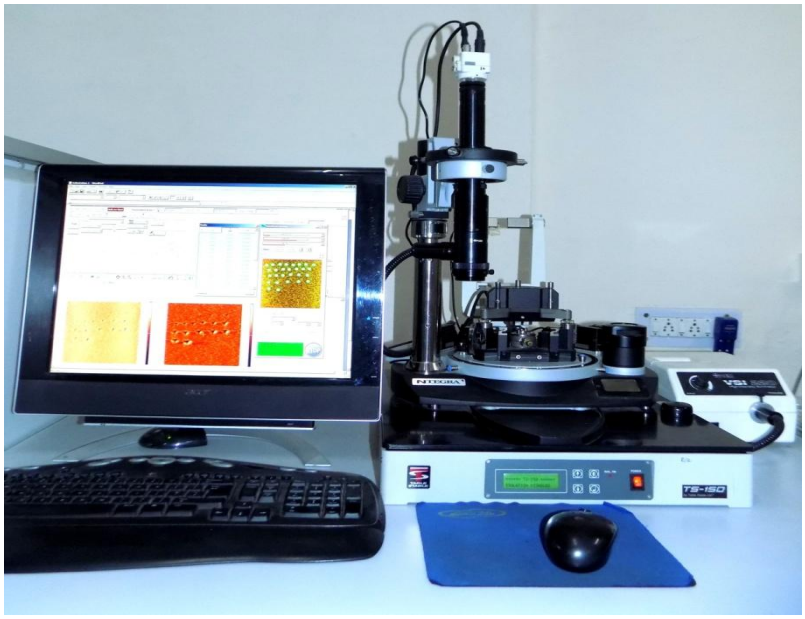

Figure 2.21 Nanoindenter (NT-MDT prima Nanosclerometry)

The photograph of nanoindenter (NT-MDT prima Nanosclerometry, Russia) used for measuring mechanical properties of Zr-W-N and Zr-W-B-N films is shown in **Fig. 2.21**. In this nanoindenter Atomic Force Microscope (AFM) attached with measuring head (performing indentation with varying loads) for selecting a specific location prior to the indentation and to image the residual imprint after indentation. The precise positioning (0.5 µm) capability of the X-Y motorized table combine with the large X-Y ranges (140 × 140 µm) of the objective ensures that the indent will always be in the centre of the field of view in AFM mode. Indentations were made on the desired area of the sample whose properties are unknown by using a three-sided, pyramid-shaped Berkovich diamond indenter with nominal angle of 65.3º between the tip axis and the faces of the pyramid whose mechanical properties are known.

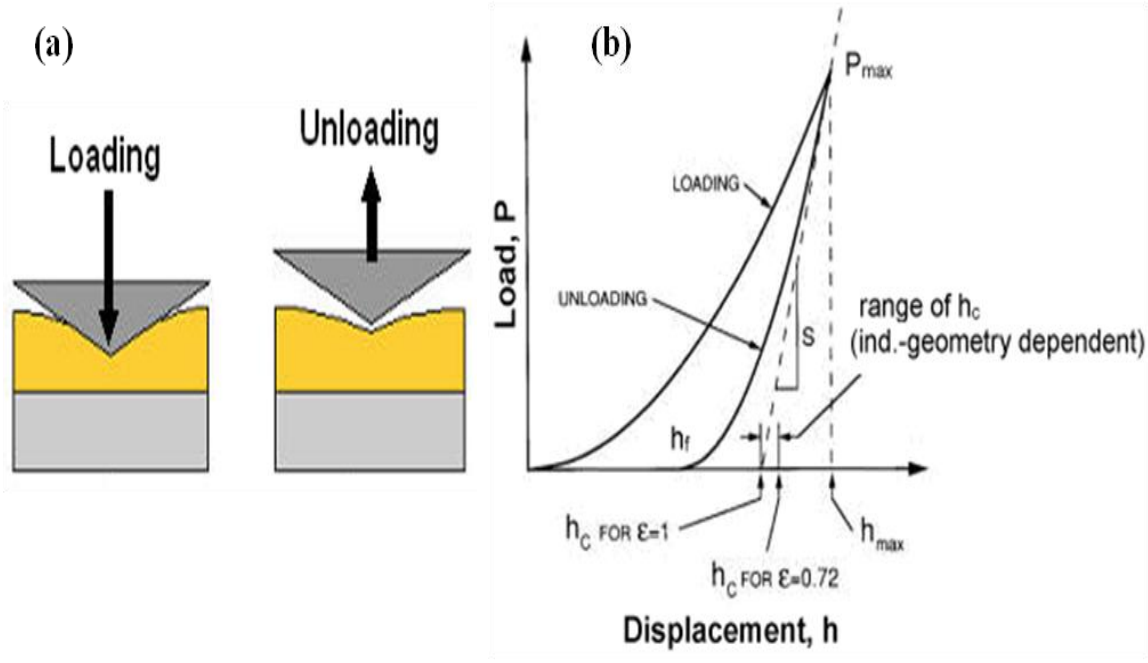

Figure 2.22: (a) Loading and unloading of the indenter on the sample, **(b)** Load is plotted against the Displacement

The Nanoindenter works on load control. In load control, the load placed on the indenter tip is increased gradually as the tip penetrates into the specimen at a selected rate and soon reaches to a selected maximum load. At this point, the load may be held constant for a period of time and then unloaded. During loading and unloading cycle, the load is increased and decreased in a linear fashion, the area of indentation is continually measured and this area

is used to obtain the load-penetration depth characteristics from which the hardness and elastic modulus values are calculated. **Fig. 2.22a** shows the loading and unloading of the indenter on the sample. For each loading and unloading cycle, the load is plotted against the displacement of the indenter as shown in **Fig. 2.22b**. The maximum load for thin film is selected as there is no influence of the substrate material on the mechanical properties of the film.

CHAPTER 3

INVESTIGATIONS ON Ni-Mn-Al THIN FILMS

3.1 Introduction

In recent years, Heusler alloys have emerged as one of the promising materials exhibiting exchange bias due to their multifunctional properties such as shape memory effect, magnetocaloric effect, giant magnetoresistance and superelasticity [6,174,177-182] Exchange bias has been studied in bulk Heusler alloys such as NiMnSn [148], NiMnSb [183] and NiMnIn [184] and Co substituted NiMnSb alloys [135]. Large EB has been observed in Ni-Mn-In bulk alloys afterZFC from an unmagnetized state [185]. For several decades, thin films have been an area of intense research due to potential application of thin films in data storage devices based on spin polarized and exchange biased materials [1, 2]. Various approaches have been undertaken in an attempt to fabricate Heusler alloy films with desirable characteristics. Thin films of Ni-Mn-Sn [143], Ni-Co-Mn-In [186] and Ni-Mn-In [187] have been successfully deposited from pre-synthesized targets. Thin films Ni-Mn-In and Ni-Co-Mn-In have been shown to exhibit martensitic phase transition while work on Ni-Mn-Sn thin film shows the evidence for exchange bias. The underlying mechanism for the observation of exchange bias in bulk and thin films of Heusler alloy is the interplay between ferromagnetic and antiferromagnetic regions present in the martensite phase only.

The practical application of thin films depends on their mechanical properties which is reflected in their hardness and resistant to corrosion properties. Among Heusler alloys, Ni–Mn–Al alloys are superior to the Ni–Mn–Xalloys in terms of mechanical properties and are potential candidate for a high-temperature shape memory effect [11]. The magnetic properties of off-stoichiometric Ni-Mn-Al alloys are structural dependent. The antiferromagnetism of Ni–Mn–Al is associated with the quenched B2 structure, whereas $L2_1$ structure promotes ferromagnetic ordering of the magnetic moments [173,188]. The stabilization of $L2_1$ phase is difficult and involves long time annealing [188]. The studied alloys are always found in a state that incorporates both ferromagnetic and antiferromagnetic ordering associated with $L2_1$ and

B2 structures respectively. The Neel temperature of antiferromagnetic phase T_N ~ 300 K and the curie temperature of the ferromagnetic phase T_C ~ 375 K [189]. At low temperatures, the magnetic susceptibility of stoichiometric and off-stoichiometric alloys exhibits splitting of zero-field cooling and field cooling curves indicating a spin-glasslike behaviour. The structural and magnetic properties of Ni-Mn-Al system has been investigated in detail in bulk form, however, thin films of Ni-Mn-Al have received so far much less attention. Literature on Ni-Mn-Al thin films shows that the stoichiometric Ni_2MnAl films deposited at lower substrate temperatures (180^0C) favour non-ferromagnetic ordering exhibiting a B2 like crystal structure; while higher growth temperature (400^0C) favours ferromagnetic films exhibiting a $L2_1$like structure [190]. Large negative magnetoresistance [191] and martensite to austenite transition [172] has been observed for off-stoichiometric Ni-Mn-Al thin films. It has been well known that the properties of thin films crucially depend on the deposition technique and processing parameters involved. The studied Ni-Mn-Al thin films have been deposited by MBE, PLD or sputtering from pre-synthesized targets. However, there are no reports on the structural and magnetic properties of Ni-Mn-Al thin films deposited by co-sputtering using different elemental targets. The mechanical properties of Ni-Mn-Al thin film have not been explored so far.

Further, the exchange bias observed in Heusler alloys has been attempted in the ferromagnetic Heusler alloys, there are no reports on the existence of exchange bias in NiMnAl Heusler alloys. The mechanical properties and structure dependent magnetic properties which includes L21 and B2 structures exhibiting ferro and antiferromagnetic behaviour. It has also been observed that the alloy mostly exhibits a mixed phase exhibiting both L21 and B2 structure which the presence of both ferro and antiferro moments in the same alloy which is the prime requisite of exchange bias. Thus NiMnAl offer a potential candidate for the study of exchange bias

In the present chapter, thin films of NiMnAl have been deposited by co-sputtering from the elemental targets of Ni, Mn and Al. The thicknesses of the films have been varied to study the effect of exchange bias on the deposited films. Since the exchange bias effect depends critically on the structure of the film which in-turn depends on the composition, the films have been deposited in two sets – (i) Ni rich Ni-Mn-Al thin films and (ii) Mn rich Ni-Mn-Al thin films. Detailed study of these films allow us to clarify the following (i) The thickness of the film increases with increasing deposition time. (ii) All smaller thickness (≤ 1.5 μm), the Ni rich Ni-Mn-Al thin films exhibit a mixed phase ($L2_1$ + B2)and a good adhesion with the substrate

but with increasing thickness, the films exhibit pure B2 phase and for thickness beyond 6 μm, films peel-off from the substrate. (iii) Among Ni rich Ni-Mn-Al, for the films exhibiting mixed phase it has been observed that Martensitic transformation occurs for the films having thickness greater than ~ 1.5 μm. All the films exhibit exchange bias at low temperature with the exchange bias field depending strongly on the thickness of the film. Exchange bias increases with increasing thickness. Maximum exchange bias (700 Oe at 2 K) has been observed for the film with thickness 6 μm. (iv) Mn rich Ni-Mn-Al thin films have pure B2 phase for all thickness.The adhesion of Mn rich Ni-Mn-Al thin films is not as good as Ni-rich Ni-Mn-Al thin films but they exhibit large exchange bias as compare to Ni rich Ni-Mn-Al thin films. In this case exchange bias shows a non-monotonic increase with increasing thickness. For the films exhibiting a pure B2 phase, study of exchange bias shows that the exchange bias field increases with increasing film thickness. Large exchange bias of 2.8 KOe at 2 K has been observed for the film with thickness 4 μm.

3.2 Crystal structure and magnetic properties of the Ni-Mn-Al System

The pioneering investigation into structural and magnetic properties of the stoichiometric Ni_2MnAl revealed that the high-temperature cubic structure is stable down to liquid Helium temperature [171]. The neutron diffraction measurements reported in that work have also indicated that disordered B2 type structure strongly dominates fully ordered $L2_1$ Heusler structure. Later studies [172, 192-194] pointed out that thermal treatment below order-disorder transition temperature, although enhances degree of the $L2_1$ superstructural ordering, does not suppress completely the chemical disorder in the specimens. Most likely, this is due to a rather low B2-$L2_1$ transition temperature [195] that results in slow kinetics of the ordering process [66].

Deviation from the stoichiometry brings about structural instability. Both the martensitic transformation temperature M_s and the low-temperature phase were found to depend on the chemical composition as well as the thermal treatment [196,197]. Particularly, M_s decreases by ~ 20-40 K after ageing below the B2-$L2_1$ temperature [195,197]. As in other NiMn-based FSMAs, the martensitic transition temperature in the Ni-Mn-Al system correlates with the average concentration of valence electrons e/a [195]. Analysis of the experimental results [171,193,195] strongly suggests that the type of magnetic ordering depends on the chemical ordering. Nowadays it is generally accepted that antiferromagnetism of Ni-Mn-Al is

associated with the disordered B2 structure whereas $L2_1$ ordering promotes the magnetic moments to order ferromagnetically. In the Ni-Mn-Al alloys, the Neel temperature $T_N \approx 300$ K was found to be virtually independent of composition [98,194,196,198,199]. Judging by several experimental reports [173,189] Curie temperature of the $L2_1$ phase, $T_C \approx 370$ K, is higher than T_N in the stoichiometric Ni_2MnAl and decreases with deviation from the stoichiometry in $Ni_{50+x}Mn_{25}Al_{25-x}$ [13] and $Ni_{50}Mn_{25+x}Al_{25-x}$ [200] series of alloys. The neutron diffraction measurements [171] of stoichiometric composition showed that the magnetic moment $\approx 4.2\ \mu_B$ is localized mainly on the Mn atoms which are a typical situation in the Ni-Mn-X family of Heusler alloys.

At low temperatures, magnetic susceptibility χ of the stoichiometric [189,193] as well as off-stoichiometric [194,198], Ni-Mn-Al alloys exhibit complex character. Initially splitting of zero field cooling and field cooling curves of χ observed in the low temperature region was attributed to a spin glass-like behaviour [194],but more recent consideration [173] of this effect implies that its origin is likely to be the blocking of magnetic clusters. Recent transmission electron microscopy study [201] of the samples annealed just below B2-$L2_1$ transition temperature established correlation between behaviour of the magnetization and the size of anti-phase domain; thus providing a reasonable explanation for a feeble magnetic properties of Ni-Mn-Al with developed $L2_1$ ordering [201].

Ni rich compositions exhibit a mixed $L2_1$ + B2 phase for thickness $\leq$ 1.5 μm and for thickness $\geq$ 2.3 B2 phase is obtained. Mn rich composition exhibit a pure B2 phase. The properties of Mn rich and Ni rich NiMnAl films have been discussed separately.

3.3 Ni rich Ni-Mn-Al thin films

Off-soichiometric Ni-rich Ni-Mn-Al thin films have been successfully deposited on Si substrates. The films have been deposited by DC/RF magnetron sputtering by co-sputtering of the targets of Ni, Mn and Al. The films have been studied for their structural and magnetic properties. Nanoindentation has also been done for film hardness and resistant to crack properties. It has been observed that Martensitic transformation occurs in the film exhibiting large thickness (1.5 μm). All the films exhibit exchange bias at low temperature with the exchange bias field depending strongly on the thickness of the film. Nanoindentation results suggest that the film exhibit high hardness and resistant to scratch.

3.3.1 Experiment

Ni-Mn-Al thin films were deposited using DC/RF magnetron sputtering from three different targets of Ni, Mn and Al. Sputtering targets of Ni, Mn and Al with purity 99.98%, 99.95% and 99.34% respectively have been used for deposition. Sputtering was carried out at constant Ar (20 sccm) flow at 500 ^{0}C substrate temperature for different deposition times t_d ($5 \leq t_d \leq 20$ min). The DC power densities for Ni and Al targets were 75 watt/cm^2 and 85 watt/cm^2 respectively. For Mn target, 115 W RF power has been used. All depositions were carried out at a fixed substrate to target distance of 6 cm. The base pressure before deposition was lower than 4.0×10^{-6} Torr and the argon pressure was kept at 10 mTorr during sputtering. Prior to the deposition, the targets were pre-sputtered for 10 minutes. The post annealing of the films deposited at $T_s = 500^0$C have been carried out in vacuum for 2.5 hr. Films have been deposited with varying deposition time of 5 min, 10 min, 15 min, 30 min, 1 hr, 2 hr. Depostion parameters are shown in **Table 3.1**.

Sample	**NiMnAl**		
Substrate	**Si (100)**		
Substrate temperature	**500^{0}C for films thickness upto(~1.5 µm)**		
Substrate-target distance	**5 cm**		
Base pressure	**3.0×10^{-6}Torr**		
Working pressure	**5 m Torr**		
Sputtering gas	**Ar**		
Target	**Ni**	**Mn**	**Al**
Sputtering power (W)	**75(DC)**	**100 (RF)**	**85 (DC)**

Table 3.1: Deposition parameters for the film.

3.3.2 Results and discussion

3.3.2.1 EDAX measurements

The elemental composition analysis of Ni-Mn-Al thin films has been carried out using energy dispersive X-ray analysis. The average elemental composition of the films is found to be $Ni_{57}Mn_{24}Al_{19}$. The EDAX patterns for different films deposited for 5 min, 1 hr and 2 hr has been shown in **Figs. 1, 2** and **3**.

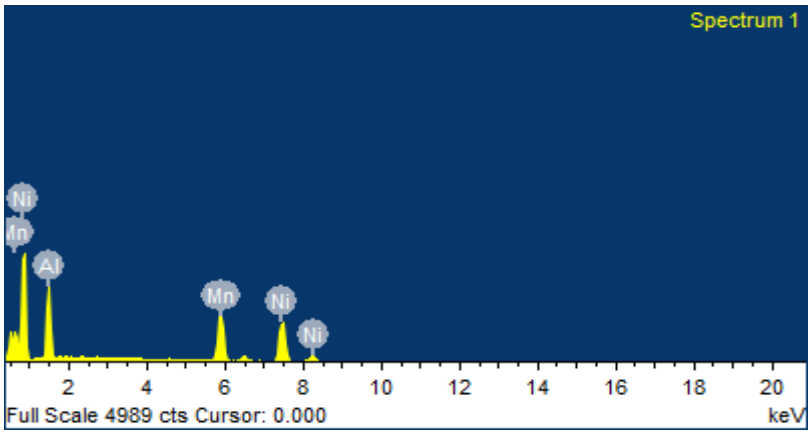

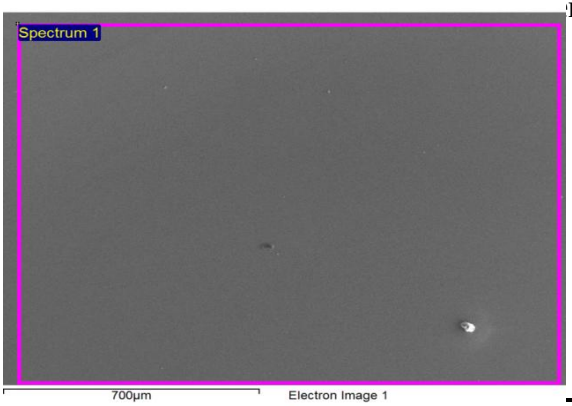

nt	Weight%	Atomic%
	11.05	19.13
	27.45	23.84
	61.50	57.13
	100.00	

Figure 3.1: The EDAX patterns for different films deposited for 5 min

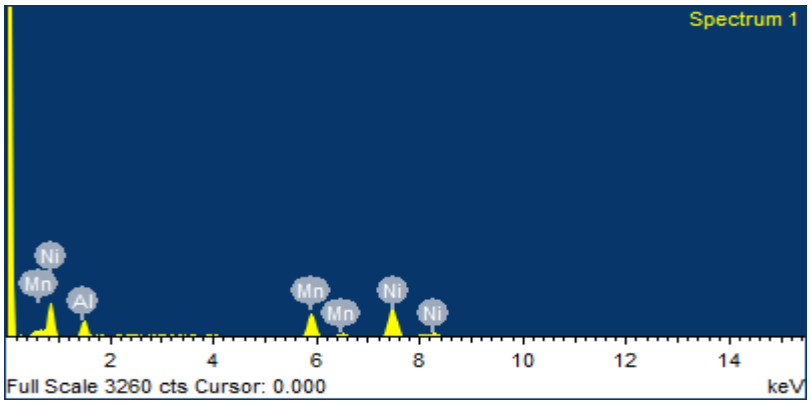

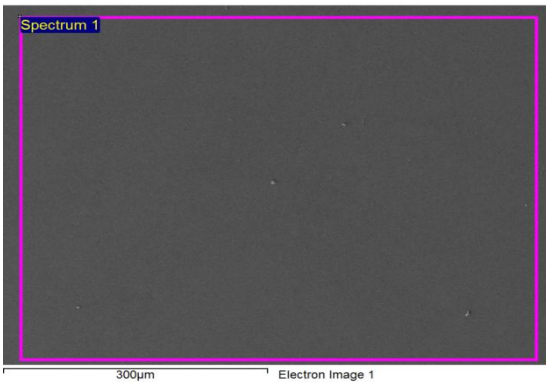

Element	Weight%	Atomic%
Al K	12.61	19.01
Mn K	20.47	23.92
Ni K	66.91	57.17
Totals	100.00	

Figure 3.2: The EDAX patterns for different films deposited for 1 hr.

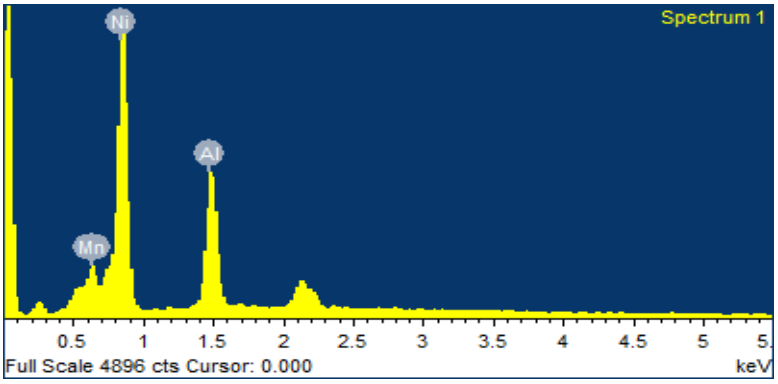

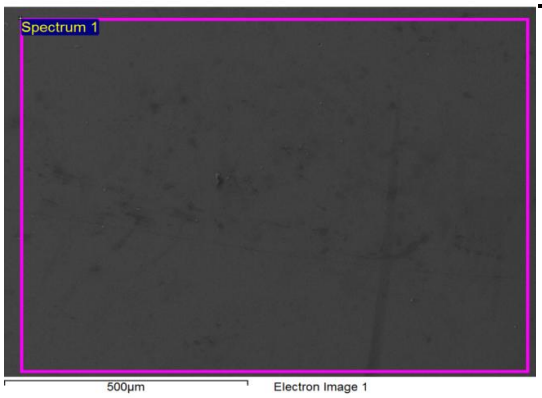

Al K	12.52	18.64
Mn K	29.20	24.24
Ni K	58.27	57.22
Totals	100.00	

Figure 3.3 The EDAX patterns for different films deposited for 2 hr

The thickness of the film has been determined for cross sectional FESEM image. As an example the cross-section of the film deposited for 0.5 µm, 1.15 µm and 1.5 µm has been shown in **Fig. 3.4**, **Fig. 3.5** and **Fig. 3.6** respectively

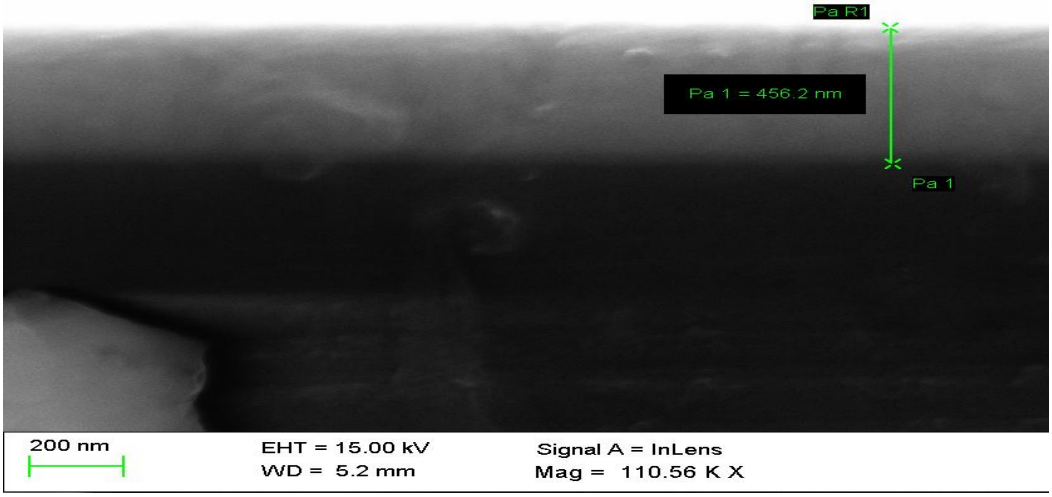

Figure 3.4 Cross-section of the film deposited for 5 min.

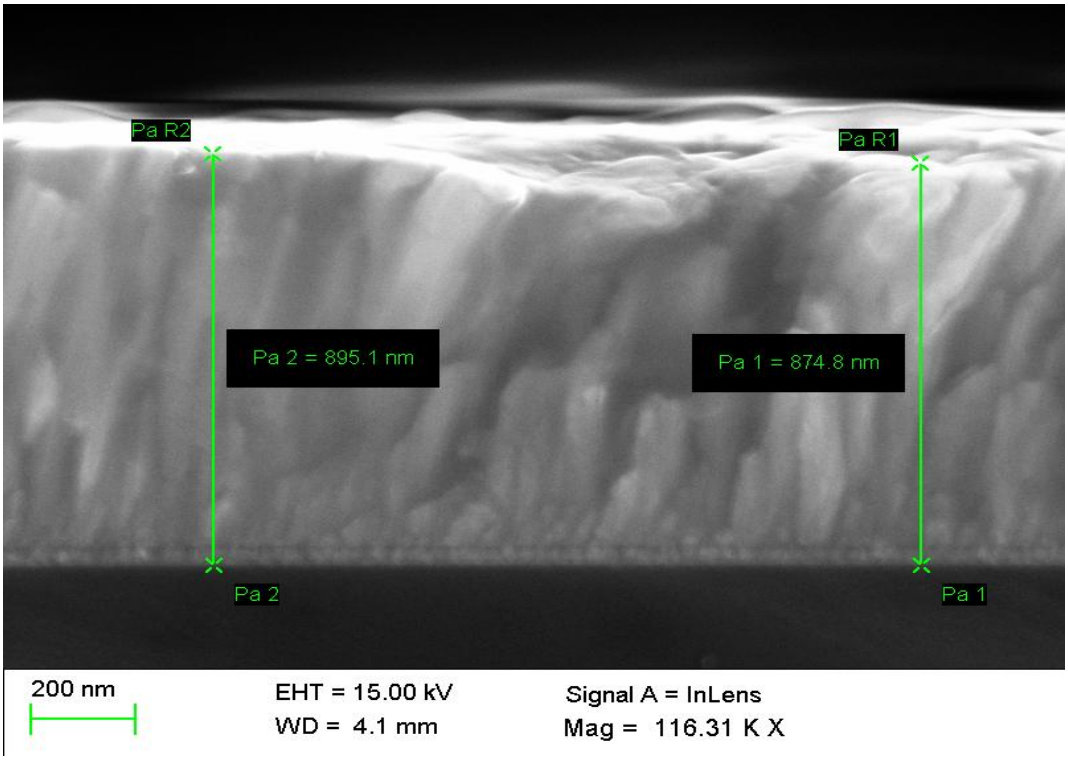

Figure 3.5 Cross-section of the film deposited for 10 min.

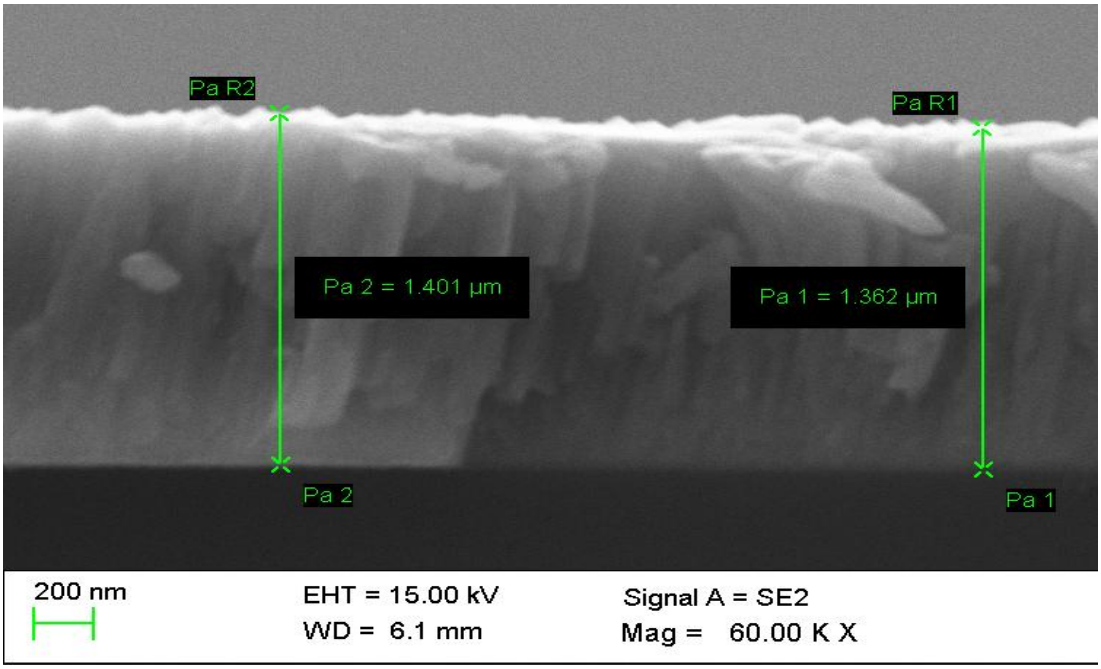

Figure 3.6 Cross-section of the film deposited for 15 min.

The thickness of the film increases with increasing deposition time. The thickness of the film obtained for different deposition time is given in **Table 3.2**.

Deposition Time	Thickness in µm (approx.)
5 min	0.5
10 min	1
15 min	1.5
30 min	2.3
1 hr.	4.5
2 hr.	6

Table 3.2 Thickness obtained for different deposition times.

3.3.2.2 Crystal Structure

Figure 3.7 shows the XRD patterns of the films deposited for 5 min, 10 min, and 15 min. For the films deposited for 5min, peak corresponding to Si (100) substrate can also be seen. A close analysis of the XRD patterns shows that the structure consists of mixed $L2_1$ and B2 phase. With increasing in deposition time from 0.5 µm to 1.5 µm, peak corresponding to $L2_1$ phase at 2θ = 50.8° (311) and 2θ = 71.7° (331) starts appearing. The reflections corresponding to $L2_1$ phase develop with increase in deposition time. With further increase in thickness of the film beyond 1.5 µm, the peaks corresponding to $L2_1$ completely suppress and the structure shows reflections corresponding to the B2 phase only.

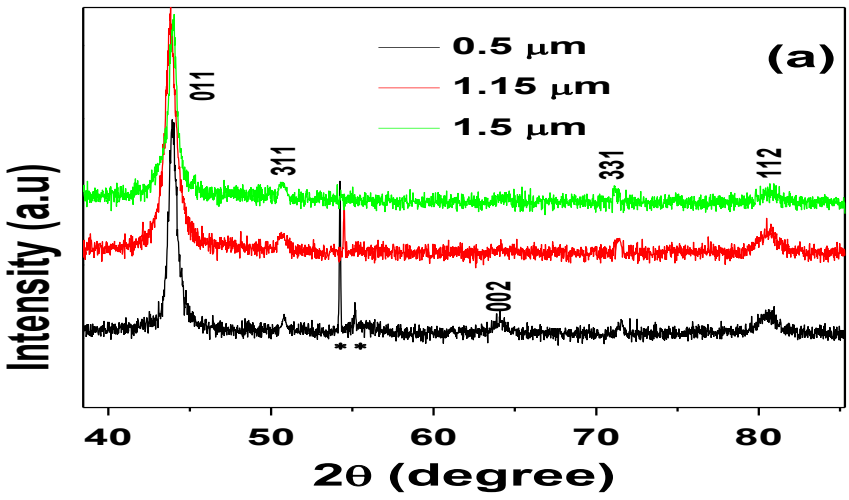

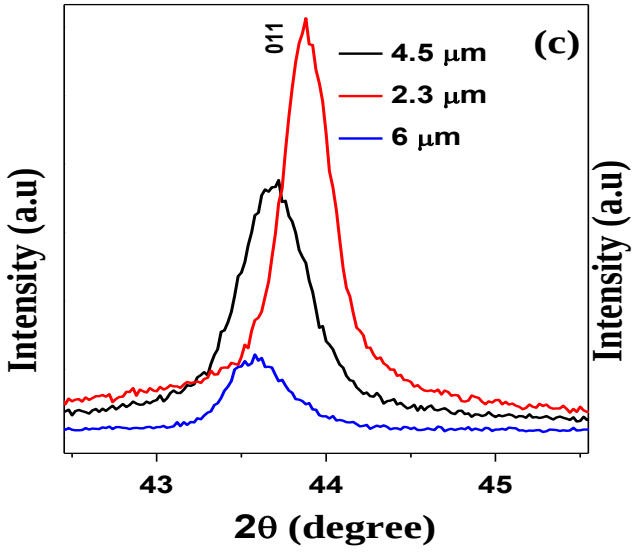

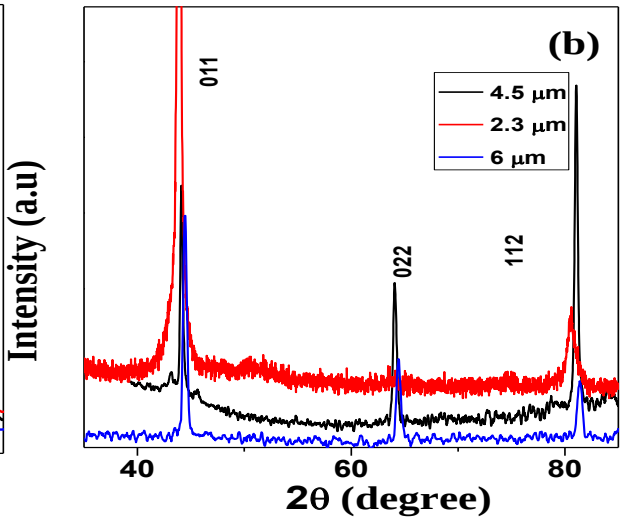

Figure 3.7: XRD patter of the thin films with different thickness.

For the samples with thickness beyond 1.5 µm, reflections corresponding to B2 phase are obtained. It can be clearly seen that with increasing deposition thickness, the 011 peak shifts towards lower angles. This shows that the strain in the film is relaxed with increasing thickness and the peak shift towards the reflection obtained for bulk NiMnAl alloy.

To further confirm the phase present in the films, the crystal structure of the films has been examined by transmission electron microscopy. As an example, selected area electron diffraction (SAED) pattern for the film deposited for the film with thickness 1.5 µm is shown in **Fig. 3.8**. The SAED pattern taken from the part of the specimen corresponds to cubic B2 structure which shows that the structure mainly consists of cubic B2 phase. Cross-sectional FE-SEM of the films shows that the thickness of the film varies monotonically with increasing deposition time.

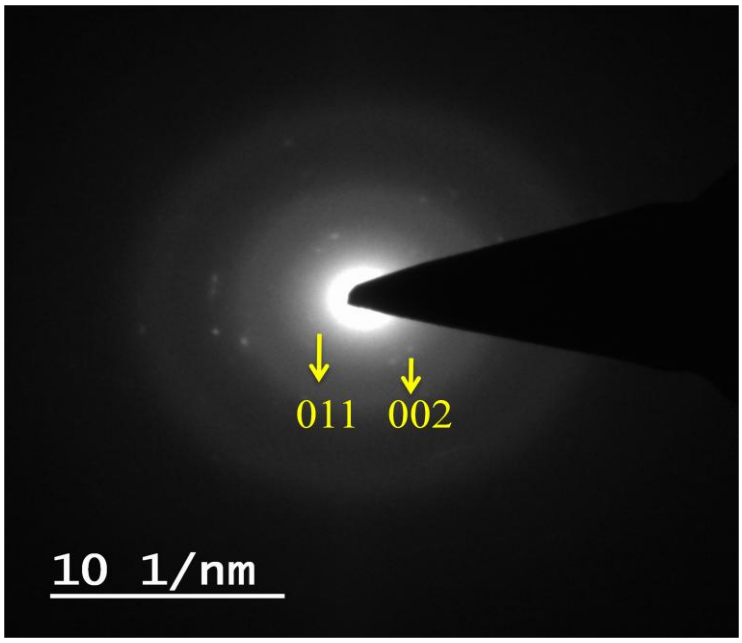

Figure 3.8: SADP for the film deposited for t = 15 min.

The SAED pattern taken from the part of the specimen for the films has been shown in **Fig. 3.9**, **Fig. 3.10** and **Fig. 3.11** for thickness 0.5 µm, 1 µm and 4 µm. It can be clearly seen that grain size increase with increasing thickness.

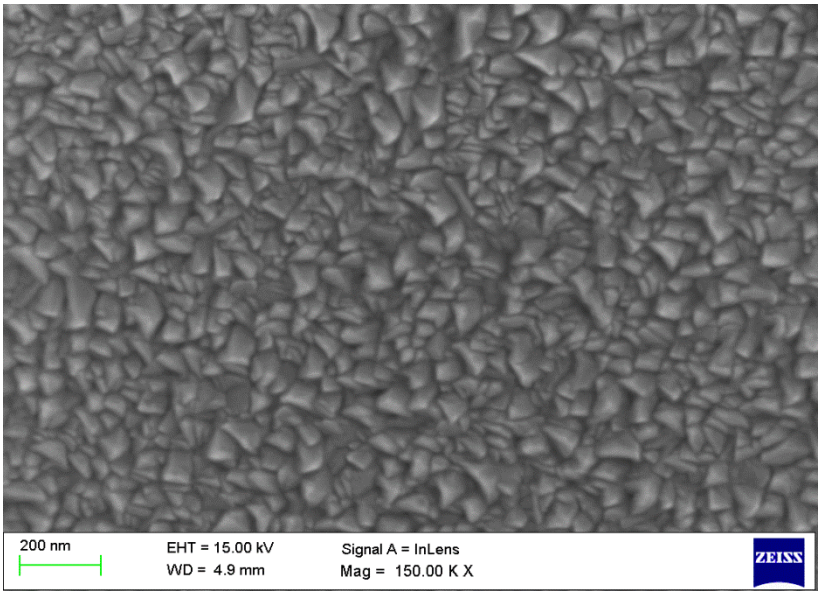

Figure 3.9: SAED pattern taken from for the film with thickness 0.5 µm.

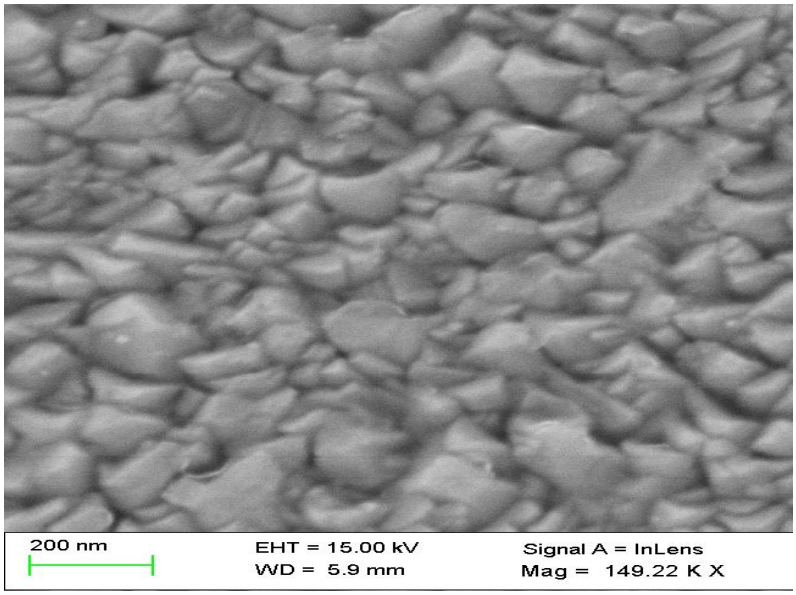

Figure 3.10: SAED pattern taken from the for the film with thickness 1 µm.

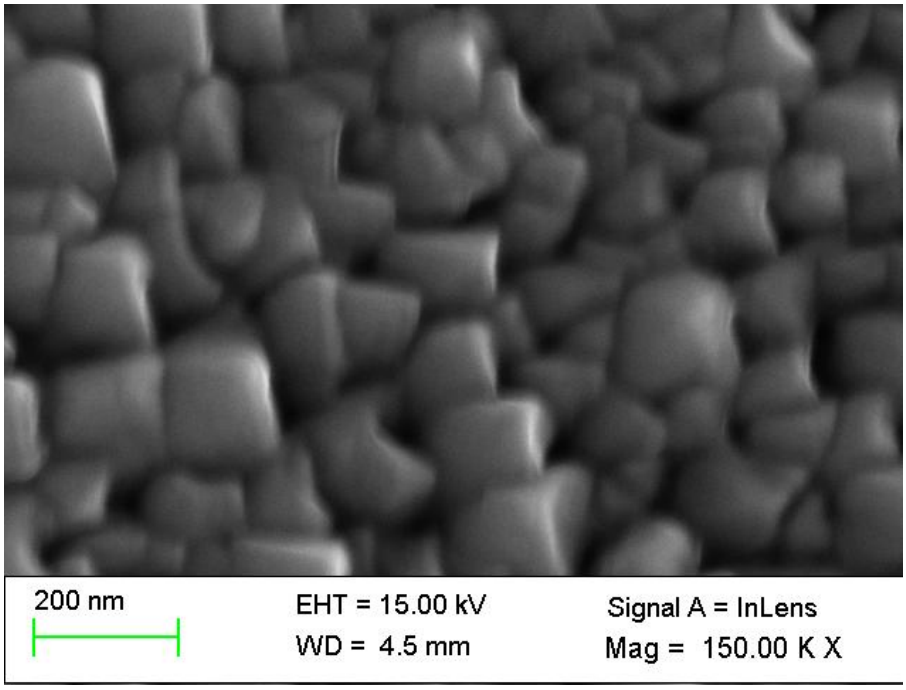

Figure 3.11: SAED pattern taken from the film with thickness 1.5 µm.

3.3.2.3 Magnetic Properties

The magnetic and structural transition temperatures of Ni-Mn-Al films have been determined from the magnetization measurement at H = 100 Oe. **Figure 3.12** shows the dc susceptibility for the films in the temperature range of 5 K ≤ T ≤ 300 K in zero-field-cooled heating (ZFCH), field-cooled heating (FCH) and field-cooled cooling (FCC) sequences. Any hysteresis in the FCH and FCC sequences is expected to be associated with a structural transition. For the films deposited for 5 min, no evidence of structural transition is seen; for the film deposited for 10 min, just a slight signature of the phase transformation was observed and for the film deposited for 15 min, there exists a clear thermal hysteresis ΔT of about 6 K between FCH and FCC has been observed at temperatures around 280 K which is attributed to a first order structural transition. The absence of thermal hysteresis for the film deposited for 5 min may be due to the hindrance of transformation by a large number of grain boundaries. With increasing film thickness, the grain size increases and above a certain value of grain size, a complete martensitic transformation can take place.

Figure 3.13 shows the dc susceptibility for the films deposited with thickness 2.3 µm, 4.5 µm and 6 µm. Clear martensitic transition may be observed for these films at temperature around 275 K. With increase in film thickness, the transition temperature shows a marginal

shift towards lower temperature. For all the samples, a steplike anomaly has been observed in the ZFCH data at low temperature (indicated by T_B) which is the typical signature of EB blocking temperature [202]. In this case also the EB blocking temperatures for all the films is ~ 20 K.

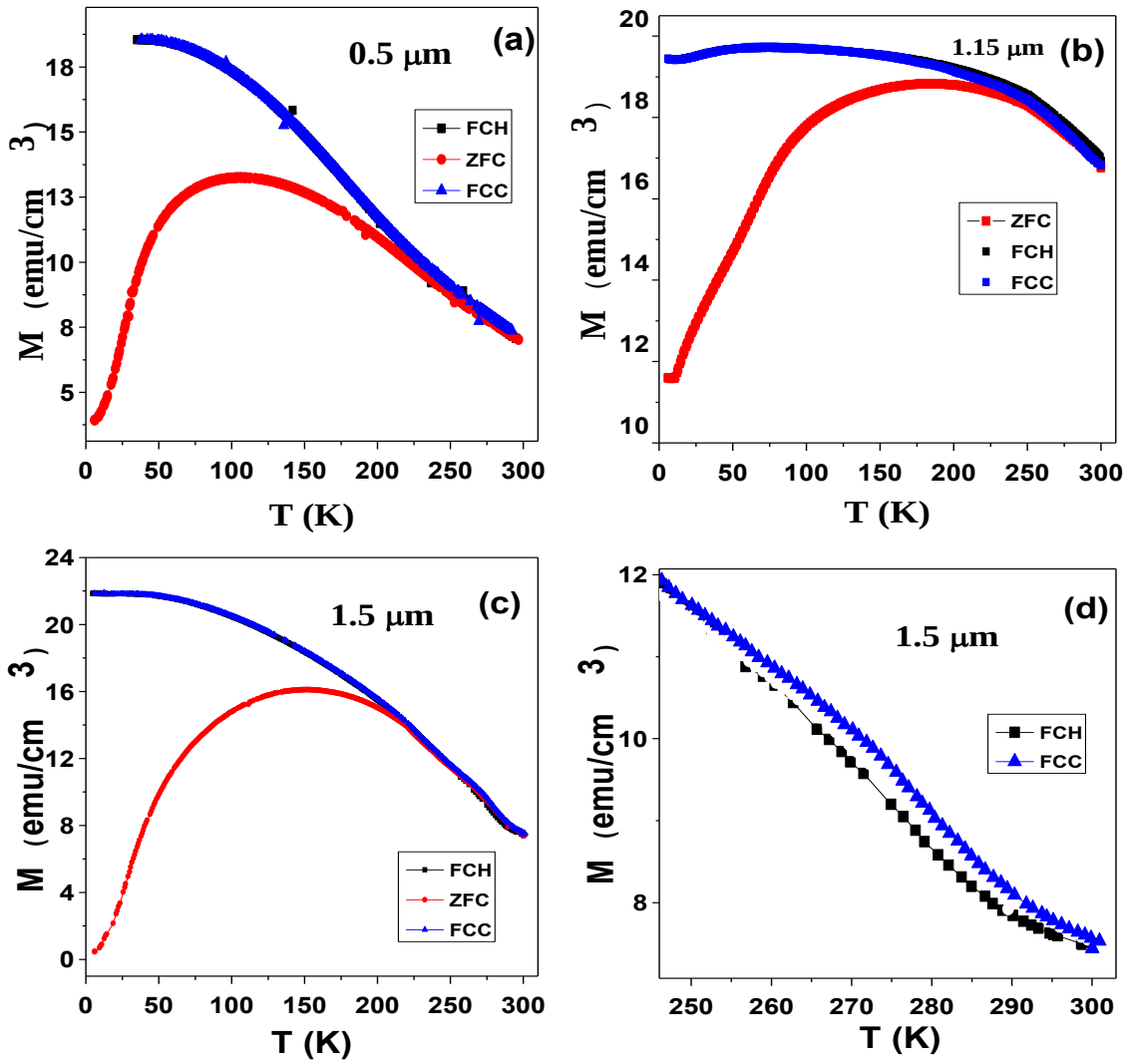

Figure 3.12: Magnetization versus temperature for the film deposited for (a) 0.5 μm, (b) 1.15 μm and (c) 1.15 min.

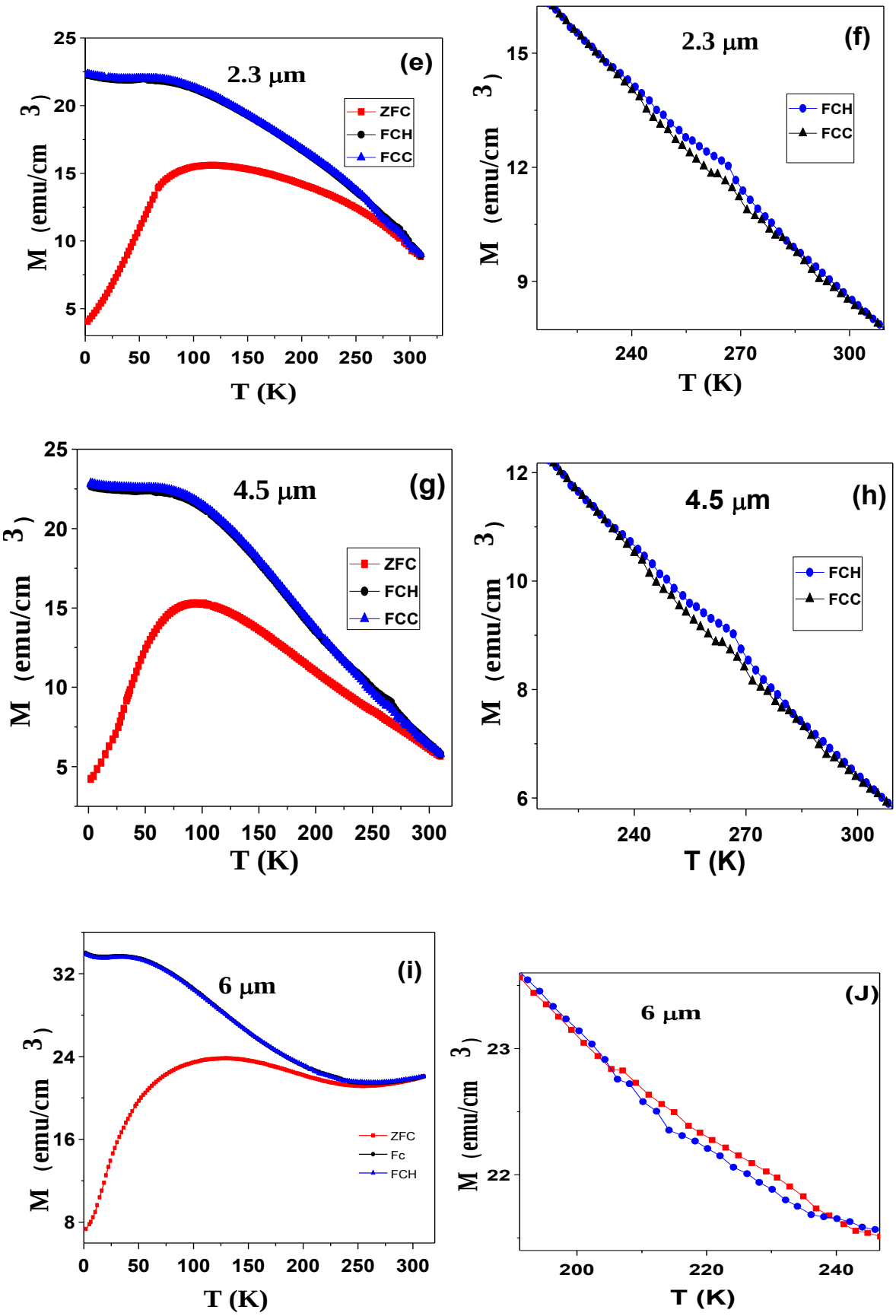

Figure 3.13: Magnetization versus temperature for the film deposited for (a) 2.3 µm, (b) 4.5 µm and (c) 6 min.

3.3.2.4 Exchange Bias Measurements

Figure 3.14 shows hysteresis loops taken at 5 K for 5 T cooling fields (H_{cool}) for all the samples. Magnified view has also been shown. Maximum exchange bias has been observed for the film deposited for 15 min. **Fig. 3.15** shows the *M-H* for the 1.5 μm thick film for different cooling fields. It can be clearly seen in the enlarged view that maximum exchange bias has been obtained for a cooling field of 5 T. The exchange bias field H_{EB} defined as ½(H^++H^-) amounts to ≈150, ≈200 and ≈250 Oe for the films with thickness 0.5 μm, 1.15 μm and 1.5 μm respectively.

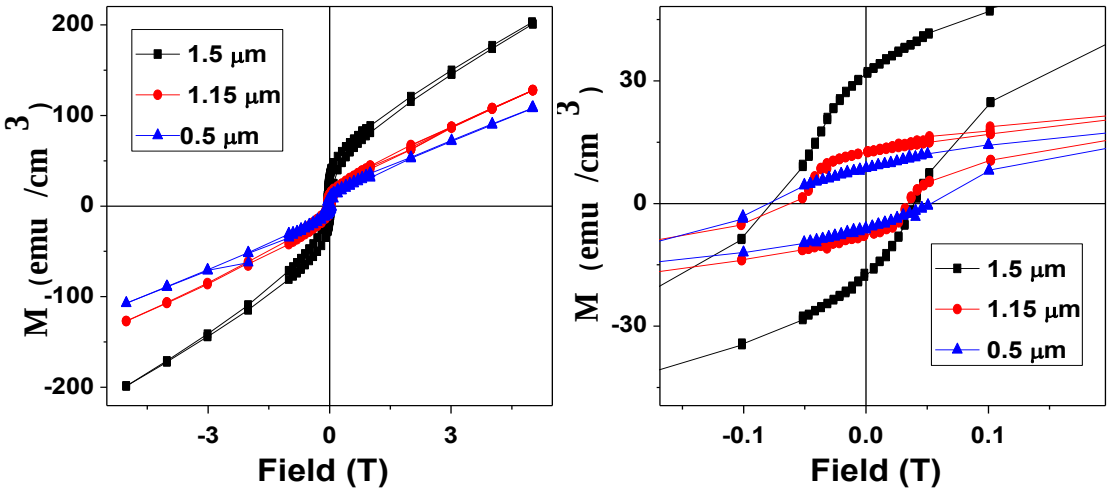

Figure 3.14: (a) *M-H* curves for all the samples. (b) Enlarged view

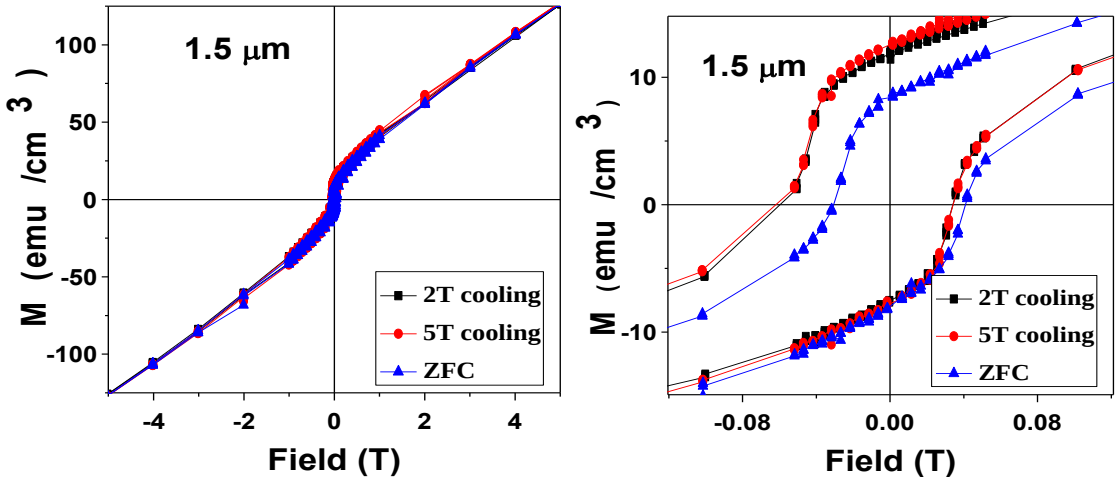

Figure 3.15: (a) *M-H* curves for the sample deposited for 15 min (b) Enlarged view.

Figure 3.16 shows hysteresis loops taken at 5 K for 5 T cooling fields (H_{cool}) for the samples with thickness 2.3 μm, 4 μm and 6 μm. As can be seen that the shifting of the hysteresis loop towards negative field axis increases with increasing film thickness. Maximum shifting has been obtained for 6 μm thick film. This shows the dependence of exchange bias property on film thickness.

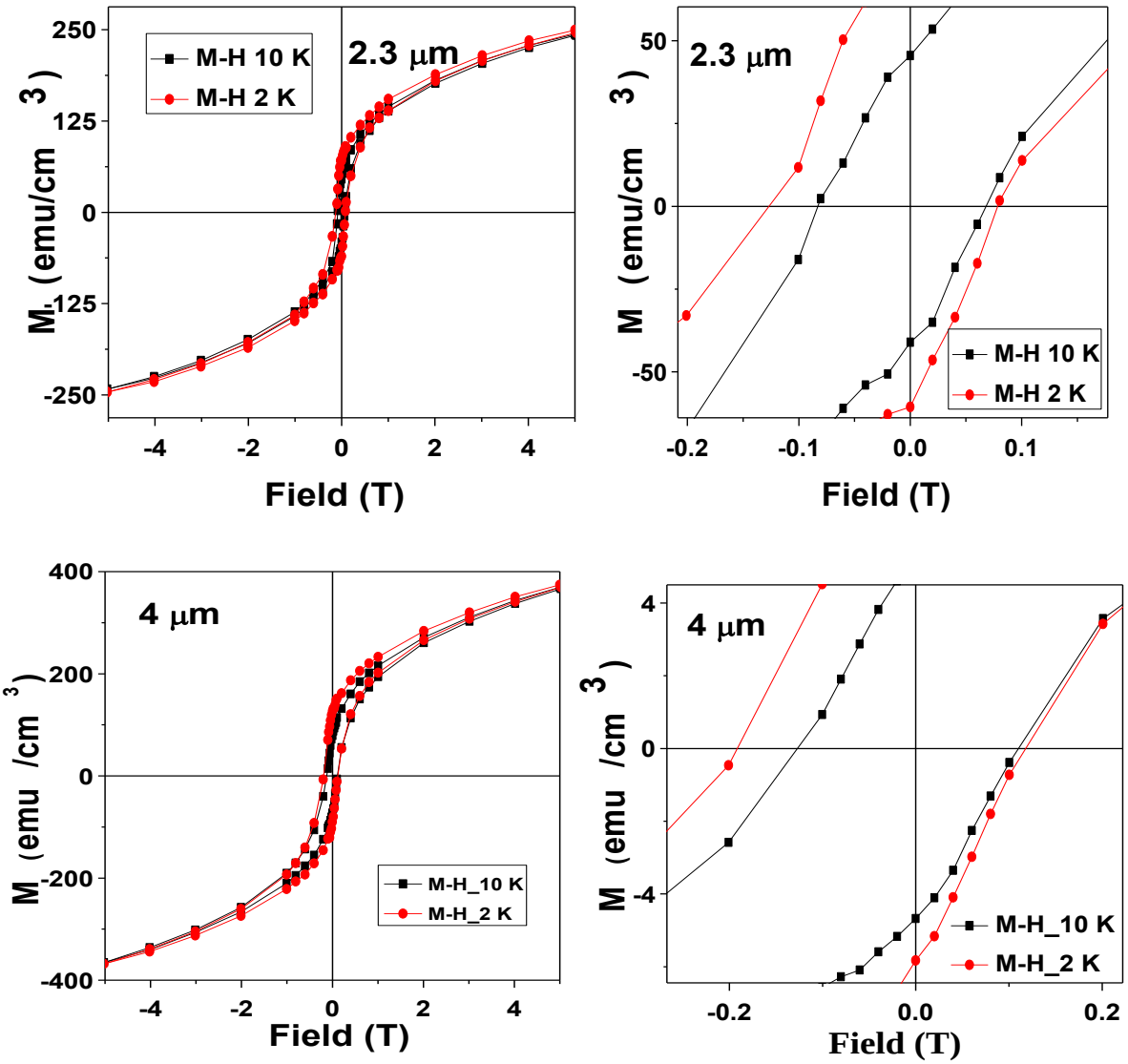

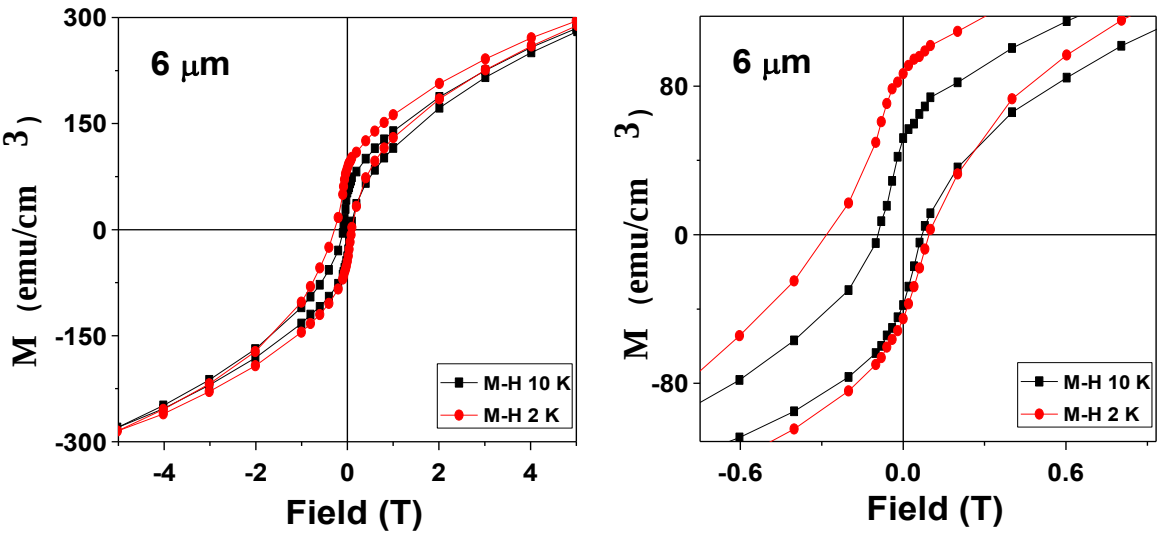

Figure 3.16: Hysteresis loops taken at 5K for 5T cooling fields (H_{cool}) for the samples with thickness 2.3 μm, 4 μm and 6 μm.

For all of the samples, splitting between ZFC and FC has been observed at low temperature. The freezing temperature (T_f) atwhich the splitting occurs was found to be around 200 K for all the films. The splitting has been usually attributed to a spin-glass like behaviour [198], but more recent consideration of this effect implies that its origin could be the blocking of magnetic clusters [198].

3.3.2.5 AC Susceptibility Measurements

To further confirm the presence of spin glass phase in the sample, ac susceptibility measurement at different frequencies has been carried out. **Fig. 3.17** shows the result of ac susceptibility measurement for the sample deposited for t = 15 min. The ac susceptibility data are depicted in the temperature range 170-300 K which covers the martensitic transition temperature and the spin glass like transition. For the sake of clarity, the data for 33 Hz and 999 Hz has been shown only in the range of transition temperatures. The hump around 196 K shows strong frequency dependence in χ' which indicates the existence of magnetic frustration associated with the spin glass state. The peak position in the curve is defined as spin freezing temperature T_f. To further confirm the nature of spin glass state, relative frequency shift ('P) has been calculated from the equation $'P = \Delta T_f / T_f (\Delta \log \omega)$, where ω is the angular frequency ($\omega = 2\pi f$) [203,204]. For the present case, P was found to be 0.04 which indicate cluster glass (randomly frozen interacting magnetic clusters of finite dimension) like state in the alloy. The

peak at T_M does not show any frequency dependence which confirms the first order nature of the transition.

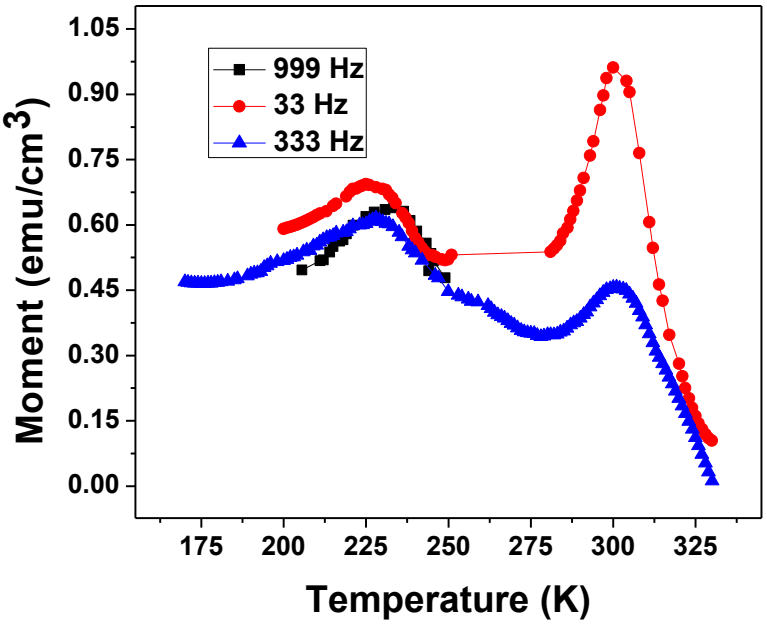

Figure 3.17: *ac* susceptibility (real part) for 1.5 µm thick film.

3.3.2.6 Indentation measurements

The indentation results show that NiMnAl film exhibit high hardness (H) ~ 21 GPa and low effective elastic modulus (E_r) ~ 140 GPa which satisfy the higher value (> 0.1) of H/E_r ratio. The higher value (>0.1) of H/E_r ratio is a strong indication of the coating resistance to wear damages. The film were scratched with 2000 to 20000 µN forces at constant loading velocity (20 nm/s) and scratch velocity (500 nm/s) for adhesion test purpose. An adhesion of the hard coatings with substrate is also an important property not only for microelectronics and magnetic recording industries, but also for emerging technologies such as data transmission through optical switches, which are dependent on micro electro-mechanical system [205]. Figure 10 shows the AFM topographical view of scratch scars done at 20000 µN force. **Fig. 3.18** reveals that the film neither peeled off nor developed any crack during the scratch test at 20000 µN force. This indicates that NiMnAl film has high adhesion with the substrate.

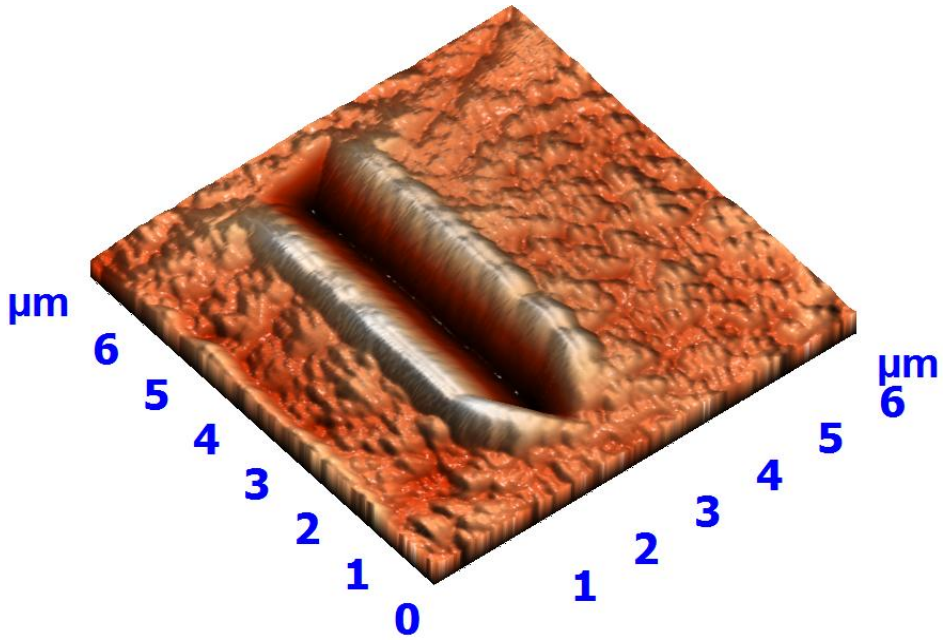

Figure 3.18: AFM topographical view of scratch scars done at 20000 µN force.

3.3.3 Conclusion

Hard Ni-Mn-Al thin films exhibit spin glass (SG) state at low temperature. The exchange bias appearing in the sample may be due to an interfaces containing spin glass SG/FM phase. As the structure mainly consists of cubic B2 phase, the antiferromagnetic interaction mainly dominates and results in small value of exchange bias for 0.5 µm thick film. The increase in exchange bias with increase in deposition time may be associated with the growth of $L2_1$ phase with increasing deposition time. This results in an increase in the ferromagnetic contribution in the film and hence the value of exchange bias increases. In conclusion, the exchange bias appearing in the sample may be associated with the coexisting ferromagnetic $L2_1$ and antiferromagnetic B2 phase in the sample. The appearance of exchange bias in all the samples shows that in Ni-Mn-Al system, exchange bias is independent of the occurrence of martensitic transition in the system which is in contrary to other Ni-Mn-X systems exhibiting exchange bias. The existence of mixed phase ($L2_1$ and B2) is an intrinsic property of Ni-Mn-Al system and the formation of $L2_1$ phase can controlled by using different deposition and annealing parameters. In the samples exhibiting a pure B2 structure the exchange bias has s associated with inhomogeneity in the film at nanoscale and existence of

spin glass phase at low temperature. The increase in exchange bias with increasing film thickness shows that inhomogeneity increases with increasing film thickness. In this respect, Ni-Mn-Al system provides an opportunity for further exploring the exchange bias properties which tuned by controlling the formation of ferromagnetic $L2_1$ phase. Nanoindentation results suggest that the film exhibit high hardness and resistant to scratch.

3.4 Mn rich Ni-Mn-Al thin films

Off-soichiometric Mn-rich Ni-Mn-Al thin films have been successfully deposited on Si substrates. The films have been deposited by DC/RF magnetron sputtering by co-sputtering of the targets of Ni, Mn and Al. The films have been studied for their structural and magnetic properties. It has been observed that Martensitic transformation occurs in all the film at low temperature. All the films exhibit exchange bias at low temperature with the exchange bias field depending strongly on the thickness of the film. Nanoindentation results suggest that the film exhibit high hardness and resistant to scratch.

3.4.1 Experiment

Ni-Mn-Al thin films were deposited using DC/RF magnetron sputtering from three different targets of Ni, Mn and Al. Sputtering targets of Ni, Mn and Al with purity 99.98%, 99.95% and 99.34% respectively have been used for deposition. Sputtering was carried out at constant Ar (20 sccm) flow at 600 ^{0}C substrate temperature for different deposition times t_d ($5 \leq t_d \leq 20$ min). The DC power densities for Ni and Al targets were 50watt/cm^2 and 60 watt/cm^2 respectively. For Mn target, 120 W RF power has been used. All depositions were carried out at a fixed substrate to target distance of 6 cm. The base pressure before deposition was lower than 4.0×10^{-6} Torr and the argon pressure was kept at 10 mTorr during sputtering. Prior to the deposition, the targets were pre-sputtered for 10 minutes. The post annealing of the films deposited at $T_s = 600^0$C have been carried out in vacuum for 2.5 hr. Films have been deposited with varying thickness of 0.5 µm, 1.009 µm, 2.52 µm and 4 µm. Beyond 4 µm thickness, film peel off from the substrate. **Table 3.3** shows the depostion parameters for the film.

Substrate	**Si (100)**			
Substrate temperature	**600^0C**			
Substrate-target distance	**5 cm**			
Base pressure	**5.0×10^{-6}Torr**			
Working pressure	**5 mTorr**			
Sputtering gas	**Ar**			
Target	**Ni**	**Mn**	**Al**	
Sputtering power (W)	**80 (DC)**	**125 (RF)**	**75**	
Deposition Time varies from 15 min to 60 min for varying thickness				

Table 3.3: Depostion parameters for the film.

3.4.2 Results and discussion

3.4.2.1 EDAX Measurements

The elemental composition analysis of Ni-Mn-Al thin films has been carried out using energy dispersive X-ray analysis.The average elemental composition of the films is found to be $Ni_{51}Mn_{30}Al_{19}$. The EDAX image of the films with thickness 1 µm and 4 µm are shown in **Fig. 3.19** and **Fig. 3.20**.

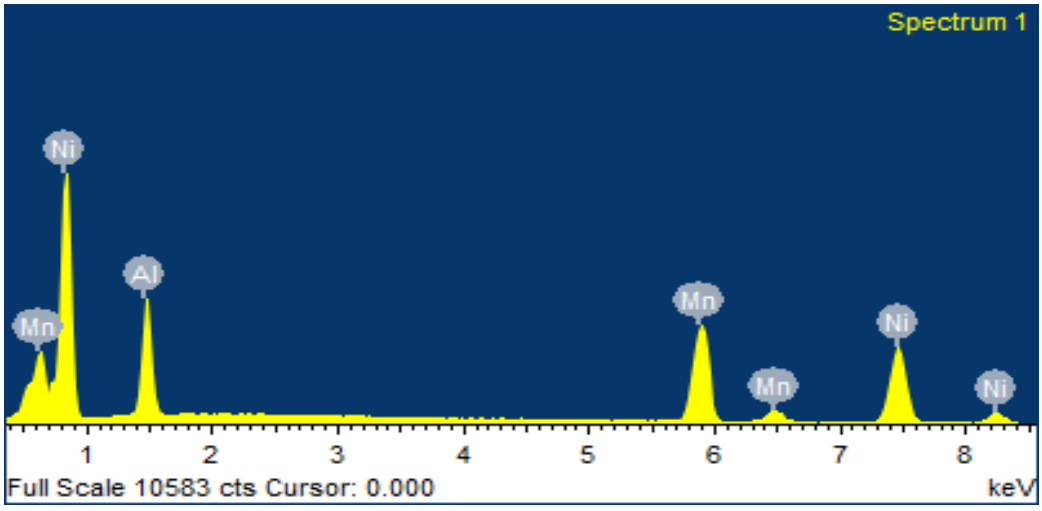

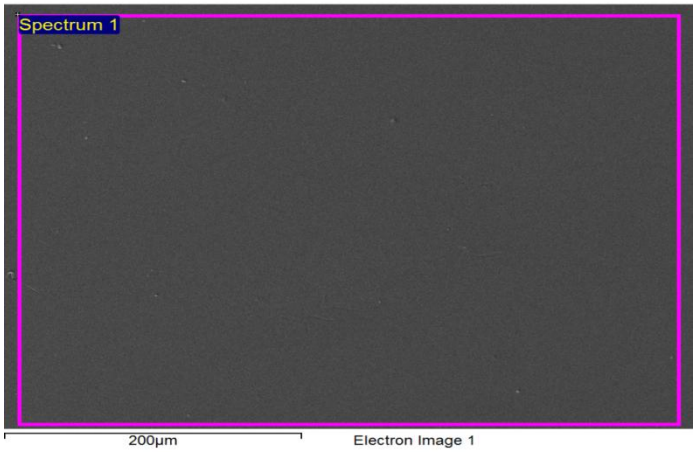

Element	Weight%	Atomic%
Al K	10.44	19.55
Mn K	32.17	30.03
Ni K	57.39	50.53
Totals	100.00	

Figure 3.19: EDAX pattern and elemental composition for 1 µm thick film

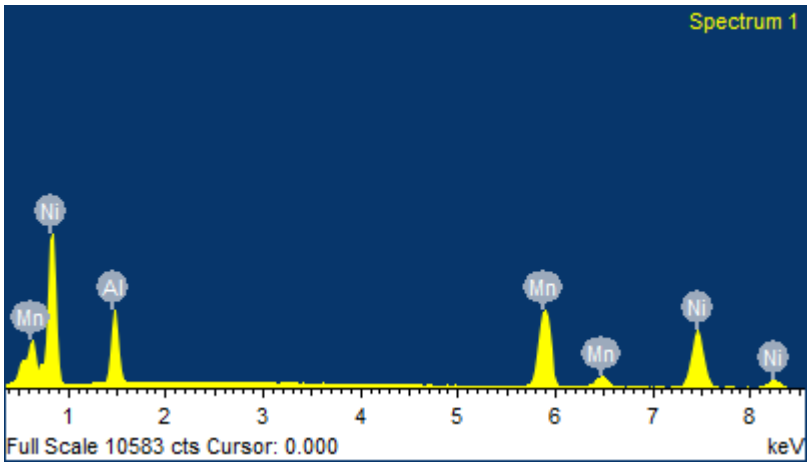

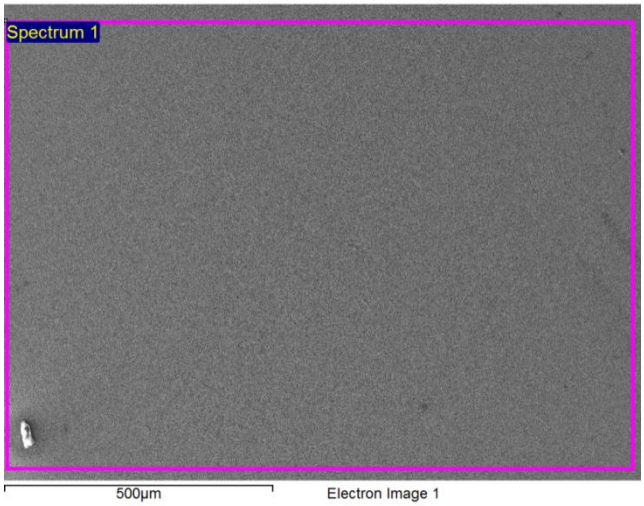

Element	Weight%	Atomic%
Al K	8.70	19.22
Mn K	34.40	30.15
Ni K	56.90	50.64
Totals	100.00	

Figure 3.20: EDAX pattern and elemental composition for 4 µm thick film

3.4.2.2 Crystal Structure

Figure 3.21 shows the XRD patterns of the films with thickness varying from 0.5 µm to 4 µm. The XRD patterns of the films show that the structure consists of B2 phase. For thickness ≤ 1.15 µm, reflection corresponding to Si substrate can also be seen. To further confirm the phase present in the films, the crystal structure of the films has been examined by transmission electron microscopy. As an example, the TEM image of the film with thickness 1 µm is shown in **Fig. 3.22**.

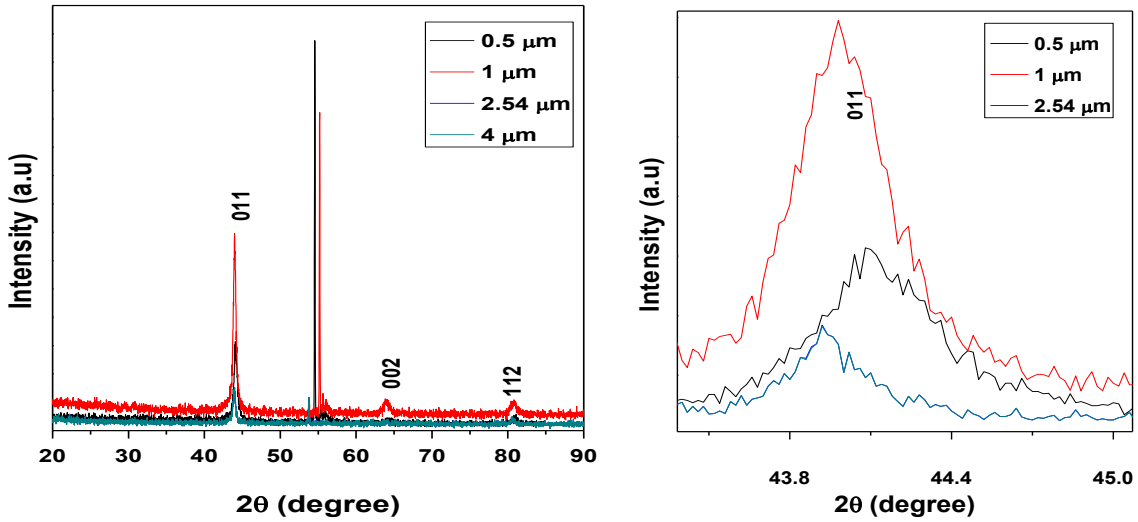

Figure 3.21: XRD image of the samples

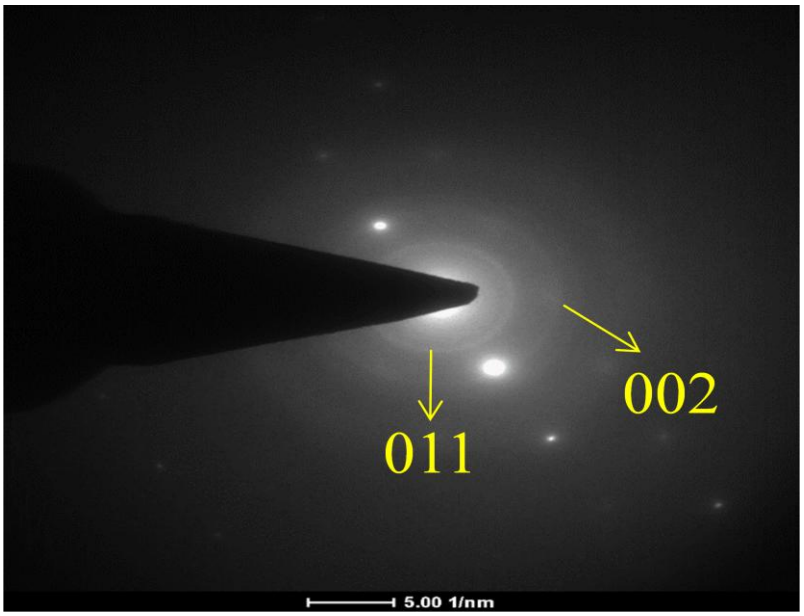

Figure 3.22: TEM image of the sample with thickness 1 µm.

Cross-sectional FE-SEM of the films shows that the thickness of the film varies monotonically with increasing deposition time. As an example, Cross-sectional FE-SEM pattern for the film with thickness 1 µm in **Fig. 3.23**. Cross-sectional FE-SEM of the films shows that the thickness of the film deposited for 30 min ~ 1 µm.

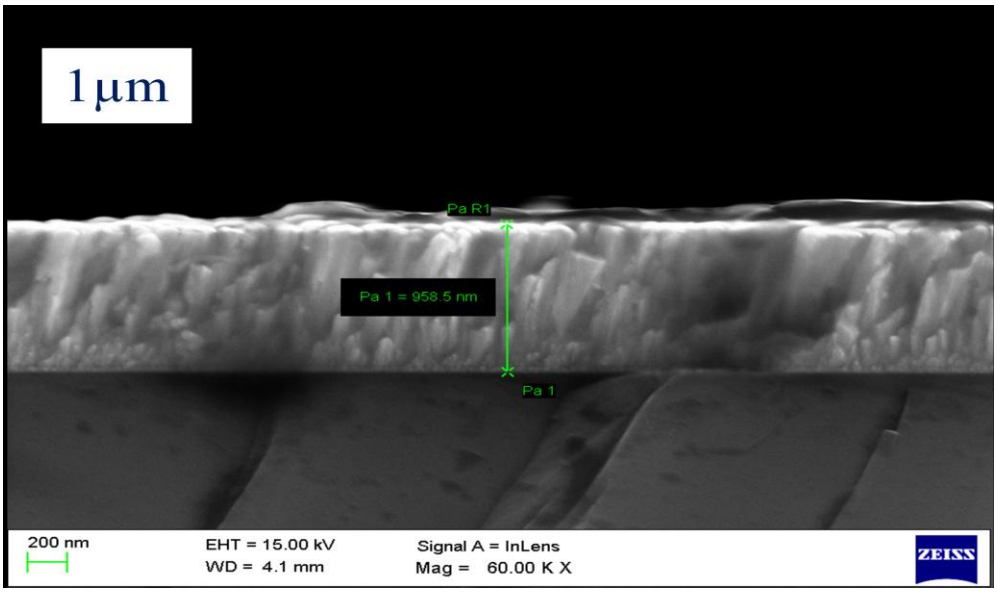

Figure 3.23: Cross-sectional FE-SEM pattern for the film with thickness 1.09 µm.

The SAED pattern taken from the part of the specimen for the films has been shown in **Fig. 3.24**, **Fig. 3.25** and **Fig. 3.26** for thickness 1 µm, 2.5 µm and 4 µm. It can be clearly seen that grain size increase with increasing thickness.

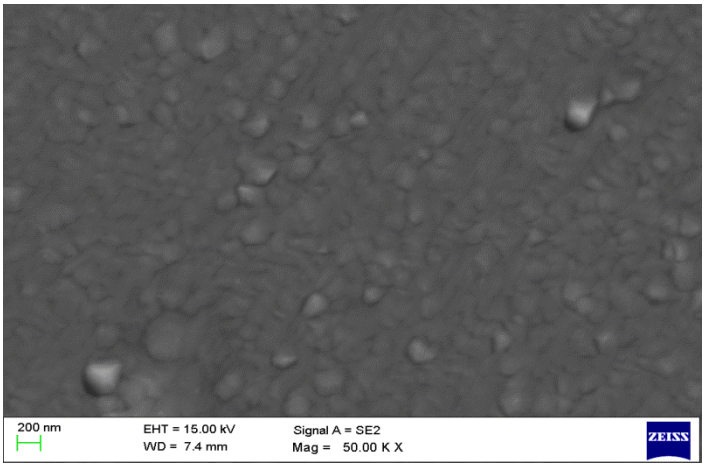

Figure 3.24: SAED pattern for the film with thickness 1 µm

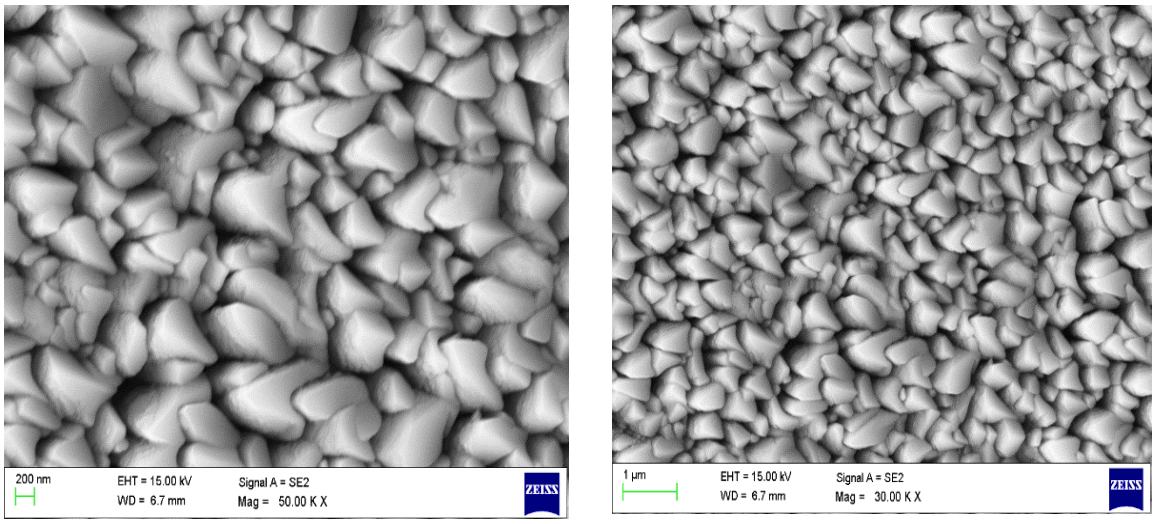

Figure 3.25. SEM image for the film with thickness 2.5 µm.

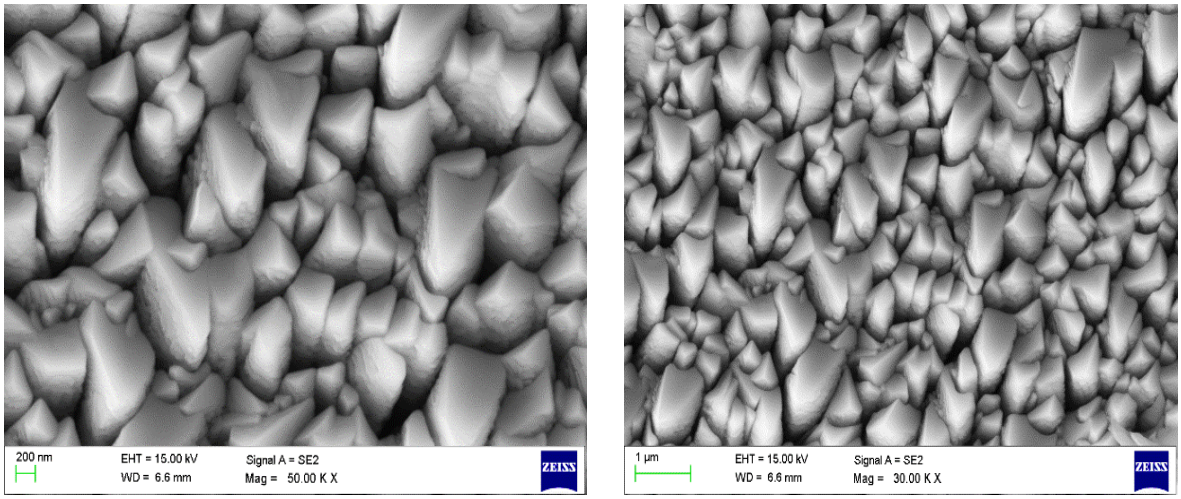

Figure 3.26: SEM image for the film with thickness 4 µm.

3.4.2.3 Magnetic Properties

The magnetic and structural transition temperatures of Mn rich Ni-Mn-Al films have been determined from the magnetization measurement at H = 100 Oe. **Fig. 3.27** shows the dc susceptibility for the films in the temperature range of 2 K ≤ T ≤ 325K in zero-field-cooled heating (ZFCH), field-cooled heating (FCH) and field-cooled cooling (FCC) sequences.

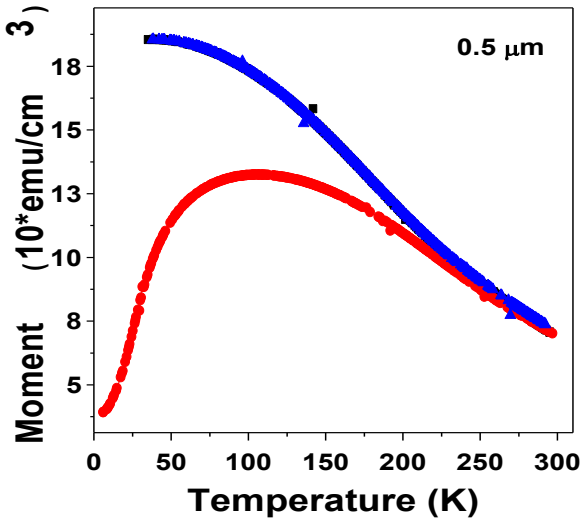
0.5 μm
Moment (10*emu/cm 3)
Temperature (K)

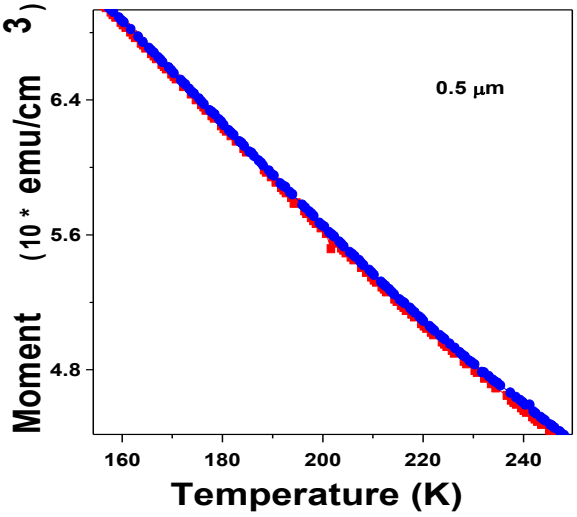
0.5 μm
Moment (10 * emu/cm 3)
Temperature (K)

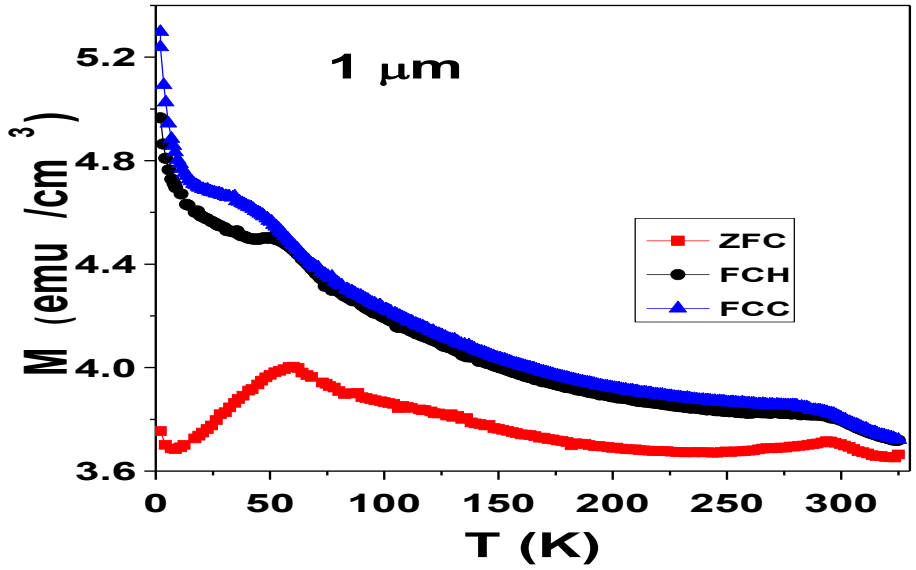
1 μm
ZFC
FCH
FCC
M (emu /cm 3)
T (K)

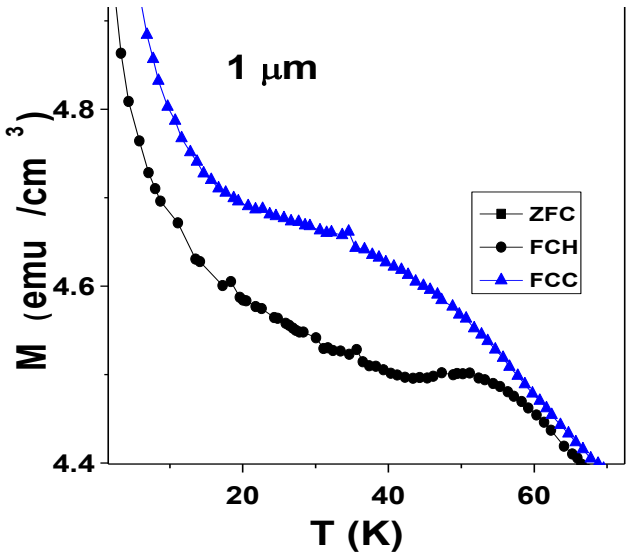
1 μm
ZFC
FCH
FCC
M (emu /cm 3)
T (K)

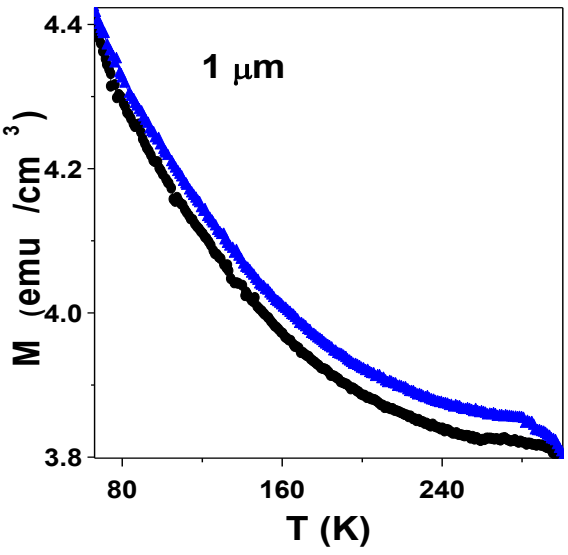
1 μm
M (emu /cm 3)
T (K)

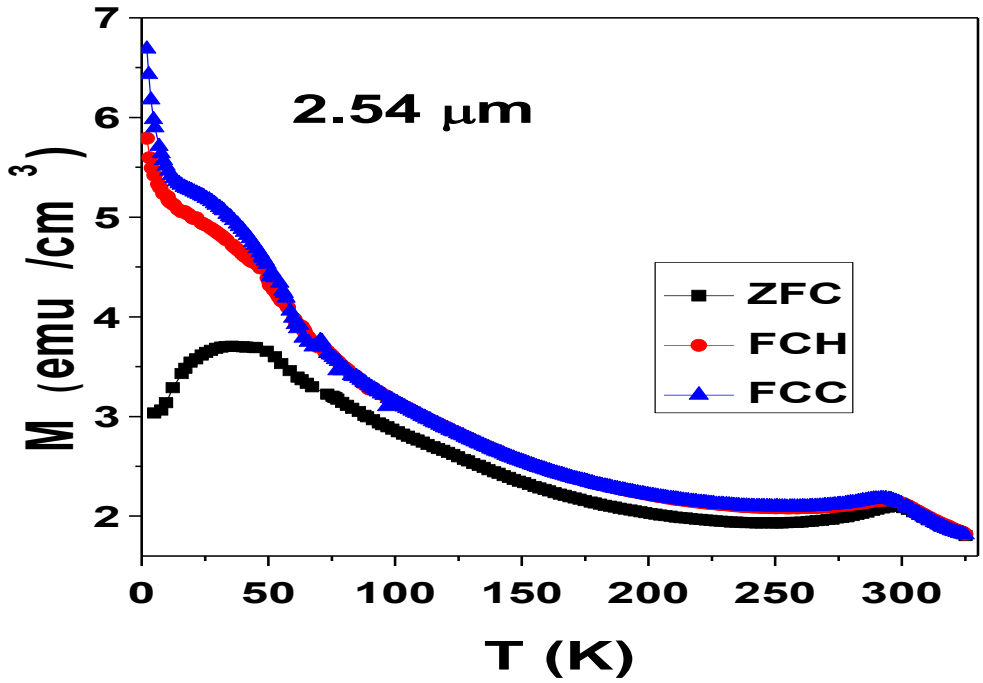
2.54 μm
ZFC
FCH
FCC
M (emu /cm 3)
T (K)

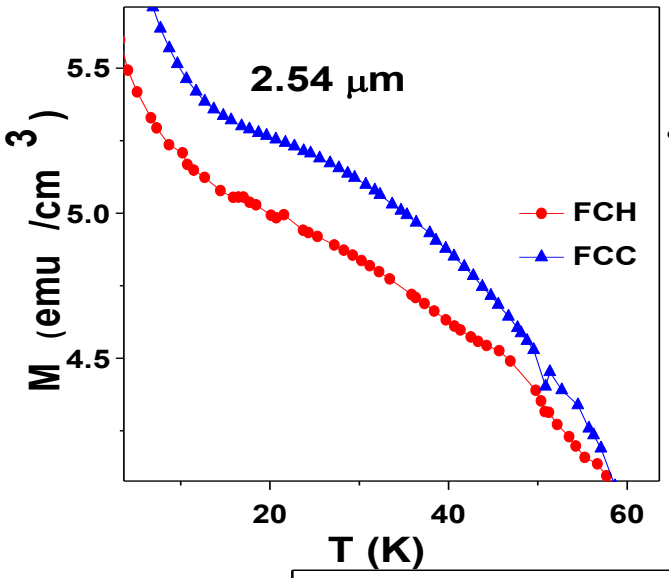
2.54 μm
FCH
FCC
M (emu /cm 3)
T (K)

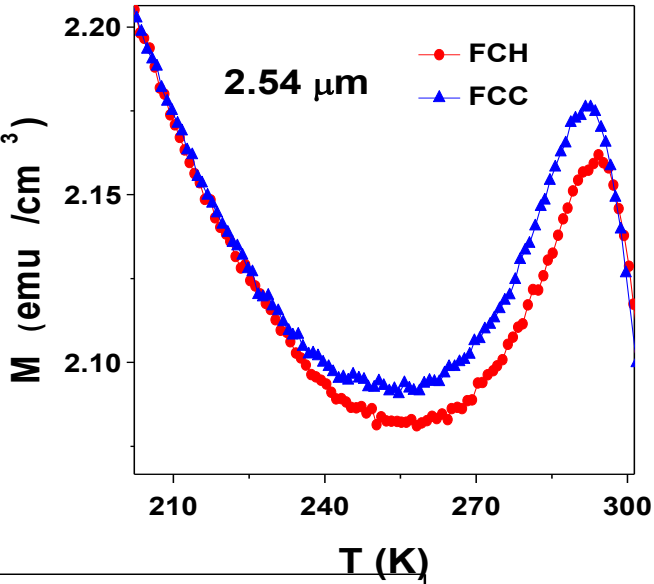
2.54 μm
FCH
FCC
M (emu /cm 3)
T (K)

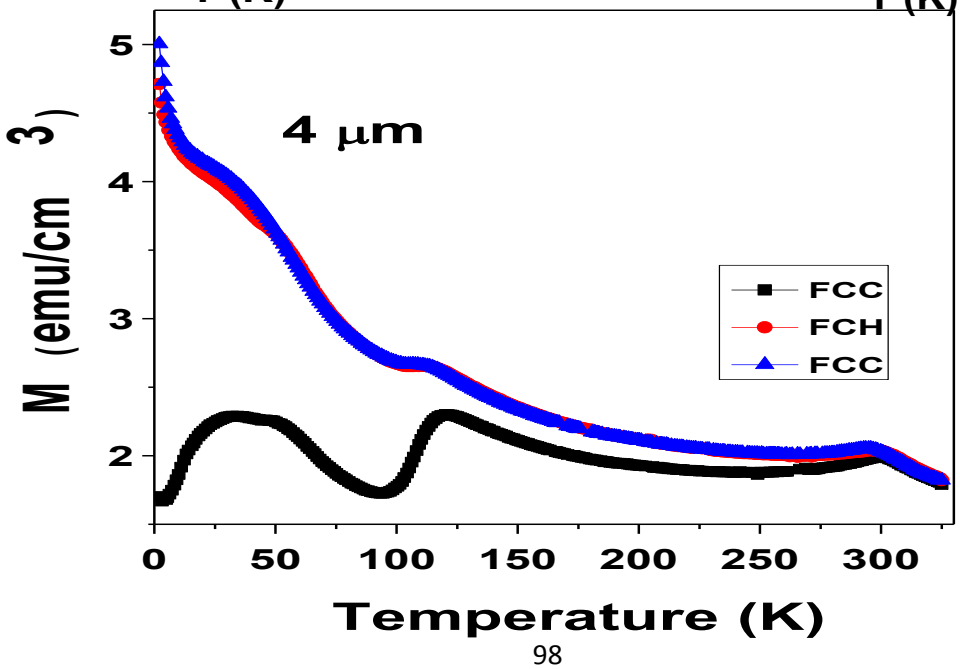
4 μm
FCC
FCH
FCC
M (emu/cm 3)
Temperature (K)

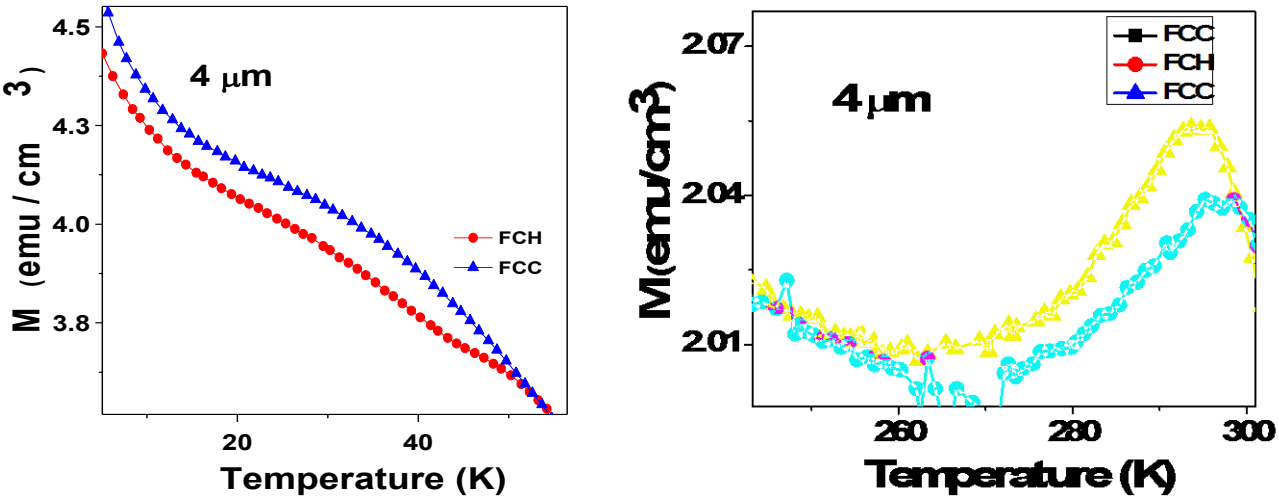

Figure 3.27: *dc* susceptibility for the films in the temperature range of 2 K ≤ T ≤ 325 K in zero-field-cooled heating (ZFCH), field-cooled heating (FCH) and field-cooled cooling (FCC) sequences.

The *M-T* curves show that for the sample with 0.5 μm no antiferromagnetic transition can be observed. Also as can be seen in the magnified view of the sample, there is no hysteresis in the FCH and FCC curves. The absence of thermal hysteresis for the film deposited for 5 min may be due to the hindrance of transformation by a large number of grain boundaries. With increasing film thickness, the grain size increases and above a certain value of grain size, a complete martensitic transformation can take place. All other samples exhibit an antiferromagnetic transition temperature at temperature ~ 300 K. With decreasing temperature moment increases and a peak is observed at low temperature that may be associated with spin glass transition. The spin glass transition temperature increases with increasing film thickness and reaches a temperature of 122 K for the film with thickness 5 μm. A close look at the *M-T* shows that a temperature below spin glass transition temperature there is an opening between FC heating (FCH) and FC cooling (FCC) curves. The occurrence of hysteresis shows a first order structural transition. This first order structural transition is reflected as a hump in ZFC data below spin glass transition temperature. *M-T* data shows that although spin glass transition temperature increases much with increasing film thickness, the structural transition temperature exhibits a small decrease with increasing film thickness. For the samples with thickness larger than 0.5 μm, a steplike anomaly has been observed in the ZFCH data at low temperature (indicated by T_B) which is the typical signature of EB blocking temperature [202]. For the sample with 0.5 μm there is no signature of EB blocking temperature. Owing to the absence of antiferromagnetic, structural and exchange bias blocking temperature in the 0.5 μm thick sample, this sample has not been further explored for exchange bias properties.

3.4.2.4 Exchange bias measurements

Figure 3.28 shows hysteresis loops taken at 10 K for different cooling fields (H_{cool}) for the sample with thickness 1 µm. Magnified view has also been shown. Maximum exchange bias of 309 Oe has been observed for cooling field of 3 T. **Fig. 3.29** shows the *M-H* for the film with thickness 2.50 µm for different cooling fields. In this case maximum exchange bias of 1050 Oe has been obtained for 3 T cooling field. For the film with 5 µm thickness as shown in **Fig. 3.30**, maximum negative exchange bias of 1435 Oe has been observed at 10 K for 2 T cooling field. This shows that with increasing film thickness exchange bias increases. With further increase in film thickness film peels off from the substrate.

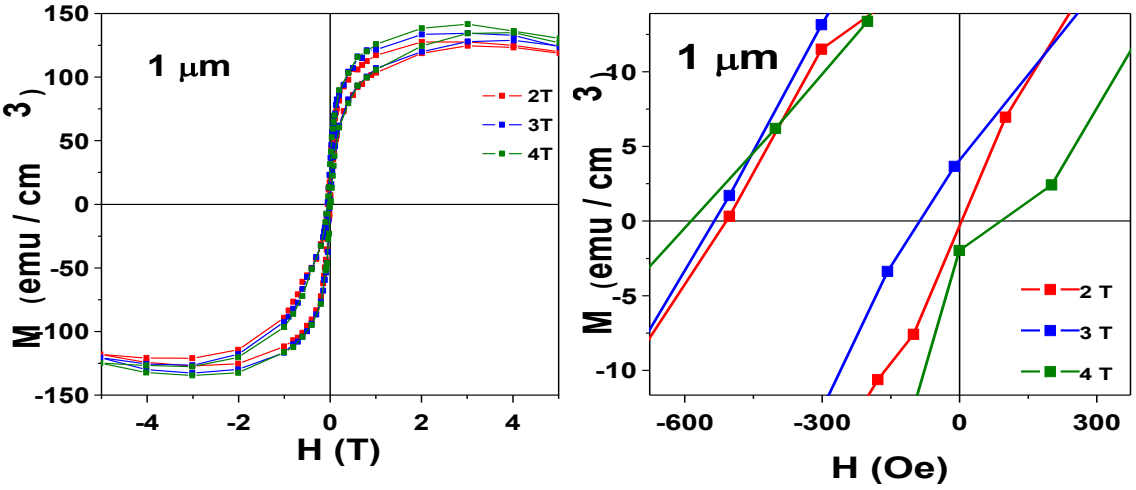

Figure 3.28: *M-H* curves for the sample with thickness 1 µm.

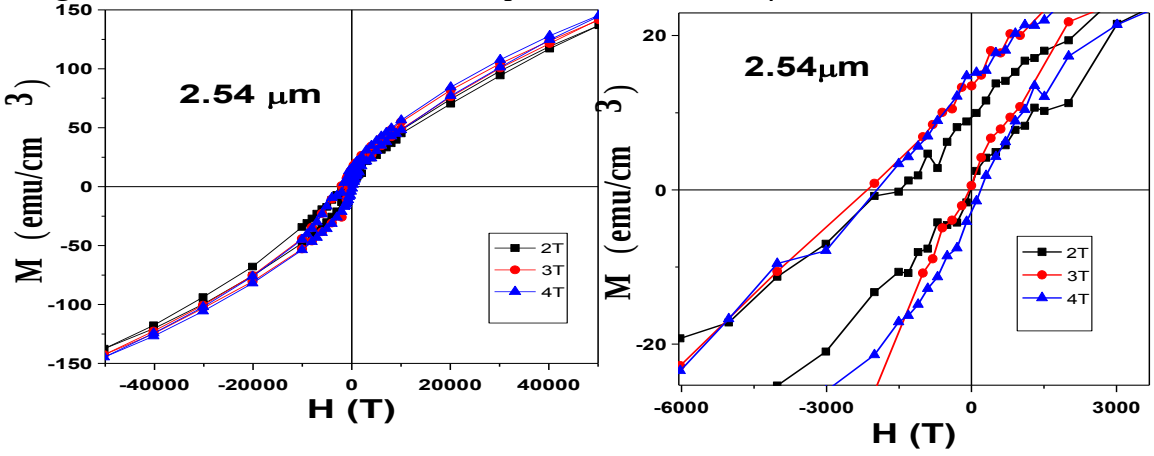

Figure 3.29: *M-H* curves for the sample with thickness 2.54 µm.

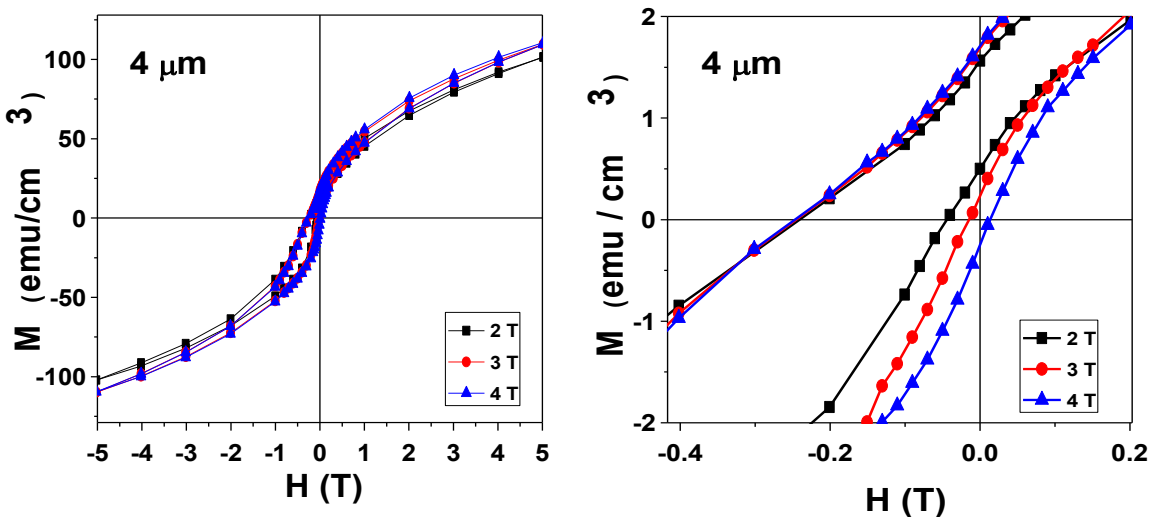

Figure 3.30: *M-H* curves for the sample with thickness 1.25 μm.

Figure 3.31 shows the variation of exchange bias with temperature for the film with thickness 4 μm. Exchange bias has been measured at different temperature of 10 K, 50 K, 90 K and 120 K.

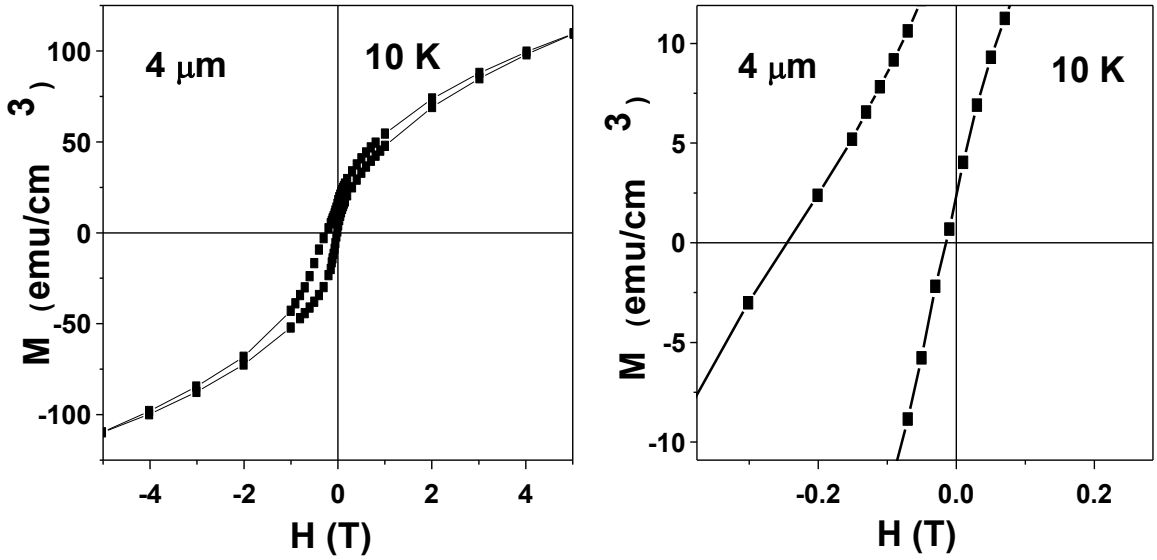

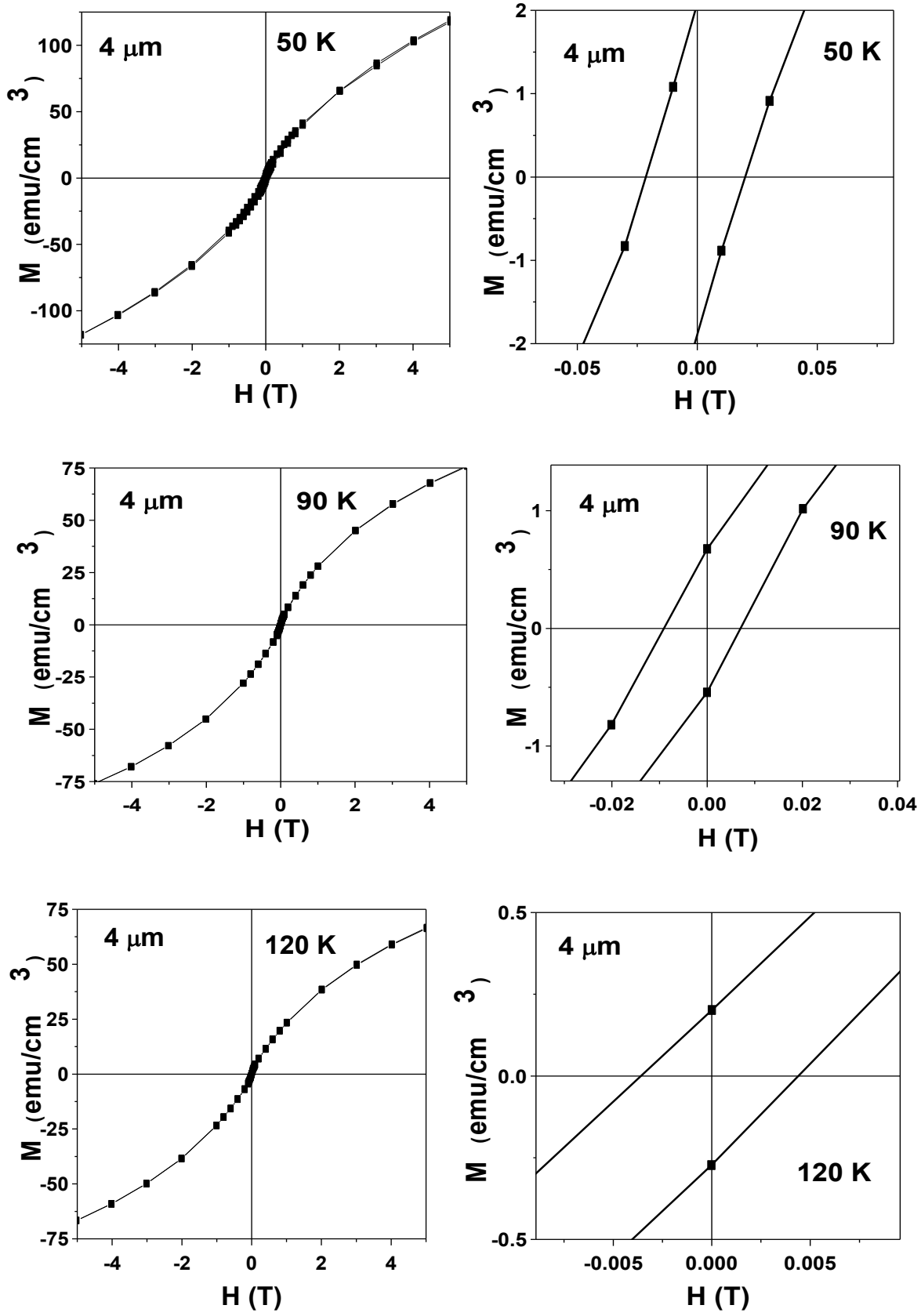

Figure 3.31: Exchange bias at different temperatures of 10 K, 50 K, 90 K and 120 K. Enlarged view is also shown for each temperature.

It can be clearly seen that exchange bias shows a non monotonic variation with increasing temperature. At 10 K, large negative EB of 1435 Oe is obtained. This decrease to ~ 10 Oe at 50 K and shows a marginal value at 90 K where EB of 5 Oe is obtained. The variation of exchange bias with temperature is shown in **Figure 3.32**

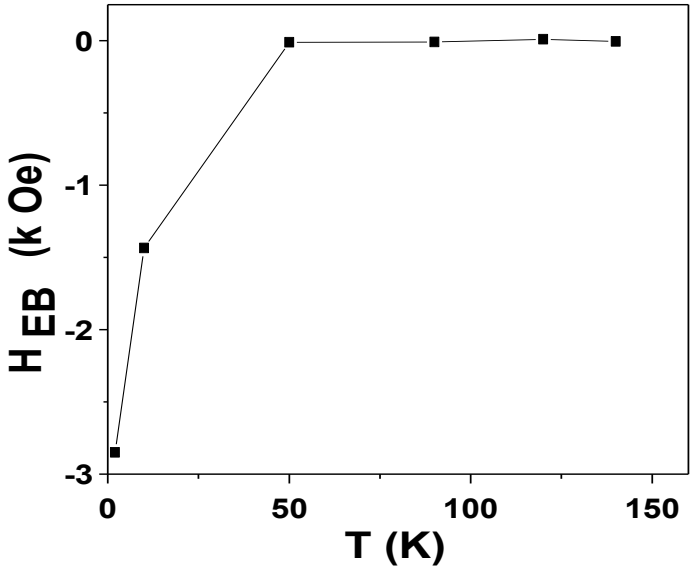

Figure 3.32 Variation of Exchange bias with temperature

The large value of exchange bias seen in the *M-H* curve can be attributed to magnetic frustration in the sample arising because of competing FM and AFM interactions [189,193,194]. To further explore such a possibility, a set of magnetic measurements have been performed to investigate the low temperature magnetic behaviour of the sample. **Fig. 3.33** shows the *M-T* curves for the sample measured under different magnetic fields of 1T, 3T, 4T and 5 T. For clarity the data has been shown in the temperature range 2 K to 150 K. A close analysis of *M-T* data show that for moderate measuring field the bifurcation between ZFC and FC curves start decreasing and the slope of the FC curve decreases which indicates some FM-like clusters appear in the AFM matrix. As the measuring field increases, bifurcation between ZFC and FCH curves decreases further and the FC curve becomes more horizontal. With further increase in measuring field (at 50 kOe), there is negligible bifurcation that is the ZFC and FCH curves coincide and a constant value of magnetization in the FC curve is obtained indicating that the nature of the *M(T)* curve is that of a typical ferromagnetic system [206].

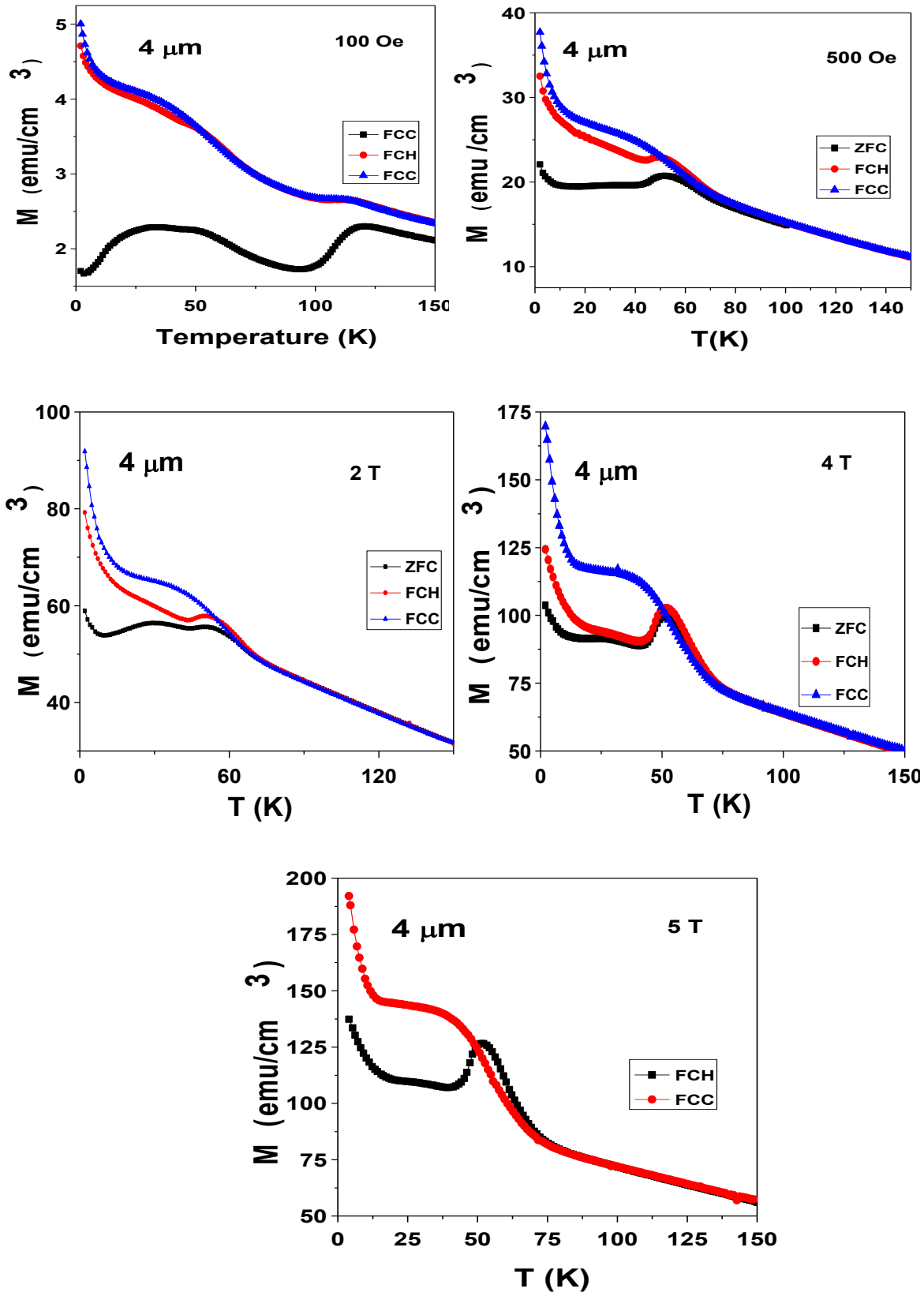

Figure 3.33: *M-T* curves for the sample measured under different magnetic fields of 1T, 3T, 4T and 5 T

Figure 3.34 shows the cooling filed H_{cool} dependence of H_{EB} and coercivity H_C. The value of H_{EB} increases with increasing cooling field and then decreases with further increase in cooling field. A similar H_{cool} dependence of H_{EB} has been obtained for canonical glass compounds [207] and metallic alloys [208]

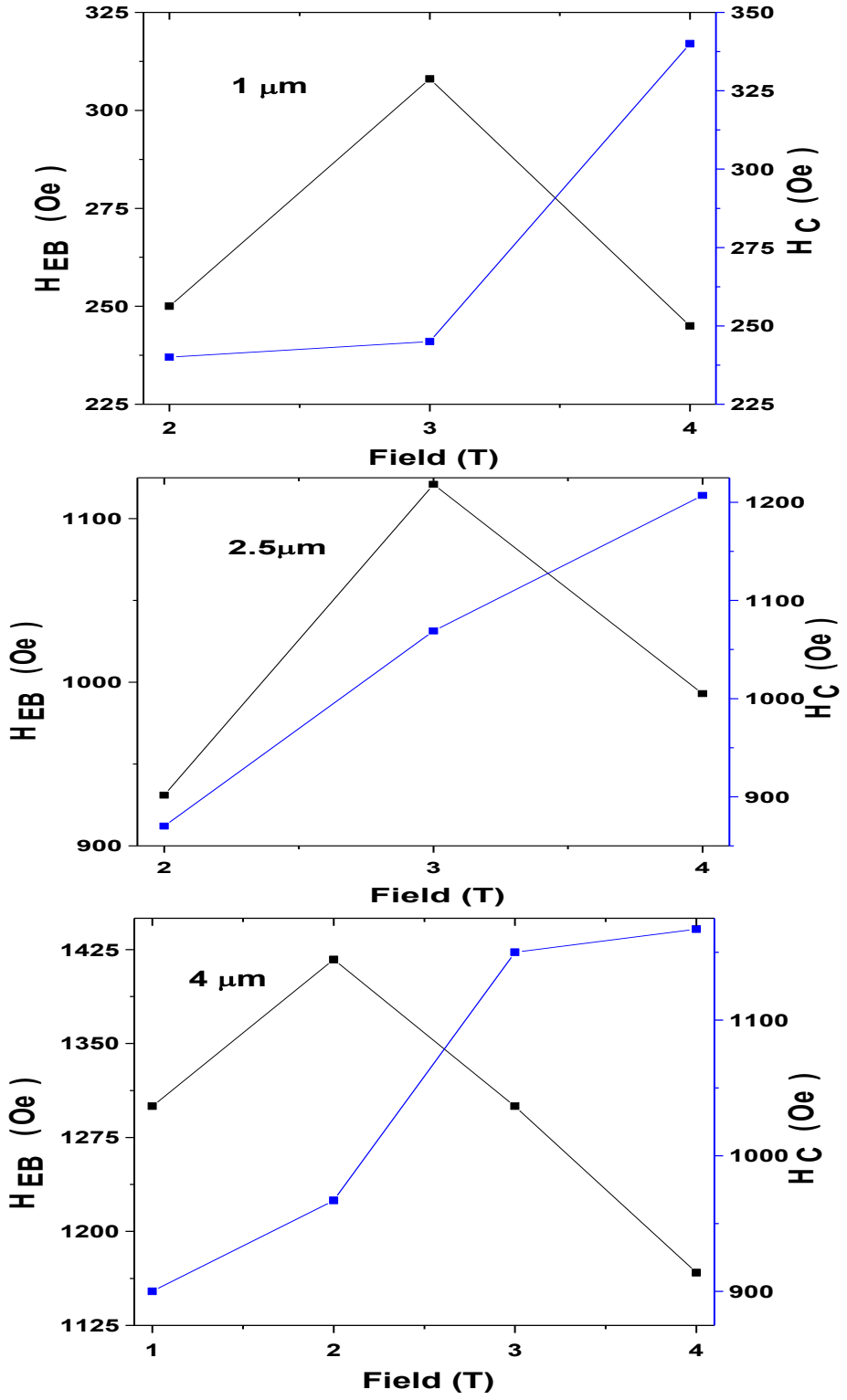

Figure 3.34: Cooling filed H_{cool} dependence of H_{EB} and coercivity H_C.

In order to further explore the nature of this transition, ac susceptibility measurements have been carried out. **Fig. 3.35** shows the *ac* susceptibility data in the temperature range 170-300 K. For the sake of clarity, the data for 333 Hz and 999 Hz has been shown only in the range of transition temperatures.

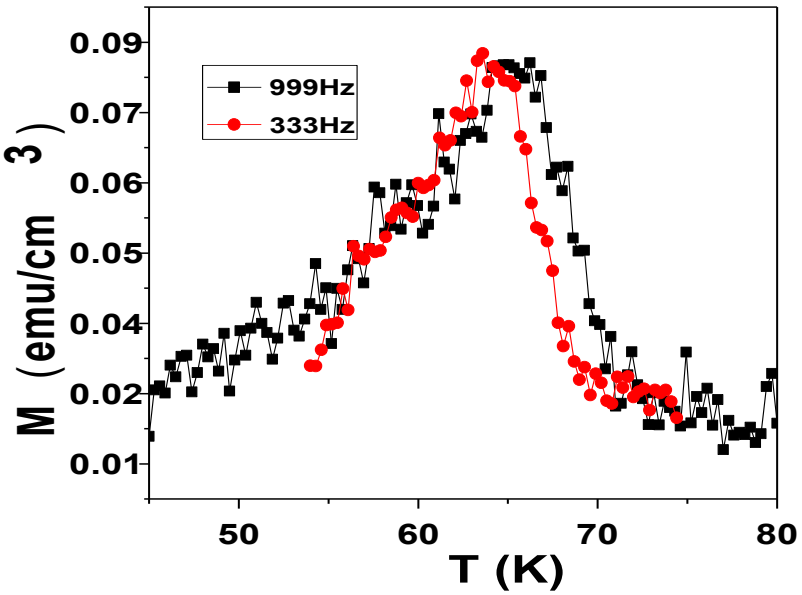

Figure 3.35: *ac* susceptibility data in the temperature range 170-300 K.

The hump around 60 K shows strong frequency dependence in χ' which indicates the existence of magnetic frustration associated with the spin glass state. The peak position in the curve is defined as spin freezing temperature T_f. To further confirm the nature of magnetic state, relative frequency shift (Ṕ) has been calculated from the equation $\acute{P} = \Delta T_f / T_f (\Delta \log\omega)$, where ω is the angular frequency ($\omega = 2\pi f$) [203,204]. For the present case, Ṕ was found to be 0.04 which indicate cluster glass (randomly frozen interacting magnetic clusters of finite dimension) like state in the alloy. Thus exchange bias may be associated to the occurrence of field induced ordering which results in frozen FM clusters in an antiferromagnetic matrix. In the case of low and moderate fields H_{EB} increases, as the FM like ordering increases and thus the degree of alignment of the moment of the frozen FM spin is enhanced along a preferred direction which reduces the effect of averaging of the anisotropy due to randomness. The increase in anisotropy is indicated by the increase of H_C with H_{cool} as shown in Fig. 6. With further increase of H_{cool}, H_{EB} decreases which is induced by both the growth of the FM clusters

and particularly by the suppression of the spin glass region which detoriates the coupling strength between the FM and spin glass regions [209].

Low temperature spin glass transition has been observed in Ni-Mn-Al system independent of high temperature structure. Acet et al. [189] attributed this splitting in B2 structure to either some residual $L2_1$ phase or ferromagnetic component present in conical antiferromagnetic structure of *B2* phase. Previous studies on polycrystalline Ni-Mn-Al samples with composition close to the studied sample by Monasa et al. [194] and Morito et al. [198] revealed that for Ni–Mn–Al system, the magnetic state contains both ferromagnetic and antiferromagnetic interactions. In the present case there occurs a ferromagnetic like field induced ordering at ~ 50 K reflected as coinciding ZFC and FCH curves with increasing magnetic field. Such field induced ordering is crucial to thin film and has also been reported by Hassdorf et al. in Mn rich NiMnAl thin films deposited by MBE technique. This field induced ordering at low temperature has been assumed to be closely related to a high degree of structural disorder on the Mn-Al sublattice. Judging by the fact that such field induced ordering is crucial to thin films and has not been observed in bulk alloys, we suggest that Mn rich Ni-Mn-Al B2 phase thin films exhibiting field induced ordering at low temperature are potential candidate for observing large exchange bias. The details of magnetic interaction at low temperature need to be further explored.

As can be seen in with increase in cooling field, hysteresis increases with maximum hysteresis appearing for 3 T cooling field. With further increase in cooling field (4 T) hysteresis diminishes. The kind of behaviour may be associated with field induced structural transition [210-214] where in incomplete structural transition is induced at low cooling fields; as cooling field increases, a change in structure takes place due to field induced transition which results in the coexistence of mixed phases, however, with further increase in cooling field, the structural transition is complete and hysteresis diminishes. This behaviour is further reflected in the dependence of negative exchange bias appearing in the sample on cooling field. Initially exchange bias increases with increasing cooling field due to the coexistence of mixed phase. Maximum exchange bias appears in the sample exhibiting maximum thermal hysteresis in M-T loops that is for 3 T cooling field. With further increase in cooling field, exchange bias decreases.

In order to further explore the nature of this transition, Arrot plots have been plotted. The use of Arrott plots to determine the T_C in weakly ferromagnetic materials is well known in literature [215]. However, Arrott plots can be used to estimate T_N in antiferromagnetic

materials [215,216]. Since we expect multiple magnetic interactions in our sample, we consider the presence of both antiferromagnetic moment (L) and ferromagnetic moment (M') in the magnetic sublattice. The expression of the free energy [215] for magnetic sublattice then may be written in the form

$$F = \frac{1}{2} AM'^2 + \frac{1}{4} CM'^4 - B_0 M' + \frac{1}{2} aL^2 + \frac{1}{4} cL^4 + \frac{1}{2} \alpha L^2 M'^2 + \beta (LM')^2 \quad \ldots\ldots\ldots(1)$$

The terms with proportionality constant α and β are the lowest order coupling terms between M' and L allowed by symmetry. The term proportional to β determines the orientation of the antiferromagnetic moment with respect to the ferromagnetic one, and may be incorporated into the term $\alpha L^2 M'^2$ with a renormalized coefficient γ and then minimizing the free energy in Eq. (1) with respect to both M' and L one obtains

$$AM' + CM'^3 - B_0 + \gamma L^2 M' = 0 \quad \ldots\ldots\ldots\ldots(2)$$

$$aL + cL^3 + \gamma LM'^2 \quad \ldots\ldots\ldots\ldots\ldots..(3)$$

where $B_0 = H$ (applied external magnetic field).

The coefficients A and a are assumed to depend on temperature as

$$A = A'(T - T_C), \qquad a = a'(T - T_N)$$

whereas C, c, A' , and a' are considered to be temperature independent and A' and a' are positive. The renormalization of both ferromagnetic (A~ coefficient) and antiferromagnetic (a~ coefficient) interactions are seen in the magnetic susceptibility as measured in magnetization experiments. The properties of Arrott plots (M^2 versus H/M) for a system with ferromagnetic and antiferromagnetic phase transitions are also deduced accordingly [215].

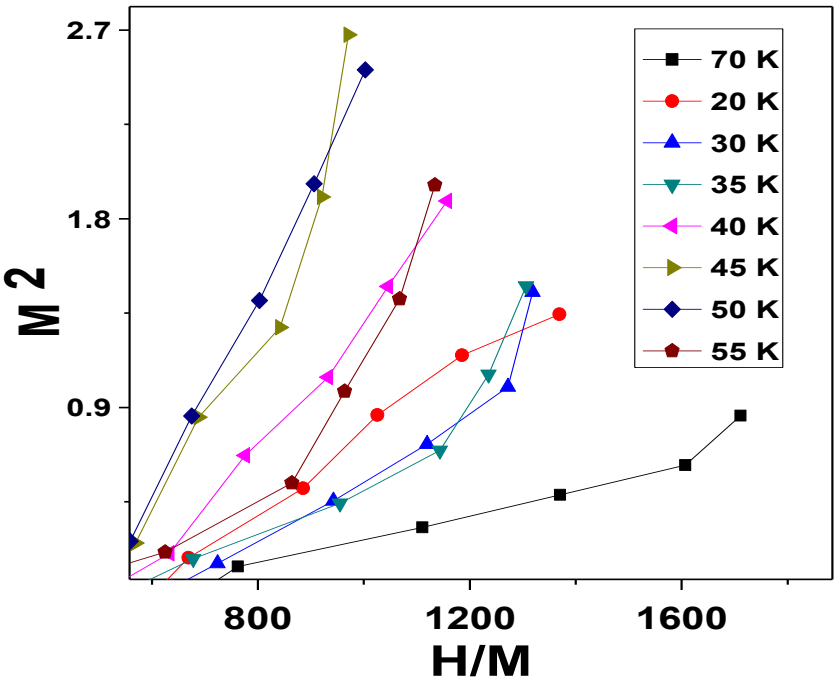

Figure 3.36: Arrott plots for our sample at different temperatures.

The Arrott plots for our sample at different temperatures are shown in **Fig. 3.36**. It can be clearly seen that the plots are not linear as expected even for weak ferromagnets. Although for T = 50 K, the line almost seems straight and passing through zero, there is no evidence of spontaneous magnetization at any temperature. This features of indicate that there is no true antiferromagnetic order in this sample. This kind of deviation from linearity of isotherms towards the origin in Arrott plots have been observed in spin-glass systems like $Gd_{37}Al_{63}$ [217], $Y_{1-x}Fe_x$ [218] or in concentrated spin glass system of $Al_{37}Mn_{30}Si_{33}$ quasicrystals [219] near the ferromagnet spin-glass critical concentration. This further supports the presence of spin glass phase in the samples.

3.4.3 Conclusion

In conclusion the exchange bias behaviour of Mn rich Ni-Mn-Al films have been explored. *M-H* measurements reveal that the value of exchange bias field H_{EB} increases and shows a maximum value with increasing cooling field. Maximum H_{EB} of 2.2 kOe at 2 K for 20 kOe cooling field has been observed for the film with thickness 5 μm. Cooling field dependence of H_{EB} and H_C indicate that an increase in anisotropy and growth of FM clusters occurs at high

field. Exchange bias appearing in the sample may be associated to the field induced ferromagnetic like ordering occurring at low temperature.

CHAPTER 4

INVESTIGATIONS ON Ni-Mn-Al / Ni Bi-LAYER THIN FILMS

4.1 Introduction

Owing to the wide scale application of thin film, Heusler alloy has also been explored for exchange bias properties in thin film form [153] and bilayer [155,159]. The underlying mechanism for the observation of exchange bias in bulk and thin films of Heusler alloy is the interplay between ferromagnetic and antiferromagnetic regions present in the low temperature phase. An enhancement of exchange bias has been attempted in Heusler type Ni-Mn-X-Y quaternary systems (X = Sn and Sb, Y = Co and Fe) [156,220].

As exchange bias is an interfacial governed property, the manipulation of EB relies on the control of magnetic structure in direct proximity to the interface [221,222]. In this regard, layered FM / AFM thin film systems have been widely explored for EB and related properties. Among Heusler alloy bilayer films, ferromagnetic Ni_2MnSn, Co_2MnSn and Co_2FeSi films in contact with antiferromagnet [155] and NiMnSb / CrN heterostructures have been studied. The observed EB has been attributed to the uncompensated and pinned AFM spin at FM–AFM interface and different AFM domain structure for different thickness of AFM layer. The observed exchange bias in multilayers depends critically on the thickness of ferro and antiferro layers. H_{EB} is expected to show an inversely linear dependence on the FM layer thickness t_{FM}, that is, $H_{EB} \alpha 1/ t_{FM}$. This inversely linear is experimentally supported if the FM layer thickness of t_{FM} is larger than a critical value [160,161], being suggestive of the interfacial nature of exchange bias. The critical FM thickness depends on FM material and the growth conditions.

Compared to the FM layer, the AFM layer exhibits quite complex influences on H_{EB}. It has been revealed that the EB is dependent on many factors related to the AFM layer. Inthe abovementioned expression of H_{EB}, the exchange couplingis considered to involve just the interfacial spins in theFM and AFM layers. The AFM layer thickness does notappear, suggesting that H_{EB} should be independent on theAFM layer thickness. However, the experimental investigations indicate that H_{EB} has strong dependence on the AFM layer

thickness [162]. When the AFM layer is sufficientlythin, H_{EB} exhibits an abrupt drop with the decreasein the AFM thickness in a narrow range. When the AFM thickness is less than a critical value, H_{EB} is rendered to zero.This critical AFM thickness depends on the specific AFMmaterial and the measurement temperature. This AFM thickness dependence of H_{EB} is a common phenomenon. When the AFM layer is relatively thick, the dependence of H_{EB} on the AFM thickness becomes quite complex. Relyingon the specific layered system, its layered configuration andmicrostructure, and the measurement temperature, the variation of H_{EB} with the increase in the AFM thickness can be generally separated into two main categories:

1) H_{EB} increases to a constant value when the AFM layer is thick enough [5,32,163-167];

2) H_{EB} first increases to a maximum and then decreases with increasing the AFM thickness [5,162-164,167-170].

Among FM / AFM bilayer films Ni layer has been extensively used as the FM layer. The Ni layer has been chosen due to limited space for source material. The lattice parameter for FCC Ni is 0.3524 nm and lattice mismatch is a consideration for selecting Ni layer as the FM layer. However, as per the literature, exchange bias has been found to be inversely proportional to the magnetization of the ferromagnetic. In view of this it has been observed that Ni has low magnetization of 485 emu/cc as compared to 1707 emu/cc for Fe, 1400 emu/cc for Co and 880 emu/cc for $Ni_{80}Fe_{20}$ [216].

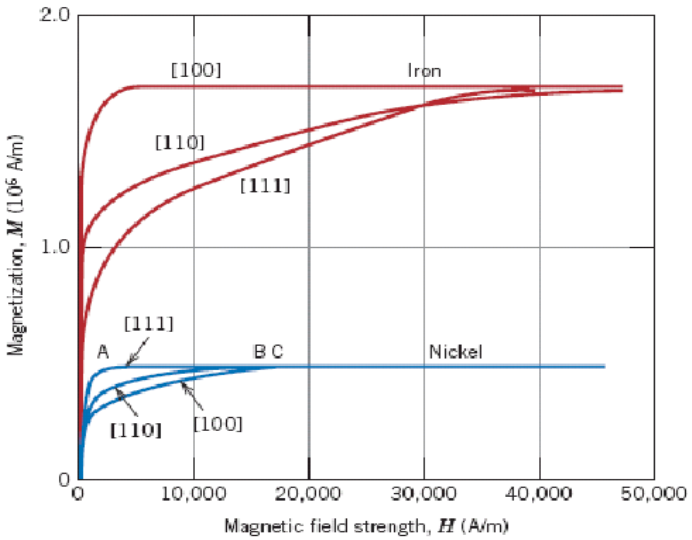

Figure 4.1: Magnetization versus applied magnetic field response along the [100], [110] and [111] orientations of iron (bcc) and Ni [223**]**

It has been observed that the exchanger bias obtained with Ni as the FM layer is almost twice the value of exchange bias achieved using a $Ni_{80}Fe_{20}$ layer with an equivalent thickness. The potentially large exchange bias that has been achieved using Ni as the ferromagnetic layer makes it the ideal ferromagnet. Ni layer has been used as FM with many antiferromagnetic materials like CoO [224], NiAgO [225], IrMn, NiMn, FeMn, and PtMn [226,227], FeF_2 [228].

In the present case, exchange bias has been studied in bilayer system with Ni as the FM layer and NiMnAl as the AFM layer. Since the ferromagnetic transition temperature of Ni is around 627 K and NiMnAl in pure B2 phase exhibits antiferromagnetic behaviour with antiferromagnetic transition temperature ~ 300 K, this combination offers a suitable bilayer system for the study of exchange bias. In this regard, thin layer of Ni has been deposited on NiMnAl samples exhibiting B2 structure. Ni layer has been deposited on both Mn rich and Ni rich Ni-Mn-Al compositions. Thickness of both Ni layer and NiMnAl layer has been varied to study the effect of thickness variation on exchange bias properties. Detailed study on these films allow us to clarify the following (i) The effect of Ni layer on exchange bias behaviour is more prominent in thin films than thick films. (ii) For Ni rich Ni-Mn-Al thin films, the magnitude of H_{EB} with Ni layer is larger as compare to pure Ni-Mn-Al film. (iii) Exchange bias increases monotonically with thickness of Ni rich Ni-Mn-Al film thickness in Ni-Mn-Al / Ni bilayer film. (iv) For a particular thickness of Ni rich Ni-Mn-Al, H_{EB} increases non monotonically with increasing Ni layer. The thickness of Ni layer at which maximum H_{EB} is obtained depends crucially on the thickness of Ni-Mn-Al layer. (v) For thin films, the effect of Ni layer is more prominent however, for thick films (> 1 hr), the effect of Ni layer on the trend of exchange bias is almost the same i.e for thick films, maximum exchange bias has been observed in for Ni thickness of 4 min. (vi) For Mn rich Ni-Mn-Al thin films with thickness ≤ 1.005 μm, Ni layer results in an increase in exchange bias as compare to pure Ni-Mn-Al film however for the films with thickness larger 1.005 μm exchange bias decreases with Ni layer as compare to pure Ni-Mn-Al film.

4.2 Experiment

Substrate	Si (100)
Substrate temperature	150^0C
Substrate-target distance	6 cm
Base pressure	5.0×10^{-6}Torr
Working pressure	10 mTorr
Sputtering gas	Ar
Target	Ni
Sputtering power (W)	80 (RF)

Table 4.1: Depostion parameters for bi-layer.

The effect of Ni layer on exchange bias properties of Mn rich and Ni rich NiMnAl films have been discussed separately.

4.3. Results and discussion Mn rich Ni-Mn-Al thin films

4.3.1 Crystal Structure

Since the deposition of Ni layer is followed by the deposition of thin layer of Pt to avoid oxidation of the Ni layer, the XRD patterns of the films with Ni layer can not be shown. However to have an estimate of the structure of the Ni layer deposited on the films, Si substrate were kept along with the films in the sputtering chamber. The Ni layer deposited on the Ni-Mn-Al samples is also deposited on the Si substrate. The XRD pattern of this Si substrate with Ni layer has been shows the peaks correspond to Ni. For small thickness of Ni layer, peak corresponding to Si (100) substrate can also be seen. Cross-sectional FE-SEM of the substrate shows that the thickness of Ni layer deposited for 1 min is 30 nm. The thickness of the Ni film varies monotonically with increasing deposition time.

4.3.2 Magnetic Properties

Due to the crucial dependence of exchange bias on the thickness of FM and AFM layer, the results obtained for different Ni layer thickness on the NiMnAl films with thickness 1 µm, 2.52 µm and 4 µm are discussed separately.

4.3.2.1 Ni-Mn-Al layer thickness of 1 µm and different thickness of Ni layer

The magnetic and structural transition temperatures of Mn rich Ni-Mn-Al films with Ni layer have been determined from the magnetization measurement at H = 100 Oe. **Fig. 4.2 (*a-j*)** shows the dc susceptibility for the films in the temperature range of 2 K ≤ T ≤ 325K in zero-field-cooled heating (ZFCH), field-cooled heating (FCH) and field-cooled cooling (FCC) sequences for the sampel with thickness 1.009 µm. **Figure 4.2 (a-j)** shows the *M-T* curves for the Ni-Mn-Al sample with different Ni layer and without Ni layer.

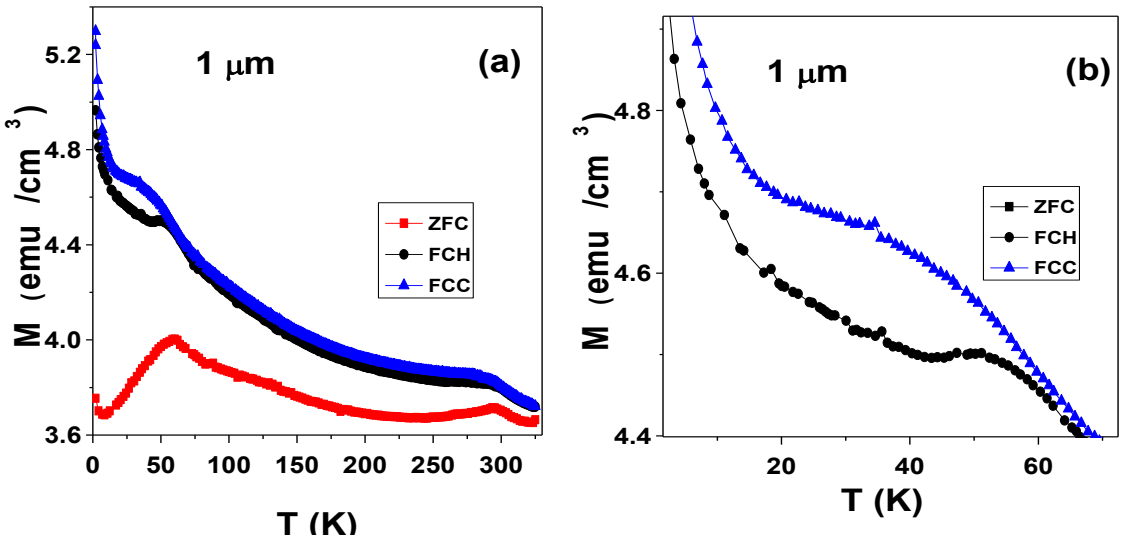

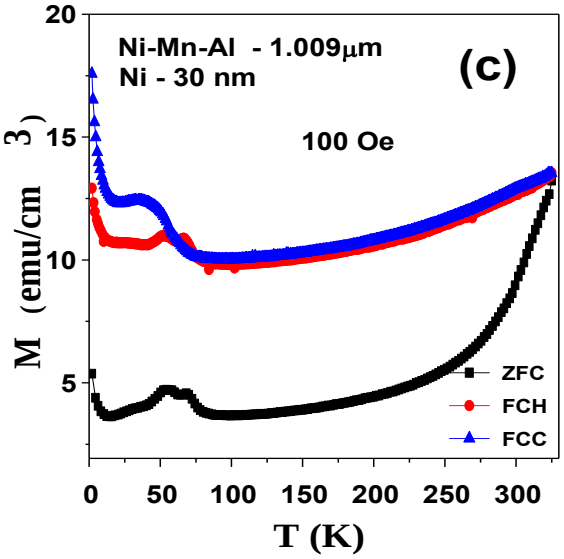
Ni-Mn-Al - 1.009μm
Ni - 30 nm
(c)
100 Oe
ZFC
FCH
FCC
M (emu/cm 3)
T (K)

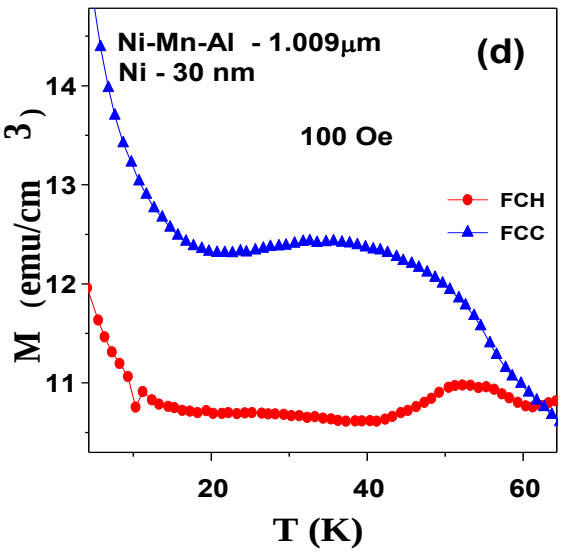
Ni-Mn-Al - 1.009μm
Ni - 30 nm
(d)
100 Oe
FCH
FCC
M (emu/cm 3)
T (K)

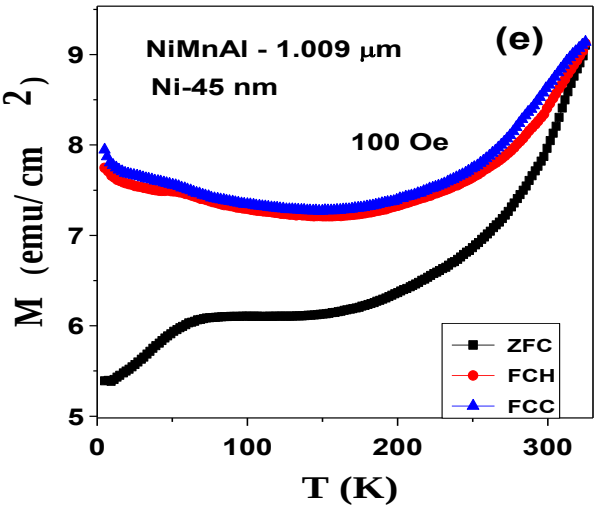
NiMnAl - 1.009 μm
Ni-45 nm
(e)
100 Oe
ZFC
FCH
FCC
M (emu/ cm 2)
T (K)

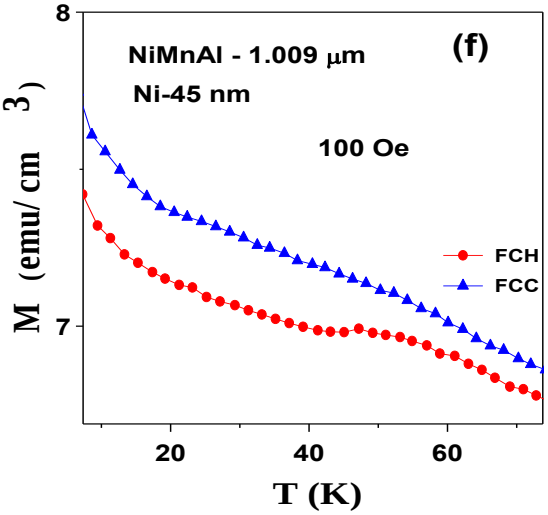
NiMnAl - 1.009 μm
Ni-45 nm
(f)
100 Oe
FCH
FCC
M (emu/ cm 3)
T (K)

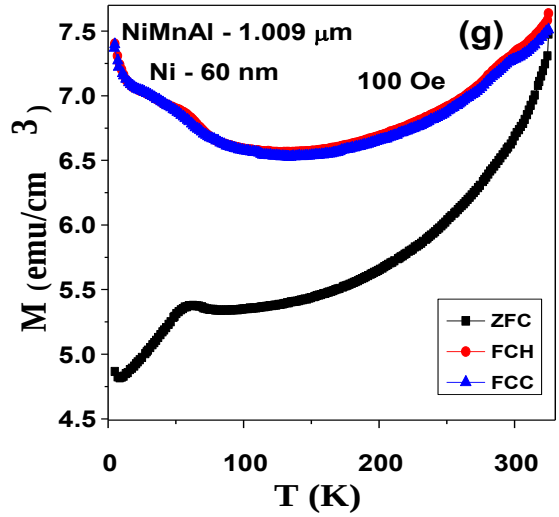
NiMnAl - 1.009 μm
Ni - 60 nm
(g)
100 Oe
ZFC
FCH
FCC
M (emu/cm 3)
T (K)

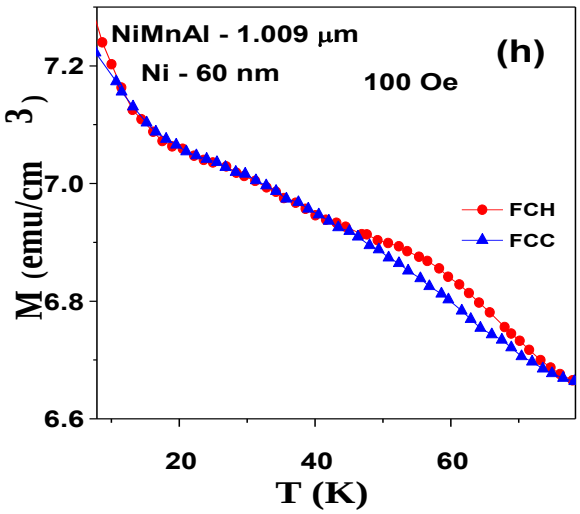
NiMnAl - 1.009 μm
Ni - 60 nm
(h)
100 Oe
FCH
FCC
M (emu/cm 3)
T (K)

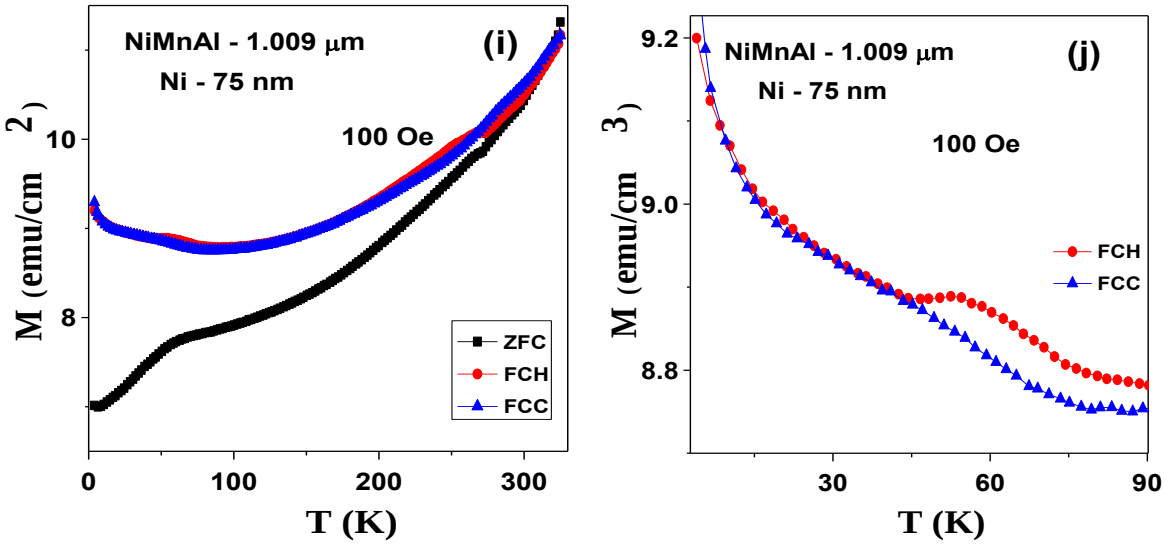

Figure 4.2 (a-j): *M-T* curves for NiMnAl films. The thickness of Ni layer and NiMnAl layer is mentioned in the figure.

As can be seen in the figure, Ni layer results in a different behaviour of the *M-T* curves as compare to the Ni-Mn-Al sample without Ni layer. The NiMnAl / Ni samples exhibit a decrease in moment with decreasing temperature while the samples without Ni layer exhibit an increase in moment with decreasing temperature. The antiferromagnetic transition observed at ~ 300 K in the Ni-Mn-Al films is also absent in Ni-Mn-Al/Ni films. Thus the antiferromagnetic behaviour observed in Ni-Mn-Al films is destroyed by the Ni layer. The temperature at which bifurcation between ZFC and FC curves occur decreases with increasing thickness of the Ni layer. The structural transition observed at low temperature (~ 70 K) for NiMnAl film can still be seen for different NiMnAl / Ni samples; however the difference in magnetization between the FCH and FCC curves below the structural transition decreases with increasing Ni layer thickness. This shows that with increasing Ni layer thickness, the field induced ordering observed at low temperature is enhanced which may be associated to increase in magnetization of the sample with increasing Ni layer thickness. The decrease in moment with decreasing temperature reflects that the ordering of the sample decreases with decreasing temperature. This shows that below room temperature, the sample exhibits a mixed interaction. To understand the magnetic state of the sample, *M-H* loops have been measured at room temperature and at low temperature as shown in **Fig. 4.3**.

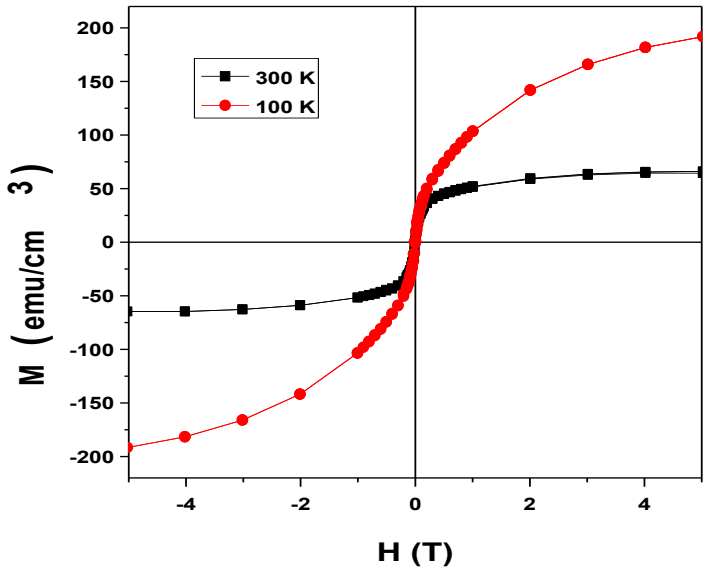

Figure 4.3: *M-H* loops of the sample at 300 K and 100 K.

As can be seen in the figure, a ferromagnetic type ordering occurs at 300 K, while at low temperature the *M-H* loop is not saturated and shows the presence of some non saturated contribution which may be the antiferromagnetic phase of Mn rich Ni-Mn-Al film. To further explore the magnetic behaviour of the film, exchange bias measurements have been carried out at 10 K in zero field cooled and different field cooled state.

Figure 4.4 shows the M-H loops of the sample for Zero field cooled and different cooling fields for the 1 µm thick NiMnAl film with different Ni layer thickness.

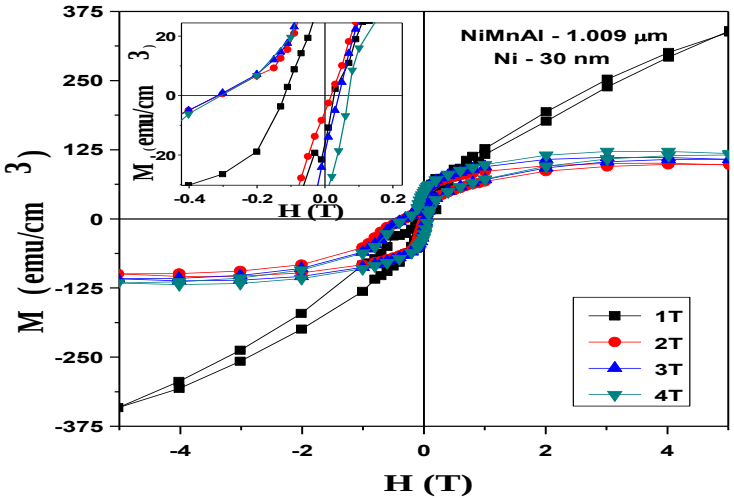

Figure 4.4 (a): M-H loops of the sample with NiMnAl film thickness 1.009 µm and Ni layer thickness 30 nm for different cooling fields.

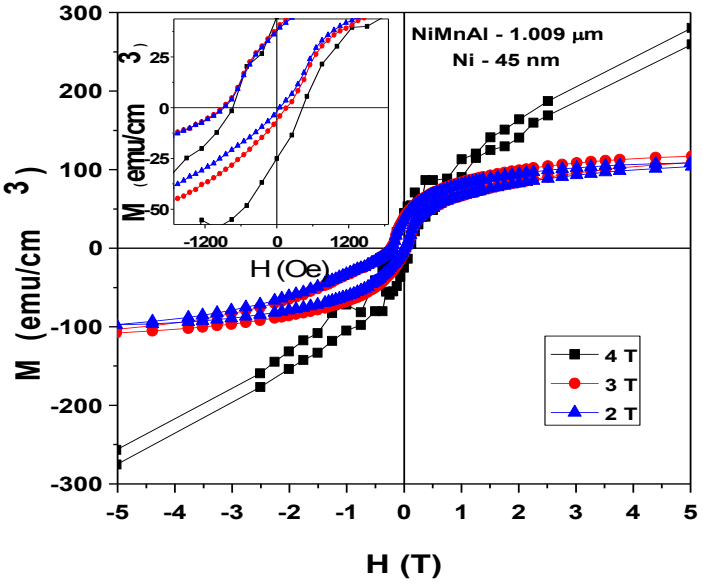

Figure 4.4 (b): *M-H* loops of the sample with NiMnAl film thickness 1.009 μm and Ni layer thickness 45 nm for different cooling fields.

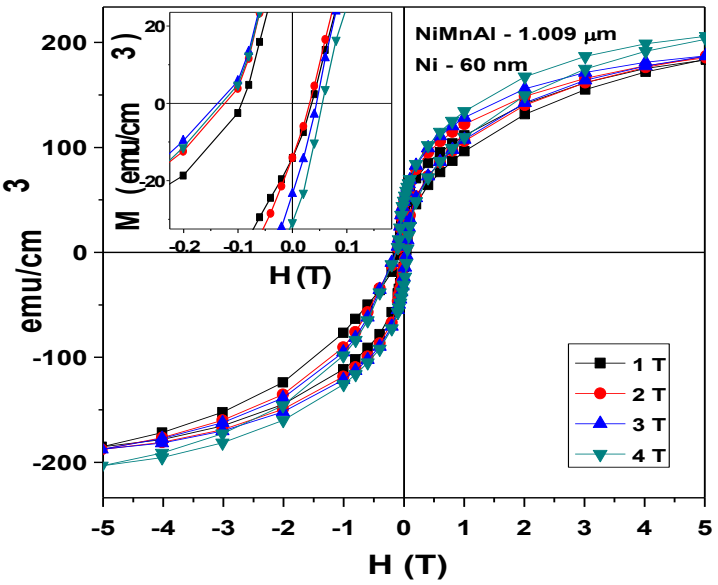

Figure 4.4 (c): M-H loops of the sample with NiMnAl film thickness 1.009 μm and Ni layer thickness 60 nm for different cooling fields.

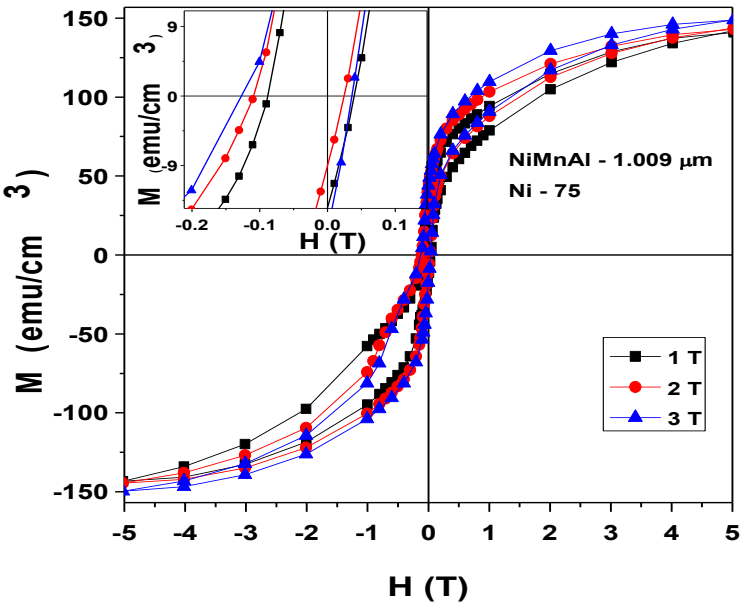

Figure 4.4 (d): *M-H* loops of the sample with NiMnAl film thickness 1.009 μm and Ni layer thickness 75 nm for different cooling fields.

As can be seen in the *M-H* curves, for each thickness of the Ni layer, exchange bias shows a non monotonic variation with increasing cooling field. Exchange bias first increases with increasing cooling field, reaches a maximum value at a certain cooling field (depending on the thickness of Ni layer) and then decreases with further increase in cooling field. The variation of H_{EB} and H_C with cooling field for different Ni layer thickness is shown in **Fig. 4.5 (a-d)**

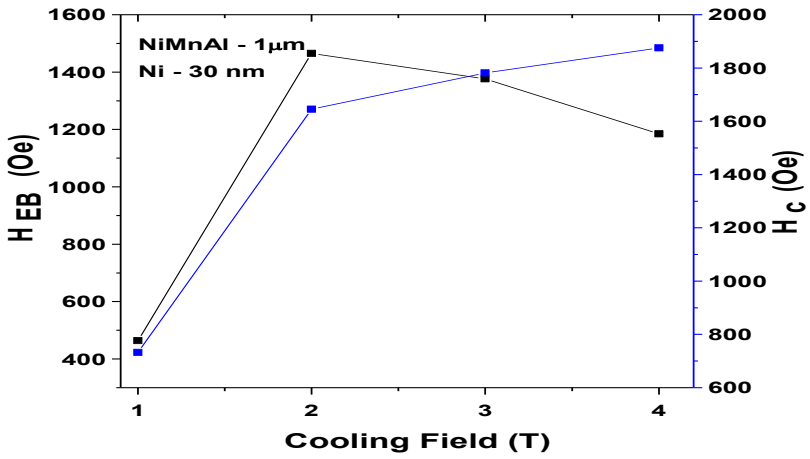

Figure 4.5(a): Variation of H_{EB} and H_C with cooling field for NiMnAl thickness of 1.009 and Ni layer thickness of 30 nm.

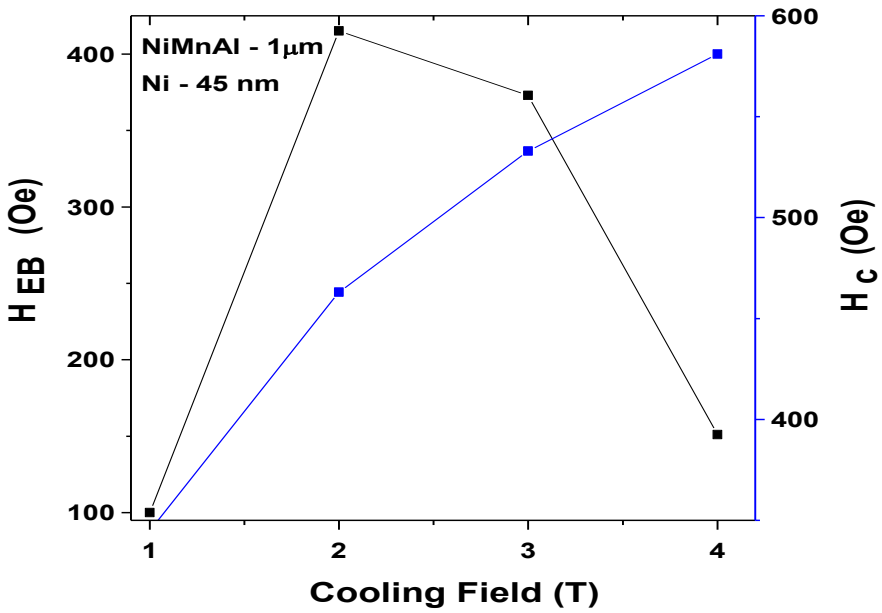

Figure 4.5(b): Variation of H_{EB} and H_C with cooling field for NiMnAl thickness of 1.009 and Ni layer thickness of 45 nm.

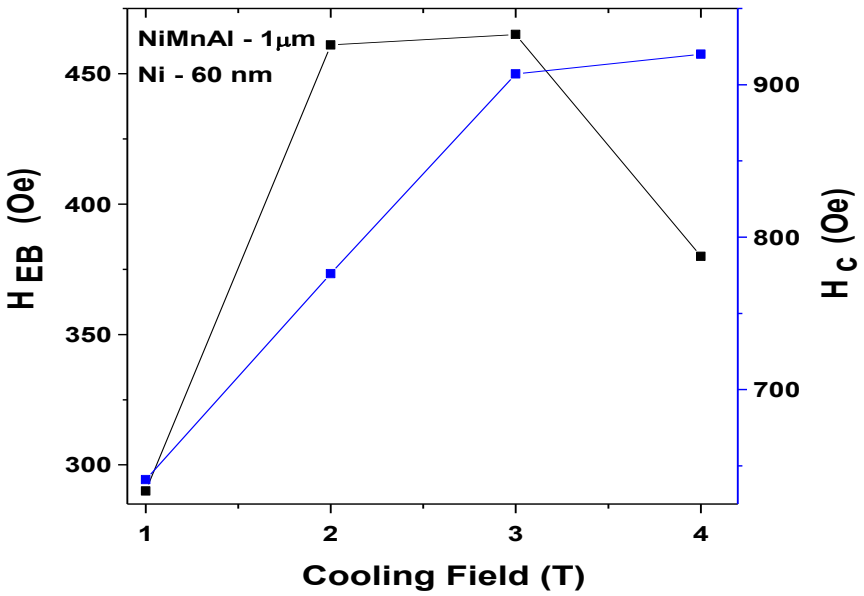

Figure 4.5(c): Variation of H_{EB} and H_C with cooling field for NiMnAl thickness of 1.009 and Ni layer thickness of 60 nm.

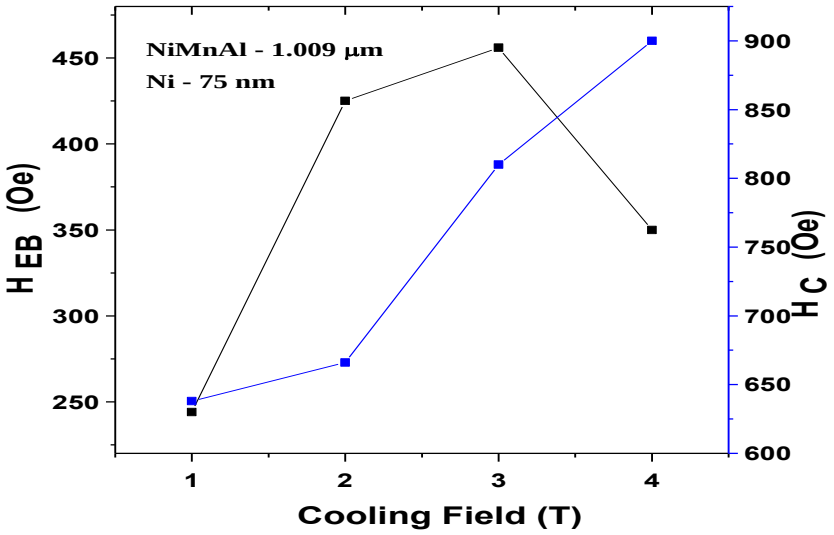

Figure 4.5(d): Variation of H_{EB} and H_C with cooling field for NiMnAl thickness of 1.009 and Ni layer thickness of 75 nm.

As can be seen in **Fig. 4.5**, for NiMnAl layer of thickness 1.009 µm, maximum exchange bias of 1465 Oe at 10 K for 2 T cooling field has been obtained for the Ni layer with thickness 30 nm. It can be seen that for Ni layer thickness of 30 nm and 45 nm, maximum exchange bias has been obtained for 2 T cooling fields while for Ni layer thickness of 60 and 75 nm, maximum exchange bias has been observed for 3 T cooling field. A comparison of maximum exchange bias obtained for different Ni layer thickens has been given in **Fig. 4.6**. Maximum exchange bias obtained for pure NiMnAl film with thickness 1 µm without Ni layer has also been shown for reference to indicate the effect of Ni layer on NiMnAl film.

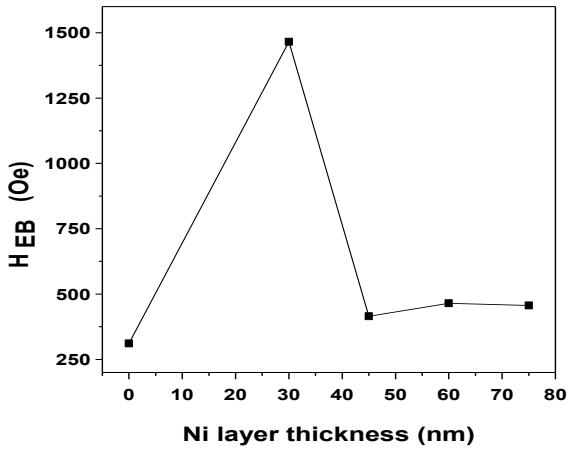

Figure 4.6: Variation of exchange bias for 1 µm thick NiMnAl layer with different thickness of Ni layer.

A comparison of exchange bias for different Ni layer thickness shows the magnitude of exchange bias field depends crucially on the thickness of Ni layer. For the NiMnAl film without Ni layer the exchange bias is 311 Oe which drastically increases to 1465 Oe for the NiMnAl film with 30 nm thick Ni layer. With further increase in Ni layer thickness, exchange bias reaches to 465 Oe and decreases with further increase in Ni layer thickness. This behaviour of variation of exchange bias with varying ferromagnetic (Ni) layer thickness is in consistent with the previous reports on the exchange bias observed in FM / AFM bilayer [222]. It has been reported that exchange bias an inversely linear dependence on the thickness of the ferromagnetic layer, that is $H_{EB} \propto 1/t_{FM}$. This inverse relation is experimentally supported if the FM layer thickness is larger than a critical value. This critical FM layer thickness depends on the FM material and the growth conditions [222]. In the present case the critical thickness of the FM layer (Ni) for 1.009 µm thick AFM layer (NiMnAl) is 30 nm. Beyond this thickness, exchange bias decrease with increasing FM layer thickness.

4.3.2.2 NiMnAl layer thickness of 2.52 µm and different thickness of Ni layer

The magnetic and structural transition temperatures of Mn rich Ni-Mn-Al films with Ni layer have been determined from the magnetization measurement at H = 100 Oe. **Figure 4.7** shows the dc susceptibility for the films in the temperature range of 2 K ≤ T ≤ 325K in zero-field-cooled heating (ZFCH), field-cooled heating (FCH) and field-cooled cooling (FCC) sequences for the sample with thickness 2.52 µm. **Figure 4.7(a-f)** shows the *M-T* curves for the Ni-Mn-Al sample with different Ni layer and without Ni.

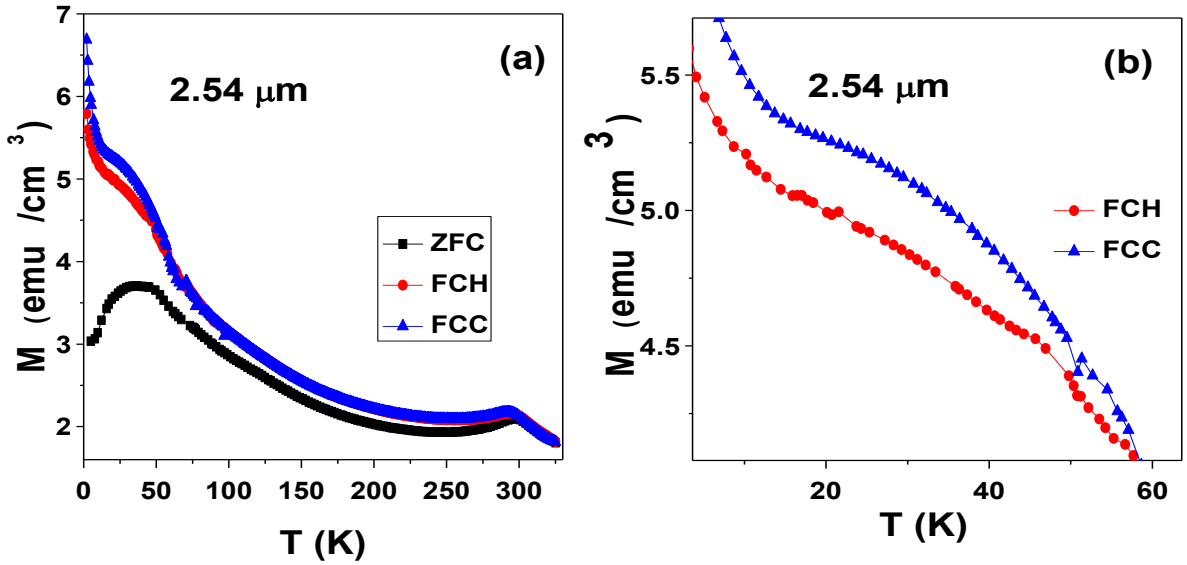

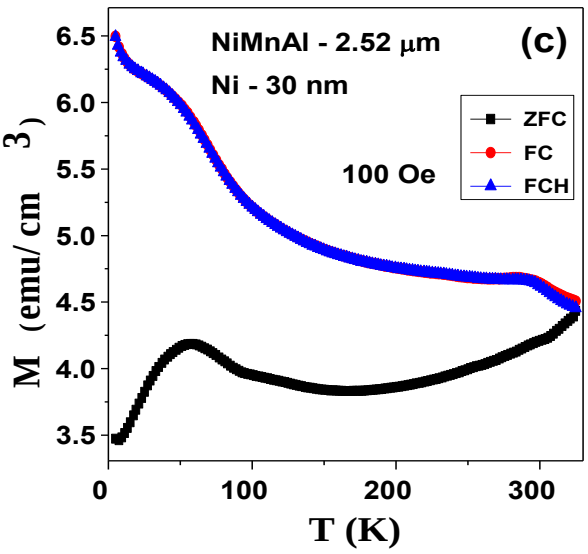
NiMnAl - 2.52 μm
Ni - 30 nm
(c)
100 Oe
ZFC
FC
FCH
M (emu/ cm 3)
T (K)

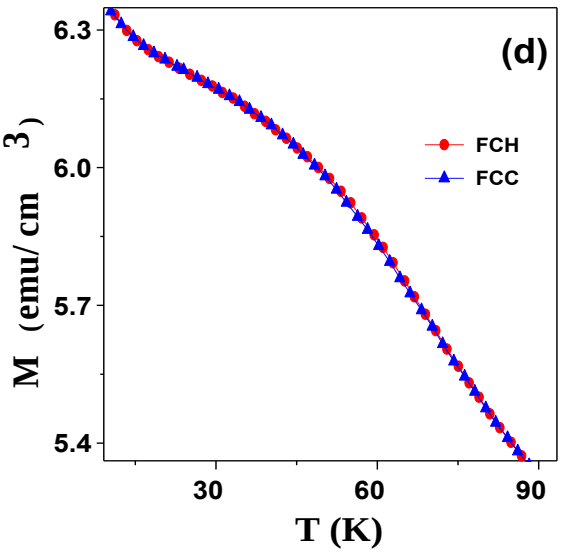
(d)
FCH
FCC
M (emu/ cm 3)
T (K)

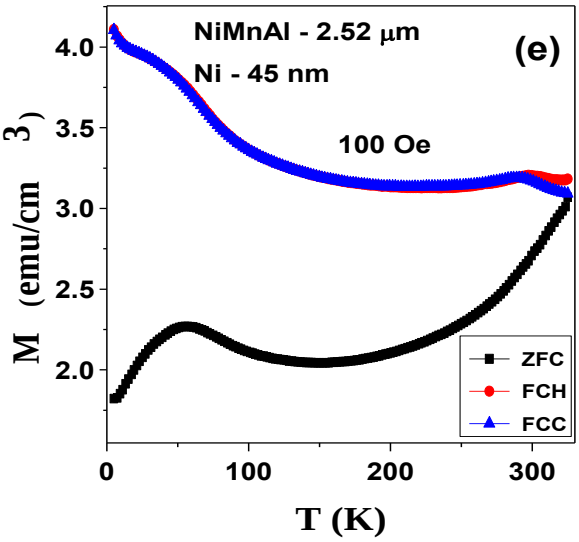
NiMnAl - 2.52 μm
Ni - 45 nm
(e)
100 Oe
ZFC
FCH
FCC
M (emu/cm 3)
T (K)

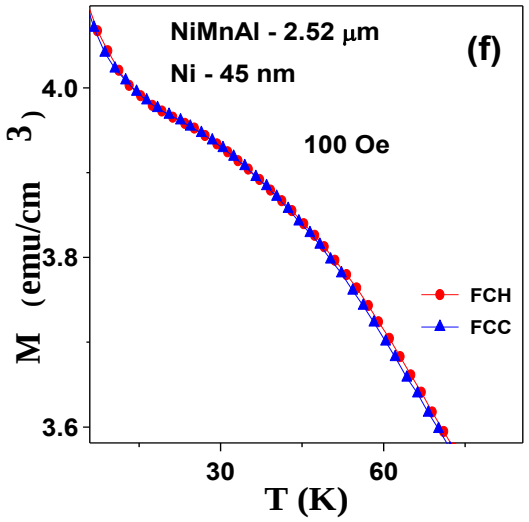
NiMnAl - 2.52 μm
Ni - 45 nm
(f)
100 Oe
FCH
FCC
M (emu/cm 3)
T (K)

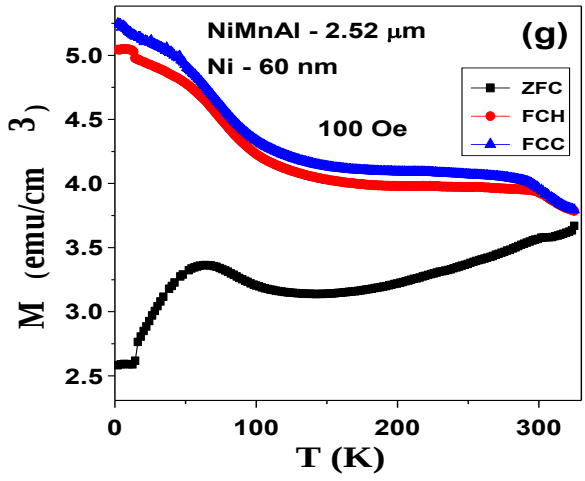
NiMnAl - 2.52 μm
Ni - 60 nm
(g)
100 Oe
ZFC
FCH
FCC
M (emu/cm 3)
T (K)

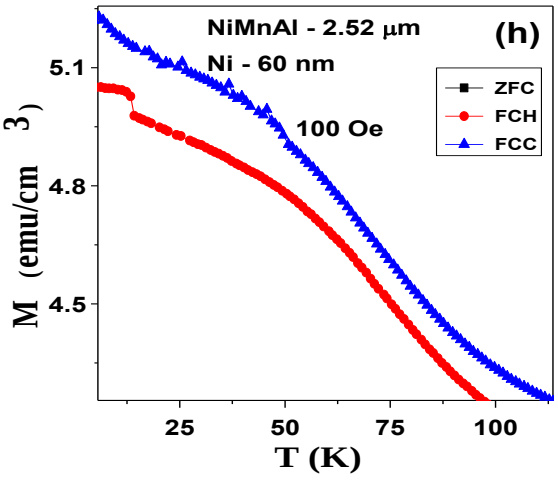
NiMnAl - 2.52 μm
Ni - 60 nm
(h)
100 Oe
ZFC
FCH
FCC
M (emu/cm 3)
T (K)

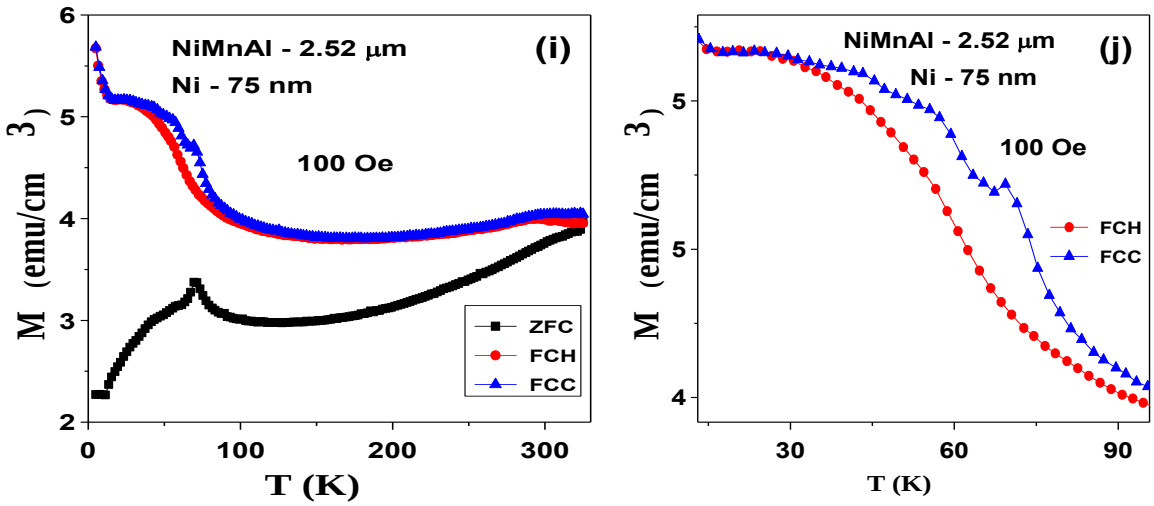

Figure 4.7 (a-f): *M-T* curves for NiMnAl films. The thickness of Ni layer and NiMnAl layer is mentioned in the figure.

As can be seen in the figure, Ni layer results in a similar behaviour of the *M-T* curves as were observed for Ni-Mn-Al sample without Ni layer. The NiMnAl / Ni samples also exhibit a decrease in moment with decreasing temperature similar to the films without Ni layer. The antiferromagnetic transition observed at ~ 300 K in the Ni-Mn-Al films is also observed in Ni-Mn-Al / Ni films. Thus the antiferromagnetic behaviour observed in Ni-Mn-Al films is not destroyed by the Ni layer. The bifurcation between the ZFC and FC curves increases drastically with Ni layer. The hysteresis observed at low temperature (~ 70 K) for NiMnAl film can not be seen for NiMnAl / Ni samples with 30 and 45 nm Ni later and the FCH and FCC curves superimpose till the lowest temperature. As the thickness of the Ni layer increase to 60 nm, the FCH and FCC curves start separating and at a thickness of 75 nm of Ni layer, a clear hysteresis can be seen in the *M-T* curve at low temperature. The separation between the ZFC and FCH curves also decreases with increasing thickness of the Ni layer. This shows that with increasing Ni layer thickness, the field induced ordering observed at low temperature is enhanced which may be associated to increase in magnetization of the sample with increasing Ni layer thickness. There exists a step like anomaly in the ZFC curves at low temperature which is a clear indication of exchange bias behaviour in the film. To understand the magnetic state of the sample, *M-H* loops have been measured at room temperature and at low temperature as shown in **Fig. 4.8**. **Figure 4.8 (a-d)** shows the *M-H* loops of the sample for Zero field cooled and different cooling fields for the 2.52 μm thick NiMnAl film with different Ni layer thickness.

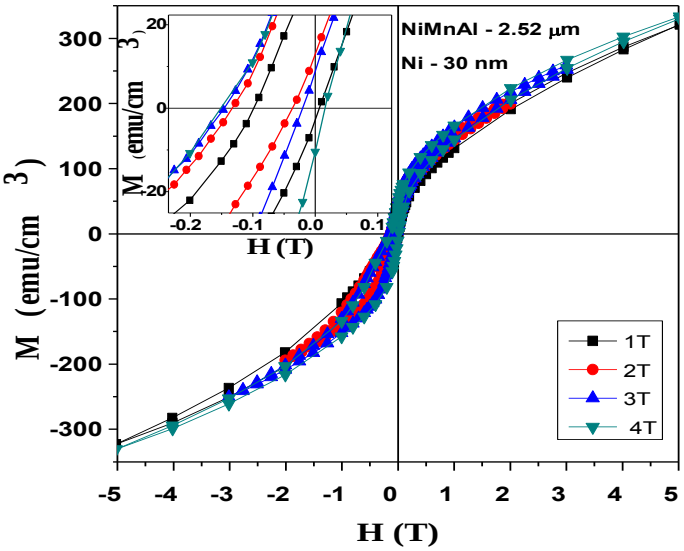

Figure 4.8(a): *M-H* loops of the sample with NiMnAl film thickness 2.52 μm and Ni layer thickness 30 nm for different cooling fields

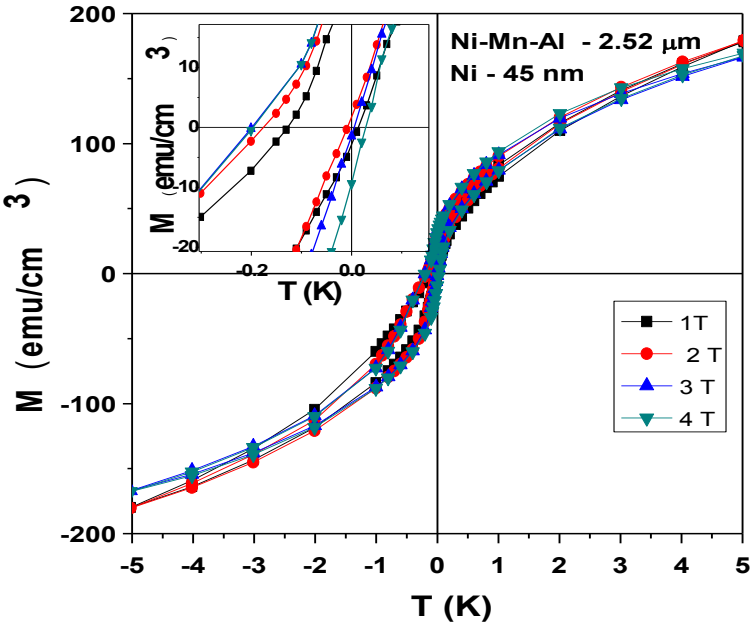

Figure 4.8 (b): M-H loops of the sample with NiMnAl film thickness 2.52 μm and Ni layer thickness 45 nm for different cooling fields

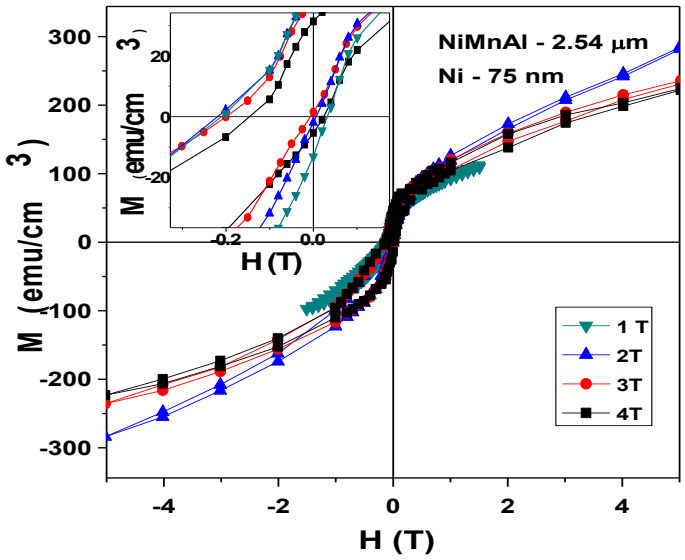

Figure 4.8(c): M-H loops of the sample with NiMnAl film thickness 2.52 µm and Ni layer thickness 60 nm for different cooling fields

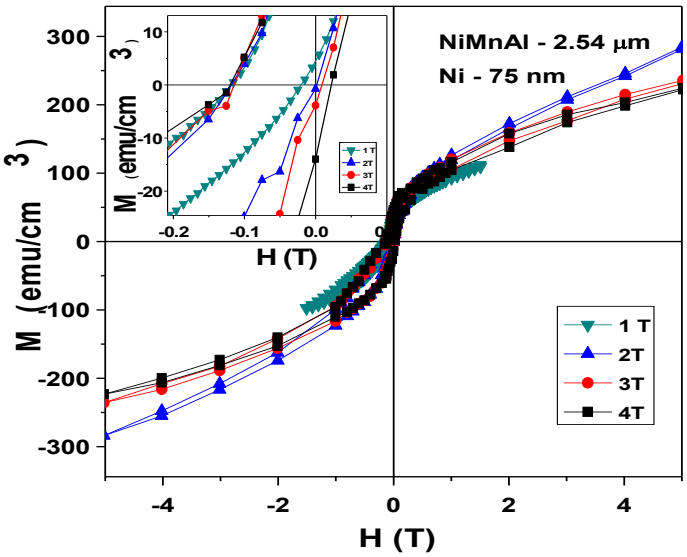

Figure 4.8 (d): M-H loops of the sample with NiMnAl film thickness 2.52 µm and Ni layer thickness 60 nm for different cooling fields

As for the sample with 1.009 µm thickness, in this case also exchange bias shows a non monotonic variation with increasing cooling field. Exchange bias first increases with increasing cooling field, reaches a maximum value at a certain cooling field (depending on the thickness of Ni layer) and then decreases with further increase in cooling field. The variation of H_{EB} and H_C with cooling field for different Ni layer thickness is shown in **Fig. 4.9 (a-d).**

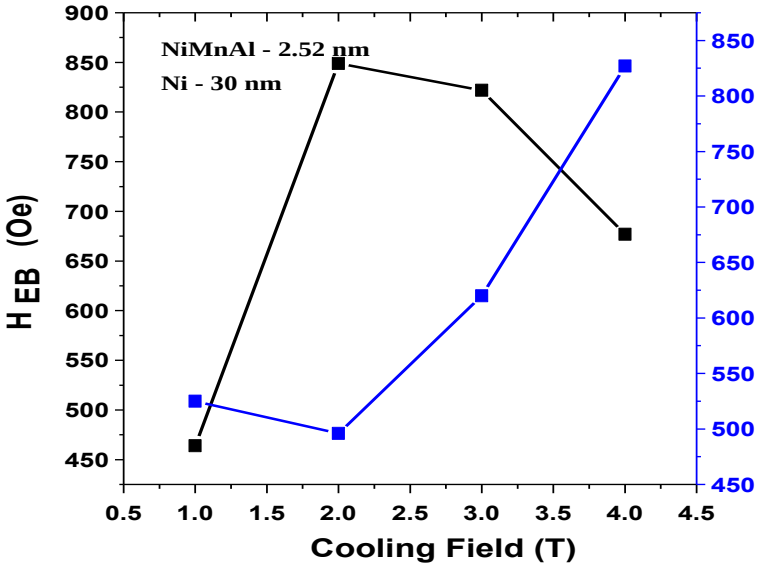

Figure 4.9(a): Variation of H_{EB} and H_C with cooling field for NiMnAl thickness of 2.52 nm and Ni layer thickness of 30 nm.

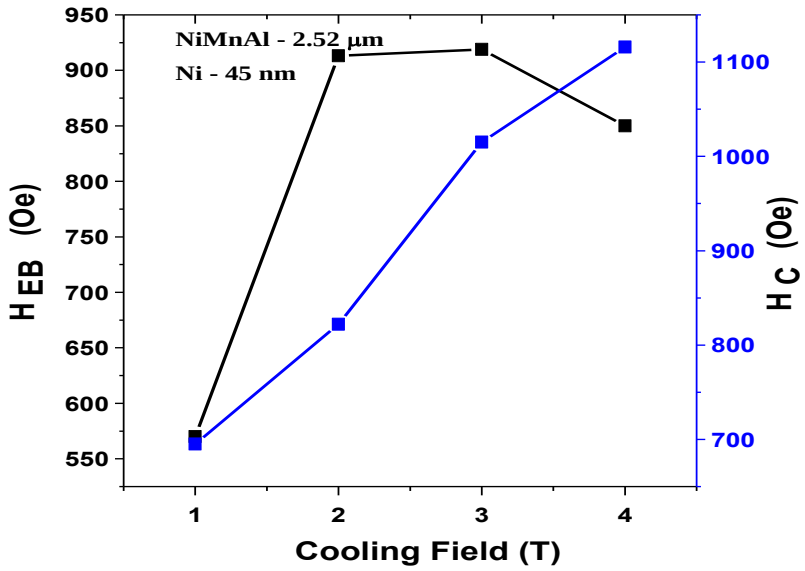

Figure 4.9(b): Variation of H_{EB} and H_C with cooling field for NiMnAl thickness of 2.52 nm and Ni layer thickness of 45 nm.

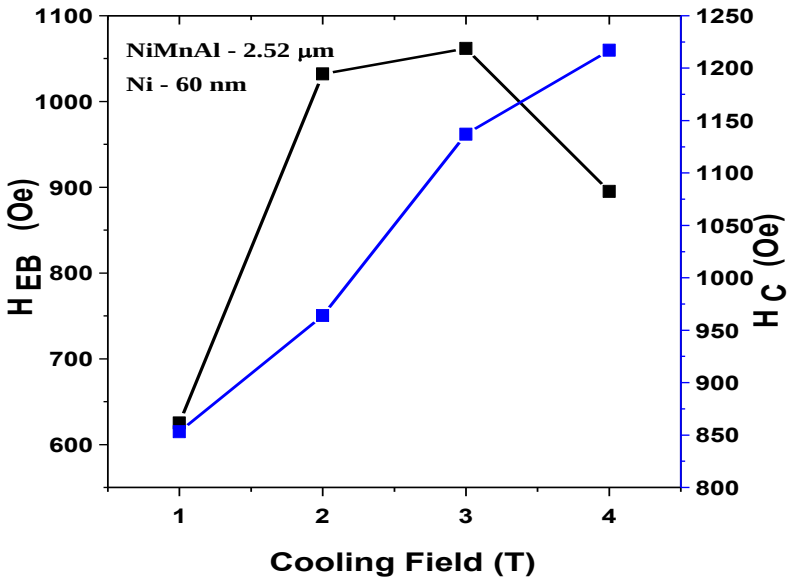

Figure 4.9(c): Variation of H_{EB} and H_C with cooling field for NiMnAl thickness of 2.52 nm and Ni layer thickness of 60 nm.

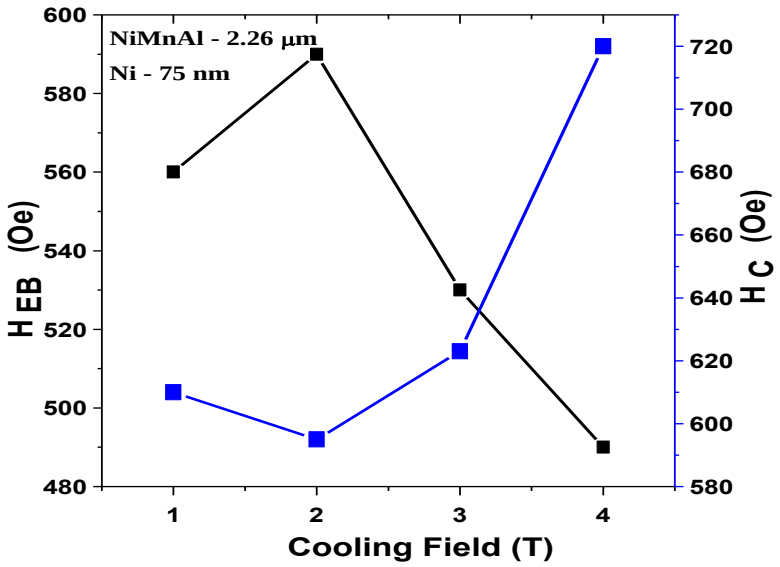

Figure 4.9 (d): Variation of H_{EB} and H_C with cooling field for NiMnAl thickness of 2.52 nm and Ni layer thickness of 75 nm.

As can be seen in **Fig. 4.9**, for NiMnAl layer of thickness 2.52 µm, maximum exchange bias of 1062 Oe at 10 K for 3 T cooling field has been obtained for the Ni layer with thickness

60 nm. It can be seen that for any Ni layer thickness, there is a marginal variation in the exchange bias obtained for 2 T and 3 T cooling fields. For Ni layer of thickness 30 nm and 75 nm, maximum exchange bias has been obtained for 2 T cooling fields while for Ni layer thickness of 45 and 60 nm, maximum exchange bias has been observed for 3 T cooling field. A comparison of maximum exchange bias obtained for different Ni layer thickens has been given in Figure 10. Maximum exchange bias obtained for pure NiMnAl film with thickness 2.54 μm without Ni layer has also been shown for reference to indicate the effect of Ni layer on NiMnAl film.

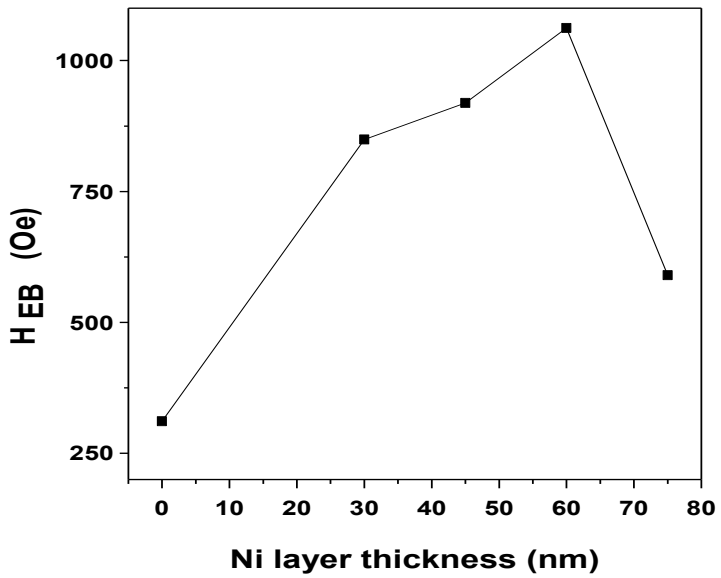

Figure 4.10: Variation of exchange bias for 2.52 μm thick NiMnAl layer with different thickness of Ni layer.

A comparison of exchange bias for different Ni layer thickness shows the magnitude of exchange bias field depends crucially on the thickness of Ni layer. For the NiMnAl film without Ni layer the exchange bias is 311 Oe which increases to 919 Oe for the NiMnAl film with 30 nm thick Ni layer. With further increase in Ni layer thickness, exchange bias reaches to 1062 Oe for 45 nm thick Ni layer and then decreases with further increase in Ni layer thickness. This behaviour of variation of exchange bias with varying ferromagnetic (Ni) layer thickness is in consistent with the previous reports on the exchange bias observed in FM / AFM bilayer [222]. In the present case the critical thickness of the FM layer (Ni) for 2.52 μm

thick AFM layer (NiMnAl) at which maximum exchange bias occurs is 45 nm. Beyond this thickness, exchange bias decrease with increasing FM layer thickness.

For 2.52 μm thick NiMnAl layer, maximum exchange bias has been obtained for the bilayer with Ni layer thickness 60 nm. To explore the behaviour of the sample further, *M-T* measurements have been performed for different cooling fields as shown in **Fig. 4.11(a-e)**.

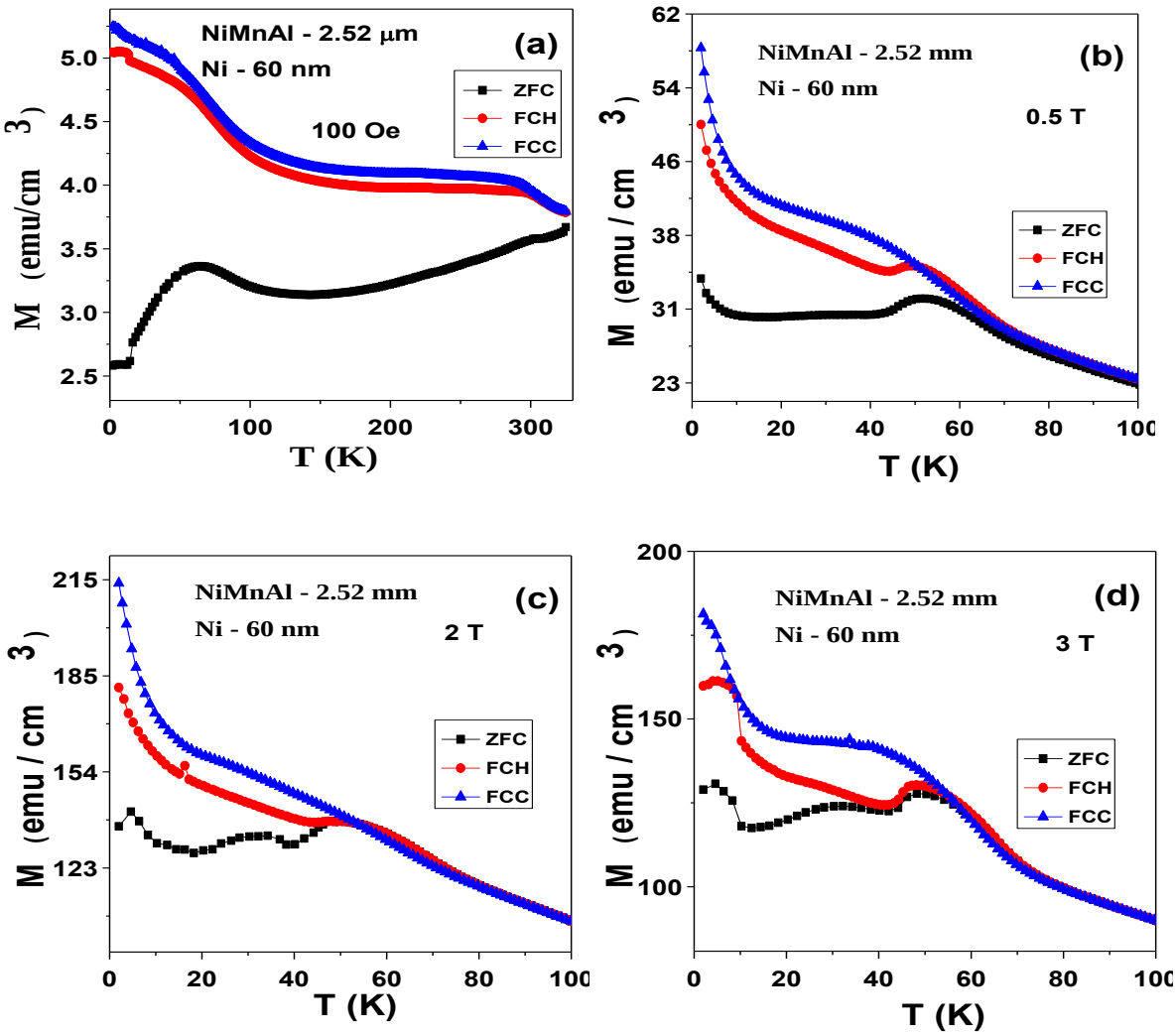

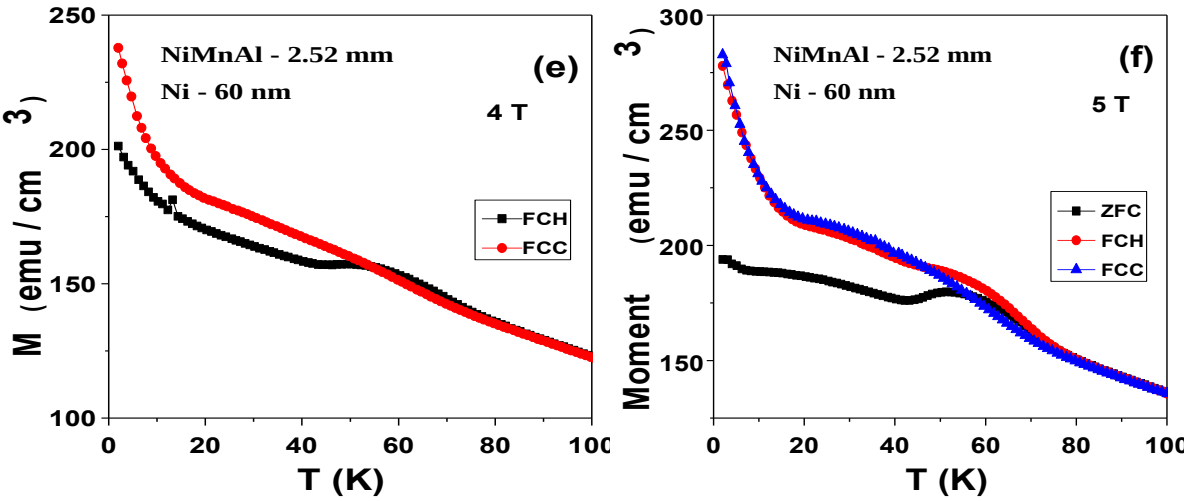

Figure 4.11 (a-f): *M-T* measurements have been performed for different cooling fields.

As can be seen in **Fig. 4.11 (a-f)**, as the cooling field increases from 0.5 T to 2 T, the difference in magnetization between the FCH and FCC curves increases in the low temperature range (below 45 K) while the overlap of the ZFC and FCH curves increases. With further increase in cooling field, the difference in magnetization between the FCH and FCC curves increases further and becomes maximum for 3 T cooling field, while the overlap of the ZFC and FCH curves is marginally effected. As the cooling field increases further to 4 T, the difference in magnetization between the FCH and FCC curves start decreasing and at 5 T cooling field FCH and FCC curves almost overlap each other. The ZFC and FCH curves remain bifurcated below 45 K. Thus maximum exchange bias occurs when the difference in magnetization between the FCH and FCC curves is maximum.

The bifurcation between ZFC and FCH curves is not removed by increasing cooling field unlike the pure sample without Ni layer where bifurcation between ZFC and FCH curves almost vanishes by increasing cooling. The occurrence of hysteresis below 45 K between the FCH and FCC curves shows first order transition and sudden increase in magnetization below 60 K shows second order transition. The effect of Ni layer reflects itself by restricting the field induced transition. The occurrence of second order transition becomes clearly prominent for an Ni layer of thickness 75 nm. This transition as can be seen in **Fig. 4.11 (f)** occurs below 80 K.

Temperature dependence of hysteresis curves has been studied to further explore the exchange bias phenomenon occurring in the film. **Fig. 4.12 (a-b)** shows the effect of variation

in temperature on maximum exchange bias observed in the sample with NiMnAl thickness 2.54 μm and Ni layer thickness 60 nm.

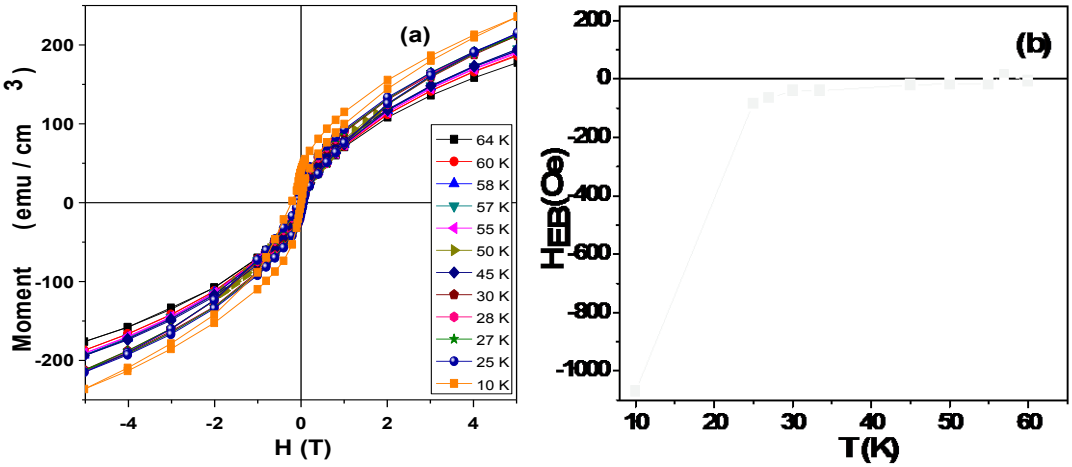

Figure 4.12: **(a)** *M-H* curves at different temperatures and **(b)** Variation of exchange bias with temperature.

Variation of exchange bias with temperature shows that the exchange bias decreases with increasing temperature. As the temperature increases form 10 K to 25 K, exchange bias decreases substantially from 1069 Oe to 84 Oe. With further rise in temperature exchange bias decreases gradually and almost disappears at 60 K. It is worth to note that there is a small positive exchange bias of 15 Oe observed for bilayer which shows that the exchange bias originating in the sample can be related to the spin glass / FM bilayer system wherein there occurs a small positive exchange bias in a narrow temperature range below the spin glass transition temperature. In the present case as evident from M-T measurements, the spin glass transition occurs ~ 60 K. The appearance of small positive exchanger bias shows that the system is similar to a spin glass / FM bilayer. To explore the spin glass behaviour of the sample, memory effect measurements have been carried out which are considered to be the unequivocal signature of spin glass. The sample was first ZFC from 300 K to 2 K and then the magnetization was recorded during heating in an applied field of 50 Oe. This curve was considered as a reference curve. The sample was again ZFC from room temperature but now with a stop-and-wait protocol to T_{wait} =25K ($<T_g$), where the sample is aged for three hours duration, and then again cooled down to 2K after which the magnetization was recorded as done in the reference curve, this curve is referred to as wait curve. The dip in the difference ΔM between the reference and the wait curve as shown in Fig. 13 indicates the memory effect which is considered as the unequivocal signature of a SG state [229].

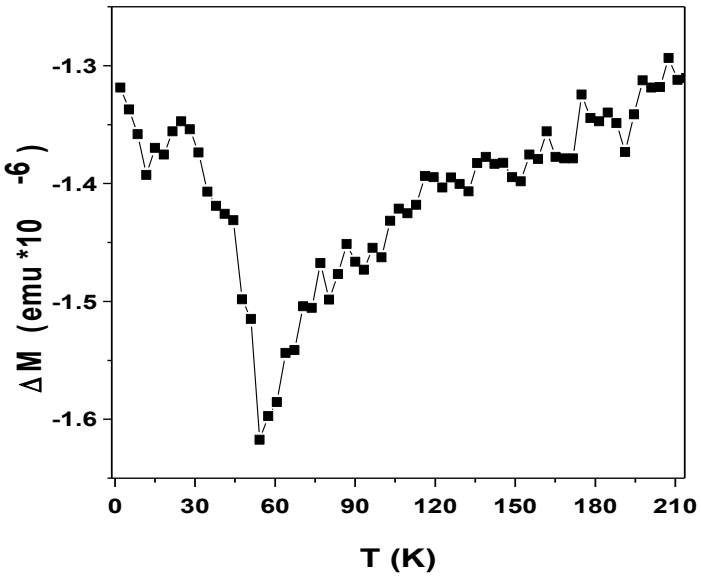

Figure 4.13: *ΔM* versus Temperature.

4.3.2.3 NiMnAl layer thickness of 4 µm and different thickness of Ni layer

For the NiMnAl film of thickness 4 µm, the Ni layer deposited is for 30 nm and 60 nm. For Ni layer thickness beyond 60 nm, film peel off from the substrate. In this regard in the 4 µm thick NiMnAl layer, the properties of the bilayer with Ni thickness 30 nm and 60 nm have been discussed, The magnetic and structural transition temperatures of Mn rich Ni-Mn-Al films with Ni layer have been determined from the magnetization measurement at H = 100 Oe. **Fig. 4.14(a-d)** shows the dc susceptibility for the films in the temperature range of 2 K ≤ T ≤ 325K in zero-field-cooled heating (ZFCH), field-cooled heating (FCH) and field-cooled cooling (FCC) sequences for the sample with thickness 4 µm. **Fig. 4.14(a-d)** shows the *M*-*T* curves for the Ni-Mn-Al sample with different Ni layer and without Ni layer.

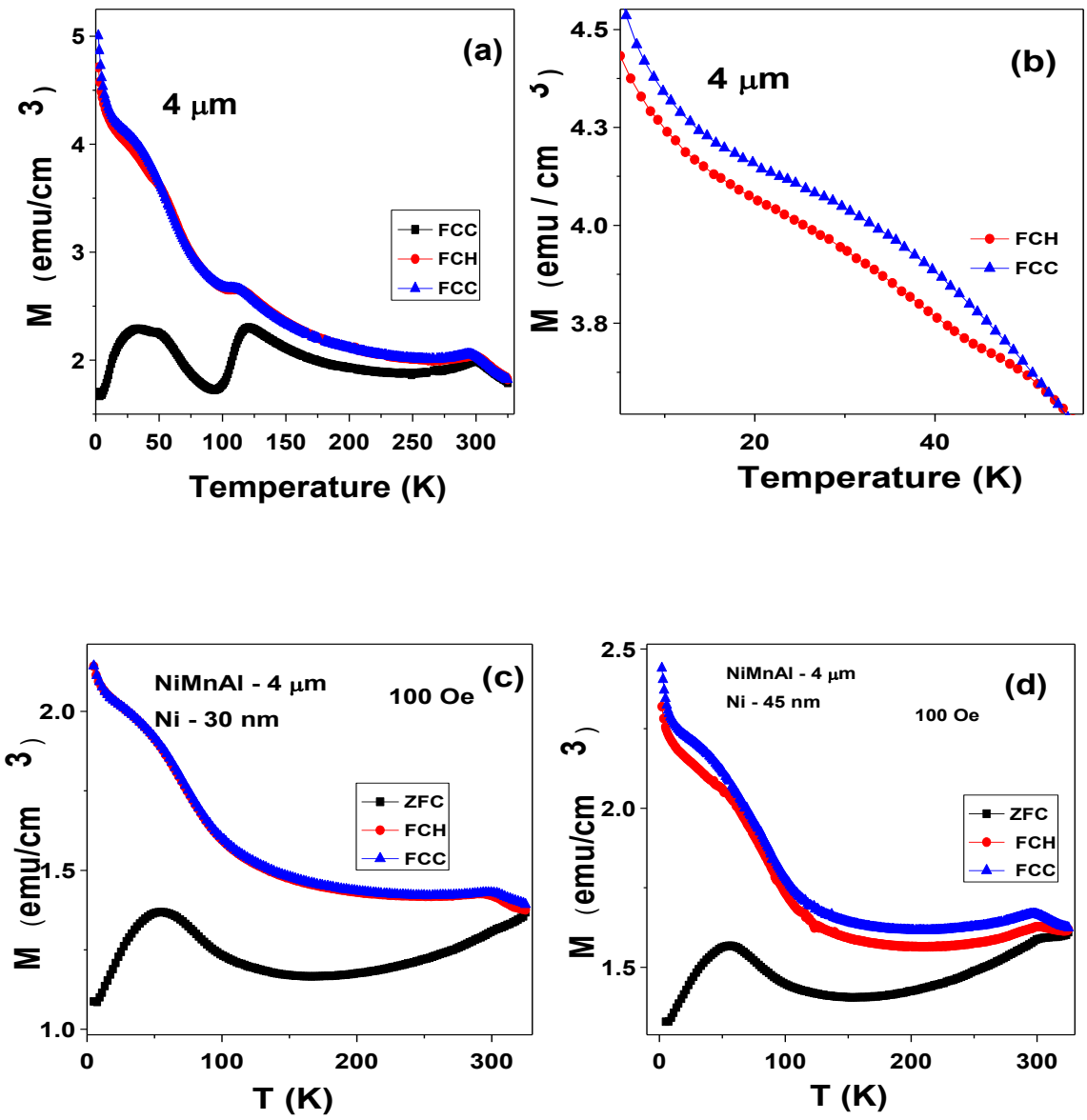

Figure 4.14(a-d): *dc* susceptibility for the film at 100 Oe (a,b) without Ni layer (c) with 30 nm Ni layer and (d) 45 nm Ni layer.

As can be seen in the figure, Ni layer results in a different behaviour of the *M-T* curves as compare to the Ni-Mn-Al sample without Ni layer. The peak observed at ~ 120 K in the sample without Ni layer cannot be observed in the NiMnAl / Ni bilayer. As mentioned in chapter 3, the disappearance of peak has been observed in the sample without Ni layer by increasing the cooling field. Thus the effect of Ni layer may be the same as that by increasing the cooling field that is the Ni layer induces the same effect as induced by increasing the magnetic field. Thus the occurrence of ferromagnetic ordering in the sample ordering may cause the observed behaviour at ~ 120 K. The antiferromagnetic transition observed at ~ 300 K in the Ni-Mn-Al films is also absent in Ni-Mn-Al / Ni films. Thus the antiferromagnetic

behaviour observed in Ni-Mn-Al films without Ni layer can still be seen in the bilayer film which is also similar to the effect of cooling filed on Ni-Mn-Al films without Ni layer. There exists a step like anomaly in the ZFC curves at low temperature which is a clear indication of exchange bias behaviour in the film. To understand the magnetic state of the sample, **Fig. 4.15(a-b)** shows the *M-H* loops of the sample for Zero field cooled and different cooling fields for the 4 µm thick NiMnAl film with different Ni layer thickness.

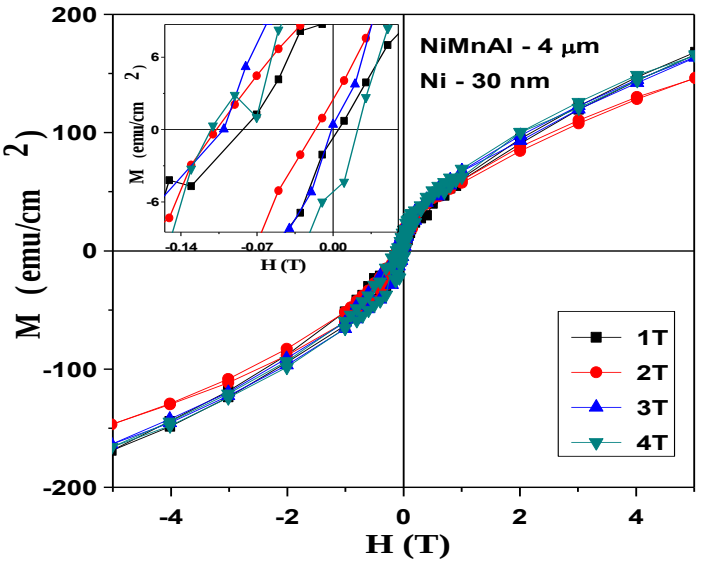

Figure 4.15(a): *M-H* loops of the sample with NiMnAl film thickness 4 µm and Ni layer thickness 30 nm for different cooling fields

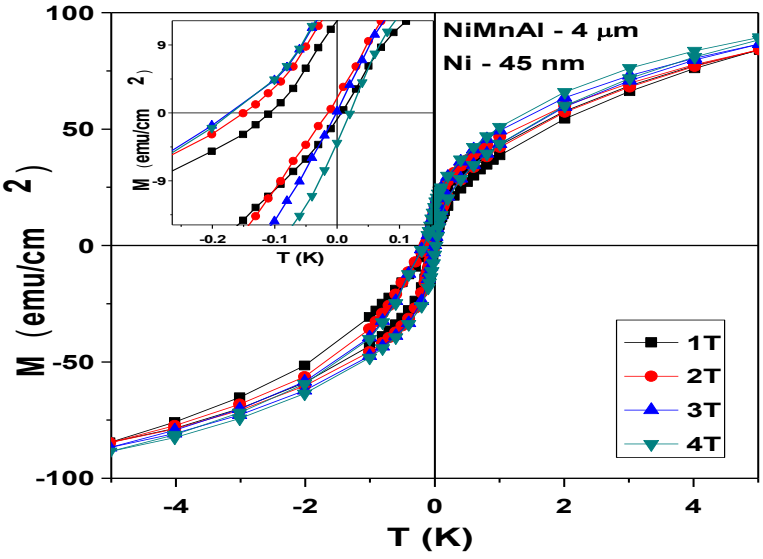

Figure 4.15(b): *M-H* loops of the sample with NiMnAl film thickness 4 µm and Ni layer thickness 45 nm for different cooling fields

As can be seen in the *M-H* curves, for each thickness of the Ni layer, exchange bias shows a non monotonic variation with increasing cooling field. Exchange bias first increases with increasing cooling field, reaches a maximum value at a certain cooling field (depending on the thickness of Ni layer) and then decreases with further increase in cooling field. The variation of H_{EB} and H_C with cooling field for different Ni layer thickness is shown in **Fig. 4.16**.

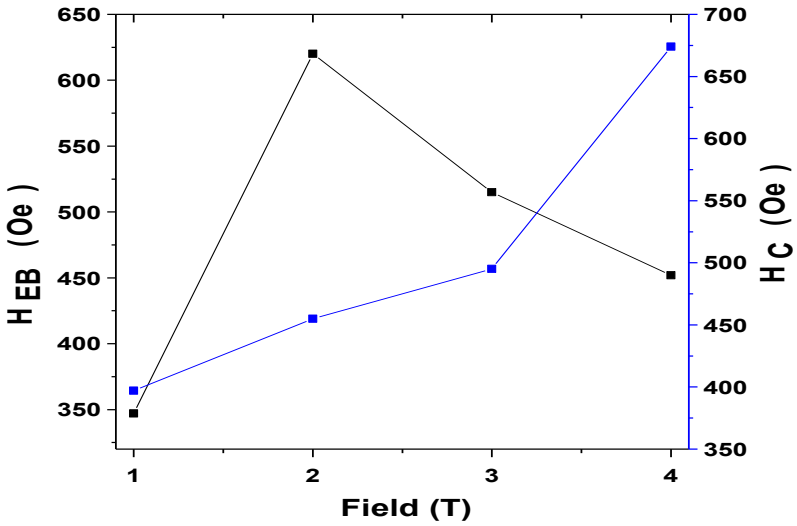

Figure 4.16(a): Variation of H_{EB} and H_C with cooling field for NiMnAl thickness of 2.52 nm and Ni layer thickness of 30 nm.

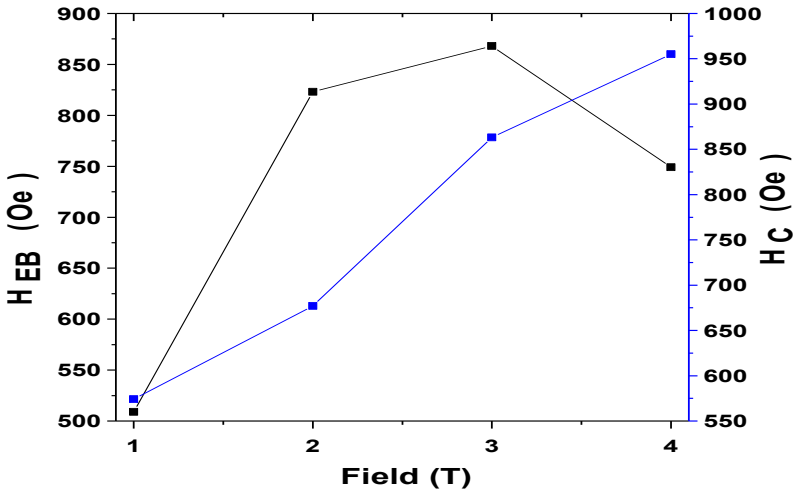

Figure 4.16(b): Variation of H_{EB} and H_C with cooling field for NiMnAl thickness of 4 nm and Ni layer thickness of 45 nm.

As can be seen in Fig. 16, for NiMnAl layer of thickness 4 μm, maximum exchange bias of 868 Oe at 10 K for 3 T cooling field has been obtained for the Ni layer with thickness 45 nm. A comparison of maximum exchange bias obtained for different Ni layer thickens shows that among 30 nm and 45 nm, larger exchange bias have been obtained for 60 nm Ni layer. However, this value of exchange bias obtained is lower than the maximum exchange bias obtained in NiMnAl 4 μm thick sample without Ni layer as shown in **Fig. 4.17**.

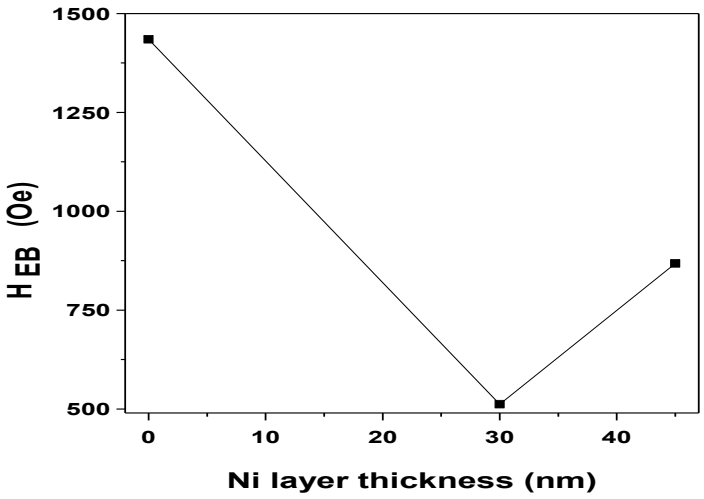

Figure 4.17: Variation of exchange bias for 4 μm thick NiMnAl layer with different thickness of Ni layer.

A close analysis of the 1 μm, 2.54 μm and 4 μm NiMnAl films with different Ni layer suggests that Ni layer results in an increase in exchange bias for the 1.009 μm, 2.54 μm and the thickness of the Ni layer at which maximum exchange bias has been obtained increases with increases with increasing thickness of the Ni layer. For 1 μm film, maximum exchange bias has been obtained for 30 nm Ni layer, for 2.54 μm NiMnAl film, maximum exchange bias has been obtained for 60 nm thick Ni layer. It has to be noted that for 4 μm thick Ni layer, the exchange bias first decreases with 30 nm Ni layer but shows an increasing trend with further increase in Ni layer to 45 nm. If this is looked upon on the same lines as the trend followed exchange bias exhibited by 1 μm and 2.54 μm for different Ni layer, it may be concluded that exchange bias should increase with increasing the Ni layer further. However, since the sample peel off from the substrate with further increase in Ni layer, we express our limitation to explore the Ni layer effect further on 4 μm thick NiMnAl thin film.

4.4. Results and discussion for Ni rich Ni-Mn-Al thin films

4.4.1 Crystal Structure

Since the deposition of Ni layer is followed by the deposition of thin layer of Pt to avoid oxidation of the Ni layer, the XRD patterns of the films with Ni layer cannot be shown. However to have an estimate of the structure of the Ni layer deposited on the films, Si substrate were kept along with the films in the sputtering chamber. The Ni layer deposited on the Ni-Mn-Al samples also deposited on the Si substrate. It can be clearly seen that the peaks obtained in the diffraction patter correspond to Ni. For small thickness of Ni layer, peak corresponding to Si (100) substrate can also be seen. Cross-sectional FE-SEM of the substrate shows that the thickness of Ni layer deposited for 1 min is 30 nm. The thickness of the Ni film varies monotonically with increasing deposition time.

4.4.2 Magnetic Properties

For the Ni rich NiMnAl samples with different Ni layer, the *M-H* loops have been taken for NiMnAl films with different Ni layer. **Figure 4.18(a-c)** shows the hysteresis curves.

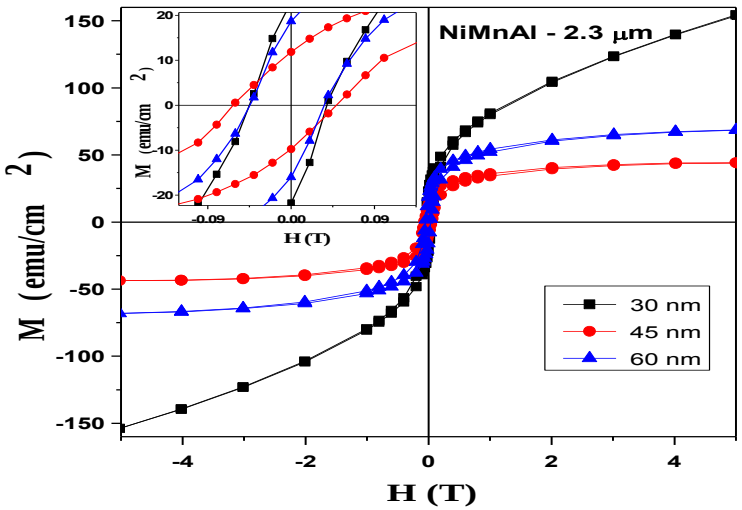

Figure 4.18 (a): *M-H* curves at 10 K and 5 T cooling field for 2.3 µm thick NiMnAl film and different Ni layers

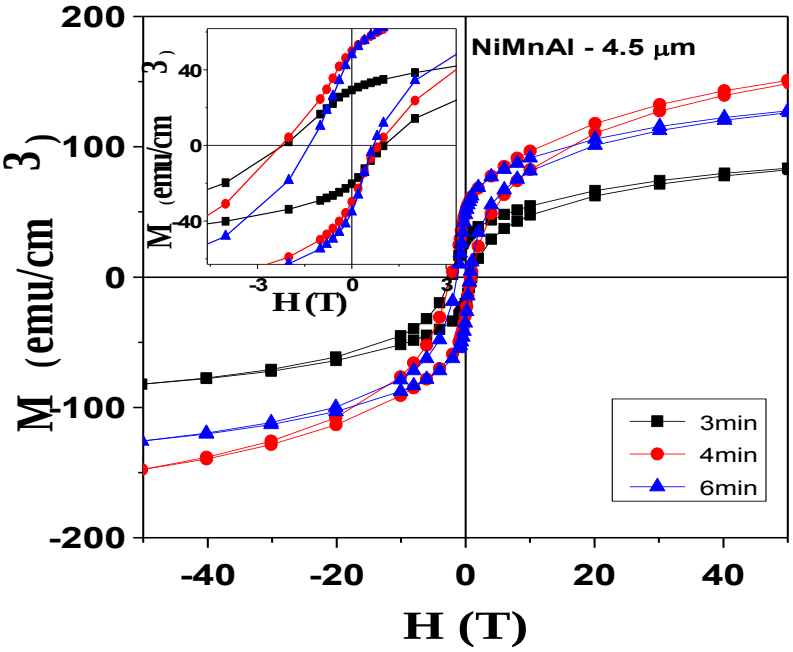

Figure 4.18 (b): *M-H* curves at 10 K and 5 T cooling field for 4.5 μm thick NiMnAl film and different Ni layers.

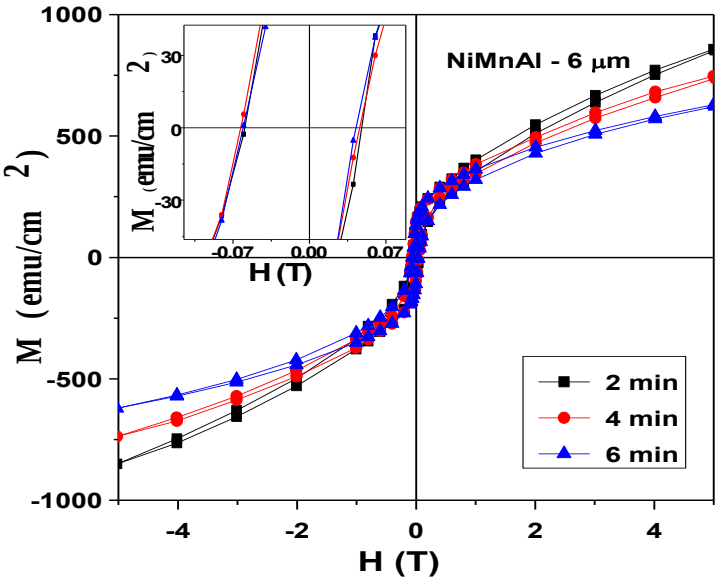

Figure 4.18 (c): *M-H* curves at 10 K and 5 T cooling field for 6 μm thick NiMnAl film and different Ni layers

H_{EB} has been calculated for the samples with different Ni layers. The variation of exchange bias for the samples with different Ni layer has been shown in **Fig. 4.19**. Data for the film without Ni layer has also been given for reference.

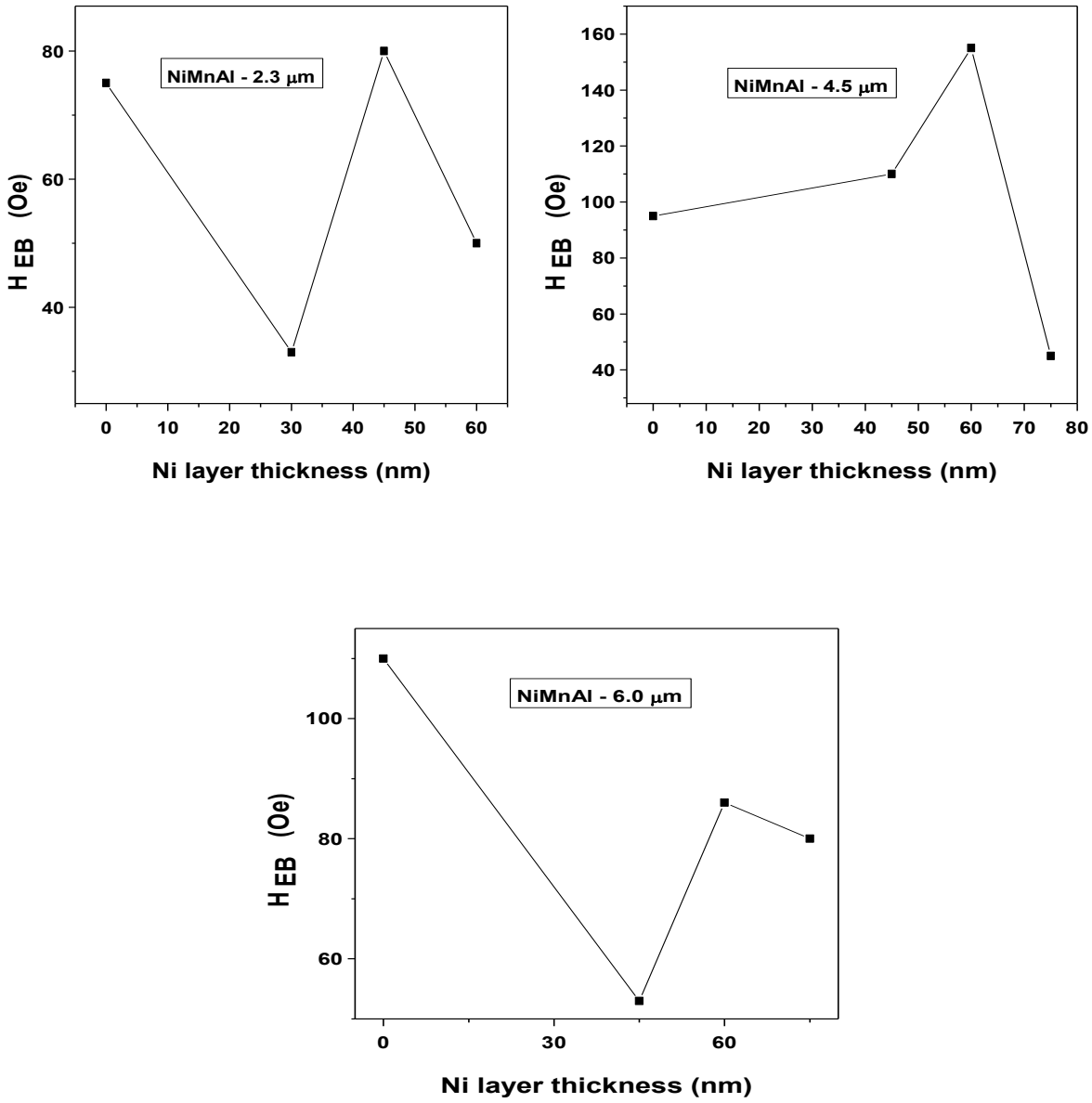

Figure 4.19: Variation of exchange bias with Ni layer.

It can be seen that for different thickness of the Ni layer on NiMnAl film, maximum exchange bias has been observed for Ni layer of thickness 60 nm. For the film with thickness 2.3 μm and 4.5 μm, exchange bias increases with increasing thickness however for the film with thickness 6 μm, exchange bias decreases with Ni layer. Thus for different thickness of NiMnAl layer, maximum exchange bias is independent of the thickness variation and

maximum exchange bias occurs for 60 nm thick Ni layer. This is contrary to the exchange bias behaviour with Ni layer observed for Mn rich NiMnAl samples where exchange bias depends crucially on the thickness of the Ni layer. Maximum exchange bias has been observed for the film with NiMnAl thickness 4.5 µm with Ni layer thickness 60 nm. Temperature dependence of exchange bias has been carried out for this sample to further explore the exchange bias behaviour.

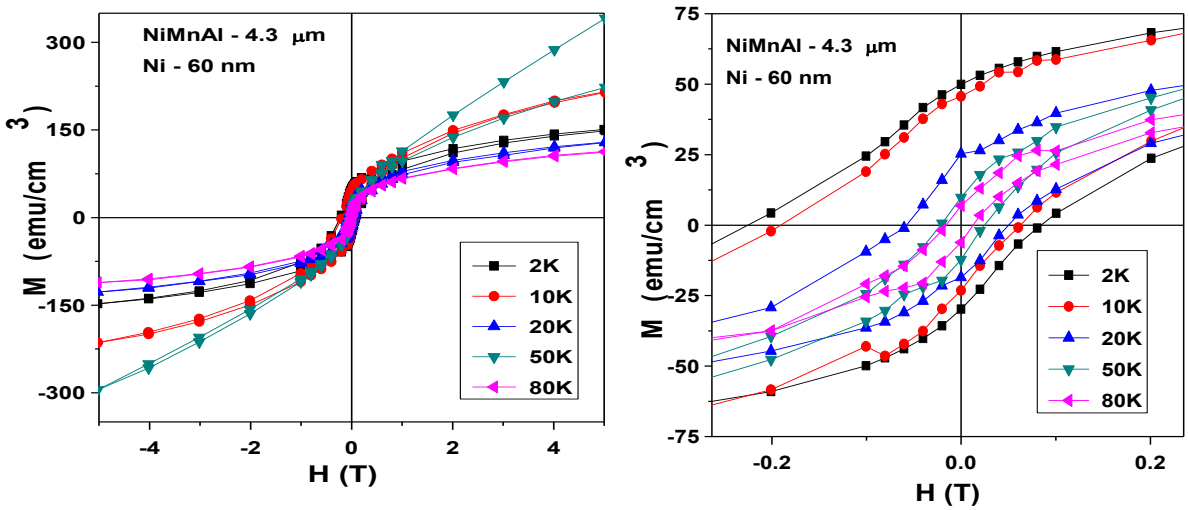

Figure 4.20: Temperature variation of exchange bias for 4.3 µm thick NiMnAl and 60 nm thick Ni layer.

The exchange bias field decreases with increasing temperature, maximum exchange bias of 718 Oe has been observed at 2 K. With further increase in temperature, at 5 K 644 Oe exchange bias has been observed. With further increase in temperature at ~ 10 K, exchange bias falls marginally to 155 Oe. To further look into the behaviour of exchange bias, exchange bias field versus temperature are plotted in **Fig. 4.21**.

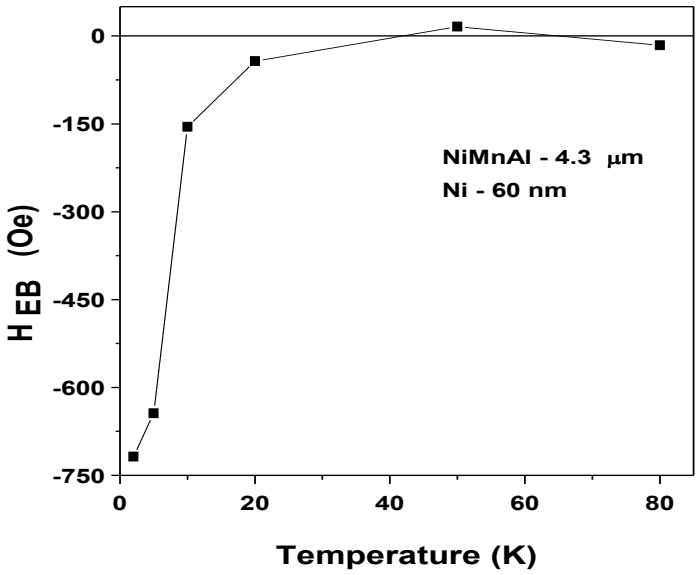

Figure 4.21: Variation of exchange bias with temperature.

Variation of exchange bias with temperature shows that the exchange bias decreases with increasing temperature. As the temperature increases form 10 K to 25 K, exchange bias decreases substantially from 730 Oe to 65 Oe. With further rise in temperature exchange bias decreases. Similar to the above case, it is worth to note that there is a small positive exchange bias of 15 Oe observed for bilayer at ~ 50 K which shows that the exchange bias originating in the sample can be related to the spin glass / FM bilayer system wherein there occurs a small positive exchange bias in a narrow temperature range below the spin glass transition temperature. In the present case as evident from M-T measurements, the spin glass transition occurs ~ 50 K. The appearance of small positive exchanger bias shows that the system is similar to a spin glass / FM bilayer.

4.5 Conclusion

The effect of Ni layer on Mn rich Ni-Mn-Al and Ni rich Ni-Mn-Al has been studied in detail. For the Mn rich films, Ni layer results in an increase exchange bias field as compare to the film without Ni layer. The thickness of the Ni layer at which maximum exchange bias has been obtained depends crutially on the thickness of Ni-Mn-Al layer. The thickness of Ni layer at which maximum exchange bias has been obtained increase with increasing thickness of Ni-Mn-Al films. This thickness increases with increasing thickness of Ni-Mn-Al film.

For Ni rich NiMnAl / Ni lsystem, the increase in exchange bias is very marginal. For the bilayer with NiMnAl film with thickness 2.3 μm and 4 μm, a marginal increase in exchange bias can be seen, however, for the bilayer with NiMnAl film with thickness 6 μm, exchange bias decreases with Ni layer.

CHAPTER 5

INVESTIGATIONS ON Ni-Mn-Al-In THIN FILMS

5.1 Introduction

Off-stoichiometric Ni-Mn-In ferromagnetic shape memory alloys have become the focus of intensive research due to the observation of magnetic field-induced reverse martensitic transformation [230]. The magnetization in martensite phase of these alloys is significantly smaller than in the austenite one. Transformation from the high-temperature austenite to the low-temperature martensite phase with greatly reduced magnetization in Ni-Mn-In alloys gives rise to a number of interesting effects such as inverse magnetocaloric effect, giant strain due to field-induced reverse martensitic transformation, and giant magnetoresistivity. These make Ni-Mn-In alloys good candidates for multifunctional application. The magnetic properties of Ni-Mn-In alloys have been reported by some researchers.

NiMnIn exhibits vide scale applications owing to their T_C around room temperature. For the $Ni_{0.50}Mn_{0.50-x}In_x$ composition, T_C depends crucially on x [101]: for x = 0.165, T_C is ~ 310 K which changes to 300 K for x = 0.17; this again changes to 310 K for x = 0.20 and reduces to 290 K for x = 0.25. This shows that depending on the application, the composition may be varied to obtain desired T_C. It has been observed that in thin films, T_C has been observed to be ~ 334 K. The uncommon magnetic properties occurring upon martensitic transformation are originated from the change of Mn-Mn interatomic distances. The critical value of Mn-Mn interatomic distance corresponding to the change of magnetic interactions has been determined. A decrease of the intensity of Ni *3d* states at the Fermi level upon martensitic transformation has been observed for x = 0.5. Moreover, the Ni *3d* - Mn *3*d hybridization plays an important role in establishing the magnetic properties and driving the martensitic transformation [230].

Normally, from the experimental evidence, the Mn-rich and the In-deficient Ni-Mn-In alloys are the usual composition designs, due to the fact that they have appropriate martensitic transformation temperatures and Curie temperatures for practical applications and the magnetic

field drivable inverse martensitic transition. The Mn-rich, In-deficient composition generates a lot of Mn antisties on the In sublattice (MnIn) defects as the MnIn defect has relatively low formation energy. For the off-stoichiometric compositions, the excess atoms of the rich component would occupy the site(s) of the deficient one(s), which is called “normal” site occupancy. The formation energies of the In antisite at the Ni sublattice (InNi) are extremely high whereas those of the In antisite at the X sublattice (InX) are energetically favorable in the serie. The point defect of In antisite at the Ni site can be formed in two ways (direct and indirect) in In-rich Ni deficient Ni-Mn-In alloy. The direct way is that the excess In atoms directly occupy the sublattice of the deficient Ni sites. However, the formation energy of such InNi defect is quite high. The indirect way is that the excess In atoms occupy the X sites (InX) and the X atoms have to move to the free nearby Ni sites (XNi), so that the final result should be the defect pair (InX + XNi). From the energy point of view, the latter path is more favorable. It has been shown by ab-initio calculation, as the total energy of the direct path for each atom is -5.88 eV whereas that of the indirect one is -5.90 eV. Therefore, the so called “indirect” site occupation is more common in the In-rich Ni-deficient alloys than the direct one.

The In atom only carries a small magnetic moment, the variation range of Ni moments is much larger than that of Mn when introducing an antisite defect into an ideal crystal. Therefore, we mainly focus on the change of Ni moments. In stoichiometric Ni_2MnIn, the magnetic moments of Ni and Mn are 0.33μB and 3.67μB, respectively. When a Ni atom occupies an In site, namely creates a Ni antisite at the In sublattice, NiIn, the magnetic moments of eight normal-Ni atoms range within 0.38~0.41 μB. The change rates of Ni atoms are from +15 to +24 % compared with that of the Ni moment in the stoichiometric alloy. The extra-Ni carries a smaller magnetic moment of 0.28μB, and the corresponding change rate is -15%. After the relaxation, the optimized volume of the unit cell with a NiIn antisite defect becomes smaller (211.90Å3) by about 3.62% as compared with the stoichiometric structure (219.85Å3). The atomic positions have changed as well: the normal-Ni atoms have moved towards the center of the unit cell (extra-Ni), resulting in the reduction of the unit cell volume. From the calculation results, when a In is replaced by Ni atom, the distance between the normal-Ni and its nearest Mn neighbor is 2.55Å, instead of 2.61Å in the ideal structure. The distance becomes smaller, thus enhances the interaction between the 3d electrons of Ni and Mn, which increases the magnetic moments of the normal-Ni atoms. On the contrary, the distance between extra-Ni and its nearest Mn neighbor is 2.98Å, much larger than 2.61Å, resulting in the weakened interaction of 3d electrons between extra-Ni and Mn. This is the

origin of the sharp decrease of the extra-Ni moment. In the situation of InNi, an In antisite on Ni site, the Ni moments range in the interval 0.26 ~ 0.33 μ_B, they are smaller than the stoichiometric one, and the corresponding change rate is within the range -21 ~ 0 %. In the depleted Ni alloy, the distance between the Ni atoms and their first Mn neighbor atoms increases from 2.61 to 2.63Å, resulting in the weakened interaction between the 3d electrons of Ni and Mn, therefore the decreased Ni moments. It can be concluded that in Ni-Mn-In ferromagnetic shape memory alloy, the value of the Ni magnetic moment sensitively depends on the distance between Ni and Mn. The smaller the distance is, the larger the Ni magnetic moment will be. The most interesting phenomenon is that in the cases of Mn rich antisite defects MnNi and MnIn, the moments of the extra Mn atoms are totally different. The extra Mn moment in the MnNi defect is 0.98 μ_B, whereas that in the MnIn defect is 3.62 μ_B. When the extra Mn occupies a Ni site, most of the free electrons gather around the extra Mn. But when the extra Mn occupies an In position, the charges are regularly distributed between Ni and Mn atoms [231-239].

A comparison of NiMnAl and NiMnIn shows that the size of Al atom is much smaller than In atom. In NiMnAl, the alloy is mostly antiferromagnetic at and around room temperature, however, in case of NiMnIn, the alloy is mostly obtained in ferromagnetic phase. A comparison of antiferromagnetic transition temperature (T_N) of NiMnAl and ferromagnetic transition temperature (T_C) of NiMnIn in thin film form shows that $T_N < T_C$ which is the primary requisite for exchange bias. This shows that a combination of NiMnAl and NiMnIn may be expected to serve the condition for exchange bias phenomenon.

In the present work, thin films of NiMnAlIn have been deposited with varying thickness and composition. It has been observed that exchange bias depends crucially on the In concentration in the film. Maximum exchange bias has been obtained 1050 Oe for the film with thickness 1.5 µm.

5.2 Experiment

NiMnAlIn have been deposited by cosputtering using the targets of NiMnAl, In and Mn. The NiMnAl pre synthesized target has been used for the deposition. The X-Ray diffraction pattern of the NiMnAl target shows that the target exhibits a B2 structure at room temperature as shown in **Fig. 5.1**.

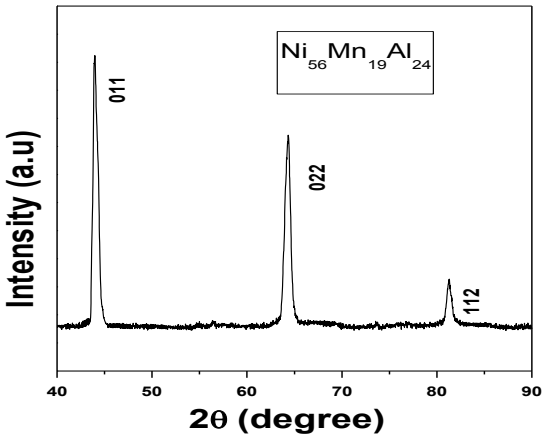

Figure 5.1: XRD of the NiMnAl target.

It has been observed that Mn rich compositions are expected to exhibit high T_C [101]. In the present case, the composition of the film obtained from NiMnAl target is $Ni_{56}Mn_{20}Al_{24}$. The composition obtained in deficient in Mn and is a Ni rich composition. For the exchange bias phenomenon, T_C of the FM part should be higher than T_N of the antiferromagnetic phase. To attain this, Mn target is also sputtered along with NiMnAl and In targets. The optimized deposition parameters are –

Sample	**NiMnAlIn**		
Substrate	**Si (100)**		
Substrate temperature	**150^0C**		
Substrate-target distance	**5 cm**		
Base pressure	**3.0×10^{-6}Torr**		
Working pressure	**5 mTorr**		
Sputtering gas	**Ar**		
Target	**Ni**	**Mn**	**In**
Sputtering power	**55**	**10**	**25**

Table 5.1: Deposition parameters for the film.

5.3. Results and discussion on Ni-Mn-Al-In thin films

5.3.1 EDAX Measurements

The elemental composition analysis of Ni-Mn-Al-In thin films has been carried out using energy dispersive X-ray analysis. The average elemental composition of the films is found to be $Ni_{57}Mn_{24}Al_{19}$. The EDAX patterns of the Ni-Mn-Al target and In target has been shown in **Fig. 5.2** and **Fig. 5.3**.

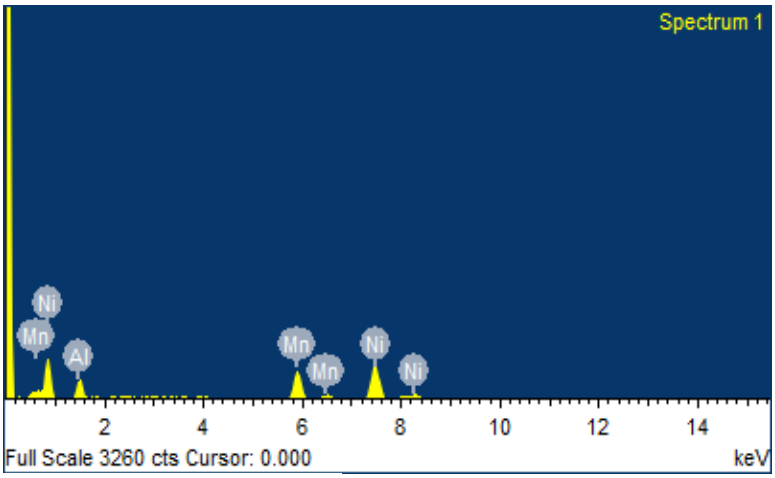

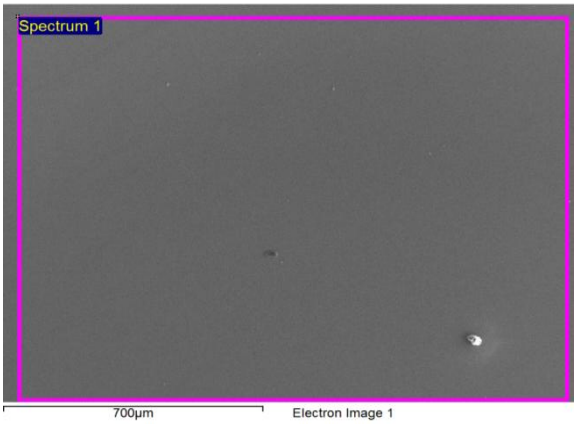

Element	Weight	Atomic%
Al K	14.05	24.13
Mn K	24.45	19.94
Ni K	61.50	56.03
Totals	100.00	

Figure 5.2: EDAX pattern of NiMnAl film synthesized from target

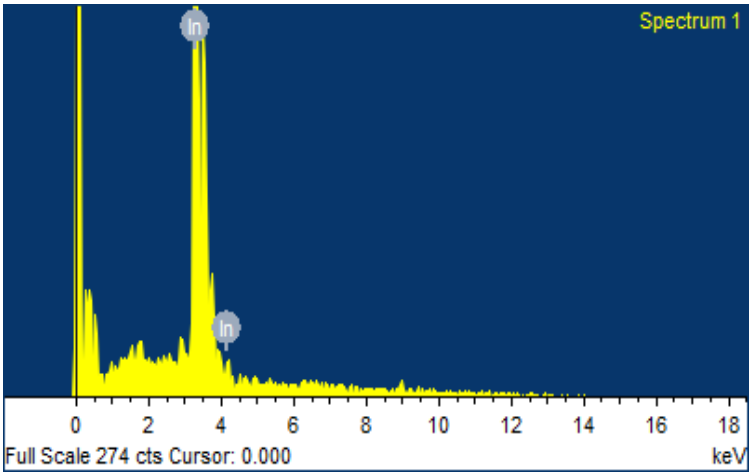

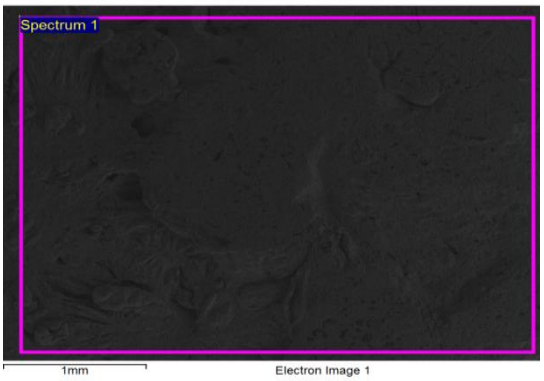

Element	Weight%	Atomic%
In L	100.00	100.00
Totals	100.00	

Figure 5.3 The EDAX pattern of the In target

The sputtering of In target needs to be carefully carried out as In has a low vapour pressure and cannot withstand high temperature. Thus the possibility of melting of the In target is always an issue. In the present case, it has been observed that the maximum power In target can withstand is 25 W. As the power is increase beyond this, In targets becomes unstable and at 30 W shows a tendency for melting. So for co-sputtering of NiMnAl, In and Mn, power of In target has been fixed at 25 W and power of NiMnAl and Mn has been varied to obtain optimum composition.

5.3.2 Crystal Structure

The desired composition can be assumed from the **Table 5.2** indicating the effect of composition variation on the structure.

x	Crystal structure	Lattice parameter a(Å)	b(Å)	c(Å)
0.25	$L2_1$	6.071	6.071	6.071
0.235	$L2_1$	6.060	6.060	6.060
0.225	$L2_1$	6.055	6.055	6.055
0.215	$L2_1$	6.043	6.043	6.043
0.20	$L2_1$	6.031	6.031	6.031
0.175	$L2_1$	6.018	6.018	6.018
0.17	$L2_1$	6.018	6.018	6.018
0.165	$L2_1$	6.004	6.004	6.004
0.16	$B2$	3.004	3.004	3.004
0.155	$10M$	4.385	5.592	21.190
0.15	$10M$	4.391	5.882	21.184
0.10	$14M$	4.284	5.811	30.109
0.05	$L1_0$	7.593	7.593	6.980

Table 5.2: Effect of concentration variation of x on crystal structure of $Ni_{0.50}Mn_{0.50-x}In_x$

The desirable range of $0.165 \leq x < 0.25$ since then the Curie temperature is higher than room temperature. Thus the desirable composition is the one with Ni content ~ 0.50, Mn content ~ 0.30 and In content ~ 0.20. In this respect, it should be noted that the power of In is fixed and the power of NiMnAl target and Mn target are varied. It is further seen that initially (NiMnAl ~ 60 W, Mn ~ 15 W and In ~ 25 W) the In content in the films is very low and no peak corresponding to NiMnIn can be seen in the XRD pattern as shown in **Fig. 5.4**.

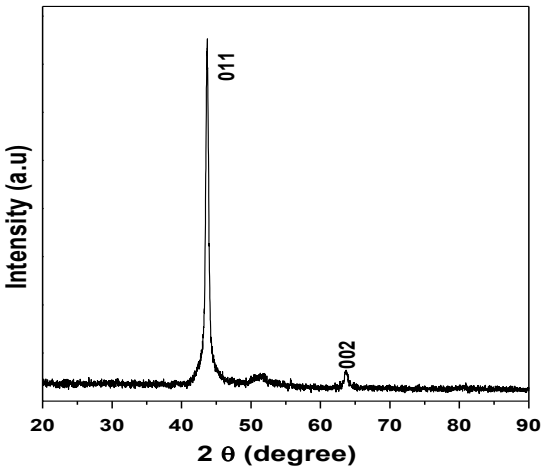

Figure 5.4: XRD pattern of the film deposited at NiMnAl ~ 60 W, Mn ~ 15 W and In ~ 25 W.

To increase the In content in the film, power of NiMnAl and Mn are lower and it has been obsereved that the minimum power at which deposition may be obtained is NiMnAl ~ 55 W, Mn ~ 10 W and In ~ 25 W. If the power of NiMnAl or Mn is further decreased, plasma is not directed on the substrate and no deposition of these materials occur on the substrate. The XRD of the films deposited at NiMnAl ~ 55 W, Mn ~ 10 W and In ~ 25 W is shown in **Fig. 5.5**.

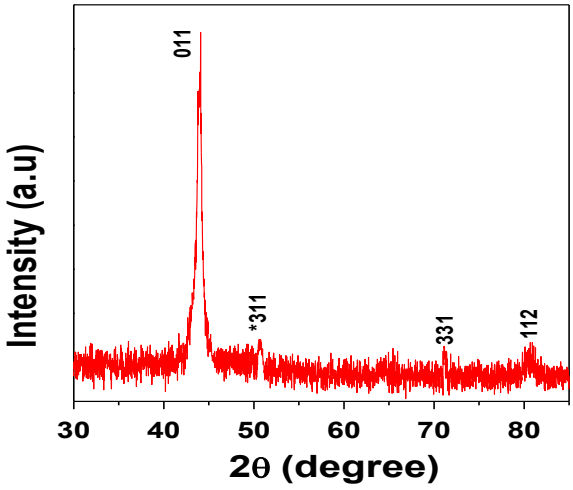

Figure 5.5: XRD pattern of the film deposited at NiMnAl ~ 55 W, Mn ~ 10 W and In ~ 25 W

It can be clearly seen that peak corresponding to B2 structure of NiMnAl and $L2_1$ structure of NiMnIn can be clearly seen. Thus the film exhibits a mixed phase corresponding to both NiMnIn and NiMnAl at an optimized parameter NiMnAl ~ 55 W, Mn ~ 10 W and In ~ 25 W. Films have been deposited for different deposition time of 15 min, 30 min and 45 min. at this optimized parameter. The thickness of the film has been determined for cross sectional FESEM image. The thickness of the film varies as 0.4 µm, 1 µm and 1.3 µm for the film deposited for 15 min, 30 min and 45 min respectively. As an example the cross-section of the film deposited for 15 min, has been shown in **Fig. 5.6**.

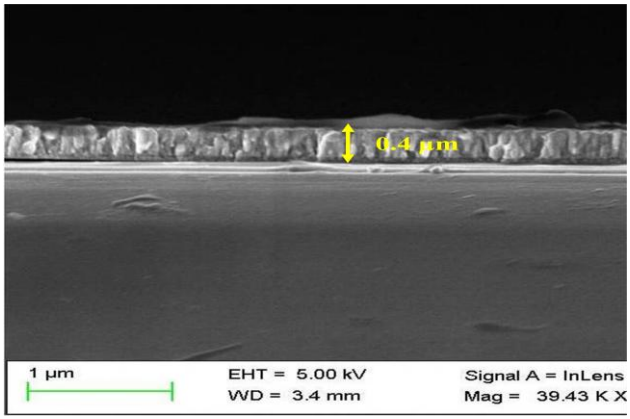

Figure 5.6: Cross-section of the film deposited for 15 min.

The EDAX of the optimized Mn rich films deposited for 15 min, 30 min and 45 min are shown in **Fig. 5.7**, **Fig. 5.8** and **Fig. 5.9**.

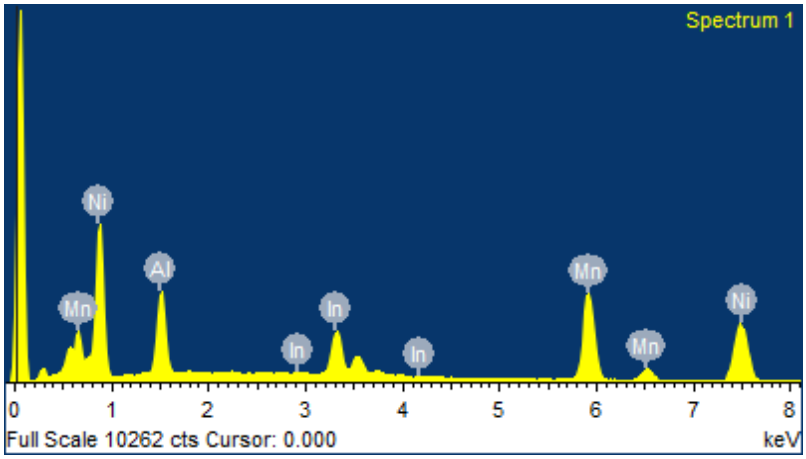

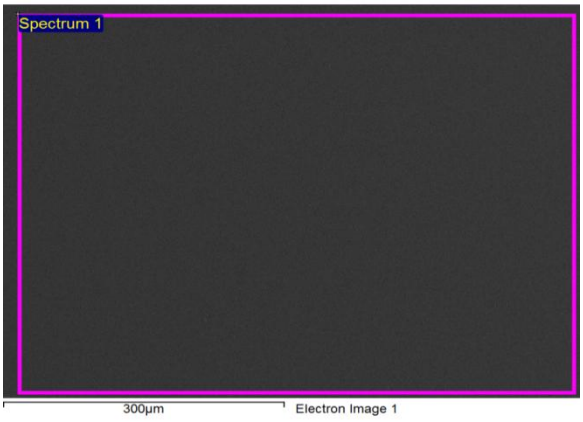

Eleme	Weight	Atomic
Al K	8.20	16.73
Mn K	32.42	28.68
Ni K	48.75	47.70
In L	10.63	07.09
Totals	100.00	

Figure 5.7: EDAX of the film with thickness 0.4 µm.

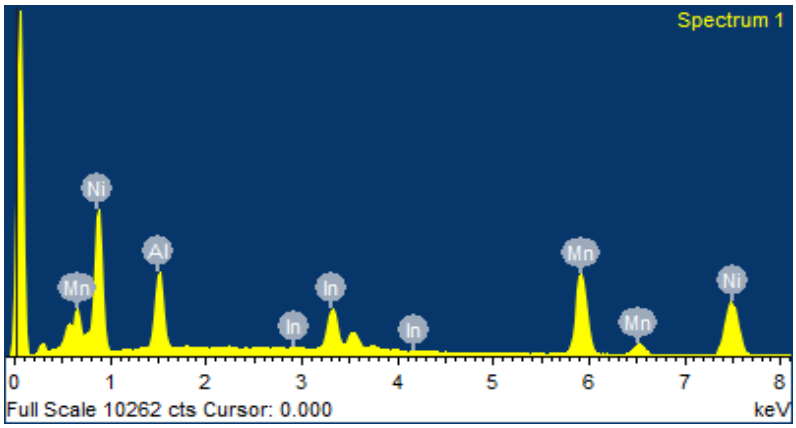

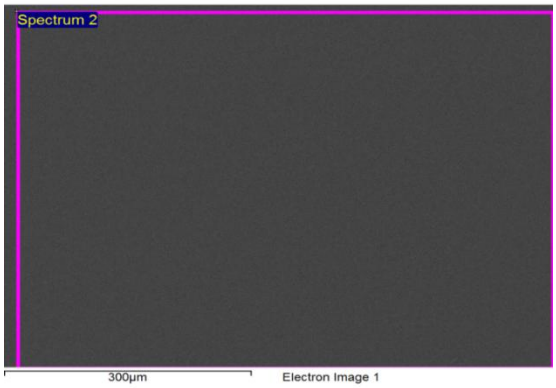

Element	Weight	Atomic
Al K	7.74	16.23
Mn K	32.05	29.82
Ni K	46.00	46.08
In L	14.21	07.96
Totals	100.00	

Figure 5.8: EDAX of the film with thickness 1 µm.

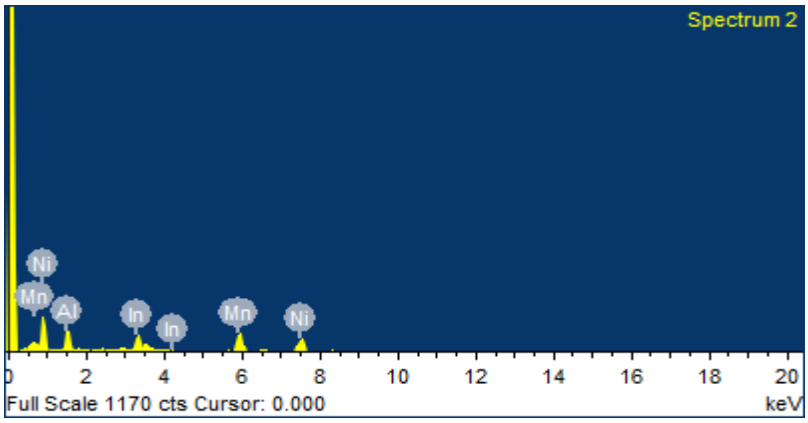

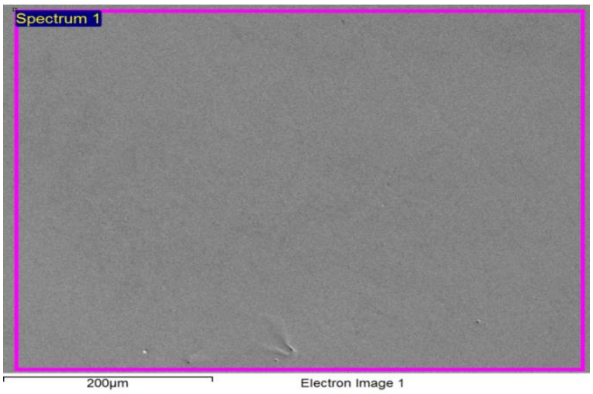

Eleme	Weight	Atomic
Al K	7.38	16.10
Mn K	27.90	28.88
Ni K	42.60	46.69
In L	22.11	08.33
Totals	100.00	

Figure 5.9: EDAX of the film with thickness 1.3 µm.

Thus the composition of the film is $Ni_{47}Mn_{29}Al_{16}In_8$. The SAED pattern taken from the part of the specimen for the films has been shown in **Fig. 5.10**, **Fig. 5.11** and **Fig. 5.12** for thickness 0.5 µm, 1 µm and 4 µm. It can be clearly seen that grain size increase with increasing thickness.

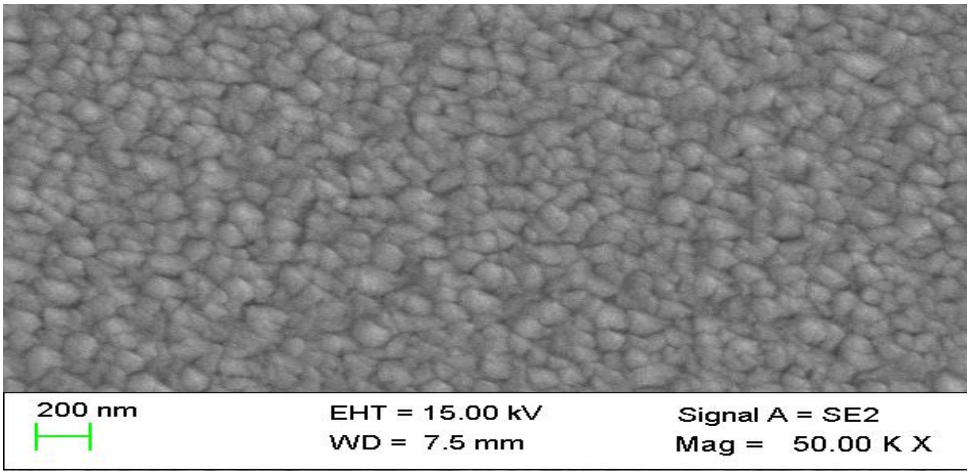

Figure 5.10: SAED pattern for the film with thickness 0.5 µm

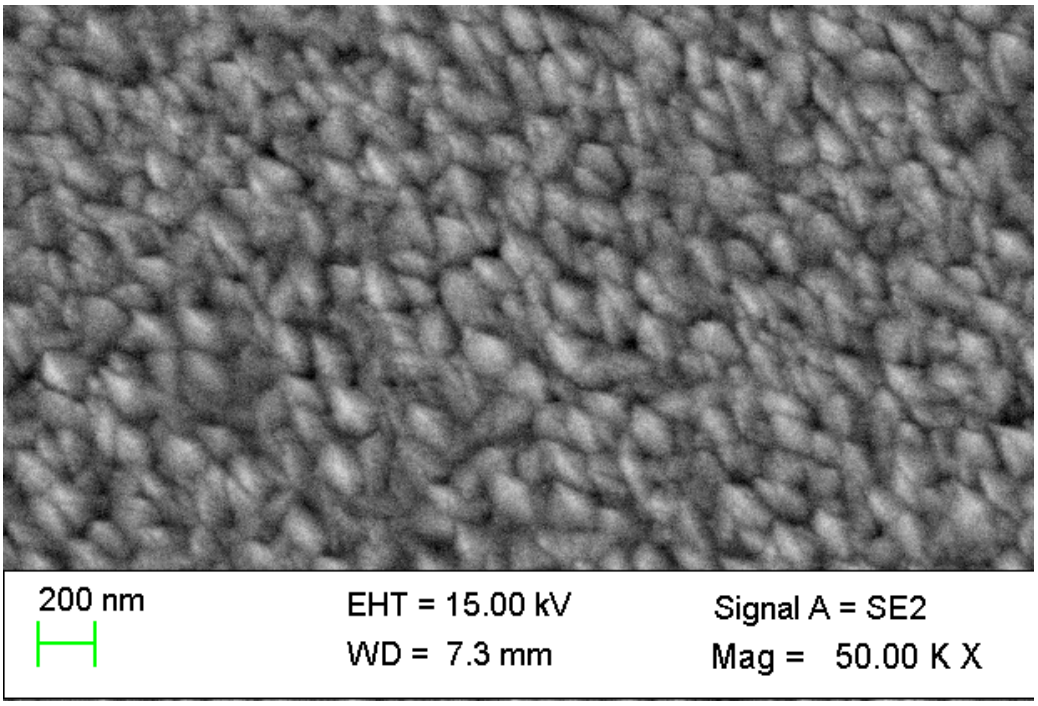

Figure 5.11: SAED pattern for the film with thickness 1 µm

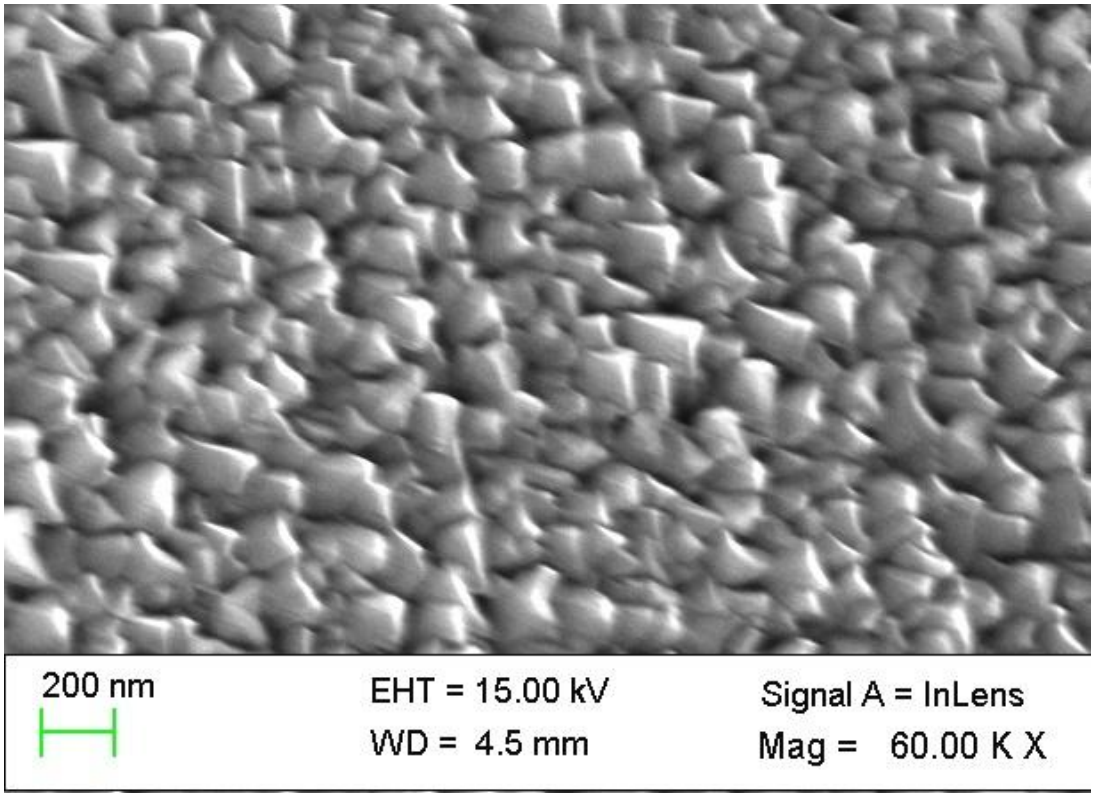

Figure 5.12: SAED pattern for the film with thickness 1.3 µm

5.3.3 Magnetic Properties

Figure 5.13 (a-c) shows hysteresis loops taken at 10 K for 5 T cooling fields (H_{cool}) for all the samples. Magnified view for has been shown in the inset. Maximum exchange bias has been observed for the film with thickness 1 µm. The exchange bias field H_{EB} defined as $\frac{1}{2}(H^{+}+H^{-})$ amounts to 250 Oe, 1050 Oe and 500 Oe has been obtained for the films with thickness 0.5 µm, 1.5 µm and 2 µm respectively.

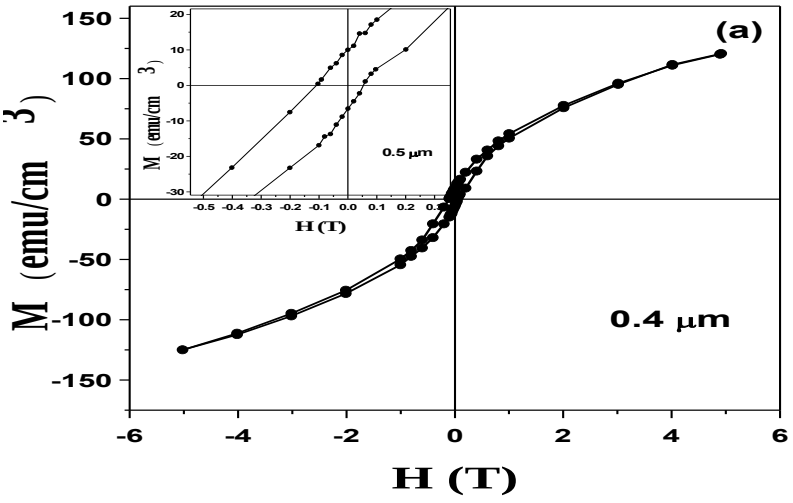

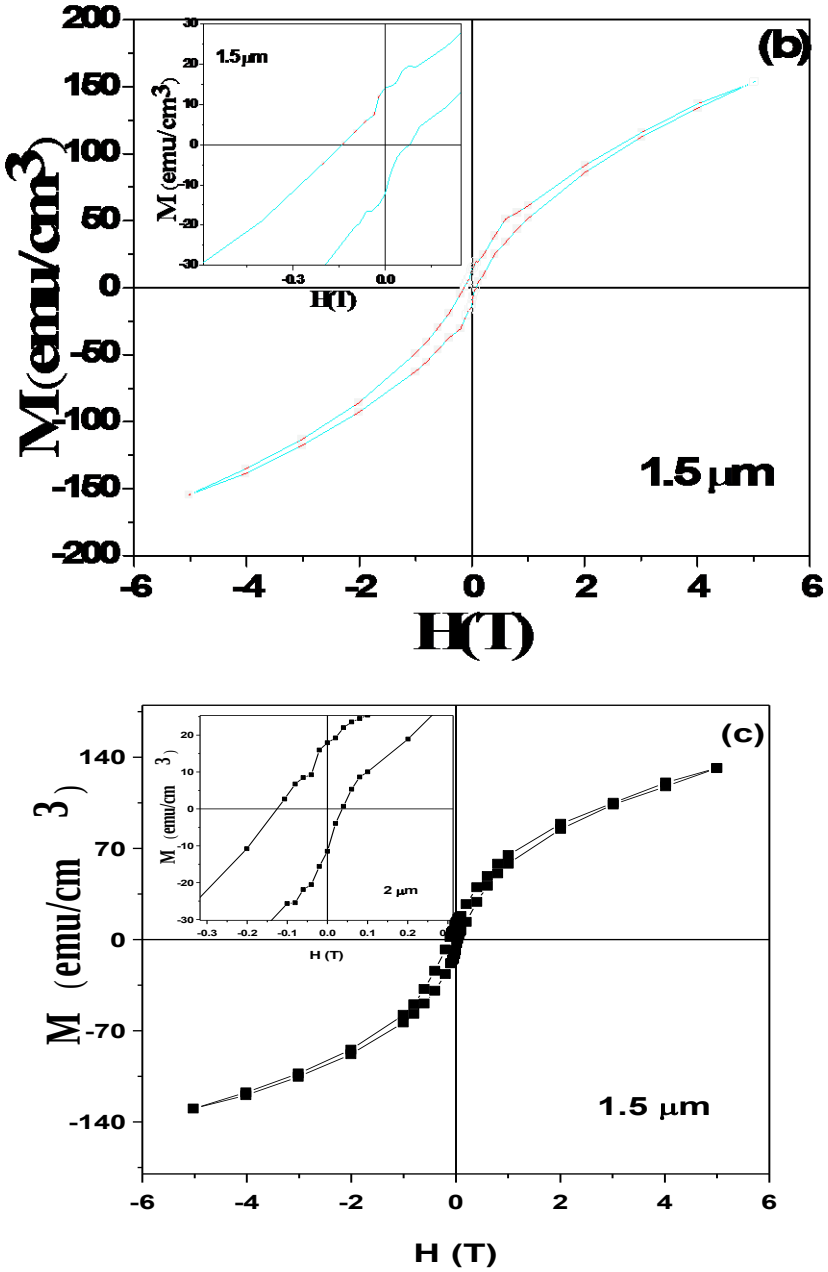

Figure 5.13 (a-c): *M-H* loops taken at 10 K for 5 T cooling fields (H_{cool}) for the films with thickness 0.4 µm, 1 µm and 1.3 µm.

Maximum exchange bias has been obtained for the film with thickness 1 µm. The magnetic and structural transition temperatures of 1.0 µm thick Ni-Mn-Al-In films have been determined from the magnetization measurement at H = 100 Oe. **Fig. 5.14** shows the dc susceptibility for the films in the temperature range of 5 K ≤ T ≤ 300 K in zero-field-cooled heating (ZFCH), field-cooled heating (FCH) and field-cooled cooling (FCC) sequences.

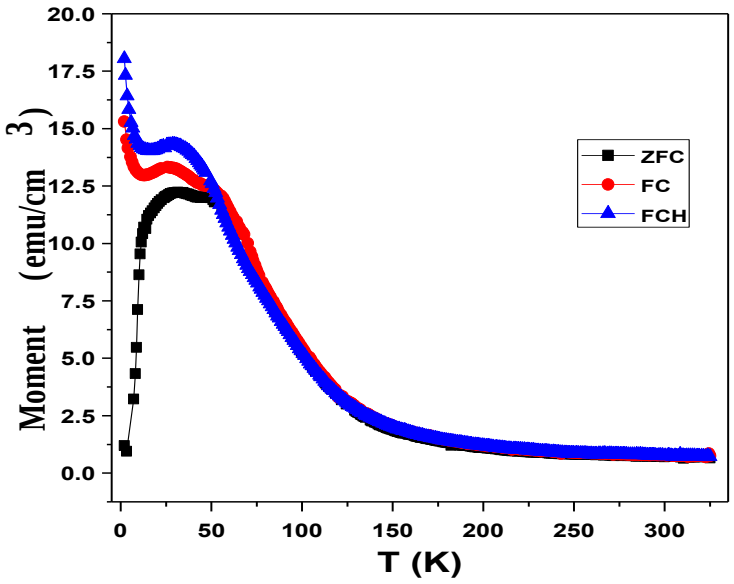

Figure 5.14: *M-T* curve for the film with thickness 1 µm.

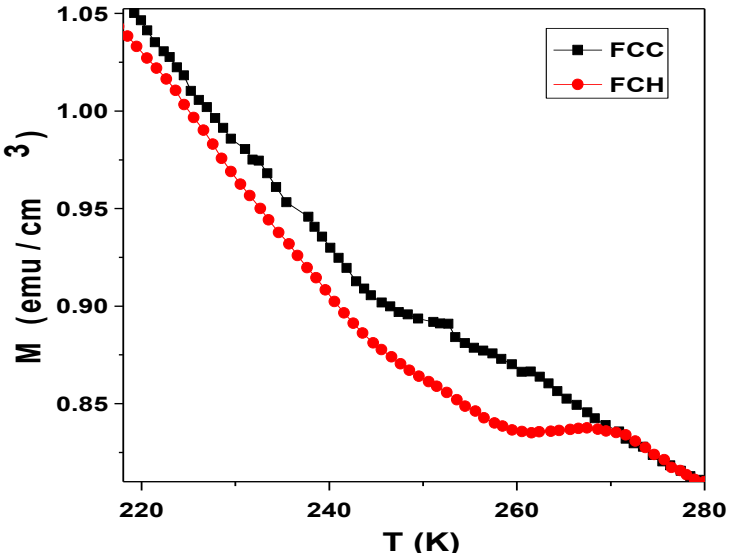

Figure 5.15: *M-T* curve for the film with thickness 1 µm.

As can be seen in the *M-T* curves, at low temperature, the behaviour of the film is similar to NiMnAl thin films which may be expected due to the composition of the film $Ni_{47}Mn_{29}Al_{16}In_8$. This can also be seen in the XRD data of the film where the intensity 0f NiMnAl lattice is much larger than the intensity of peaks corresponding to NiMnIn lattice. The antiferromagnetic transition observed for NiMnAl film cannot be observed for NiMnAlIn film. However, the structural transition observed for NiMnAl can be seen in the M-T curves at

around 250 K shown in **Fig. 5.15**. The transition at low temperature observed for NiMnAl associated with field induced ordering can be seen.

The field dependence of exchange bias has been shown in **Fig. 5.16**. It can be seen that exchange bias shows a nonmonotonic variation with field. H_{EB} initially increases with increasing magnetic field reaches a maximum. Similar to the previous case, the variation of exchange bias with field furthter confirms indicates that exchange bias may bew associated to FM / SG interface. The spin glass phase arises due to the contribution of NiMnAl matrix and the FM behaviour arises due to the presence of NiMnAl phase.

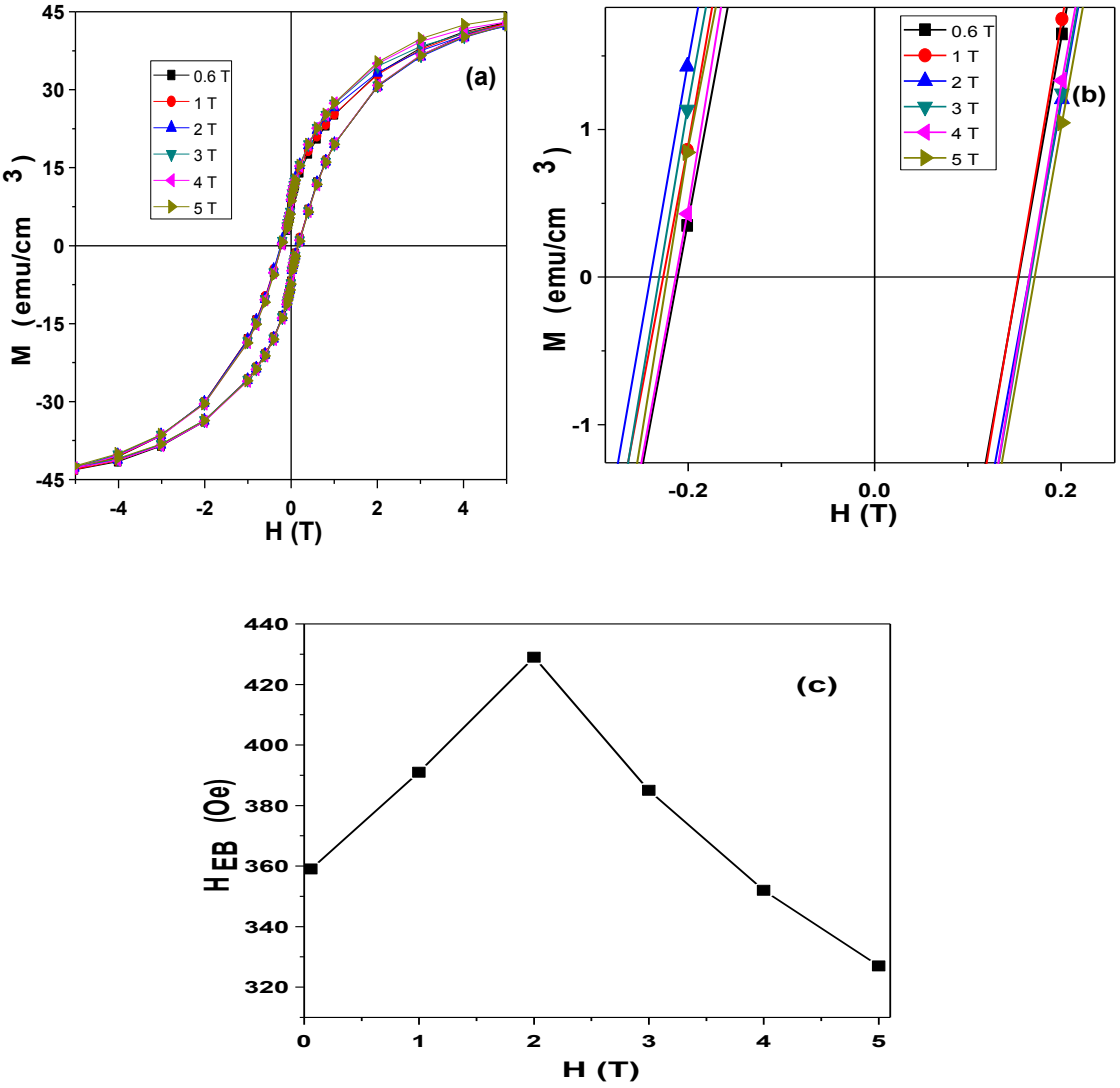

Figure 5.16: (a) *M-H* curves at different fields **(b)** Enlarged view, and **(c)** Variation of H_{EB} with field.

To look into the behaviour of the sample, *M-T* curves have been recorded at different fields of 100 Oe, 500 Oe and 1T . As can be seen in **Fig. 5.17**, with increasing field, the peak observed in the ZFC curves referred to as T_f shifts to lower temperature. This shows that the behaviour of the systems resembles spin glass phase.

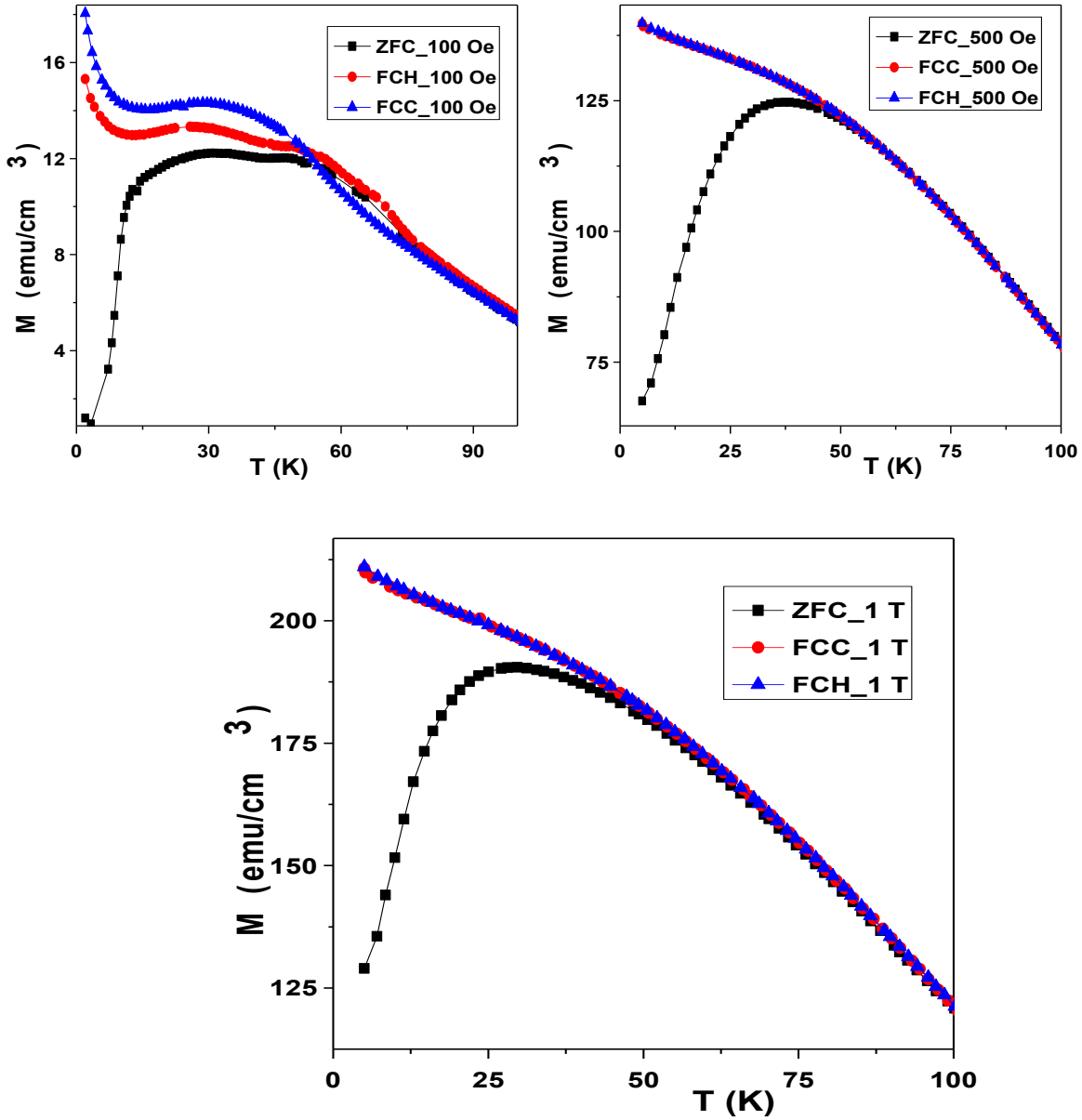

Figure 5.17 (a) *M-T* curves at 100 Oe **(b)** 500 Oe, and **(c)** 1 T fields.

To further explore the behaviour of exchange bias in the samples, temperature dependence of exchange bias has been carried out. Maximum exchange bias of 2200 Oe has been observed at 2 K. H_{EB} decreases with furthere increase in temperature. The temperature dependence of exchange bias shows that there occurs a small positive exchange bias of 10 Oe observed for In co-sputtered NiMnAl thin films, which indicates that the exchange bias

originating in the sample can be related to the spin glass / FM interfaces [240] (**Fig. 5.18**). Thus the system can be modelled as the as the presence of FM NiMnIn phase in NiMnAl matix. This feature is also indicated in *M-T*.

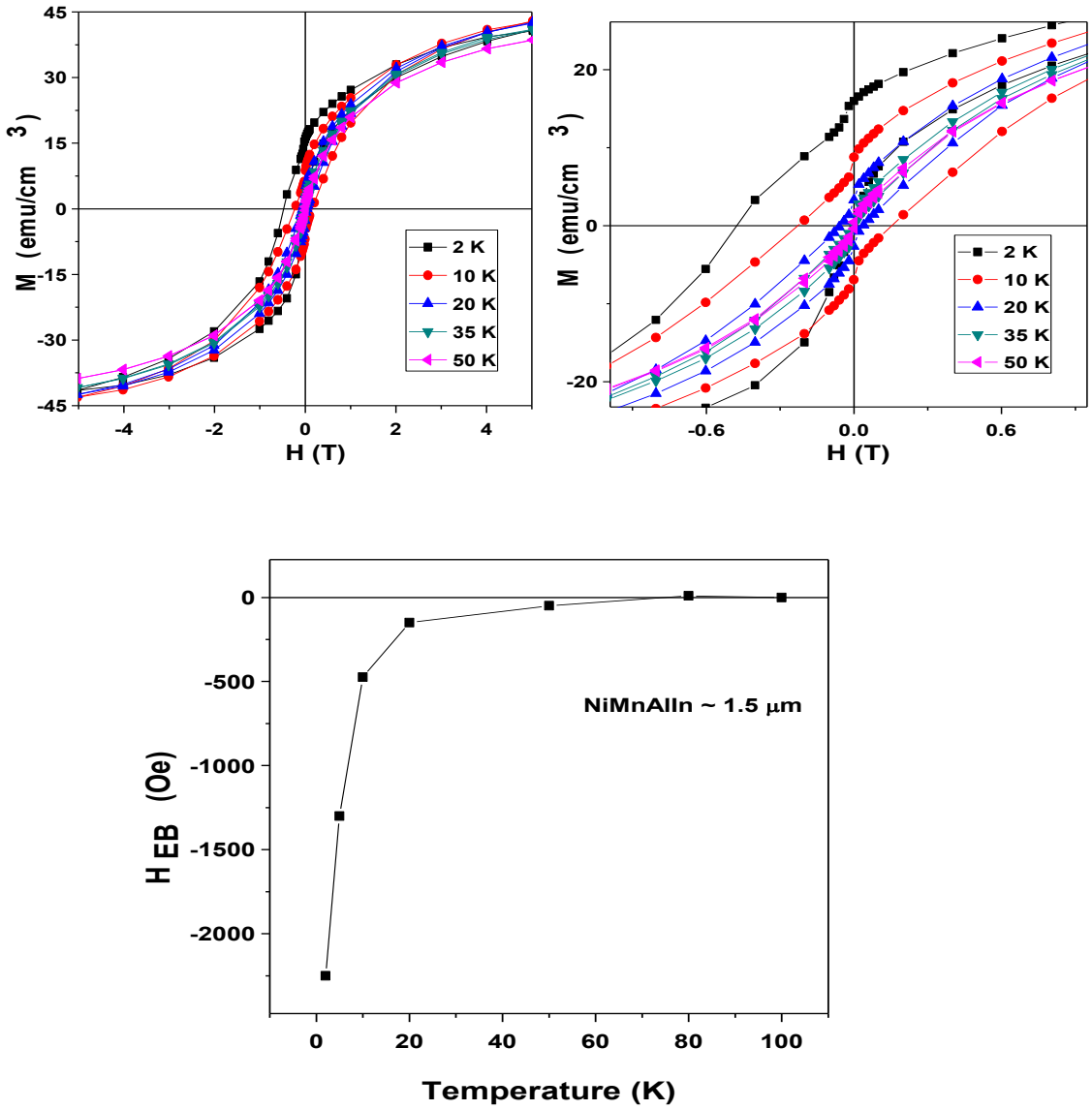

Figure 5.18: (a) *M-H* at different temperatures and **(b)** enlarged view and **(c)** variation of exchange bias with temperature.

5.4 Conclusion

In Conclusion the NiMnAlIn films have been sussesfully fabrication for the NiMnAl and In tangets. It can be clearly seen that exchange bias has been very sensititve to the thickness of the film. H_{EB} first increases with increasing thickness and then decreases with further increase in film thickness. This behavious of variation of exchange bias with field and temperature

further indicates that the system can be modelled as FM/SG system. Maximum exchange bias of 2200 Oe has been observed at 2 K for 1 μm thick film.

CHAPTER 6

CONCLUSIONS AND FUTURE SCOPE

The main objectives of the present research work is to synthesize and study exchange bias properties of Ni-Mn-Al, Ni-Mn-Al-In thin films and Ni-Mn-Al/Ni bi-layer. The films have been prepared by DC/RF magnetron sputtering technique. The motivation for the study is centered on the enhancement of exchange bias in thin films of Hiesler alloys. Ni-Mn-Al have been takes as the study material owing to its superior mechanical properties and mixed phase. Following is a brief summary and conclusions made which are based on the results obtained on the aforementioned coatings. The suggestions for the future work are proposed at the end.

6.1 Study of exchange bias properties of Ni-Mn-Al thin films

It has been observed that Ni rich compositions exhibit a mixed $L2_1$ + B2 structure at thickness $\leq$ 1.5 μm. For larger thickness, a pure B2 structure has been observed. The Mn rich compositions exhibit a pure B2 structure independent of thickness. The structure and magnetic properties of Ni rich and Mn rich Heusler alloys have been studied in detail. Martensitic transition has been observed for the films exhibiting B2 as well as mixed (B2+ $L2_1$) structure. For very thin films no martensitic transition has been observed in both the systems. Owing to the presence of ferromagnetic ($L2_1$) and antiferromagnetic (B2) phase in film with mixed structure ($L2_1$+ B2), the exchange bias has been observed in these films. The exchange bias observed in Ni rich samples has been explained in terms of the existence of a spin glass state at low temperature. Exchange bias has also been observed in B2 phase films associated with the field induced ferromagnetic type ordering occurring in the antiferromagnetic matrix. An increase in exchange bias with increasing film thickness has been observed in Ni rich and Mn rich compositions. Large exchange bias has been observed Mn rich compositions.

6.2 Study of exchange bias properties of NiMnAl/ Ni bilayer films

Ni layer with varying thickness have been deposited on Ni rich and Mn rich Ni-Mn-Al thin films. The results demonstrate that that for a particular thickness of Mn rich NiMnAl

layer, effect of Ni variation is non monotonic. The thickness of Ni layer at which maximum exchange bias occurs depends on the thickness of NiMnAl layer. Maximum EB has been obtained for Ni layer thickness of 60 nm for Ni rich samples. For the Ni layer deposited on Mn rich compositions, exchange bias shows non-monotonic variation with increasing cooling field. For 1 μm thick film maximum H_{EB} has been obtained for 30 nm thick film. For 2.5 μm thick film maximum H_{EB} has been obtained for 60 nm thick film. The exchange bias increases with Ni layer for NiMnAl thickness of 1 μm, for other films H_{EB} decreases with Ni layer. The effect on H_{EB} for Ni layer on Mn rich samples is much more pronounced as compare to the Ni rich samples.

6.3 Study of exchange bias properties of Ni-Mn-Al-In thin films

In this chapter exchange bias properties of NiMnAlIn thin films have been studied. Thin films have been deposited by co-sputtering from target of NiMnAl and In. Thin films of thickness have been deposited. Owing to the ferromagnetic nature of NiMnIn films and antiferromagnetic NiMnAl films, coexisting ferro – antiferro interactions occur in the deposited films which give rise to exchange bias interactions. The effect of cooling field and temperature on exchange bias properties has been discussed. Training effect has also been done to study the exact nature of exchange bias phenomenon in this alloy system. Large exchange bias of 100 Oe at 10 K has been obtained for the film with thickness 1.2 μm.

6.4 Suggestions for future work

Ni-Mn-Al system is a less explored system with interesting mechanical and structural properties. With the key processing-structure-property relationships for the thin film system developed in the present research thus far, there are several directions which can be followed to further expand upon this work:

- Mn rich sample needs to be further explored by advance technique like neutron diffraction
- Composition may be further varied for Mn rich NiMnAl samples.
- Bilayer of NiMnAl and NiMnIn may be studied.
- Bilayer of NiMnAl with other ferromagnetic materials like Fe and Co may also be attempted.

REFERENCES

[1] K. Bhattacharya and R.D. James "A theory of thin films of martensitic materials with applications to microactuators", J. Mech. Phys. Solids **47** 531 (1999).

[2] J. W. Dong, J. Q. Xie, J. Lu, C. Adelmann, C. J. Palmstrom, J. Cui, Q. Pan, T.W. Shield, R.D. James, S. Mckernan, "Shape memory and ferromagnetic shape memory effects in single-crystal Ni2MnGa thin films" J. Appl. Phys. **95** 2593 (2004).

[3] J. Krishna Murthy and A. Venimadhav, "Reentrant cluster glass behavior in La_2CoMnO_6 nanoparticles" J. Appl. Phys. **113**, 163906 (2013).

[4] J. Nogues, J. Sort, V. Langlais, V. Skumryev, S. Surinach, J. S. Munoz, and M. D. Baro, "Exchange bias in nanostructures" Phys. Rep. **65,** 422, (2005).

[5] R. Jungblut, R. Coehoorn, M. T. Johnson, J. aan de Stegge, and A. Reinders, "Orientational dependence of the exchange biasing in molecular-beam-epitaxy-grown $Ni_{80}Fe_{20}/Fe_{50}Mn_{50}$ bilayers" J. Appl. Phys. **75**, 6659 (1994).

[6] Y. Sutou, Y. Imano, N. Koeda, T. Omori, R. Kainuma, K. Ishida, and K. Oikawa, "Magnetic and martensitic transformations of NiMnX (X=In,Sn,Sb) ferromagnetic shape memory alloys" Appl. Phys. Lett. **85**, 4358 (2004).

[7] K. Otsuka and C. M. Wavman "Shape Memory Materilas", Cambridhe University Press, **18**, 284 (1998).

[8] X. Moya, D. Gonzalez-Alonso, L. Manosa, A. Planes, O. Garlea, T. A. Lograsso, D. L. Schlagel, J. L. Zarestky, S. Aksoy, and M. Acet, "Lattice dynamics in magnetic superelastic Ni-Mn-In alloys: Neutron scatterings and ultrasonic experiments" Phys. Rev. B **79**, 214118 (2009).

[9] S. Stadler, M. Khan, Joseph Mitchell, Naushad Ali, Angelo M. Gomes, Igor Dubenko, Armando Y. Takeuchi, and Alberto P. Guimaraes, "Magnetocaloric properties of $Ni_2Mn_{1-x}Cu_xGa$" App. Phys. Lett. **88,** 192511 (2006).

[10] M. Sato, T Okazaki1, Yasubumi Furuya and Manfred Wuttig, "Magnetostrictive and Shape Memory Properties of Heusler Type Co_2NiGa Alloys* Mater. Trans. **44**, 372 (2003).

[11] S. K. Srivastava, V. K. Srivastava, L. K. Varga, V. V. Khovaylo, R. Kainuma, M. Nagasako, R. Chatterjee, "Systematic study of structural, transport, and magnetic

properties of $Ni_{52+x}Mn_{26-x}Al_{22}$ $(1 \le x \le 5)$ melt-spun ribbons" J. Appl. Phys. **109** 083915 (2011).

[12] W. H. Meiklejohn and C. P. Bean. New Magnetic Anisotropy. Phys. Rev. **102**, 1413 (1956).

[13] W. H. Meiklejohn and C. P. Bean. New Magnetic Anisotropy. Phys. Rev. **105**, 904 (1957).

[14] W. H. Meiklejohn. Exchange Anisotropy- A Review. J. Appl. Phys. **33**, 1328 (1962).

[15] S. T. Singh, N. Kumar, R. Bhargava, M. Sahni, K. Sung, J. H. Jung "Magnetodielectric effect in BaTiO 3/ZnFe 2 O 4 core/shell nanoparticles" Journal of Alloys and Compounds, **587** 437 (2014).

[16] B. Singh and S. Chaudhary, "Study of angular dependence of exchange bias and misalignment in uniaxial and unidirectional anisotropy in NiFe(111)/FeMn(111)/CoFeB (amorphous) stack" J. Mag. Mag. Mat. **385** 166 (2015)

[17] H. Fulara, S. Chaudhary, S. C. Kashyap and S. Granville, "Enhancement of exchange bias and training effect in ion-beam sputtered $Fe_{46}Mn_{54}/Ni_{81}Fe_{19}$ bilayers" J. Appl. Phys. 115(4) (2014) 043910.

[18] A. E. Berkowitz and J. H. Greiner, J. Appl. Phys. **36**, 3330 (1965).

[19] M. Takahashi, A. Yanai, S. Taguchi and T. Suzuki, "A Study of Exchange Anisotropy in Co-CoO Evaporated Thin Films" Jpn. J. Appl. Phys. **19**, 1093 (1980).

[20] P. J. van der Zaag, R. M. Wolf, A. R. Ball and C. Bordel, L. F. Feiner, R. Jungblut," A study of the magnitude of exchange biasing in [111] Fe_3O_4/CoO bilayers" J. Magn. Magn. Mater. **148**, 346 (1995).

[21] W. C. Cain and M. H. Kryder, "Investigation of the exchange mechanism in NiFe-TbCo bilayers" J. Appl. Phys. **67**, 5722 (1990).

[22] R. Malik, N. Sehdev, S. Lamba, P. Sharma, A. Makino, and S. Annapoorni, "Magnetic memory effects in nickel ferrite/polymer nanocomposites" Appl. Phys. Lett. **104** 122407 (2014).

[23] H. T. Lin, Y. F. Chen, P. W. Huang, S. H. Wang,, J. H. Jung, C. H. Lai, W. N. Lee and T. S. Chin, "Enhancement of exchange coupling between GaMnAs and IrMn with self-organized Mn(Ga)As at the interface" Appl. Phys. Lett. **89**, 262502 (2006).

[24 K. K. Bharathi, R.J. Tackett, C.E. Botez and C.V. Ramana, "Coexistence of spin glass behavior and long-range ferrimagnetic ordering in La-and Dy-doped Co ferrite" J. Appl. Phys. **109** 07A510 (2011).

[25] D. Paccard, C. Schlenker, O. Massenet, R. Montmory, and A. Yelon. “A New Property of Ferromagnetic-Antiferromagnetic Coupling” Phys. stat. sol. **16**, 301 (1966).

[26] J. Nogués and I. K. Schuller. “Exchange Bias” J. Magn. Magn. Mat. **192**, 203 (1999)

[27] E. C. Stoner and E. P. Wohlfarth. “A mechanism of magnetic hysteresis in heterogeneous alloys” Phil. Trans. Roy. Soc A **240**, 599 (1948).

[28] M. J. Carey and A. E. Berkowitz. “Exchange anisotropy in coupled films of N i81F e19 with N iO and $Co_xN\ i_{1-x}O$” Appl. Phys. Lett. **60**, 3060 (1992).

[29] L. Néel. Etude Theorique-du Couplage “Ferro-Antiferromagnetique Dans les Couches Minces” Annales de Physique **2**, 61 (1967).

[30] D. Mauri, H. C. Siegmann, P. S. Bagus, and E. Kay. “Simple model for thin ferromagnetic films exchange coupled to an antiferromagnetic substrate” J. Appl. Phys. **62** 3047 (1987).

[31] J. Geshev “Analytical solutions for exchange bias and coercivity in ferromagnetic/ antiferromagnetic bilayers” Phys. Rev. B **62**, 5627 (2000).

[32] H. Xi and R. M. White “Antiferromagnetic thickness dependence of exchange biasing” Phys. Rev. B **61**, 80 (2000).

[33] H. Xi, R. M. White, and S. M. Rezende. “Irreversible and reversible measurements of exchange anisotropy” Phys. Rev. B **60**, 14837 (1999).

[34] A. I. Morosov and A. S. Sigov. “Interface roughness and unidirectional anisotropy of thin ferromagnetic film on uncompensated surface of antiferromagnet” J. Magn. Magn. Mat. **242**, 1012 (2002).

[35] A. I. Morosov and A. S. Sigov. “Unidirectional anisotropy in a ferromagnetantiferromagnet system” Physics of the Solid State **44**, 2098 (2002).

[36] A. I. Morosov and A. S. Sigov “Proximity effect in ferromagnet-antiferromagnet systems” J. Magn. Magn. Mat. **258**, 388 (2003).

[37] M. Kiwi, J. Mejía-López, R. D. Portugal, and R. Ramírez, “Exchange bias model for Fe/F eF_2 Role of the domains in the ferromagnet” Europhys. Lett. **48**, 573 (1999).

[38] M. Kiwi, J. Mejía-López, R. D. Portugal, and R. Ramírez. “Exchange bias systems with compensated interfaces” Europhys. Lett. **75**, 3995 (1999).

[39] M. Kiwi, J. Mejía-López, R. D. Portugal, and R. Ramírez. “Positive exchange bias model: F e/FeF_2 and Fe/MnF_2 bilayers” Solid State Communications **116**, 315 (2000).

[40] J. V. Kim, R. L. Stamps, B. V. McGrath, and R. E. Camley. “Angular dependence and interfacial roughness in exchange-biased ferromagnetic/antiferromagnetic bilayers” Phys. Rev. B **61**, 8888 (2000).

[41] J. V. Kim and R. L. Stamps. “Theory of long-wavelength spin waves in exchange biased bilayers” J. Appl. Phys. **89**, 7651 (2001).

[42] J. V. Kim and R. L. Stamps. “Hysteresis from antiferromagnet domain-wall processes in exchange-biased systems” J. Magn. Magn. Mat. **286**, 233 (2005).

[43] J. V. Kim and R. L. Stamps “Defect-modified exchange bias” Appl. Phys. Lett. **79**, 2785 (2001).

[44] J. V. Kim and R. L. Stamps “Hysteresis from antiferromagnet domain-wall processes in exchange-biased systems: Magnetic defects and thermal effects” Phys. Rev. B **71**, 094405 (2005).

[45] R. L. Stamps “Dynamic magnetic hysteresis and anomalous viscocity in exchange bias systems” Phys. Rev. B **61**, 12174 (1999).

[46] R. L. Stamps. “Mechanisms of exchange bias” J. Phys. D **3**, R247 (2000).

[47] A. Hoffmann. “Symmetry Driven Irreversibilities at Ferromagnetic-Antiferromagnetic Interfaces” Phys. Rev. Lett. **93**, 097203 (2004).

[48] N. C. Koon “Calculations of Exchange Bias in Thin Films with Ferromagnetic/Antiferromagnetic Interfaces” Phys. Rev. Lett. **78**, 4865 (1998).

[49] T. C. Schulthess and W. H. Butler. “Coupling mechanisms in exchange biased films”. J. Appl. Phys. **85**, 5510 (1999).

[50] P. Miltényi, M. Gierlings, J. Keller, B. Beschoten, G. Güntherodt, U. Nowak, and K. D. Usadel. “Diluted Antiferromagnets in Exchange Bias: Proof of Domain State Model”. Phys. Rev. Lett. **84**, 4224 (2000).

[51] U. Nowak, A. Misra, and K. D. Usadel. “Domain state model for exchange bias.” J. Appl. Phys. **89**, 7269 (2001).

[52] Y. Imry and S. Ma. “Random-Field Instability of the ordered state of Continuous symmetry” Phys. Rev. Lett. **35**, 1399 (1975).

[53] U. Nowak, K. D. Usadel, P. Miltényi, J. Keller, B. Beschoten, and G. Güntherodt. “The domain state model for exchange bias I: Theory” Phys. Rev. B **66**, 014430 (2002).

[54] U. Nowak, A. Misra, and K. D. Usadel. “Modeling exchange bias microscopically.” J. Magn. Magn. Mat. **240**, 243 (2002).

[55] A. Misra, U. Nowak, and K. D. Usadel. “Structure of domains in an exchange-bias model” J. Appl. Phys. **95**, 1357 (2004).

[56] A. Misra, U. Nowak, and K. D. Usadel. “Control of exchange bias by diluting the antiferromagnetic layer” J. Appl. Phys. **93**, 6593 (2003).

[57] T. Mewes, R. Lopusnik, J. Fassbender, B. Hillebrands, M. Jung, D. Engel, A. Ehresmann, and H. Schmoranzer. "Suppression of exchange bias by ion irradiation" Appl. Phys. Lett. **76**, 1057 (2000).

[58] A. Mougin, T. Mewes, M. Jung, D. Engel, A. Ehresmann, H. Schmoranzer, J. Fassbender, and B. Hillebrands. "Local manipulation and reversal of the exchange bias field by ion irradiation in FeNi/FeMn double layers". Phys. Rev. B **63**, 60409 (2001).

[59] B. Beckmann, U. Nowak, and K. D. Usadel. "Asymmetric reversal modes in ferromagetic/antiferromagnetic multilayers" Phys. Rev. Lett. **91**, 187201 (2003).

[60] G. Scholten, K. D. Usadel, and U. Nowak. "Coercivity and exchange bias of ferromagnetic/antiferromagnetic multilayers" Phys. Rev. B **71**, 064413 (2005).

[61] J. Spray and U. Nowak. "Exchange bias in ferromagnetic/antiferromagnetic bilayers with imperfect interfaces" J. Phys. D: Applied Physics **39**, 4536–4539 (2006).

[62] C. Papusoi, J. Hauch, M. Fecioru-Morariu, and G. Guntherodt. "Tuning the exchange bias of soft metallic antiferromagnets by inserting nonmagnetic defects" J. Appl. Phys. **99**, 123902 (2006).

[63] N. A. Usov and S. A. Gudoshnikov. "Numerical simulation of magnetization process in antiferromagnetic-ferromagnetic bilayer with compensated interface" J. Magn. Magn. Mat. **300**, 164 (2006).

[64] F. Heusler, Starck, and Haupt, Verh. Deuts, Phys. Ges. **5,** 219 (1903).

[65] S .K. Arora, B.J. O'Dowd, P. Thakur, N.B. Brookes, B. Ballesteros, P. Gambardella, and I.V. Shvets, "*Magnetization reversal behaviour of planar nanowire arrays of Fe*"Current Nanoscience **9** 613 (2013)

[66]L. Joshi and R. Prakash, "Synthesis of conducting poly (5-carboxyindole)/Au nanocomposite: Investigation of structural and nanoscale electrical properties" Thin Solid Films, **534** 120 (2013)

[67] S. Tiwari, W. Takashima, S. K. Balasubramanian, S. Miyajima, S. Nagamatsu, S. Sudhir Pandey and R.Prakash, "P_3HT-fiber-based field-effect transistor: Effects of nanostructure and annealing temperature Japanese" Journal of Applied Physics **53** 021601 (2014).

[68] Y. K Mishra, G Modi, V Cretu, V Postica, O Lupan, T Reimer, I Paulowicz, "Direct growth of freestanding ZnO tetrapod networks for multifunctional applications in photocatalysis, UV photodetection, and gas sensing" ACS Applied Materials & Interfaces 7 (26) 14303–14316.

[69] R. malik, R. Sharma, D kanjilal, Annapoorni Subramanian, "Alignment of magnetic clusters in polymer using Ar ion beam" J. Phys D:Appl Phys 42 (2009) 235501.

[70] K. Kamala Bharathi and C.V. Ramana, "Anomalous Hall effect and perpendicular magnetic anisotropy in $Sm_{28}Fe_{72}$ and $Sm_{32}Fe_{68}$ thin films" Journal of Magnetism and Magnetic Materials 323 (2011) 51-54.

[71] N. Kumar, N. G. Kim, Y. A. Park, N. Hur, J. H. Jung, K. J. Han, and K. J. Yee "Epitaxial growth of terbium iron garnet thin films with out-of-plane axis of magnetization" Thin Solid Films **516** 7753 (2008).

[72] K. G. Rana, S. Parui, T. Banerjee,. "Probing electron transport across a LSMO/Nb: STO heterointerface at the nanoscale" Physical Review B: Condensed Matter and Materials Physics, **87(8)** 085116 (2013).

[73] A. M. Kamerbeek, E. K. de Vries, A. Dankert, S. P. Dash, B. J. van Wees, T. Banerjee, "Electric field effects on spin accumulation in Nb-doped $SrTiO_3$ using tunable spin injection contacts at room temperature" Appl. Phys. Lett, **104** 212106 (2014).

[74] F. A. Hames," Ferromagnetic-Alloy Phases Near the Compositions Ni_2MnIn , Ni_2MnGa , Co MnGa , Pd_2MnSb , and PdMnSb" J. Appl. Phys. Suppl. **31**, 370 (1960).

[75] Y. Noda and Y. Ishikawa, "Spin Dynamics in a Heusler Alloy Pd_2MnSn" J. Phys. Soc. Jpn **40**, 669 (1976).

[76] B. Caroli and A. Blandin, "Champs hyperfins dans les alliages d'Heusler" J. Phys. Chem. Solids **27**, 503 (1966).

[77] T. Kasuya, "Exchange mechanism in Heusler alloys: virtual double exchange" Solid State Commun. **15**, 1119 (1974).

[78] L. C. Chang and T. A. Read, "The Gold-Cadmium Beta Phase" Trans AIME, **191**, 47 (1951).

[79] Yuxi Wu, Wanglin Zhang, Jia Guo, Jieshan Hou, Xiuyan Li, Renzhong Huang, Xiufang Ma, Qianfeng Zhang, "The First-principles Study on the Occupation Behavior and the Ductility Mechanism of Zr in NieNi3Al System with Lattice Misfit" Journal of Materials Science & Technology, **30(5)**, 517, (2014).

[80] P. Lazpita, G. Rojo, J. Gutierrez, J. M. Barandiaran, and R. C. O'Handley, "Correlation Between Magnetization and Deformation in a NiMnGa Shape Memory Alloy Polycrystalline Ribbon" Sensor Letters **5**, 65 (2007).

[81] M. Pasquale, C. Sasso, S. Besseghini, E. Passaretti, E. Villa, and A. Sciacca, "NiMnGa polycrystalline magnetically activated shape memory alloys" IEEE Transactions on Magnetics, **36**, 3263 (2000).

[82] U. Gaitzsch , M. Potschke , S. Roth , B. Rellinghaus and L. Schultz, "A 1% magnetostrain in polycrystalline 5M Ni–Mn–Ga" Acta Mater. **57,** 365 (2009).

[83] H. A. Das and F. H. M., "Spit On the limits of low level measurements of 137Cs as a natural radiotracer" J. Radioanal. Nucl. Chem. Lett. **117**, 171 (1987).

[84] D. Raabe "Simulation and Experimental Examination of the Evolution of Orientation Gradients in Single Grains during Rolling of Body Centered Cubic Polycrystals" physica status solidi (b) **181**, 291 (1994)

[85] K. Bhattacharya, A. DeSimone, K.F. Hane, R.D. James, C.J. Palmstrøm "Tents and tunnels on martensite films" Mater. Sci. Eng. A **685** 273, (1999)

[86] J.W. Dong, L.C. Chen, C.J. Palmstrøm, R.D. James, S.McKernan "Molecular beam epitaxy growth of ferromagnetic single crystal (001) Ni_2MnGa on (001) GaAs" Appl. Phys. Lett. **75**, 1443 (1999)

[87] J.W. Dong, L.C. Chen, J.Q. Xie, T.A.R. Müller, D.M. Carr, C.J. Palmstrøm, S. McKernan, Q. Pan, R.D. James, "Epitaxial growth of ferromagnetic Ni2MnGa on GaAs(001) using NiGa interlayers" J. Appl. Phys. **88**, 7357 (2000)

[88] J.W. Dong, J. Lu, J.Q. Xie, L.C. Chen, R.D. James, S. McKernan, C.J. Palmstrøm, "MBE growth of ferromagnetic single crystal Heusler alloys on (0 0 1)$Ga_{1-x}In_xAs$" Physica E **10**, 428 (2001),

[89] Q. Pan, J.W. Dong, C.J. Palmstrøm, J. Cui, R.D. James, "Magnetic domain observations of freestanding single crystal patterned Ni2MnGa films" J. Appl. Phys. **91**, 7812 (2002)

[90] I. Takeuchi, O.O. Famodu, J.C. Read, M.A. Aronova, K.-S. Chang,C. Craciunescu, S.E. Lofland, M. Wuttig, F.C. Wellstood, L. Knauss,A. Orozco, "Identification of novel compositions of ferromagnetic shape-memory alloys using composition spreads" Nat. Mater. **2**, 180 (2003),

[91] S.I. Patil, D. Tan, S.E. Lofland, S.M. Bhagat, I. Takeuchi, O. Famodu,J.C. Read, K.-S. Chang, C. Craciunescu, M.Wuttig, "Ferromagnetic resonance in Ni–Mn–Ga films" Appl. Phys. Lett. **81**,1279 (2002)

[92] P.G. Tello, F.J. Castaño, R.C. O'Handley, S.M. Allen, M. Esteve, F. Castaño,A. Labarta, X. Batlle, "Ni–Mn–Ga thin films produced by pulsed laser deposition" J. Appl. Phys. **91**, 8234 (2002)

[93] F.J. Castaño, B. Nelson-Cheeseman, R.C. O'Handley, C.A. Ross, C. Redondo,F. Castaño, "Structure and thermomagnetic properties of polycrystalline Ni–Mn–Ga thin films" J. Appl. Phys. **93**, 8492 (2003)

[94] V. Podgurski, S. Galambos: in Proc. DAAAM Int. Conf. (Tallinn, Estonia,2000) p. 229

[95] T. Busgen, J. Feydt, R. Hassdorf, S. Thienhaus, M. Moske, M. Boese, A. Zayak, and P. Entel, "Ab initio calculations of structure and lattice dynamics in Ni−Mn−Al shape memory alloys" Phys. Rev. B **70**, 014111 (2004)

[96] J. Kubler, A. R. Williams and C. B. Sommers, "Formation and coupling of magnetic moments in Heusler alloys" Phys. Rev. B **28,** 1745 (1983).

[97] A. Ayuela, J. Enkovaara, K. Ullakko, and R. M. Nieminen, J. Phys, "Structural properties of magnetic Heusler alloys" Condens. Matter **11**, 2017 (1999).

[98] R. Kainuma, K. Ishida, and H. Nakano, "Martensitic transformations in NiMnAl β phase alloys" Metall. Mater. Trans. A **27,** 4153 (1996).

[99] V. A. Chernenko, "Compositional instability of β-phase in Ni-Mn-Ga alloys" Scripta Mater. **40**, 523 (1999).

[100] Thorsten Krenke, Mehmet Acet, E. F. Wassermann, X. Moya, L. Manosa, and A. Planes, "Martensitic transitions and the nature of ferromagnetism in the austenitic and martensitic states of Ni−Mn−Sn alloys" Phys. Rev. B **72**, 014412 (2005).

[101] Thorsten Krenke, Mehmet Acet, and Eberhard F. Wassermann Xavier Moya, Lluis Manosa, and Antoni Planes, "Ferromagnetism in the austenitic and martensitic states of Ni−Mn−In alloys" Phys. Rev. B **73**, 174413 (2006).

[102] N. Scheerbaum, O. Heczko, J. Liu, D. Hinz, L. Schultz, and O. Gutfleisch, "Magnetic field-induced twin boundary motion in polycrystalline Ni–Mn–Ga fibres" New Journal of Physics **10**, 073002 (2010).

[103] M. Ohtsuka, M. Matsumoto, K. Koike, T. Takagi, and K. Itagaki, "Martensitic transformation and shape memory effect of Ni-rich Ni2MnGa sputtered films under magnetic field" J. Magn. Magn. Mater, **310**, 2782 (2007).

[104] U. Gaitzsch, M. Potschke, S. Roth, B. Rellinghaus, and L. Schultz, Scripta Materialia **57**, 493 (2007).

[105] M. Pasquale, C. Sasso, S. Besseghini, E. Passaretti, E. Villa, and A. Sciacca, "NiMnGa polycrystalline magnetically activated shape memory alloys" IEEE Transactions on Magnetics, **36**, 3263 (2000)

[106] A. N. Vasil'ev, A. D. Bozhko, V. V. Khovailo, I. E. Dikshtein, S. G. Shavrov, V. D. Buchelnikov, M. Matsumoto, S. Suzuki, T. Takagi and J. Tani, Phys. Rev. B **59,** 1113 (1999)

[107] R. Tickel and R. D. James, J. Magn. Magn. Mater., **195**, 627 (1999).

[108] P.J. Webster, K.R.A. Ziebeck, S.L. Town, and M.S. Peak: Phil. Mag. B **49** 295 (1984).

[109] R. E. Watson, and M. Weinert, “Solid State Physics” (New York: Academic Press) **56**, 1 (2001).

[110] N. Lansk, O. Soderber, A. Sozinov, Y. Ge, K. Ullakko, and V. K. Lindroos, “Composition and temperature dependence of the crystal structure of Ni–Mn–Ga alloys” J. Appl. Phys. **95**, 8074 (2004).

[111] C. Jiang, M. Yousaf, D. Lifeng, W. Wei, and X. Huibin, “Composition dependence on the martensitic structures of the Mn-rich NiMnGa alloys” Acta Mater. **52** 2779 (2004).

[112] K. Oikawa, R. Kainuma and K. Ishida, “Phase Equilibria and Phase Transformations in New B2-type Ferromagnetic Shape Memory Alloys of Co-Ni-Ga and Co-Ni-Al Systems” Mater. Trans. **42,** 2472 (2001).

[113] K. Oikawa, L. Wulff, T. Iijima, F. Gejima, T. Ohmori, A. Fujita, K. Fukamichi, R. Kainuma, and K. Ishida, “Promising ferromagnetic Ni–Co–Al shape memory alloy system” Appl. Phys. Lett. **79,** 3290 (2001).

[114] K. Oikawa, T. Ota, T. Ohmori, Y. Tanaka, H. Morito, A. Fujita, R. Kainuma, K. Fukamichi, and K. Ishida, “Magnetic and martensitic phase transitions in ferromagnetic Ni–Ga–Fe shape memory alloys” Appl. Phys. Lett. **81,** 5201 (2002).

[115] K. Oikawa, T. Ota., R. Kainuma, and K. Ishida, “Magnetic and Martensitic Phase Transformations in a $Ni_{54}Ga_{27}Fe_{19}$Alloy” Mater. Trans. **43,** 2360 (2002).

[116] Trudel, S., Gaier, O., Hamrle, J. & Hillebrands, B, “Magnetic anisotropy, exchange and damping in cobalt-based full-Heusler compounds: an experimental review” Journal of Physics D: Applied Physics **43**, 193001, (2010).

[117] Cullity, B. D. & Graham, C. D. Introduction to Magnetic Materials. Wiley, (2009).

[118] W. Z. Heisenberg, Physik **38**, 411 (1926).

[119] R. C. O'Handley, “Modern Magnetic Materials: Principles and Applications” Wiley, (1999).

[120] A. H. Morrish, & I. M. Society, “The Physical Principles of Magnetism” Wiley, (1965).

[121] M.A.Ruderman, & C.Kittel, “Indirect Exchange Coupling of Nuclear Magnetic Moments by Conduction Electrons” Physical Review **96** 99 (1954).

[122] T.Kasuya, “A theory of metallic ferro- and antiferromagnetism on Zener's model” Prog. Theor. Phys. **16**, 45 (1956).

[123] Yosida, K. “Magnetic Properties of Cu-Mn Alloys” Physical Review **106**, 893 (1957).

[124] I. A. Campbell, “Indirect exchange for rare earths in metals” Journal of Physics F: Metal Physics **2**, L47, (1972).

[125] S. S. P.Parkin, N. More, & K. P. Roche, "Oscillations in exchange coupling and magnetoresistance in metallic superlattice structures Co/Ru, Co/Cr, and Fe/Cr" Physical Review Letters **64**, 2304-2307, (1990).

[126] N.Ashcroft, & D.Mermin, "Solid State Physics" Thomson Learning, (1976).

[127] J.Crangle, "Solid State Magnetism" New York: Van Nostrand Reinhold, (1991).

[128] S. S. P.Parkin, , R.Bhadra, & K. P.Roche, "Oscillatory magnetic exchange coupling through thin copper layers" Physical Review Letters **66**, 2152-2155, (1991).

[129] K.O'Grady, , R.Chantrell, & I.Sanders, "Magnetic Characterisation of Thin Film Recording Media" IEEE Transactions on Magnetics **29**, 286-291, (1993).

[130] C. Zener, "Interaction between the d-Shells in the Transition Metals IV The Intrinsic Antiferromagnetic Character of Iron" Phys. Rev. **85**, 324 (1952).

[131] P. J. Webster and K. R. A. Ziebeck "Heusler Alloys" 19C**,** 75 (Springer, Berlin), (1988).

[132] D. Hobbs, J. Hafner, and D. Spišak, "Understanding the complex metallic element Mn. I.Crystalline and noncollinear magnetic structure of α-Mn" Phys. Rev. B **68**, 014407 (2003).

[133] J. Hafner and D. Hobbs, "Understanding the complex metallic element Mn.II. Geometric frustration in β-Mn, phase stability, and phase transitions" Phys. Rev. B **68**, 014408 (2003).

[134] Ph. Kurz, G. Bihlmayer, K. Hirai, and S. Blügel, "Three-Dimensional Spin Structure on a Two-Dimensional Lattice: Mn /Cu(111)" Phys. Rev. Lett. **86**, 1106 (2001).

[135] B. Malaman, G. Venturini, R. Welter, and E. Ressouche, "Neutron diffraction studies of $CaMn_2Ge_2$ and $BaMn_2Ge_2$ compounds: first examples of antiferromagnetic Mn planes in $ThCr_2Si_2$-type structure compounds" J. Alloys Compd. **210**, 209 (1994). 160

[136] G. Venturini, B. Malaman, and E.Ressouche. "Thex − T magnetic phase diagram of the $La_{1-x}Y_xMn_2Ge_2$ system by neutron diffraction study" J. Alloys Compd., **241**, 135 (1996).

[137] M. Hofmann, S. J. Campbell, S. J. Kennedy, and X. L. Zhao, "A neutron diffraction study of $LaMn_2Si_2$ (10–473 K)" J. Magn. Magn. Mater. **176**, 279 (1997).

[138] G. Venturini, R. Welter, E. Ressouche, and B. Malaman, "Neutron diffraction studies of $LaMn_2Ge_2$ and $LaMn_2Si_2$ compounds: evidence of dominant antiferromagnetic components within the Mn planes" J. Alloys Compd. **210**, 213 (1994)

[139] J. Krishna Murthy and A.Venimadhav, "Gaint xero field cooled spontaneous exchange bias in phase separated $La_{1.5}Sr_{0.5}CoMnO_6$ Appl. Phys Lett., **103** 252410 (2013).

[140] K. D Sung, Y. A. Park, M. S.Seo, Y. Jo, N. Hur, J. H. Jung, "Observation of intriguing exchange bias in $BiFeO_3$ thin films" J. Appl. Phys. **11** 033915 (2012) .

[141] J. McCord, S. Mangin, "Separation of low- and high-temperature contributions to the exchange bias in Ni81Fe19-NiO thin films" Physical Review B **88** 014416 (2013) .

[142] V. Hrkac, E. Lage, G. Köppel, J. Strobel, J. McCord, E. Quandt, D. Meyners, L. Kienle, "Amorphous FeCoSiB for exchange bias coupled and decoupled magnetoelectric multilayer systems: Real-structure and magnetic properties" Journal of Applied Physics **116** 134302 (2014).

[143] Z. Han, J. Chen, B. Qian, P. Zhang, X. Jiang, D. Wang, and Y. Du, "Phase diagram and magnetocaloric effect in $Mn_2Ni_{1.64-x}Co_xSn_{0.36}$alloys" Scripta Mater. **66**, 121 (2012).

[144] V. Srivastava, Y. Song, K. Bhatti, and R: D. James, "The direct conversion of heat to electricity using multiferroic alloys" Adv. Energy Mater. **1**, 97 (2011).

[145] R. Kainuma, Y. Imano, W. Ito, Y. Sutou, H. Morito, S. Okamoto, O. Kitakami, K. Oikawa, A. Fujita, T. Kanomata, and K.Ishida, "Magnetic-field-induced shape recovery by reverse phase transformation" Nature **439**, 957 (2006).

[146] A. Satish Kumar, M. Ramudu, and V. Seshubai, "Effect of selective substitution of Co for Ni or Mn on the superstructure and microstructural properties of $Ni_{50}Mn_{29}Ga_{21}$" J. Alloy. Compd. **509**, 8215 (2011).

[147] A. K. Nayak, K. G. Suresh, and A. K. Nigam, "Observation of enhanced exchange bias behaviour in NiCoMnSb Heusler alloys" J. Phys. D: Appl. Phys. **42**, 115004 (2009).

[148] Z Li, C Jing, J Chen, S Yuan, S Cao, and J Zhang, Appl. Phys. Lett. **91**, 112505 (2007).

[149] H. C. Xuan, Q. Q. Cao, C. L. Zhang, S. C. Ma, S. Y. Chen, D. H.Wang, and Y.W. Du, "Observation of exchange bias in the martensitic state of Ni50Mn36Sn14 Heusler alloy" Appl. Phys. Lett. **96**, 202502 (2010).

[150] M. Khan, I. Dubenko, S. Stadler, and N. Ali, "Exchange bias in bulk Mn rich Ni–Mn–Sn Heusler alloys" J. Appl. Phys. **102**, 113914 (2007).

[151] B. M. Wang, Y. Liu, B. Xia, P. Ren, and L. Wang, "Large exchange bias obtainable through zero-field cooling from an unmagnetized state in Ni-Mn-Sn alloys" J. Appl. Phys. **111**, 043912 (2012).

[152] A K. Nayak, R. Sahoo, K. G. Suresh, A. K. Nigam, X. Chen, and R. V. Ramanujan, "Anisotropy induced large exchange bias behavior in ball milled Ni–Co–Mn–Sb alloys" Appl. Phys. Lett. **98**, 232502 (2011).

[153] R. Machavarapu and G. Jakob, "Exchange bias effect in the martensitic state of Ni-Co-Mn-Sn film" Appl. Phys. Lett. **102**, 232406 (2013)

[154] R. Vishnoi and D. Kaur, J. Alloys Compd. **509**, 2833 (2011).

[155] J. Dubowik, Goscianska, K. Zalteski, H. Glowinski, Y. Kudryavtrev, and A. Ehresmann, J. Appl. Phys. **113**, 193907 (2013)

[156] R. Machavarapu and G. Jakob AIP Advances **5**, 037108 (2015).

[157] A. Behler, N. Teichert, B. Dutta, A. Waske, T. Hickel, A. Auge, A. Hütten, and J. Eckert AIP Advances **3**, 122112 (2013).

[158] I. Gociaskaa , K. Zae skib , H. Gowiskib , Yu.V. Kudryavtsevc and J. Dubowikb, "Exchange Bias in Ni-Mn-Sn Heusler Alloy Films" Acta Physica Polonica A, **121** 1179-1181 (2011).

[159] H. Akkera, R. Barman, N. Kaur, N. Choudhary, and D. Kaura, "Exchange bias effect in NiMnSb/CrN heterostructures deposited by magnetron sputtering" Jour. Applied phys. **113**, 17D723 (2013).

[160] Mauri D, Kay E, Scholl D, et al. "Novel method for determining the anisotropy constant of MnFe in a NiFe/MnFe sandwich" J Appl Phys, **62**, 2929 (1987)

[161] Seua K A, Huang H, Lesoine J F, et al. "Co layer thickness dependence of exchange biasing for IrMn/Co and FeMn/Co" J Appl Phys, **93**, 6611 (2003)

[162] Liu Z Y, Adenwalla S. "Variation of domain formation in a 15 nm NiFe layer exchange coupled with NiO layers of different thicknesses" Appl Phys Lett, **82**, 2106 (2003)

[163] H Xi, R. M. White, "Critical thickness effect in the exchange-coupled NiFe/CrMnPtx bilayer system" Phys Rev B, **61** 1318 (2000)

[164] M. Ali, C. H. Marrows, M. Al-Jawad, B. J. Hickey, A. Misra, U. Nowak, and K. D. Usadel, "Antiferromagnetic layer thickness dependence of the IrMn/Co exchange-bias system" Phys Rev B **68** 214420 (2003)

[165] A. L. Kobrinskii, A. M. Goldman, Maria Varela, and S. J. Pennycook, "Thickness dependence of the exchange bias in epitaxial manganite bilayers" Phys Rev B, **79** 094405 (2009)

[166] Choi H C, You C Y, Kim K Y, **"**Antiferromagnetic layer thickness dependence of noncollinear uniaxial and unidirectional anisotropies in NiFe/FeMn/CoFe trilayers" Phys Rev B, **81** 224410 (2010)

[167] Van Driela J, de Boer F R, Lenssen K M H, "Exchange biasing by Ir19Mn81: Dependence on temperature, microstructure and antiferromagnetic layer thickness" J Appl Phys, **88** 975 (2000)

[168] Li H Y, Chen L Y, Zhou S M, "Thermal stability of exchange coupling in permalloy/FeMn bilayers and its dependence on the antiferromagnetic layer thickness" J Appl Phys, **91** 2243 (2002)

[169] Ali M, Marrows C H, Hickey B J, "Onset of exchange bias in ultrathin antiferromagnetic layers" Phys Rev B, **67** 172405 (2003)

[170] Rodríguez-Suúrez R L, Vilela-Leúo L H, Bueno T, "Critical thickness investigation of magnetic properties in exchange-coupled bilayers" Phys Rev B, **83** 224418 (2011)

[171] K. R. A. Ziebeck and P J Webster, "Helical magnetic order in Ni_2MnAl" J. Phys. F: Met. Phys. **5** 1756 (1975).

[172] Vijay Kumar Srivastava, Saurabh Kumar Srivastava, Ratnamala Chatterjee, Govind Gupt, S. M. Shivprasad, and A. K. Nigam, "Structural and magnetic phenomena in Ni53Mn25Al22 thin film prepared by rf magnetron sputtering" Appl. Phys. Lett. **95**, 114101 **(**2009).

[173] A. Fujita, K. Fukamichi, F Gejima, and R. Kainuma, K. Ishida, "Magnetic properties and large magnetic-field-induced strains in off-stoichiometric Ni–Mn–Al Heusler alloys" Appl. Phys. Lett. **77**, 3054 (2000).

[174] T. Krenke, E. Duman, M. Acet, E. F. Wassermann, X. Moya, L. Manosa, A. Planes, "Magnetic superelasticity and inverse magnetocaloric effect in Ni-Mn-In" Phys Rev B **75** 104414 (2007)

[175] D. N. Lobo, K. R. Priolkar,1, S. Emura, and A. K. Nigam, "Ferromagnetic interactions and martensitic transformation in Fe doped Ni-Mn-In shape memory alloys" J Appl Phys **116**, 183903 (2014).

[176] J. I. Pérez-Landazábal, V. Recarte, V. Sánchez-Alarcos, C. Gómez-Polo and E. Cesari Magnetic properties of the martensitic phase in Ni-Mn-In-Co metamagnetic shape memory alloys" Appl. Phys. Lett. **102**, 101908 (2013))

[177] K. Ullakko, J. K. Huang, C. Kantner, R. C. O'Handley, and V. V. Kokorin, "Large magnetic-field-induced strains in Ni_2MnGa single crystals" Appl. Phys. Lett. **69** 1966 (1996).

[178] T. Krenke, E. Duman, M. Acet, E. F. Wassermann, X. Moya, L. Manosa, and A. Planes, "Inverse magnetocaloric effect in ferromagnetic Ni–Mn–Sn alloys" Nature Materials **4** 450 (2005)

[179] A. K. Pathak, B. R. Gautam, I. Dubenko, M. Khan, S. Stadler and N. Ali, Phase transitions and magnetoresistance in $Ni_{50}Mn_{50-x}In_x$ Heusler alloys" J. Appl. Phys. **103** 07F315 (2008)

[180] B. M. Wang, L. Wang, Y. Liu, B. C. Zhao, Y. Zhao, Y. Yang and H. Zhang, "Strong thermal-history-dependent magnetoresistance behavior in $Ni_{49.5}Mn_{34.5}In_{16}$" J. Appl. Phys. **106** 063909 (2009).

[181] D. Pal, K. Mandal, O. Gutfleisch," Large negative magnetoresistance in nickel-rich Ni–Mn–Ga Heusler alloys" J. Appl. Phys. **107** 09B103 (2010).

[182] H. C. Xuan, L. J. Shen, T. Tang, Q. Q. Cao, D. H. Wang, Y. W. Du, "Magnetic-field-induced reverse martensitic transformation and large magnetoresistance in $Ni_{50-x}Co_xMn_{32}Al_{18}$ Heusler alloys" Appl. Phys Lett. **100** 172410 (2012).

[183] M. Khan I. Dubenko, S. Stadler, N. Ali, "Exchange bias behavior in Ni–Mn–Sb Heusler alloys" Appl. Phys. Lett. **91** 072510 (2007).

[184] B. M. Wang,Y. Liu, L. Wang, S. L. Huang, Y. Zhao, Y. Yang, H. Zhang, "Exchange bias and its training effect in the martensitic state of bulk polycrystalline $Ni_{49.5}Mn_{34.5}In_{16}$" J. Appl. Phys. **104**, 043916 (2008).

[185] B. M. Wang, Y. Liu, P. Ren, B. Xia, K. B. Ruan, J. B. Yi, J. Ding, X. G. Li, and L. Wang, Phys Rev Lett. **106**, 077203 (2011).

[186] S. Rios, D. Bufford, I. Karaman, H. Wang, and X. Zhang, "Magnetic field induced phase transformation in polycrystalline NiCoMnAl thin films" Appl. Phys. Lett. **103** 132404 (2013).

[187] A. Sokolov, Le Zhang, I. Dubenko, T. Samanta, S. Stadler, N. Ali, "Evidence of martensitic phase transitions in magnetic Ni-Mn-In thin films" Appl. Phys. Lett. **102** 072407 (2013).

[188] C. Paduani, A. Migliavacca, M.L. Sebben, J. D. Ardisson, M.I. Yoshida, S. Soriano, M. Kalisz, "Ferromagnetism and antiferromagnetism in $Ni_{2+x+y}Mn_{1-x}Al_{1-y}$ alloys" Solid State Communication **141** 145 (2007).

[189] M. Acet, E. Duman, E. F. Wassermann, L. Manosa, A. Planes, "Coexisting ferro- and antiferromagnetism in Ni_2MnAl Heusler alloys" J. Appl. Phys. **92** 3867 (2002).

[190] M. S. Lund, J. W. Dong, J. Lu, X. Y. Dong, C. J. Palmstrøm, C. Leighton, "Anomalous magnetotransport properties of epitaxial full Heusler alloys" Appl. Phys. Lett. **80** 4798 (2002).

[191] A. Vovk, M. Yu, L. Malkinski, C. O'Connor, Z. Wang, E. Durant, J. Tang, V.Golub, "Magnetic and transport properties of NiMnAl thin films" Jour. Appl. Phys **99** 08R503 (2006).

[192] Y. Sutou, I. Ohnuma, R. Kainuma, and K. Ishida, "Ordering and martensitic transformations of Ni_2AlMn Heusler Alloys" Metall. Mater. Trans. A **29,** 2225 (1998).

[193] L. Manosa, A. Planes, Ch. Somsen, Ch. Fell and M. Acet,, "Structural and magnetic investigations on Ni_2MnAl" J. Phys. France IV **11**, 245 (2001).

[194] L. Manosa, A. Planes, M. Acet, E. Duman, and E. F. Wassermann, "Magnetic properties and martensitic transition in annealed $Ni_{50}Mn_{30}Al_{20}$" J. Appl. Phys. **93**, 8498 (2003).

[195] R. Kainuma, F. Gejima, Y. Sutou, I. Ohnuma and K. Ishida, "Ordering, martensitic and ferromagnetic transformations in Ni-Al-Mn Heusler shape memory alloys" Mater. Trans. JIM **41**, 943 (2000).

[196] T. Inoue, S. Morito, Y. Murakami, K. Oda, and K. Otsuka, "New martensite structures and composition dependence of martensitic transformations in $Ni_{50}Al_xMn_{50-x}$ alloys" Mater. Lett. **19**, 1333 (1994).

[197] T. Mehaddene, J. Neuhaus, W. Petry, K. Hradil, P. Bourges, and A. Hiess, "Interplay of structural instability and lattice dynamics in Ni_2MnAl" Phys. Rev. B **78**, 104110 (2008).

[198] S. Morito, T. Kakeshita, K. Hirata, and K. Otsuka, "Magnetic and martensitic transformations in $Ni_{50}Al_xMn_{50-}$xalloys" Acta Metall. **46,** 5377 (1998).

[199] S. Morito, K. Otsuka, "Electron microscopy of new martensites with long period stacking order structures in $Ni_{50}Al_xMn_{50-x}$ alloys I. Structures and morphologies" Mater. Sci. Engg. A **208** 47 (1996).

[200] F. Gejima, Y. Sutou, R. Kainuma, and K. Ishida, Metall. Mater. Trans. A **30**, 2721 (1999).

[201] H. Ishikawa, R. Y. Umetsu, K. Kobayashi, A. Fujita, R. Kainuma, and K. Ishida, Acta Mater. **56**, 4789 (2008).

[202] S.E. Muthu, N.V.R. Rao, D.V.S. Rao, M.M. Raja, U. Devrajan, J. Appl. Phys. **110** 023904 (2011)

[203] S. Chatterjee, S. Giri, S.K. Giri, S. Majumdar, Phys. Rev. B 79 092410 (2009)

[204] B. Maji, K.G. Suresh, A.K. Nigam, J. Phys. Condens. Matter 23 506002 (2011)

[205] F. Vaz, P. Cerqueir, L. Rebouta, S.M.C. Nasciment, E. Alves, P. Goudeau, J.P. Riviere, K. Pischow, J.D. Rijk, Thin Solid Films **447** 449 (2004)

[206] M. Halder, S. M. Yusuf, A. Kumar, A. K. Nigam, and L. Keller "Crossover from antiferromagnetic to ferromagnetic ordering in the semi-Heusler alloys Cu1−xNixMnSb with increasing Ni concentration" Phys. Rev. B **84**, 094435 (2011)

[207] M Thakur, M Patra, K De, S Majumdar and S Giri "Particle size dependent exchange bias and cluster-glass states in $LaMn_{0.7}Fe_{0.3}O_3$" J. Phys.: Condens. Matter 20 195215 (2008)

[208] R. Singh, B. Ingale, L. K. Varga, V. V. Khovaylo, S. Taskaev, Ratnamala Chatterjee, "Large exchange bias in polycrystalline ribbons of $Ni_{56}Mn_{21}Al_{22}Si_1$ Jour. of Magn. Mag. Mat. **394** 143 (2015)

[209] S. Yuan, K. Xu, Z Li, L. Yu, B. Kang and S. Cao "Exchange bias and spin glassy behavior in low doped $La_{1-x}Sr_xCoO_0$ cobaltites" J. Appl. Phys. **105**, 093910 (2009)

[210] Annaorazov M P, Nikitin S A, Tyurin A L, Asatryan K A and Dovletov A Kh 1996 J. Appl. Phys. 79 1689

[211] Yu M H, Lewis L H and Moodenbaugh A R 2003 J. Appl. Phys. 93 10128

[212] Chattopadhyay M K, Manekar M A and Roy S B 2006 J. Phys. D: Appl. Phys. 39 1006

[213] Zhang Y Q and Zhang Z D 2004 J. Alloys Compounds 365 35

[214] J Du, Q Zheng, W J Ren, W J Feng, X G Liu and Z D Zhang, J. Phys. D: Appl. Phys. 40 (2007) 5523–5526

[215] P. J. Webster and K. R. A. Ziebeck, "Heusler Alloys, in Magnetic Properties of Metals, Landolt-Bornstein New Series Group III €" edited by H. R. J. Wijn (Springer, Berlin, 1988), vol. 19C, p. 75.

[216] C. Kittel, Introduction to Solid State Physics (John Wiley Sons, New York, 1976).

[217] A. P. Malozemoff, B. Barbara, and Y. Imry, "further studies of nonlinear susceptibility of GdAl and MnCu spin glasses" J. Appl. Phys. **53**, 2205 (1982).

[218] J. M. D. Coey, D. Givord, A. Lienard, and J. P. Rebouillat, "Amorphous yttrium-iron alloys. I. Magnetic properties" J. Phys. F: Met. Phys. **11**, 2707 (1981).

[219] R. Chatterjee, R. A. Dunlap, V. Srinivas, and R. C. O'Handley, "Concentrated spin-glass behavior in Al37Mn30Si33 quasicrystals" Phys. Rev. B **42**, 2337 (1990).

[220] E. C. Passamani, F. Xavier, E. Favre-Nicolin, C. Larica, A. Y. Takeuchi, I. L. Castro and J. R. Proveti, "Magnetic properties of NiMn-based Heusler alloys influenced by Fe atoms replacing Mn" J. Appl. Phys. **105**, 033919 (2009)

[221] Ali C. Basaran, T. Saerbeck, J. de la Venta, H. Huckfeldt, A. Ehresmann and I. K. Schuller, "Exchange bias: The antiferromagnetic bulk matters" Appl. Phys. Lett. **105**, 072403 (2014)

[222] Z. Y. Liu, "Recent advances in exchange bias of layered magnetic FM/AFM systems" Science China Physics, Mechanics & Astronomy **56** 61 (2013)

[223] Callister WD "Materials Science and Engineering: An introduction" New York, NY: John Wiley & Sons, 2006

[224] P. Kuswik, P. L. Gastelois, M. M. Soares, H. C. N. Tolentino, M. De Santis, A. Y. Ramos, A. D. Lamirand, M. Przybylski, and J. Kirschner, "Effect of CoO/Ni orthogonal

exchange coupling on perpendicular anisotropy of Ni films on Pd(001)" Phys. Rev. B **91**, 134413 (2015)

[225] P.Y. Yang, F. Zeng, F. Pan, "Exchange bias and training effect in Ni/Ag-doped NiO bilayers" Journal of Magnetism and Magnetic Materials **322**, 542–547 (2010)

[226] R. Jungbtut et al. J. Appl. Phys. 75 6424 (1994)

[227] B. Schulz and K. Baberschke, Phys. Rev. B 50, 13467 (1994)

[228] E. Arenholza, K. Liu, Z. Li and I. K. Schuller Appl. Phys. Let. 88, 072503 (2006)

[229] S. Bedanta and W. Kleemann, J. Phys. D: Appl. Phys. **42**, 013001 (2009)).

[230] C. L. Tan, Y. W. Huang, X. H. Tian, J. X. Jiang, and W. Cai, "Origin of magnetic properties and martensitic transformation of Ni-Mn-In magnetic shape memory alloys" Appl. Phys. Let. 100, 132402 (2012)

[231] J. Enkovaara, A. Ayuela, L. Nordström and R. M. Nieminen, "Structural, thermal, and magnetic properties of Ni2MnGa" J. Appl. Phys. 91, 7798 (2002).

[232] M. Kreissl, K.-U. Neumann, T. Stephens and K. R. A. Ziebeck, J. Phys.: Condens. Matter 15, 3831 (2003).

[233] A.T. Zayak and P. Entel, Mater. Sci. Eng. A 378, 419 (2004).

[234] J. M. Raulot and C. Domain, "Fe-doped CuInSe2: An ab initio study of magnetic defects in a photovoltaic material" Phys. Rev. B 71, 035203 (2005).

[235] V. Sánchez-Alarcos, V. Recarte, J. I. Pérez-Landazábal and G. J. Cuello, Acta Mater. 55, 3883 (2007).

[236] Q. M. Hu, C. M. Li, R. Yang, S. E. Kulkova, D. I. Bazhanov, B. Johansson, L. Vitos, "Site occupancy, magnetic moments, and elastic constants of off-stoichiometric Ni2MnGa from first-principles calculations" Phys. Rev. B 79, 144112 (2009).

[237] R. Kainuma, Y. Imano, W. Ito, Y. Sutou, H. Morito, S. Okamoto,O. Kitakami, K. Oikawa, A. Fujita, T. Kanomata, and K. Ishida, "Magnetic-field-induced shape recovery by reverse phase transformation" Nature 439, 957 (2006).

[238] K. Oikawa, W. Ito, Y. Imano, Y. Sutou, R. Kainuma, K. Ishida, S. Okamoto, O. Kitakami, and T. Kanomata, "Effect of magnetic field on martensitic transition of Ni46Mn41In13Heusler alloy" Appl. Phys. Lett. 88, 122507 (2006).

[239] T. Krenke, M. Acet, E. F. Wassermann, "Ferromagnetism in the austenitic and martensitic states of Ni−Mn−In alloys" Phys. Rev. B 73, 174413 (2006)

[240] Rakesh Rana, Parul Pandey, R. P. Singh & D. S. Rana, "Positive exchange-bias and giant vertical hysteretic shift in $La_{0.3}Sr_{0.7}FeO_3/SrRuO_3$bilayers" Scientific Reports **4**, 4138 (2014).